UNIVERISTÀ DEGLI STUDI DI PADOVA

Dipartimento di Ingegneria Industriale

Scuola di Dottorato in Ingegneria Industriale

Indirizzo Progettazione Meccanica e Ingegneria Motociclistica

XXV Ciclo

Tesi di Dottorato

Design and analysis of a RFQ resonant cavity for the IFMIF project

Direttore della Scuola: Ch.mo Prof. Paolo Colombo

Coordinatore di Indirizzo: Ch.mo Prof. Alberto Doria

Supervisori :Ch.mo Prof. Giovanni Meneghetti e Ing. Adriano Pepato

Dottorando: Francesco Scantamburlo

I want to dedicate his work to my fiancée Betty and to my Family, giving me fundamental and special support.

Special thanks to Eng. A. Pepato, Prof. G. Meneghetti, Eng. R. Dima: they have been constantly a guide on these three years and giving to me lot of indications for the work of this three years, teaching to me lot of things and also for the special human relationship that was created.

Special thanks also to all my colleagues of the engineering department of the INFN of Padova, the mechanical workshop of INFN of Padova and all the IFMIF team of LNL: I learned lot of things with you and a special human relationship was created.

The author wants also to thank the Cinel Strumenti Scientifici S.r.l. for the active sustaining during the R&D phase and the BYTEST S.r.l. for the collaboration on the R&D

INDEX

List of abbreviation

IFMIF: International Fusion Material Irradiation Facility

RFQ: RadioFrequency Quadrupole

INFN: Istituto Nazionale di Fisica Nucleare

LNL: Laboratori Nazionali di Legnaro

PD: Padova

CERN: Conseil Europèen pour la Recherche Nuclèaire

CMM: Coordinate Measuring Machine

PCMM: Portable Coordinale Measuring Machine

UT: ultrasonic non destructive inspection

INTRODUCTION

The greatest increase in demand for energy is envisaged to come from developing countries where, with rapid urbanization, large-scale electricity generation will be required. In conjunction to the requirements of zero CO_2 emissions, an important possibility is the nuclear fusion, although technically difficult.

Lot of international efforts are done in this field, with many active projects.

In particular ITER (International Thermonuclear Experimental Reactor) aims to the construction of a fusion reactor to demonstrate the feasibility of energy production. Many countries are involved, such as the members of European Union, Japan, India, Russia, etc.

Another important project will be DEMO (DEMOnstratio Power Plant), which aims to the construction of a fusion reactor to demonstrate the feasibility of the production of electric energy for long time in a stable way.

Among all the projects on the research of nuclear fusion, IFMIF (International Fusion Material Irradiation Facility) plays a very important role. The target is the realization of a facility for the test of the materials to be used in the fusion reactors.

The work will be presented in this PhD thesis is collocated among this project.

INFN (Istituto Nazionale di Fisica Nucleare) is involved on the design and the realization of the RFQ (RadioFrequency Quadrupole) of IFMIF, with the collaboration of the laboratories of Legnaro (LNL) and the sections of Padova, Torino and Bologna.

The work will be presented in this PhD thesis regards the RFQ (RadioFrequency Quadrupole) of IFMIF, since the INFN (Istituto Nazionale di Fisica Nucleare) was involved on the design and the realization of the resonator.

During the three years of PhD the candidate was involved on different aspects, from the mechanical design to the quality control on the production process.

Chapter 1 presents a general overview of the IFMIF project and the scientific context.

On chapter 2 the design of the cooling system of the modules of the accelerator will be described, with the development of thermal-structural and fluid-thermal-structural numerical analyses.
Chapters 3 and 4 will describe the development of an in-house technology for the vertical brazing and the fixation tooling, by means a strict collaboration of the section of Padova of INFN and the LNL. The developments of 1D and 3D FE analyses for the prediction of the thermal brazing cycle will be described.
Moreover, the improvements on the control (visual and ultrasonic inspection) of the brazed joints and the feedbacks to the mechanical design will be presented.
Chapter 5 will describe the various phases of the production of the modules of the RFQ with the most important mechanical design aspects.
The focus will be in particular to the quality control of the single elements and the entire modules during the production:

- The dimensional quality control, prevalently by CMM with active scanning probe.
- The quality assurance of the brazed joints by visual and the ultrasonic inspection.

Their influence for the design choices and the solution of eventual problem will be described.

This three years PhD work lead to the following publications:

- A. Pepato, F. Scantamburlo “ENGINEERING DESIGN AND FIRST PROTOTYPE TESTS ON THE IFMIF-EVEDA RFQ”, et al., IPAC 10 (International Particle Accelerator Conference), 23-28 May 2010, Kyoto (Japan), p.600

- F. Scantamburlo, A. Pepato, “3D THERMO MECHANICAL STUDY ON IFMIF-EVEDA RFQ”, LINAC 10 (Linear Accelerator Conference), 12-17 September 2010, Tsukuba (Japan), p. 539

- A. Palmieri, F. Grespan, F. Scantaburlo “3D ASPECTS OF THE IFMIF-EVEDA RFQ: DESIGN AND OPTIMIZATION OF THE VACUUM GRIDS, OF THE SLUG TUNERS AND OF THE END CELL”, LINAC 10 (Linear Accelerator Conference), 12-17 September 2010, Tsukuba (Japan), p.533

- A. Pisent, A. Pepato, F. Scantamburlo, “RFQ MODULE TECHNOLOGICAL PROTOTYPE”, A. Pisent, A. Pepato, IFMIF DMS (Document Management System) reference BA_D_229547, October 2011.

- F. Scantamburlo, A. Pepato, R. Dima, “PRODUCTION AND QUALITY CONTROL OF THE FIRST MODULES OF THE IFMIF-EVEDA RFQ”, LINAC12 (Linear Accelerator Conference), 9-14 September 2012, Tel Aviv (Israel), on proceeding

(*Thispage is left intentioanlly black)*

INTRODUZIONE

Il più grande aumento della domanda di energia è previsto provenire da paesi in via di sviluppo dove, con la rapida urbanizzazione, sarà richiesta la produzione di energia elettrica su larga scala. Con le richieste ambientali di zero emissioni di CO_2 un'importante possibilità è la fusione nucleare, anche se tecnologicamente molto difficile. L'impegno internazionale è molto forte in questo campo, con molti progetti attivi.

In particolare ITER (International Thermonuclear Experimental Reactor), che coinvolge gruppi di ricerca di diversi paesi (come ad esempio gli stati membri dell'Unione Europea, Giappone, India, Russia, etc.), mira alla costruzione di un reattore a fusione per dimostrare la fattibilità di ottenere energia.

Un altro progetto molto importante sarà DEMO, che mira alla costruzione di un reattore a fusione per dimostrare la fattibilità di produrre energia elettrica a tempo indeterminato in maniera stabile.

Tra tutti questi progetti anche IFMIF (International Fusion Material Irradiation Facility) riveste un ruolo di fondamentale importanza. Lo scopo è la realizzazione di un impianto per testare i materiali da impiegare nel rivestimento interno dei reattori a fusione.

Il lavoro svolto in questa tesi di dottorato si colloca all'interno di questo progetto.

L'INFN è coinvolto nella progettazione e realizzazione della cavità risonante di tipo RFQ (Radio Frequency Quadrupole), attraverso i laboratori di Legnaro (LNL), le sezioni di Padova, Torino e Bologna.

In questo lavoro di tesi il candidato si è occupato di diversi aspetti, dalla progettazione meccanica della cavità al controllo qualità del processo produttivo.

Il capitolo 1 fornisce una presentazione generale del progetto IFMIF e del contesto scientifico ad esso legato. Il capitolo 2 presenta in dettaglio gli aspetti della progettazione del sistema di raffreddamento dei moduli della linea acceleratrice, attraverso simulazioni numeriche termostrutturale e fluido termo strutturali.

Nei capitoli 3 e 4 è descritto lo sviluppo di una propria tecnologia per la brasatura verticale dell'attrezzatura di brasatura attraverso una stretta collaborazione tra l'INFN di Padova per la progettazione e i laboratori INFN di Legnaro per la realizzazione. Inoltre lo sviluppo di strumenti per il calcolo dei cicli termici di brasatura tramite analisi monodimensionali e tridimensionali tramite codici agli elementi finiti è descritto. Lo sviluppo di metodologie per il controllo dei giunti brasati e la loro influenza sulle scelte progettuali saranno presentati.
Il capitolo 5 fornisce un quadro delle varie fasi della produzione dei moduli della cavità. L'attenzione è stata focalizzata soprattutto sul controllo qualità dei singoli elementi e dei moduli completi nel processo produttivo:

- Il controllo dimensionale prevalentemente tramite CMM dotata di testa a scansione attiva.
- Il controllo delle brasature tramite ispezione visiva e l'utilizzo della tecnica degli ultrasuoni.

La loro influenza sulle scelte progettuali e la soluzione di eventuali problemi saranno descritte.

Il seguente lavoro di tesi ha portato inoltre alle seguenti pubblicazioni:

- A. Pepato, F. Scantamburlo "ENGINEERING DESIGN AND FIRST PROTOTYPE TESTS ON THE IFMIF-EVEDA RFQ", et al., IPAC 10 (International Particle Accelerator Conference), 23-28 May 2010, Kyoto (Japan)

- F. Scantamburlo, A. Pepato, "3D THERMO MECHANICAL STUDY ON IFMIF-EVEDA RFQ", LINAC 10 (Linear Accelerator Conference), 12-17 September 2010, Tsukuba (Japan)

- A. Palmieri, F. Grespan, F. Scantaburlo “3D ASPECTS OF THE IFMIF-EVEDA RFQ: DESIGN AND OPTIMIZATION OF THE VACUUM GRIDS, OF THE SLUG TUNERS AND OF THE END CELL”, LINAC 10 (Linear Accelerator Conference), 12-17 September 2010, Tsukuba (Japan)

- A. Pisent, A. Pepato, F. Scantamburlo, “RFQ MODULE TECHNOLOGICAL PROTOTYPE”, A. Pisent, A. Pepato, IFMIF DMS (Document Management System) reference BA_D_229547, October 2011.

- F. Scantamburlo, A. Pepato, R. Dima, “PRODUCTION AND QUALITY CONTROL OF THE FIRST MODULES OF THE IFMIF-EVEDA RFQ”, LINAC12 (Linear Accelerator Conference), 9-14 September 2012, Tel Aviv (Israel), on proceeding

(This page is intentionally left blank)

CHAPTER 1: THE IFMIF PROJECT

1.1 The nuclear fusion[1]

Today, the European Union imports more than 50% of its energy, mostly in the form of oil and gases, from outside the Union. The European energy bill amounts to a negative trade balance of 240 billion Euros every year.

The EU Member States consume more than 1725 million tonnes of oil every year at a cost of 500 billion Euros. By 2015, it is expected that European energy demand will grow to 1900 million tonnes.

Many of the regions of the world that supply our energy are geographically remote and some may be politically unstable. With current trends, it is predicted that by 2030 the EU will depend on imported energy for 70% of its total needs.

Over the next 50 years, the global demand for energy may double in countries such as China and India, where they would need increasing amount of power for their growing economies and their standards of living.

For a world critically dependent on energy, maintaining a reliable and secure supply is essential.

Europe needs to develop a wide sustainable energy mix. According to the Eurobarometer, 82% of Europeans acknowledge that the way they consume and produce energy has a negative impact on climate. At the same time, 50% perceive climate change as one of the most serious problems our world faces and call for immediate action.

The majority of the EU citizens agree with the fact that Europe has to take a leading role on the development of new energy forms to reduce its dependence from other countries.

Fusion is an energy source that fits well the requirements mentioned above:

- Abundance of fuel: the basic fuels from which deuterium and tritium are extracted and generated are water and lithium. 70% of the surface of the earth is covered by water and 30% is covered by rock. There is enough

[1] All the information on this paragraph have been taken from [1]

deuterium for years, and easily mined lithium for hundreds years. Tritium cannot be extracted directly in nature. It can be made using the high energy neutron released from the fusion reaction and offers the possibility of making tritium in situ in a fusion reactor. The neutron is absorbed by the lithium to produce tritium.

- Very low global impact on the environment: A 100 MW electric fusion power plant would consume around 100 kg of deuterium and three tonnes of natural lithium in a year whilst generating 7 billion kWh. To generate the same amount of electricity, a coal-fired power plant would need around 1.5 million tonnes of coal. Our use of fossil fuels produces pullants, including nitrous oxides and carbon dioxide. In particular, the increasing levels of carbon dioxide in the atmosphere due to the burning fossil fuels are a significant contributor to global warming. Continued and increasing use of fossil fuels, with the consequent increase in carbon dioxide and the other greenhouse gases emissions, could have a profound effect on local climates. Energy consumption results in 78% of EU gas emissions.
- Power stations would be inherently safe, with no possibility of "meltdown" or "runaway reactions". A fusion reactor is like a gas burner with all the fuel injected being 'burnt' in fusion reaction. The density of fuel in the reaction chamber will be very low at around 1 gram of deuterium/tritium fuel in a volume of 1000 m^3. Any malfunction will cool down the plasma and stop the reactions. The fusion fuels, deuterium and lithium, and the helium produced by the reactions are not radioactive. Tritium is radioactive but decays quite quickly (a half life of 12.6 years) producing a low energy electron (beta decay). However, the tritium will be produced and used within the fusion reactor and appropriate safety features will be incorporated into any plant to avoid its release.
- Day-to-day-operation of a fusion power station would not require the transport of radioactive materials.
- No long-lasting radioactive waste to create a burden on future generations. The neutrons produced during the fusion reaction will interact with

materials close to the reactor. In future fusion power plants, careful choice of materials around the hot plasma will ensure that no long-term legacy of radioactive waste is produced by fusion power. A careful choice of the materials for these components will allow them to be released from regulatory control and possibly recycled about 100 years after the power plant stops operating.

- No requirement for evacuation of neighboring populations.

Fusion will be available as a future energy option by the middle of the current century and should be able to acquire a significant role in providing a sustainable, secure and safe solution to tackle global energy needs.

Fusion is the process which power the sun and the stars and its energy makes life on earth possible. It is called 'fusion' because the energy is produced by fusing together light atoms, such as hydrogen, at extremely high pressures and temperatures which exist at the center of the sun (15 million °C).

At the high temperature experienced in the sun any gas become plasma, the fourth state of the matter (gas, liquid, solid and plasma). Plasma can be described as an 'electrically-charged' gas in which the negative charged electrons in atoms are completely separated from the positively charged atomic nuclei (or ions). Although plasma is rarely found on earth, it is estimated that more than 99% of the universe exist as plasma.

In order to replicate this process on earth, gases need to be heated to extremely high temperatures of about 150 millions °C., whereby atoms become completely ionized. The fusion reaction that is easiest to accomplish is the reaction between two hydrogen isotopes: deuterium, extracted from water and tritium, produced during the fusion reaction through contact with lithium.

When deuterium and tritium nuclei fuse, they form a helium nucleus, a neutron and a lot of energy (figure 1.1)

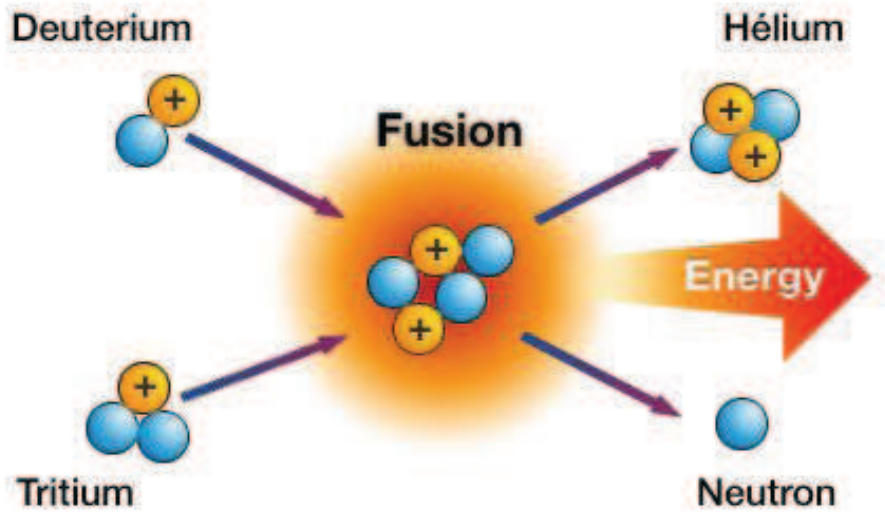

Figure 1.1 Two atoms, deuterium and tritium, fuse together, forming a helium nucleus, a neutron and a lot of energy. [1]

Scientists have built devices able to reach temperatures more the ten times higher than those in the sun.

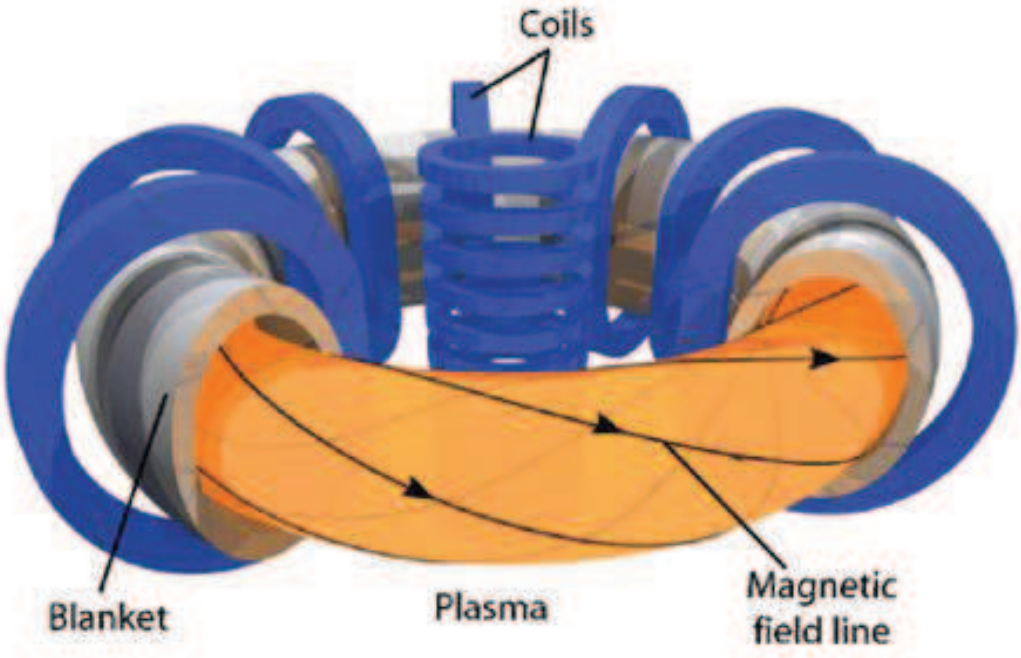

Figure 1.2 In a tokamak the plasma is held in a doughnut-shaped vessel. Using special coils, a magnetic field is generated, which causes the plasma particles to run around in spirals, without touching the wall of the chamber. (Image courtesy of EFDA). [1]

Scientists have built devices able to produce temperatures more than ten times higher than those in the sun. To reach these temperatures there must first be powerful heating, and thermal losses must be minimized by keeping the hot fuel particles away from the walls of the container. This is achieved by creating a magnetic “cage” made by strong magnetic fields which prevent the particles from escaping. For energy production this plasma has to be confined for a sufficiently long period for fusion to occur.

The most developed configuration at present is the tokamak (figure 1.2), a Russian word for a torus shaped magnetic chamber. Scientists have succeeded in producing gas with temperatures ten times higher in fusion devices. Megawatts of power have been produced for a few seconds. In Europe, this has been achieved in the Joint European Torus (JET), the world's largest fusion device which currently holds the world record for fusion power.

Nearly 2000 scientists and engineers are currently working on a broad range of fusion R&D projects in more than 20 laboratories, including JET.

Fusion energy has the potential to provide a sustainable solution to European and global energy needs. ITER, which means the way in Latin, is an international collaboration on an experimental facility. It is the world’s greatest energy project which aims to demonstrate that fusion can be part of the solution by improving our energy mix to meet the global energy needs.

However, this kind of machines will not be useful for the production of electrical energy, because the maintenance of the plasma status is not maintained in continuous, only few time.

DEMO will be the first effective fusion reactor with the aim to demonstrate the feasibility of the production of electrical energy.

1.2 Brief description of the IFMIF plant

Since DEMO will require continuous operation, the qualification of the materials inside the vessel under irradiation conditions is mandatory.

IFMIF is a project of a machine for the study of the neutron irradiation effect on such materials.

The choice of the materials of the components that face to the plasma (first wall and divertor), is one of the major problems for the design of DEMO, and, more important, of the commercial power plants based on the nuclear fusion.

In fact, the radiation emitted from the plasma (neutron overall), will have a very high impact on the modification of mechanical thermal and electrical properties of the materials of such components. Wear will be increase and even a contamination from the plasma is possible.

The IFMIF project is based on the simulation of the irradiation due to the processes of fusion, by means the production of an opportune neutronic spectrum on specimens with an opportune volume. The goal is to experiment the damage on the components that face the plasma on the typical conditions of a fusion reactor.

The realization of IFMIF will imply very high costs and a development of theoretical skills and technological solutions for LINAC (Linear Accelerator) of high intensity.

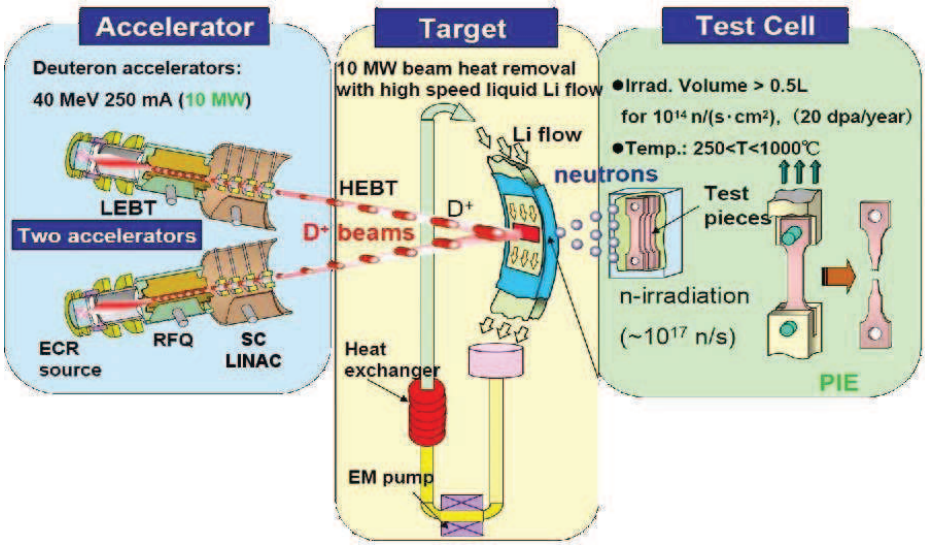

Figure 1.3 Scheme of the main parts which constitutes the machine [2]

The main component of IFMIF will be (figure 1.3):

- The system of the generation of deuterons, composed by two linear accelerators and producing a current of 125 mA and a power of 10 MW each.
- The system of the lithium target and the associated circuit for the evacuation of power. The lithium target will have to produce an intense flux of neutrons of 14 MeV.

- The test cell containing the specimens to be tested.

Figure 1.4 sketches the layout of the IFMIF plant. The accelerator system for the deuterons beam of 40 MeV is composed by: two modules of a linear accelerator RFQ (RadioFrequency Quadrupole) of 125 mA each, working in parallel, one ion source and a system for the transport of the low energy deuteron beam (LEBT – Low Energy Beam Transport), that drives the beam from the source to the RFQ accelerator. The RFQ accelerates the beam of 125 mA up to 8 MeV. The beam is then directed to a DTL (Drift Tube Linac) where it is accelerated up to 40 MeV.

On the test cell, the two beams of deuterons are focalized to a target of liquid lithium with an angle of 20 degrees, producing a neutronic irradiation. The configuration of the cell consists of two vertical assemblies (VTA) containing the specimens to be submitted to the high neutronic flux and long irradiation tests. The cell includes a system of a vertical tubes (VIT) on which are mounted the specimens for the medium and low flux test.

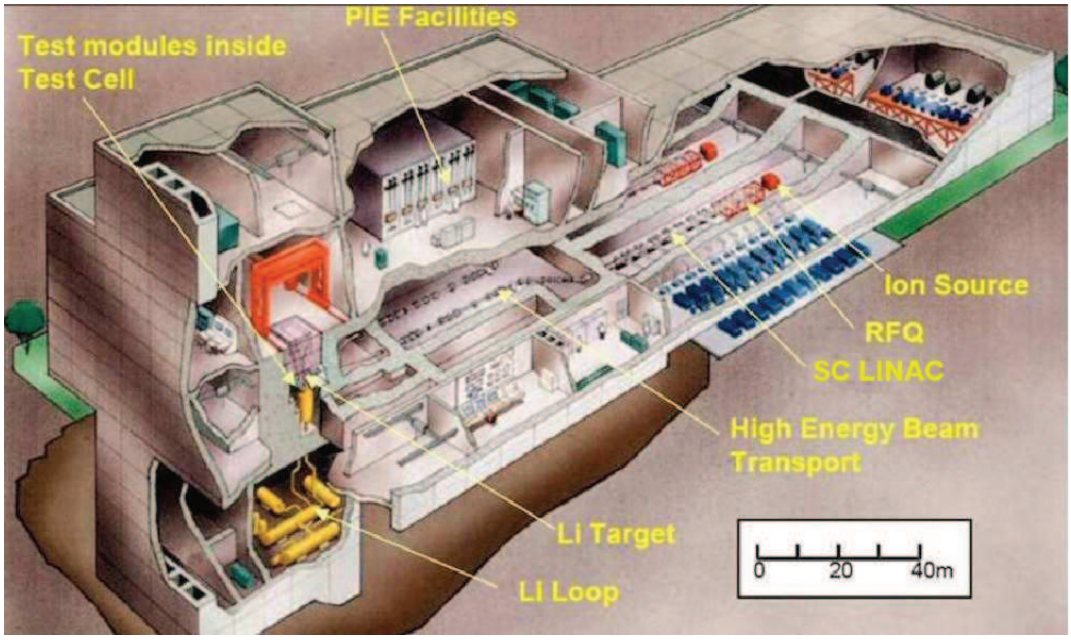

Figure 1.4 Schematich view of the IFMIF plant layout [3]

1.3 IFMIF-EVEDA: the Italian contribute and the role of the LNL laboratories and the INFN sections

The first phase of the project, as defined on the Broader Approach Agreement, is named IFMIF-EVEDA (the *Engineering Validation and the Engineering Design Activities*) and is composed by three activities to be concluded into six years:

- Overall design of IFMIF and evaluation of the operational, constructive and decommisioning costs; analysis of the safety and the ambiental impact and of the specifical techniques for the construction.
- Final design and R&D of the accelerator, of the target and the test cell; construction of a prototype of reduced scale of the test facility.
- Design, develop and test of a prototype of an accelerator of reduced energy to be constructed in Europe and installed in Rokkasho (Japan).

Once all the phases have been completed and validated, the full scale facility will be constructed in France.

The three activities are divided between the Project Team located in Rokkasho and other groups distributed between Europe and Japan.

The Italian contribute to IFMIF-EVEDA consist of two principal aspects. The first concerns the deuternons accelerator, the RFQ accelerator particularly, in charge to INFN. The second concerns the target for the production of the neutrons, in charge to ENEA (Agenzia Nazionale per le nuove tecnologie, l'Energia e lo sviluppo Economico sostenibile – National Agency for the new technologies, the Energy and the sustainable Economic development).

Italy commitment to design and construct the prototype of the RFQ for the high energy beams necessary for the IFMIF-EVEDA phase in Rokkasho, involving the INFN, in particular LNL because of the competences, experience on the physical design of linear accelerators, such as TRASCO, PIAVE. As mentioned above, the RFQ Below the list of the laboratories and the section of the INFN involved:

- LNL:
    - Phisycs design of the cavity (beam dinamics);
    - Design of the RF cavity;
    - Chemical and heat treatments on the material which constitute the modules of the RFQ;

    - The brazing on the LNL vacuum furnace of the six central (middle energy) modules of the RFQ;
    - The RF test on the final assembly;
    - The design and the realization of the vacuum, cooling and control systems;
    - RF power tests;
- INFN section of Padova:
    - Mechanical design of the modules of the RFQ;
    - Production of the six central (middle energy) modules of the RFQ;
    - Dimensional quality assurance of the modules of the RFQ;
- INFN section of Torino:
    - Development of integration: design of the support and alignment system of the RFQ, the production of the slug tuners, cooling connections;
- INFN section of Bologna:
    - Production of the stainless steel components to be brazed on the modules of the RFQ.

Since the RFQ is composed by eighteen modules (see next paragraph) and time of production are very tight, only one third of the entire production of the modules of the RFQ is built in-house. The production of the remaining modules is subdivided between two farms with a certain experience on the production of linear accelerator: the Italian farm CINEL for the last six modules of the lines and the German farm RI (Research Instruments) for the first six modules.

1.4 RFQ accelerators

This paragraph will give a short description on the operating principles of an RFQ, with all the information taken from [4]

The quadrupole RFQ (RadioFrequency Quadrupole) is a particular accelerator type which functioning principle was introduced on the early ‘60s by two Russian scientists, Kapchinskiy and Teplialov.

The peculiarity of such RFQs is to bunch, focus and accelerate the particles of the beams using the RadioFrequency Electric field only.

Such characteristic is particularly appropriate to accelerate ion beams of small velocities, typically on the range of 0.01 and 0.06 times the light speed.

In fact considering the Lorentz's force equation $\bar{F} = q \cdot (\bar{v} \times \bar{B} + \bar{E})$ (1-1), it can be noticed that it is not convenient to use the magnetic force to focus the beam: a very high magnetic field would be necessary, but its realization is not simple. The exploit of the electric component is much more convenient.

To simply understand the functioning principle of an RFQ, let us consider four electrodes symmetrically disposed about z axis (figure 1.5) with alternate polarities each other: two opposite electrodes with the same polarity and adjacent electrodes with opposite polarities.

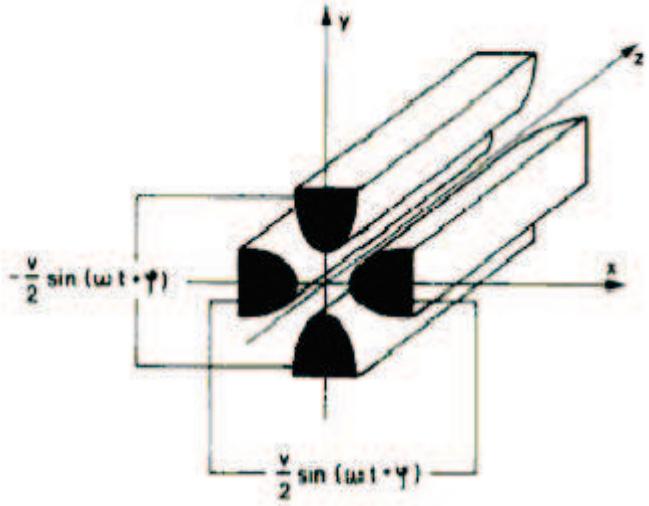

Figure 1.5 Electrical quadrupole feed with alternated voltage [4]

The electrical quadrupole has been created. Feeding the structure with a RF voltage, with the law $\pm(V_0/2)\cos(\omega t)$, an electrical RF quadrupole has been obtained.

A charged particle that moves out of the z axis is affected by an alternate electric field with quadrupole symmetry that focuses the particle on the two transversal direction x and y.

In this way the focus function of the RF on the particle is achieved. The beam must also be accelerated and a longitudinal component of the electric field must be extracted.

With the four electrodes disposed symmetrically about the z axis the particle is not affected by any accelerating force.

If the electrodes are modulated along z (figure 1.6), the potential on the axis varies with z corresponding to a non-zero component of the electrical field along the z axis. An opportune form of the electrodes would be on a first approximation a sinusoid with period $\beta\lambda$, with the sinusoid of two adjacent electrodes shifted of 180°.

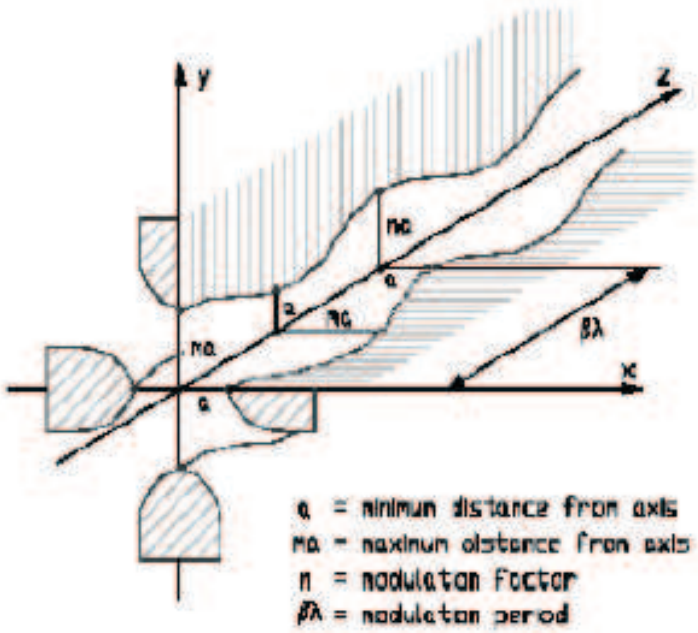

Figure 1.6 Longitudinal modulation of the electrodes [4]

1.5 The RFQ of IFMIF

As already mentioned on paragraph 1.2, the RFQ has to accelerate a deuteron beam of 125 mA from 0.1 to 5 MeV with a frequency of 175 MHz. Table 1.1 reports the input parameter of the design of the RFQ. With those parameters, the RFQ will be the first one ever built of such intensity.

The RFQ of IFMIF (figure 1.7) will be composed of 18 modules of about 550 mm length and 430x430 mm of transversal section, connected each other by means of bolted flanges.

Each module presents some lateral aperture. The greater ones are for the connections of the vacuum lines, the smaller ones are necessary for the insertion of the tuners or the input of the RF. Tuners can be schematized as cylinders with the same diameter of the aperture that can penetrate into the cavity varying the

volume of the cavity. The electromagnetic parameter that influences the mechanical design of the modules of the cavity is frequency. Since the variation from the nominal geometry of the cavity vary the operating frequency, tuners can be used to compensate the machining, assembly procedure errors and deformations due to the brazing process.

Particles	D+	
Frequency	175	MHz
Input Current	125	mA
Energy (in-out)	0.1-5	MeV
Max Surface Field	25.2	MV/m (1.8 Kp)
Length L	9.78	M
Voltage min/max	79/132	kV
Mean aperture R_0 (min//max)	4.1 / 7.1	Mm
Pole tip radius ρ	3.10/5.33	Mm

Table 1.1 Main input parameter of the RFQ

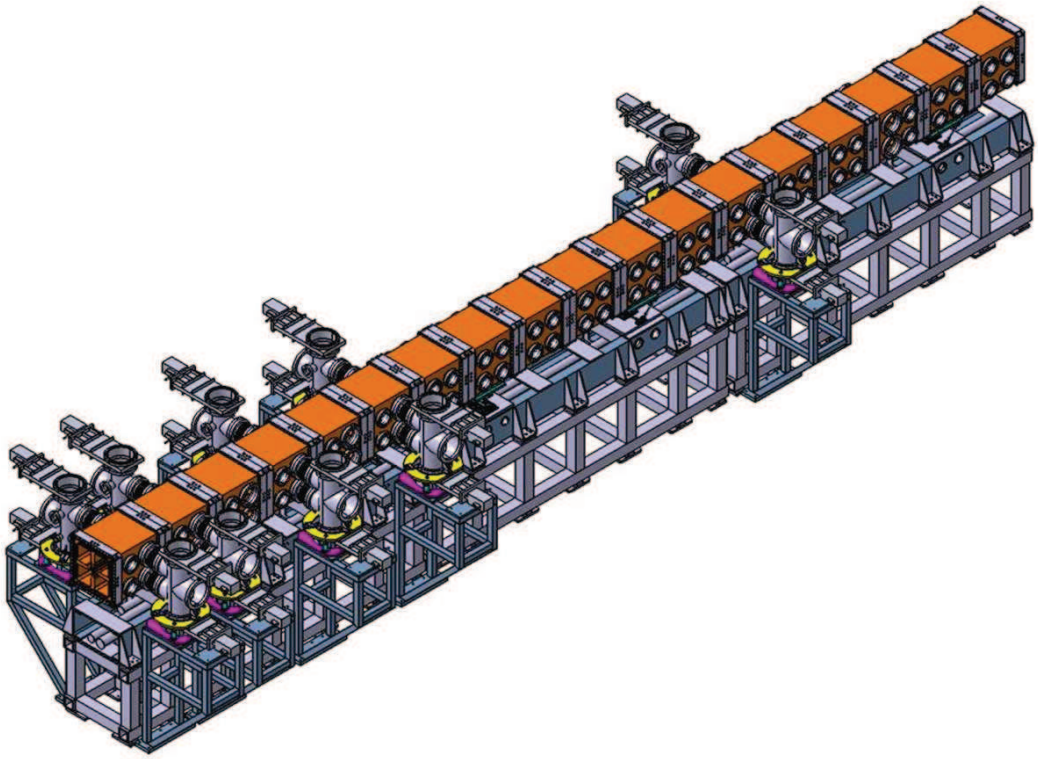

Figure 1.7 Overall view of the RFQ of IFMIF

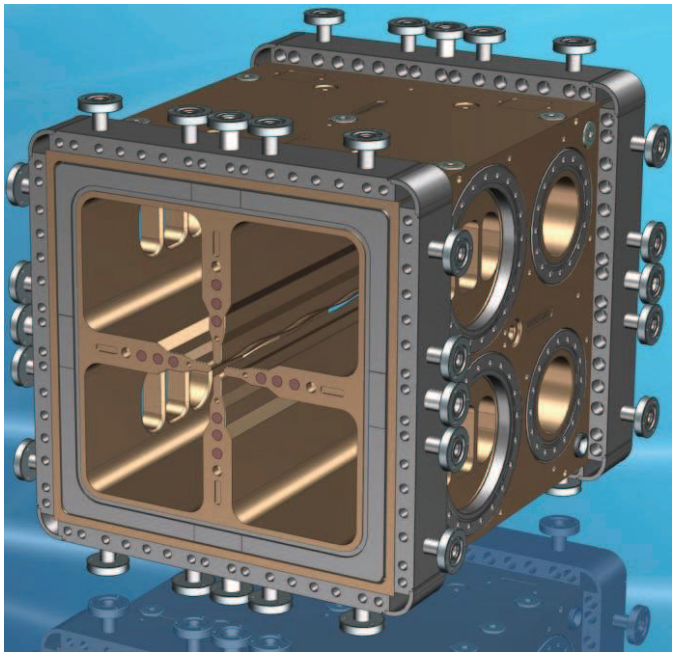

Figure 1.8 Example of a module of IFMIF

Figure 1.8 shows an example of a module of the RFQ. Each module is composed by 4 copper OFE CuC2 electrodes, two T shaped and other two E shaped machined elements (figure 1.9) joined together by vacuum brazing. On the E shaped component the apertures for the tuners or the vacuum ports are also machined.

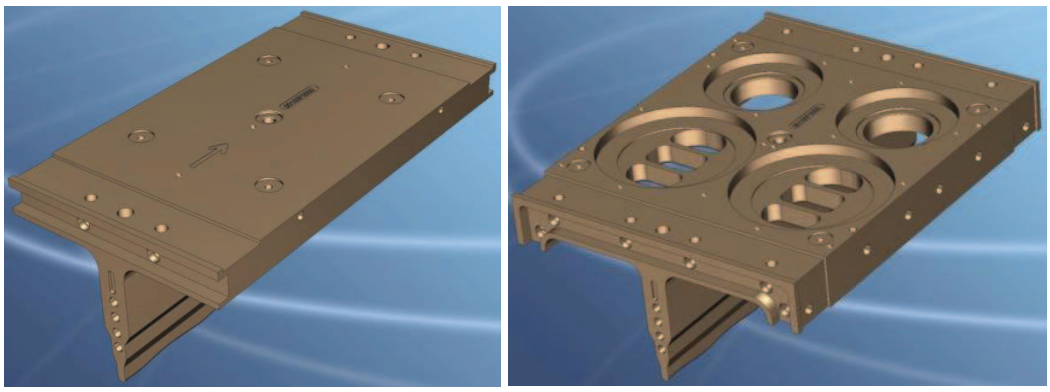

Figure 1.9 The T-shaped electrode (left) and the E-shaped electrode (right)

The internal geometry of the RFQ is something very complex.

The internal geometry of the cavity is not constant along the full length of the RFQ. In particular, in order to minimize the beam losses and to maintain the cut off frequency the width of the electrode (figure 1.10 and 1.11) varies in a range of

30-80 mm, the pole tip radius (0.75 times R_0, according to table 1.1) as well the distance from the beam axis (R_0, according to table 1.1) varies (figure 1.12).

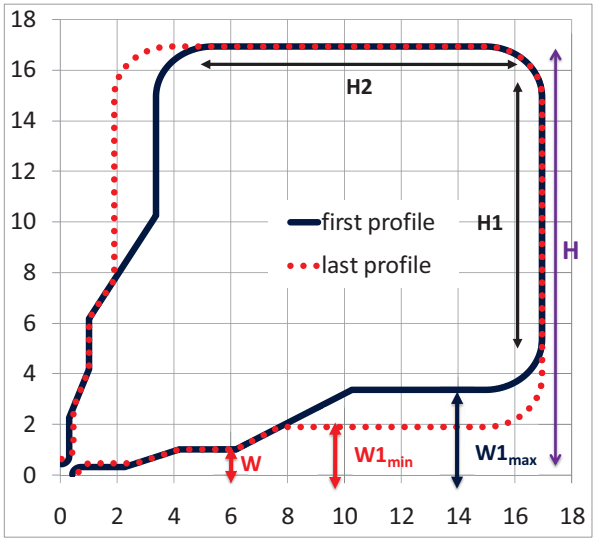

Figure 1.10 Internal profile variation of the RFQ

Since the machine operate at pressure of 10^{-7} mbar and the dimensional tolerances are very tight, brazing technique has been chosen because it is one of the promising in term of vacuum tightness and the respect of high precision alignment (table 1.2) [5].

OFE CuC2 copper found its typical application on the RF cavities and it has been chosen because of the need of high thermal, electrical conductance; it is also particular recommended in case of vacuum brazing [6]. Since the copper OFE soften during the thermal brazing cycle, with losses on the mechanical properties (the yield strength reduces to 69 MPa after a annealing/brazing cycle [7]) Glidcop® (Copper reinforced with Alumina oxide) could be used [6]; it do not suffer of softening during the thermal heat treatments, but the high cost of the material were not sustainable.

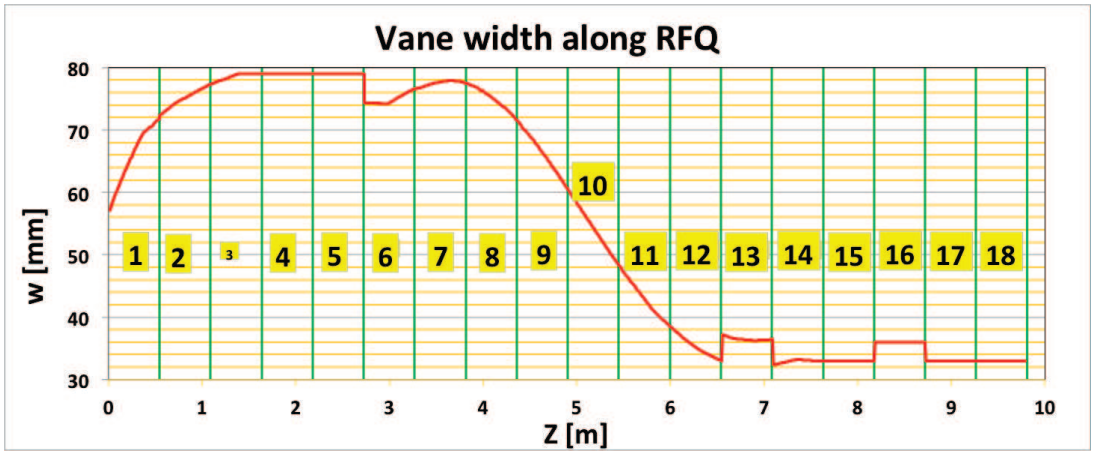

Figure 1.11 Vane width on each module along the RFQ

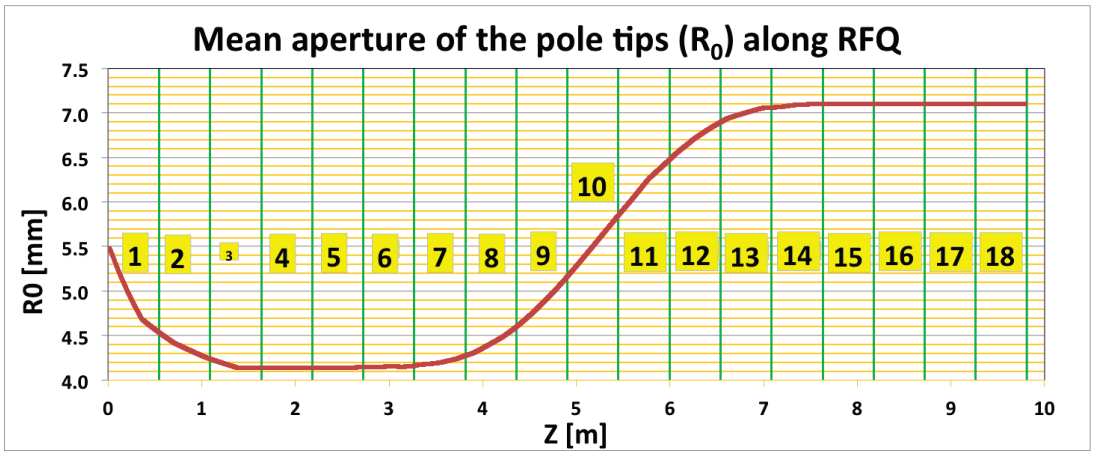

Figure 1.12 Mean distance of the pole tip from the beam axis along the RFQ

Since the RF power dissipates energy, a series of cooling duct has been provided with the aim to remove the losses and to provide the stability on the deformation of the cavity (figure 1.13).

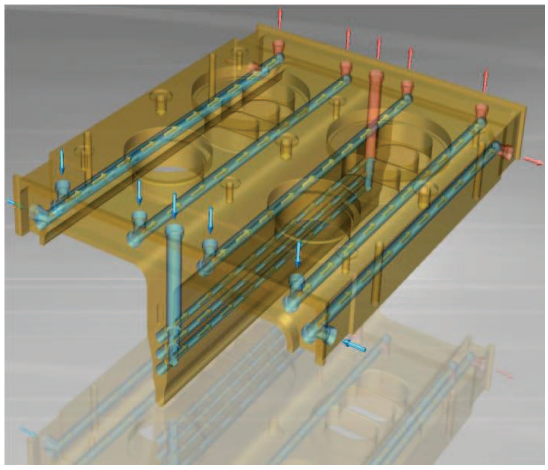

Figure 1.13 Cooling duct drilled on the copper electrodes of the RFQ

A series of AISI 316LN components are also joined by brazing:

- The side flanges for the bolted connection;
- The square seal front rings which provide the groove for the housing of the Garlock Helicoflex vacuum seal;
- The side round flanges to link the vacuum line, for the coupling of the tuners and the RF power inputs;
- The tubes and flanges for the connection of the cooling lines;
- The pins for the support plate and for the mounting of the references of the laser tracker

Finally a series of AISI 316 LN angular are welded by TIG technique to increase the stiffness and recover the symmetry on the deformation under vacuum conditions, and to guarantee a certain continuity on the bolted flanges.

AISI 316LN [9] is a low carbon (C<0.02 %) austenitic stainless steel with the addition of nitrogen. The nitrogen enlarges the asthenic field, improve high mechanical properties (yield strength up to 600 MPa) and do not suffer from softening during the heat treatments thermal cycle. It is particularly appropriate to be used on vacuum brazing conditions because there is no transformation on residual ferrite.

Moreover, since the pressure necessary for the Garlock Helicoflex vacuum seal is very high (about 17 tons on each square side of the cavity), it will result a too high specific pressure on copper. A square stainless steel frame is necessary to diffuse the load induced by the pressure of the Helicoflex.

For the same reason stainless steel bolted flanges were considered, because the specific pressure of the head of the bolts cannot be supported directly from copper.

Finally, table 1.2 reports the main mechanical parameters in terms of admissible tolerances on the single elements of the module and on the entire module and the admissible deformation (frequency) by means of the cooling system.

Requirement	Target value	Acceptance criteria	Comment
Modulation accuracy (pole tip) – form and position	±10 μm	±30 μm	Each module before brazing
Roughness	0.7 μm	1 μm	
Vane tips relative position respect to beam axis	±50 μm	±100 μm	Each module after brazing
Beam axis position	±50 μm	±100 μm	Correlation to external references and alignment of the entire assembled structure
Frequency Tuning range with water temperature	+ 100 kHz	+ 50 kHz	Measured in high power tests on last modules

Table 1.2 Main mechanical parameters of the RFQ

REFERENCES

[1] Fusion4energy: www.fusionforenergy.europa.eu

[2] JAEA (Japan Atomic Energy Agency);
http://www.jaea.go.jp/english/index.shtml

[3] INFN; http://www.infn.it/energia/ifmif.pdf

[4] F. Grespan, "Stabilizzazione del campo accelerante nel quadrupolo a radiofrequenza per il progetto SPES: Caratterizzazione teorica e risultati sperimentali", Master Degree Thesis, University of Padua, Department of Physics, Italy, 2004.

[5] S. Mathot, "RFQ Vacuum Brazing at CERN", EPAC08 Conference Proceedings, 2008, Genova (Italy), p.1494

[6] S. Sgobba, "Materials for high vacuum technology: An Overview", CAS-CERN Accelerator School and ALBA Synchrotron Light Facility: Course on Vacuum in Accelerator, Platja d'Oro, Spain, 16-24 May 2006, pp. 117-144

[7] M. Aicheler, "Surface phenomena associated with thermal cycling of copper and their impact on the service life of particle accelerator structures", PhD thesis, University of Bochum, Department of Mechanical Engineering, 2010 .

CHAPTER 2: THERMAL STRUCTURAL ANALYSIS OF THE IFMIF RFQ

2.1 Introduction

As anticipated on chapter 1, the important parameter for the mechanical design of the RFQ cavity is the conservation of the operational frequency of the cavity. The frequency depends on the internal geometry of the cavity. Deviations from the nominal geometry induced by errors of machining of the single electrodes, errors in position of the single elements, deformation occurred by brazing procedure and deformation induced by the vacuum operating conditions and the RF power input need to be compensated.

The tuners are comparable to a cylinder that penetrates on the cavity, in order to perform a variation of the geometry of the cavity, thus varying the frequency of the RFQ. The tuners compensate the shifts of the frequency due to:

- Errors of machining of the electrodes;
- Errors on the alignment of the modules on the dry assembly phase;
- Deformations by brazing steps;
- Vacuum effect during operating conditions.

So the tuners do not compensate the effect on the frequency the thermal deformations. Such effect can be controlled with the design of the cooling system. In order to keep controlled the displacements of the internal cavity of the RFQ the cooling system on each module in term of dimensions and position of the cooling ducts needs to be studied accurately.

Thermal-structural and fluid-thermal-structural numerical simulations using common commercial codes involving different packages such as Ansys, Comsol and STAR CCM+ and operators were performed.

In this chapter the design of the cooling system inside the modules of the RFQ will be described.

2.2 The Cooling system of the RFQ

As anticipated in the introduction, the roles of the cooling system of the RFQ are:

- Avoid the RF power losses, about 700 kW on the whole structure;
- Guarantee as much as possible an uniform deformation on the modules along the beam axis, for the stability of the electric field;
- Keep in control the deformation of the cavity: the displacements of the cavity should correspond on a tuning range of about -/+ 100 kHz (recommended), -/+ 50 kHz minimum, around the nominal frequency of 175 MHz.

Figure 2.1 shows the power losses on each module of the accelerating structure to be removed. The calculations of such losses was performed by electromagnetic calculations made by expert physicians of the LNL.

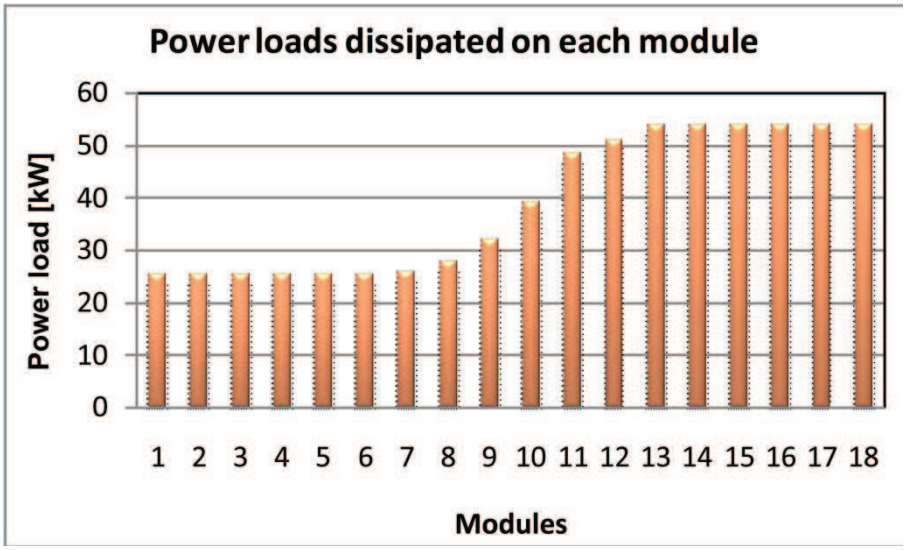

Figure 2.1 Power losses distribution along the modules of the RFQ

As shown in figure 2.1, the losses are not constant along the RFQ.
Three zones are distinguishable, that are called “supermodules”:

- “Supermodule” 1 (low energy supermodule) : it is composed by the modules 1 to 6. It is the low energy zone, where the beam is concentrated and focalized. The power losses are constant on each module; also the geometry of the electrodes remains invariant on each module.
- “Supermodule” 2 (middle energy supermodule): it is composed by the modules 7 to 12. In this zone the beam starts to be accelerated. The

distribution of the power losses is non-linear. The geometry of the electrodes is variable on each module along the beam axis.

- "Supermodule" 3 (high energy supermodule): it is composed by the last six modules (13 to 18). This is the real acceleration zone of the beam. The power losses distribution is constant on each module, and double to that of the first six ones.

The elements of the modules that require cooling are the vanes and the vessel. It has been decided to use water as coolant, because the high thermal capacity and the physical properties are stable on wide ranges of pressure and temperature. In order to induce a controlled displacement of the pole tips and vary in a controlled way the frequency of the cavity (satisfying the the requirements of -/+ 100 kHz tuning range), it was think of two independent cooling circuits, one for the vane and one for the vessel. In particular the temperature of the inlet of the vanes is fixed at 15 °C, while the inlet of the vessel is variable from 15 °C to a maximum of 27/28 °C. The optimal solution would be to cool each module separated from the others. But such a solution would require large amount of cooling water. Thus it has been decided to cool three module in serie, maintaining a certain symmetry. Let define each group of the three modules joined in serie "thermal module". At the interface of two thermal modules there will be inlets or outlets, in order to maintain a certain symmetry of the temperature profile, and so deformation on the modules. The cooling system of the RFQ is shown on figure 2.2.

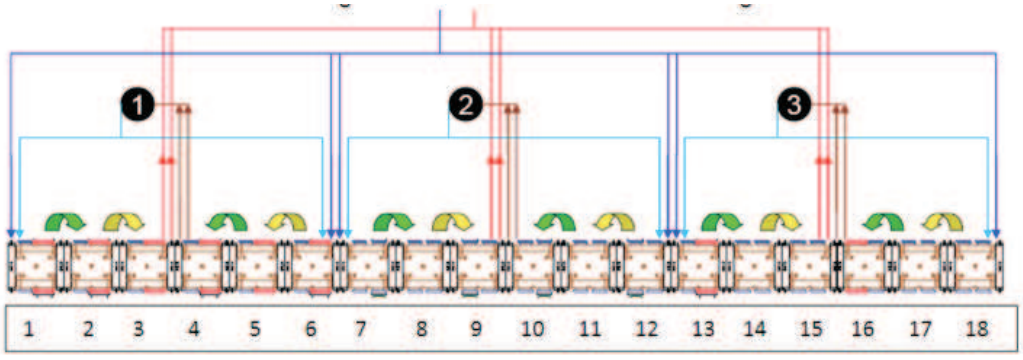

Fig. 2.2 Scheme of the cooling system of the RFQ of IFMIF

2.3 Initial configuration of the cooling ducts of the modules of the RFQ

Since the power losses due to RF power increase with the distance from the beam axis, the cooling ducts of the vessel have to remove more power, quite double, then those of the vanes. A solution increasing the convective heat transfer coefficient for the cooling ducts of the vessel was studied.

Some techniques to increase the turbulence and the heat transfer coefficient are described in literature with experimental and numerical studies, but difficult to realize on our modules [1, 2].

The hypothesis of threading those ducts was considered to increase the convective coefficient with the turbulence and to increase the heat exchanging area. Figure 2.3 reports the previewed configuration of the cooling ducts of the modules.

Two prototypes of modules of 400 mm length were constructed to test the feasibility and efficiency of such types of the cooling ducts. The layout of the cooling ducts was the same of that in figure 2.3.

Cause the accelerator is sensitive to small deformations of the cavity (displacement in the order of few microns on the pole tip), the evaluation of the effects on the heat transfer induced by the two different types of cooling ducts in terms of efficiency and uniformity of the temperature distribution on the electrodes was retained mandatory.

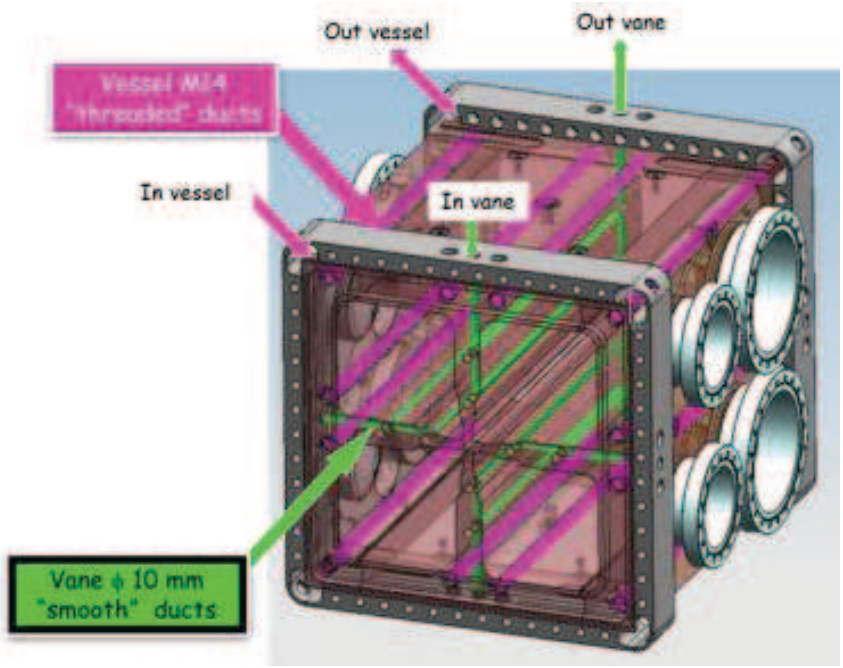

Fig. 2.3 The initial layout of the cooling ducts on the modules of the RFQ

2.4 Estimation of the convective heat transfer coefficient for the smooth and threaded duct via numerical simulations

In order to evaluate the behavior and efficiency of the smooth and threaded cooling ducts, it has been decided to perform initial coupled thermal-fluid studies via numerical simulation using different commercial codes such as Ansys® CFX and Comsol.

2.4.1 Theoretical frame for the solution of fluid-thermal problems

In this paragraph a theoretical background on the equation for the solution of the coupled fluid flow and thermal problem will be given. All formulas and figures of this paragraph are taken from the Ansys CFX guide [3] and [4]. In particular, since for the cooling of the vane and the vessel the fluid will be turbulent (Re > 10000), the simplest k-ε turbulence model will be illustrated.

In case of a compressible fluid, the equations that governs the fluid transport are the Navier Stokes equations: continuity equation (2-1) and the momentum equations (2-2). The continuity equation state that, in any steady state process, the rate at which the mass enters a system is equal to the rate at which the mass leaves the system:

$$\frac{\partial \rho}{\partial t} + \nabla \cdot (\rho \cdot \boldsymbol{V}) = 0 \quad (2-1)$$

where ρ is the density of the fluid, V is the velocity field of the flow.

The resulting equation of the application of Newton's second law to a fluid element is called momentum equation. The momentum equation states that the rate of increase of momentum in a control volume is equal to the sum of forces acting on the control volume plus the net flux of momentum into the control volume. The general form of the momentum equation is reported below:

$$\frac{\partial (\rho \boldsymbol{V})}{\partial t} + \nabla \cdot (\rho \boldsymbol{V} \otimes \boldsymbol{V}) = -\nabla p + \nabla \cdot \tau + \boldsymbol{S_M} \quad (2-2)$$

where:

- p is the static pressure
- $\mathbf{S}_M$ represents the momentum source
- τ denotes the stress tensor and it is related to the strain rate by:

$$\tau = \mu\left(\nabla \boldsymbol{V} + (\nabla \boldsymbol{V})^T - \frac{2}{3}\delta \nabla \cdot \boldsymbol{V}\right) \qquad (2-3)$$

where:

- μ is the dynamic viscosity
- δ represent the identity matrix

The last governing equation for the fluid flow is that expresses the conservation of energy. This physical principle states that the rate of change inside fluid element equals the sum of the net flux of heat into element and the rate of work done on element due to body and surface forces. The mathematical expression used in Ansys CFX is:

$$\frac{\partial(\rho \cdot h_{tot})}{\partial t} - \frac{\partial P}{\partial t} + \nabla \cdot (\rho \boldsymbol{V} h_{tot}) = \nabla \cdot (\lambda \cdot \nabla T) + \nabla \cdot (\boldsymbol{V} \cdot \tau) + \boldsymbol{V} \cdot \boldsymbol{S_M} + \boldsymbol{S_E} \qquad (2-4)$$

where:

- h_{tot} is the total enthalpy of the fluid, related to the static enthalpy h (T,p) by:

$$h_{tot} = h + \frac{1}{2}\boldsymbol{V}^2 \qquad (2-5)$$

- T is the absolute temperature
- λ is the thermal conductivity
- $\mathbf{S_E}$ is the energy source

The term $\nabla \cdot (\boldsymbol{V} \cdot \tau)$ represents the work due to viscous stresses and is called the viscous work term. This models the internal heating by viscosity in the fluid, and is negligible in most flows.

The term $\boldsymbol{V} \cdot \boldsymbol{S_M}$ represents the work due to external momentum sources and can be neglected in most cases.

In case heat transfer involves also a solid domain, another equation has to be taken into account:

$$\frac{\partial(\rho \cdot h)}{\partial t} + \nabla \cdot (\rho \boldsymbol{V_S} h) = \nabla \cdot (\lambda \nabla T) + S_E \qquad (2-6)$$

where:

- h, ρ and λ are the enthalpy, density and thermal conductivity of the solid
- $\mathbf{V_S}$ is the solid velocity

- S_E is the heat source on the solid

Solving a fluid dynamic (or coupled thermal-fluid) problem is actually solving a coupled system of nonlinear equation, but presently, there is no general analytical solution to these equations. The numerical solutions play an important role on the description of the flow by mathematical equation.

The domains for the solution of these equations must be discretized. In a such way, a mathematical expression that is defined at infinite points, is replaced by finitely many values at discrete nodes or points. The form of governing equations is changed from differential equations to a system of algebraic equations after discretization. The system of equations not only should approximate the solution, but also it has to guarantee numerical stability: the errors in the intermediate calculation should not accumulate.

Three common discretization techniques are in use today:

1. Finite Element Method (FEM). The domain is divided into finite elements, connected by nodes, apply the governing equations to these elements, and compute the values at each node. Finite Element Method has been implemented in Comsol to solve CFD problems.
2. Finite Difference Method (FDM). The finite Difference method replaces a partial derivative with a suitable algebraic quotient. Most common finite-difference representations of derivatives are based on Taylor's series expansions. Such a method is highly efficient, but do not maintain the property of conservation, resulting in lower accuracy.
3. Finite Volume Method (FVM). The finite-volume method is very popular among the commercial CFD packages, such as Ansys CFX, Ansys Fluent and Adapco STAR CCM. The fluid domain is divided into a set of control volumes, which are used to conserve relevant quantities such as mass, momentum and energy.

   The Finite Volume Method determines the following advantages:

   - It rigorously enforces conservation;
   - It is flexible in terms of both geometry and the variety of fluid phenomena;

The next passages will show how the Navier Stokes equations modify considering a turbulent flow.

Turbulence consists of fluctuations in the flow field in time and space. It is a very complex problem, because it is three dimensional, unsteady and consists of many scales. Considering the definition of the Reynolds number, turbulence occurs at high Reynolds numbers when the inertia forces are great compared to the viscous forces. In principle the Navier-Stokes equations describe both the laminar and turbulent flows. However, turbulent flows at realistic Reynolds numbers span a large range of turbulent length and time scales, and would generally involve length scales much smaller than the smallest dimension of the cell mesh, which can be practically used in a numerical analysis. Also the computing resources for the direct solution of these equation are many times higher than those will we available in the foreseeable future.

A large amount of CFD researchers concentrated on methods that can approximate as closely as possible the real turbulent flows, introducing the so called turbulence models. In this way the turbulence can be modeled without recourse to extremely fine meshes and the direct solution of the Navier-Stokes equations.

Most turbulence models are statistical turbulence models. When looking at time scales much larger than the time scales of turbulent fluctuations, turbulent flow could be said to exhibit average characteristics, with an additional time-varying, fluctuating component. For example a velocity can be divided into an average component and a time varying component.

With the introduction of the turbulence models, the original Navier-Stokes equation are so modified introducing the averaged and fluctuating quantities. The modified equations are called as RANS (Reynolds Averaged Navier Stokes) equations. The models based on RANS equation are also known as Statistical Turbulence Models due to the statistical averaging procedure employed to obtain equations. However the averaging procedure introduces additional unknown terms containing products of the fluctuating quantities, which act like additional stresses in the fluid. These terms, called ‘turbulent’ or ‘Reynolds’ stresses, are difficult to be determined and become further unknows.

Additional equations have to be introduced to model these stresses in order to achieve "closure". Depending on which equations to be used for closure, different types of turbulence models are. The most common turbulence model are k-ε, □−ω and SST (shear stress transport equation). The k-ε turbulence model for the closure of the RANS equations will be presented on this paragraph. It was chosen because one of the most used and implemented on the CFD codes. It is stable, numerically robust and offers a good compromise in terms of accuracy and robustness. For the other models the lecturer is invited to see the Ansys manual, or other literature reference books.

It will be described only how the Navier-Stokes equation are modified to consider the turbulence.

As described above, turbulence models solve the modified transport equation (RANS) introducing averaged and fluctuating components. For example considering the velocity variable V_i, it may be divided into an average component $\bar{V}_i$ and a time varying component, v_i.

$$V_i = \bar{V}_i + v_i \quad (2-7)$$

The averaged component is given by:

$$\bar{V}_i = \frac{1}{\Delta t}\int_t^{t+\Delta t} V_i \, dt \qquad (2-8)$$

where Δt is a time scale that is large relative to the turbulent fluctuations, but small relative to the time scale to which the equations are solved. For compressible flows, the averaging is actually weighted by density (Favre-averaging), but for simplicity the following presentation assumes that the density fluctuations are negligible.

Substituting the averaged quantities into the original transport equations, RANS equation will be obtained. The (2-9) and (2-10) will report the new continuity and momentum equations:

$$\frac{\partial \rho}{\partial t} + \frac{\partial}{\partial x_j}\left(\rho V_j\right) = 0 \qquad (2-9)$$

$$\frac{\partial \rho V_i}{\partial t} + \frac{\partial}{\partial x_j}\left(\rho V_i V_j\right) = -\frac{\partial p}{\partial x_i} + \frac{\partial}{\partial x_j}\left(\tau_{ij} - \rho\overline{v_i v_j}\right) + S_M \quad (2-10)$$

where τ is the molecular stress tensor.

The duplicate index variable in a single term implies the operation of summing over all the possible values. For a three dimensional space, the values for the index could be 1, 2, 3. This notation will be used also on the following equations.

The continuity equation (2-9) is not change from (2-1). The new momentum equation (2-10) differs from (2-2) from an additional term of the turbulent fluxes in addition to the molecular diffusive fluxes. The term $\rho\overline{v_i v_j}$ represents the Reynolds stresses. They reflect the fact that convective transport due to turbulent velocity fluctuations will act to enhance mixing over and above that caused by thermal fluctuations at the molecular level.

The new energy equation becomes:

$$\frac{\partial \rho h_{tot}}{\partial t} - \frac{\partial p}{\partial t} + \frac{\partial}{\partial x_j}\left(\rho U_j h_{tot}\right) = \frac{\partial}{\partial x_j}\left(\lambda \frac{\partial T}{\partial x_j} - \rho\overline{v_j h}\right) + \frac{\partial}{\partial x_j}\left[V_j\left(\tau_{ij} - \rho\overline{v_i v_j}\right)\right] + S_E \qquad (2-11)$$

This equation contains an additional turbulence flux term, $\rho\overline{v_j h}$.

The term $\frac{\partial}{\partial x_j}\left[V_j\left(\tau_{ij} - \rho\overline{v_i v_j}\right)\right]$ is the viscous work term.

The mean total enthalpy can be given by:

$$h_{tot} = h + \frac{1}{2}V_i V_j + k \qquad (2-12)$$

where k represents the turbulent kinetic energy:

$$k = \frac{1}{2}\overline{v_i^2} \qquad (2-13)$$

The following passages will describe the closure equations to model the Reynolds stresses for the k-ε model.

Turbulence can be considered of small eddies which are continuously forming and dissipating. The Reynolds stresses can be assumed proportional to mean velocity gradients. Such a model is called “eddy viscosity model”. The eddy viscosity hypothesis assume that the Reynolds stresses can be related to the mean velocity gradients and the eddy (turbulent) viscosity by the gradient diffusion hypothesis:

$$-\rho\overline{v_i v_j} = \mu_t\left(\frac{\partial V_i}{\partial x_j} + \frac{\partial V_j}{\partial x_i}\right) - \frac{2}{3}\delta_{ij}\left(\rho k + \mu_t \frac{\partial V_k}{\partial x_k}\right) \qquad (2-14)$$

where μ_t is the eddy or turbulent viscosity, which must be modeled.

The k-ε solves two different transport equations: one for the velocity, the other for the length scale. The turbulent velocity is computed from the turbulent kinetic energy. The turbulent length scale is estimated from two properties of the turbulent fluid, usually the turbulent kinetic energy and its dissipation rate.

In k-ε model k means the turbulence kinetic energy and is described as the variance of the fluctuations in velocity. ε is the turbulent eddy dissipation (the rate at which the velocity fluctuations dissipate).

In k-ε model, the continuity equation remained unchanged from (2-9). Combining the (2-14) into (2-10), the momentum equation becomes:

$$\frac{\partial \rho V_i}{\partial t} + \frac{\partial}{\partial x_j}\left(\rho V_i V_j\right) = -\frac{\partial p'}{\partial x_i} + \frac{\partial}{\partial x_j}\left(\mu_{eff}\left(\frac{\partial V_i}{\partial x_j} + \frac{\partial V_j}{\partial x_i}\right)\right) + S_M \quad (2-15)$$

where μ_{eff} is the effective viscosity accounting for turbulence, and p' is the modified pressure as:

$$p' = p + \frac{2}{3}\rho k + \frac{2}{3}\mu_{eff}\frac{\partial V_k}{\partial x_k} \quad (2-16)$$

The last term of (2-16) is neglected in CFX and the assumption is strictly correct considering a incompressible flow.

The effective viscosity is expressed by:

$$\mu_{eff} = \mu_t + \mu \quad (2-17)$$

In k-ε the turbulence viscosity is linked to the turbulent kinetic energy and the dissipation rate:

$$\mu_t = C_\mu \rho \frac{k^2}{\varepsilon} \quad (2-18)$$

where C_μ is a constant equal to 0.09.

The values of k and ε come directly from the differential transport equations for the turbulence kinetic energy and turbulence dissipation rate:

$$\frac{\partial(\rho k)}{\partial t} + \frac{\partial}{\partial x_j}\left(\rho V_j k\right) = \frac{\partial}{\partial x_j}\left[\left(\mu + \frac{\mu_t}{\sigma_k}\right)\frac{\partial k}{\partial x_j}\right] + P_k - \rho\varepsilon + P_{kb} \quad (2-19)$$

$$\frac{\partial(\rho\varepsilon)}{\partial t} + \frac{\partial}{\partial x_j}\left(\rho V_j \varepsilon\right) = \frac{\partial}{\partial x_j}\left[\left(\mu + \frac{\mu_t}{\sigma_\varepsilon}\right)\frac{\partial \varepsilon}{\partial x_j}\right] + \frac{\varepsilon}{k}\left(C_{\varepsilon 1}P_k - C_{\varepsilon 2}\rho\varepsilon + C_{\varepsilon 1}P_{\varepsilon b}\right) \quad (2-20)$$

where $C_{\varepsilon 1}$, $C_{\varepsilon 2}$, σ_k and σ_ε are constants. Their values are respectively 1.44, 1.92, 1 and 1.3.

Pkb and Peb represent the influence of the buoyancy forces. Pk is the turbulence production due to viscous forces.

The other important aspect for the solution of the flow is how it can be modeled near a no-slip wall. Strong gradients of the dependent variables and viscous effects on the transport processes are large. For a numerical simulation it important the way of accounting for viscous effects at the wall and the solution of a rapid variation of the flow variables which occurs within the boundary layer region.

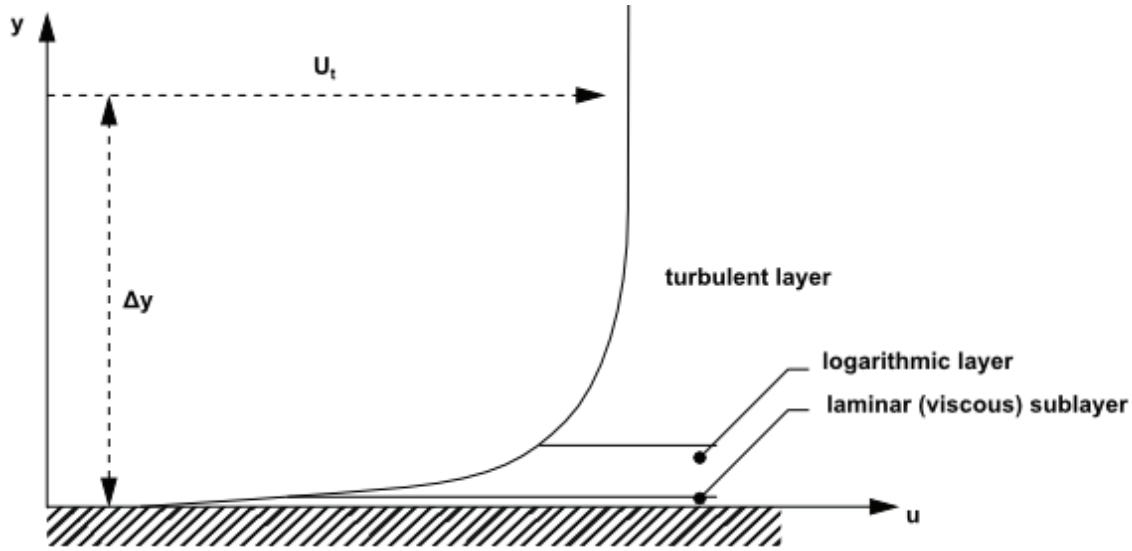

Figure 2.4 Flow velocity profile near the wall [1]

Considering experimental and mathematical analyses, the near-wall region can be subdivided into two layers, according to figure 2.4:

- The inner layer, known as the viscous sublayer, where the flow is almost laminar and the molecular viscosity plays a dominant role in momentum and heat transfer
- The logarithmic layer, where turbulence dominates the mixing proceses.
- An intermediate zone between the logarithmic wall and the viscous sublayer, known as the buffer zone, where the molecular viscosity and turbulence becomes of equal importance.

Assuming that the logarithmic profile reasonably approximate the velocity distribution near the wall, it provides a means to compute the fluid shear stresses as a function of the velocity at a given distance from the wall. This is know as wall function and because of the logarithmic profile of the velocity the name "logarithmic wall functions".

Two approaches are possible to model the flow near the flow in the near-wall region. In the first approach the boundary layer is not solved. Semi-empirical formulations ("wall functions") are used to bridge the viscosity-affected region to the fully-turbulent region.

The advantage of this method is that the mesh inflation near the wall can not be very fine respect to the second method, saving computational requirements.

The second approach is called as "near-wall" modeling approach. The turbulence models are modified to enable the viscosity-affected region to be resolved with a very fine mesh inflation near the wall. This approach is used by the low Reynolds turbulence models and k-ω and Shear Stress Transport turbulence models. The name low Reynolds means that the models solve also for the low Reynolds zones near the wall.

In Ansys CFX the logarithmic equations that bridges the wall conditions to the dependent variables at the near-wall mesh node which is presumed to lie in the fully turbulent region of the boundary layer is given by:

$$u^+ = \frac{U_t}{u_\tau} = \frac{1}{\kappa}\ln(y^+) + C \quad (2-21)$$

where:

$$y^+ = \frac{\rho\, \Delta y\, u_\tau}{\mu} \quad (2-22)$$

$$u_\tau = \left(\frac{\tau_\omega}{\rho}\right)^{\frac{1}{2}} \quad (2-23)$$

- u^+ is the near wall velocity
- u_τ is the friction velocity
- U_t is the well known tangential velocity at a distance Δy from the wall
- y^+ is the dimensionless distance from the wall and depend from the distance of the first and second point of the grid from the wall

- τ_ω is the wall shear stress
- κ is the Von Karman constant equal to 0.41
- C is a constant depending on the wall roughness

The equation (2-21) presents some problem: when U_t approaches zero, it becomes singular. In the logarithmic region, an alternative velocity scale, u^*, can be used instead of u_τ:

$$u^* = C_\mu^{1/4} k^{1/3} \quad (2-24)$$

Based on this definition, the following equation for u_τ can be obtained:

$$u_\tau = \frac{U_t}{\frac{1}{\kappa}\ln(y^*) + C} \quad (2-25)$$

where:

$$y^* = \frac{(\rho \cdot u^* \cdot \Delta y)}{\mu} \quad (2-26)$$

Concerning the heat transfer on the near wall zone, using similar assumptions as above, the non-dimensional near-wall temperature profile follows a universal profile through the viscous sublayer and the viscous region. The dimensionless temperature, T^+, that is function of y^* is defined as:

$$T^+ = \frac{\rho c_P u^*}{q_w}\left(T_w - T_f\right) \quad (2-27)$$

where T_w is the temperature at the wall, T_f is the near-wall fluid temperature, cP is the fluid capacity and q_w the heat flux at the wall. Rearranging the equation (2-27):

$$q_w = \frac{\rho c_P u^*}{T^+}\left(T_w - T_f\right) \quad (2-28)$$

The equation (2-28) presents a more familiar form. Considering that in general, in thermodynamics:

$$h = \frac{\dot{q}}{(T_w - T_f)} \quad (2-29)$$

where h is the convective heat transfer, and $\dot{q}$ is the heat flux at the wall, the first term on the right is equal to h.

2.4.2 Numerical simulations of the smooth and threaded duct [5]

A simple model was considered: a copper block of 60x30x200 mm with a smooth Φ 10 mm or threaded M14 cooling ducts (figure 2.5). The geometry has been generated with Siemens NX CAD and exported in Parasolid format. The two cases were also analyzed by experts of the CFD Team of CERN with CD ADAPCO STAR CCM+ code.

The boundary conditions and the characteristic parameters of the simulations were:

- copper block material properties:
  - Thermal conductivity (k):400 $\frac{W}{m \cdot K}$
  - Specific heat (c): 385 $\frac{J}{kg \cdot K}$
  - Density (ρ): 8920 $\frac{kg}{m^3}$

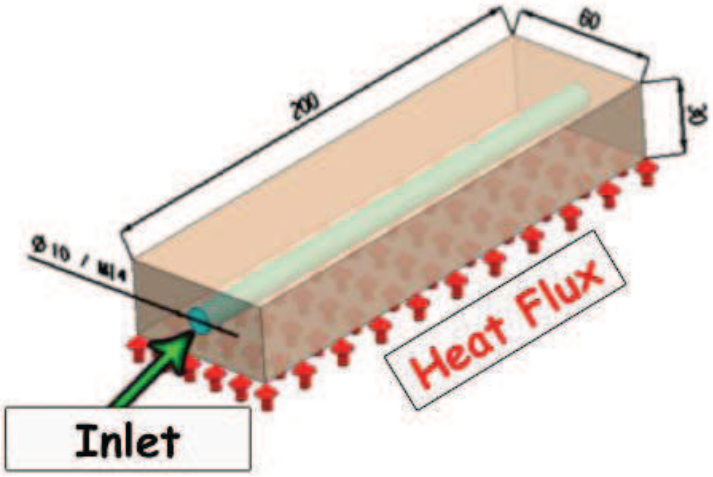

Figure 2.5 CAD model for numerical simulations

- water physical properties:
  - Thermal conductivity: 0.6 $\frac{W}{m \cdot K}$
  - Specific heat: 4182 $\frac{J}{kg \cdot K}$
  - Density: 998 $\frac{kg}{m^3}$
  - Viscosity: $1e-3\ Pa \cdot s$
- boundary conditions:

- Heat flux on copper base: $42000\,\frac{W}{m^2}$
- Turbulence model: k-ε
- Mass flow at the inlet of the smooth and threaded ducts: $0.34\,\frac{kg}{s}$
- Turbulence intensity at the inlet of the smooth and threaded duct: 5%
- Temperature at the inlet of the smooth and threaded duct: $20.5^{\circ}C$
- Relative pressure at the outlet of the smooth and threaded duct: $0\ Pa$

The figures of the next pages report the result of the simulations of the smooth and threaded cooling duct performed with the different commercial codes. Problems on the convergence were found with the simulation of the threaded cooling duct with Comsol. The geometry seemed to be imported, repaired and mesh correctly. However the conservation of the mass flow along the channel and the heat balance between the copper block and the fluid domain were not satisfied.
Figures 2.6, 2.7 and 2.8 report the flow distribution on the smooth duct, calculated with the three different packages.
Figures 2.9, 2.10, 2.11, 2.12 and 2.13 show the wall heat transfer coefficient and the plots of the average wall heat transfer coefficient along the smooth duct calculated with the three different packages.
Figure 2.14, 2.15 and 2.16 show the temperature calculated with the three software on the copper block for the case of the smooth cooling duct.
Figures 2.17 and 2.18 report the flow distribution on the threaded duct, calculated with STAR CCM+ and Ansys CFX.
Figures 2.19, 2.20 and 2.21 show the wall heat transfer coefficient and the plots of the average wall heat transfer coefficient along the threaded duct calculated with the different packages.
Figure 2.22 and 2.23 show the temperature calculated on the copper block for the case of the threaded cooling duct.

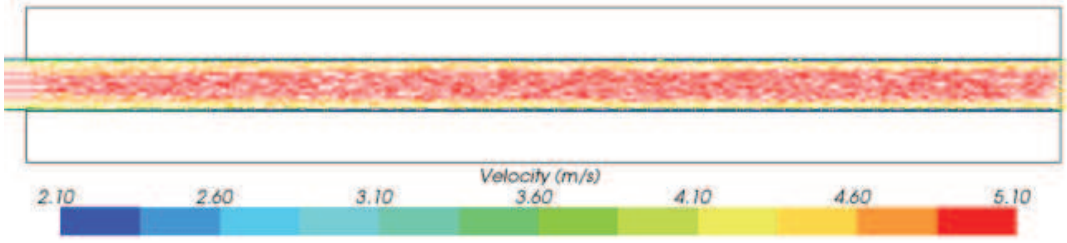

Figure 2.6 Flow distribution on the smooth duct calculated with STAR CCM+

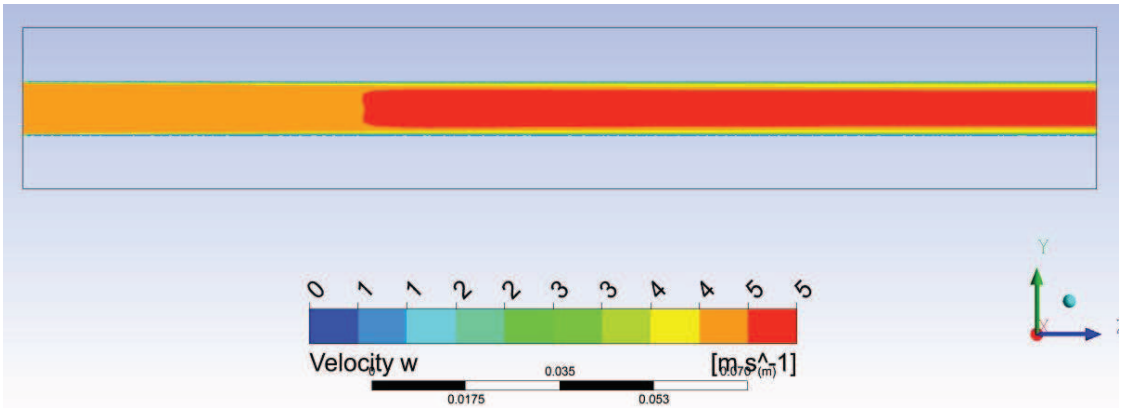

Figure 2.7 Flow distribution (velocity magnitude in m/s) calculated with Ansys CFX.

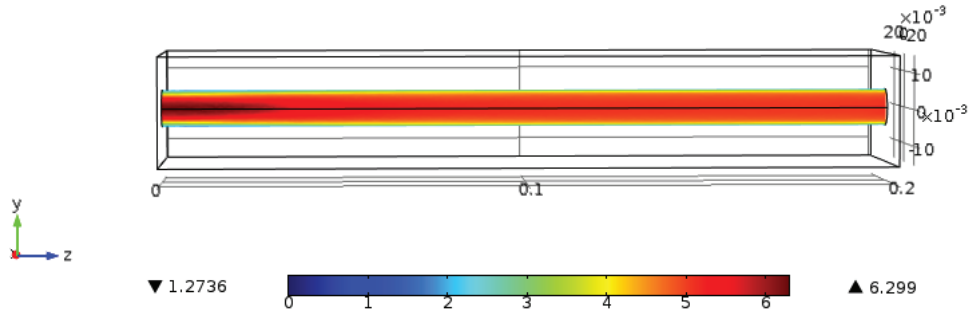

Figure 2.8 Flow distribution (velocity magnitude in m/s) calculated with Comsol.

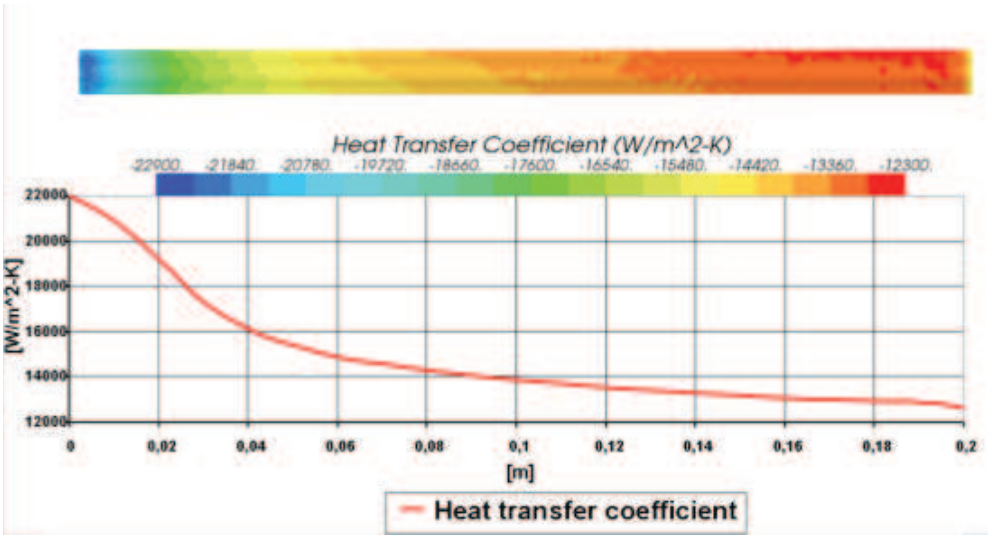

Figure 2.9 Convective heat transfer coefficient along the smooth duct calculated with STAR CCM+ with a reference temperature of 20.5 °C

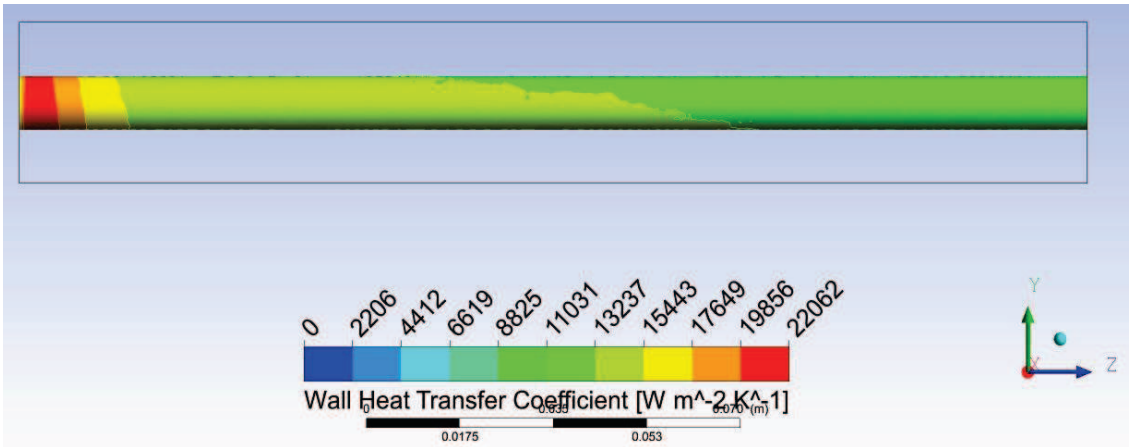

Figure 2.10 Convective heat transfer coefficient along the smooth duct calculated with Ansys CFX with a reference temperature of 20.5 °C

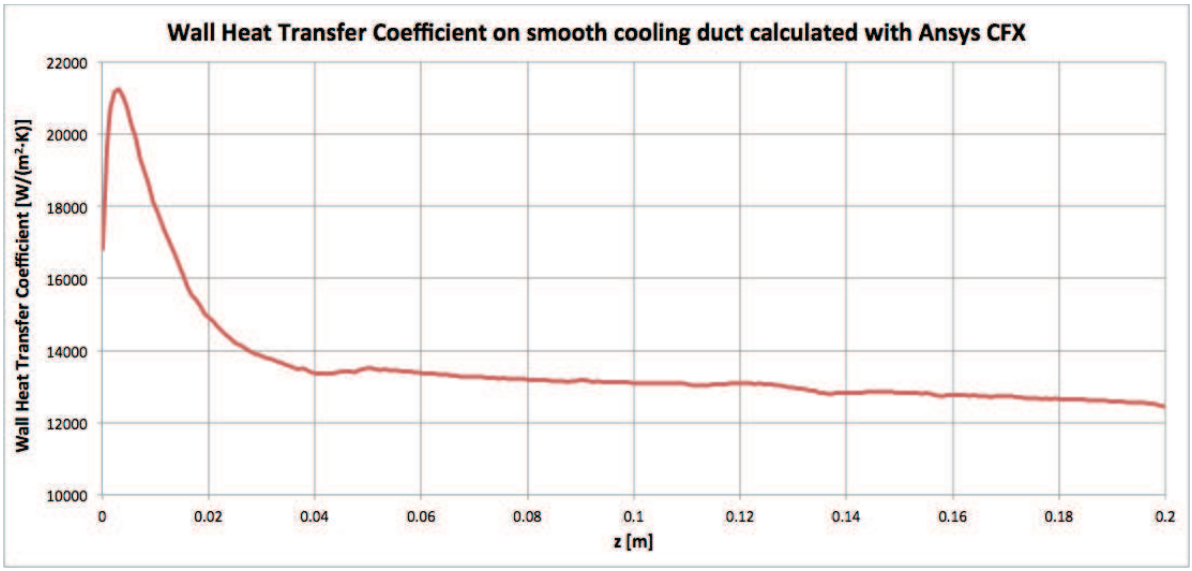

Figure 2.11 Convective heat transfer coefficient along the smooth duct calculated with Ansys CFX with a reference temperature of 20.5 °C

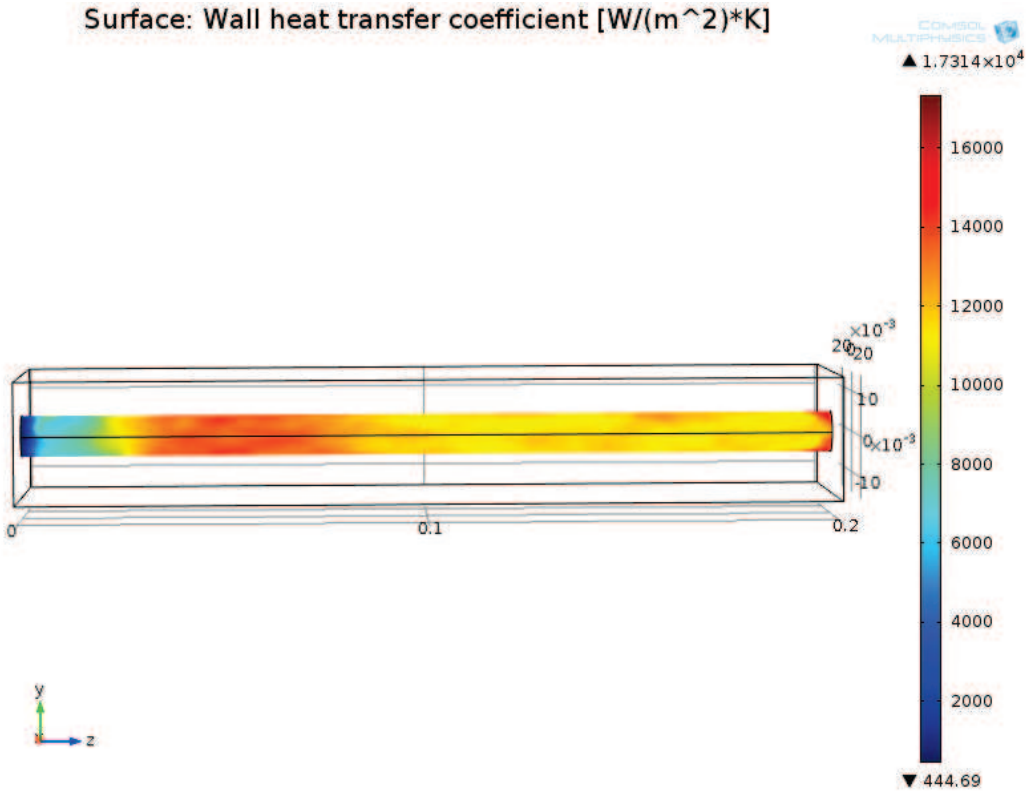

Figure 2.12 Convective heat transfer coefficient along the smooth duct calculated with Ansys CFX with a reference temperature of 20.5 °C

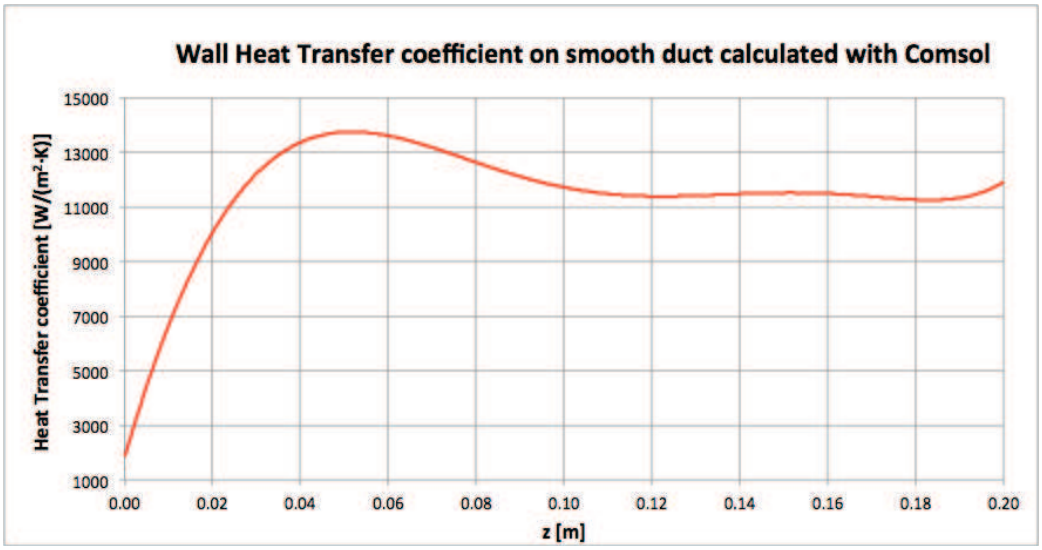

Figure 2.13 Convective heat transfer coefficient along the smooth duct calculated with Comsol with a reference temperature of 20.5 °C

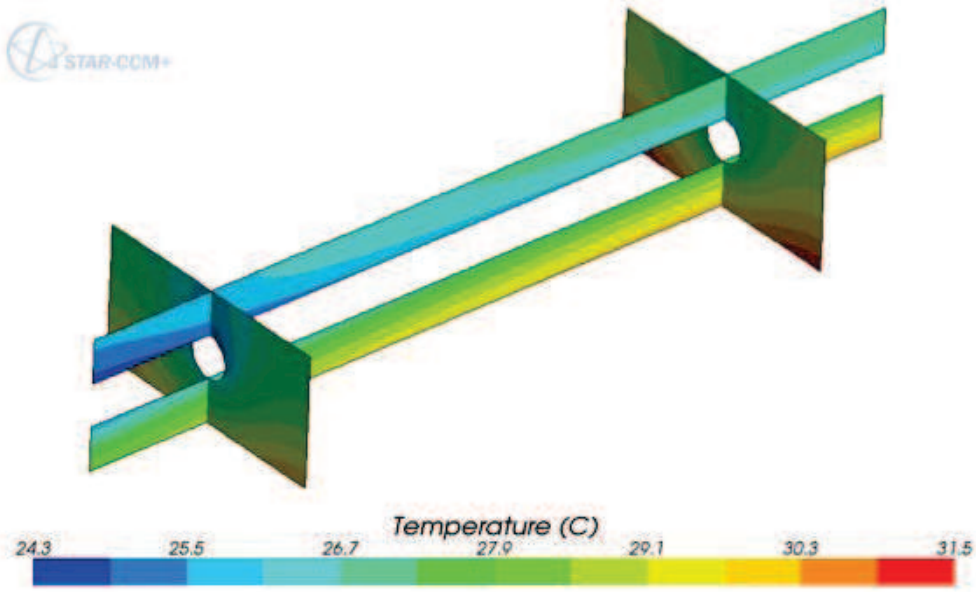

Figure 2.14 Temperature along the smooth cooling duct calculated with STAR CCM+

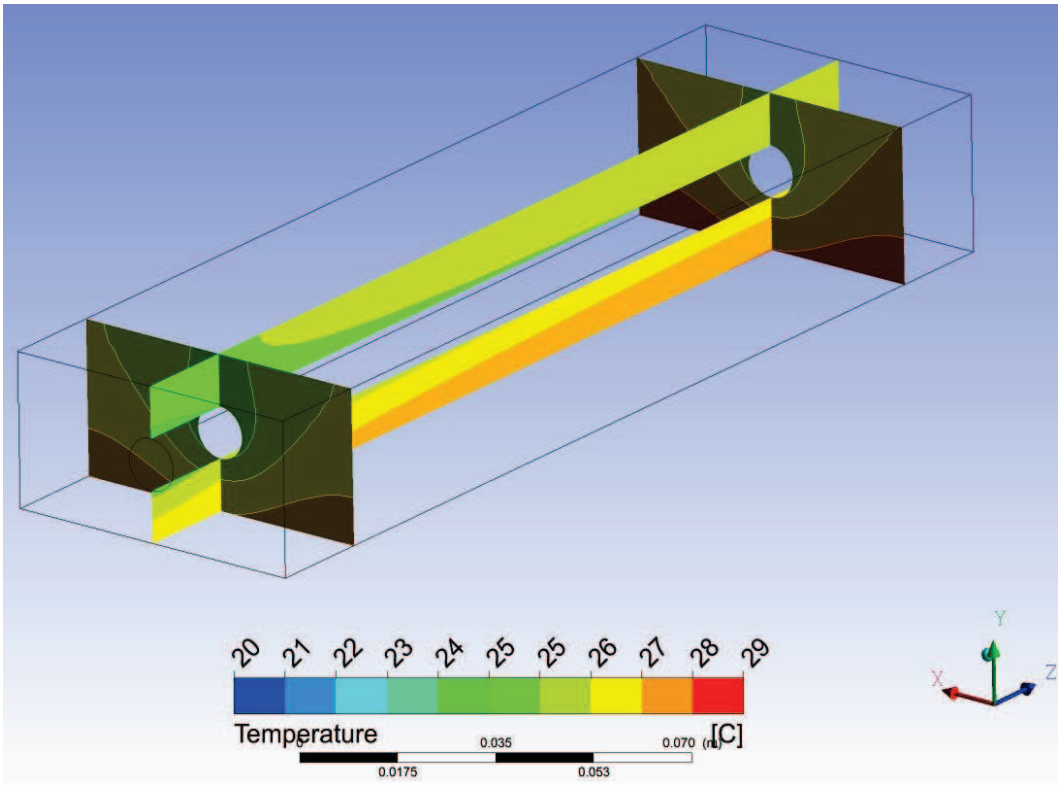

Figure 2.15 Temperature along the smooth cooling duct calculated with Ansys CFX

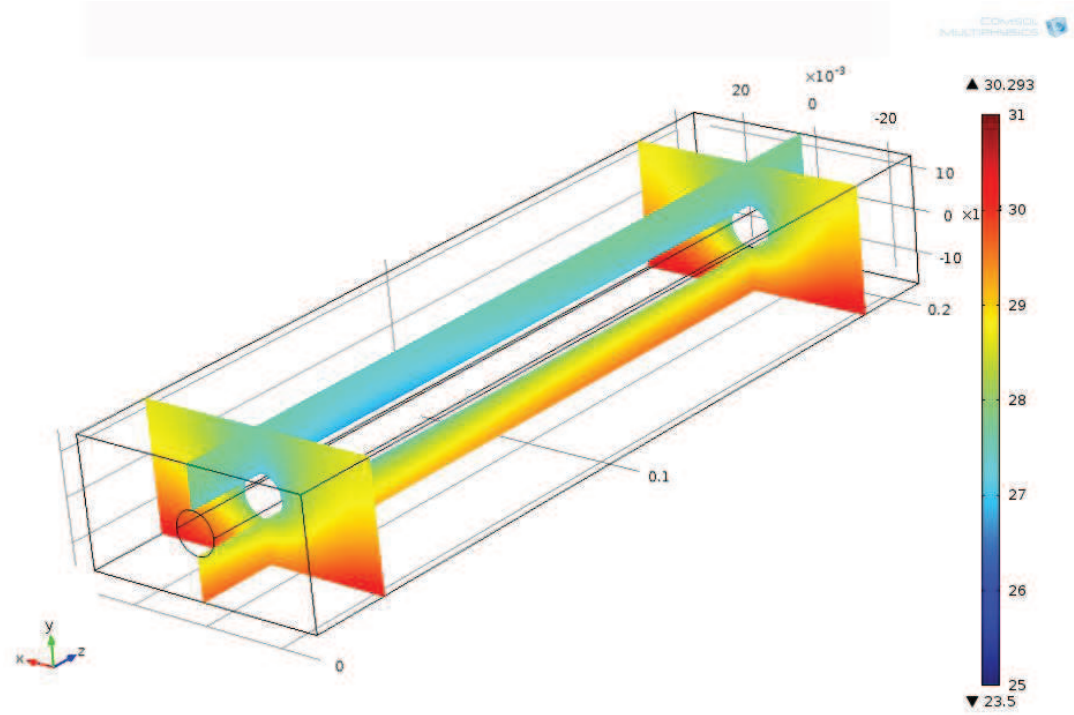

Figure 2.16 Temperature along the smooth cooling duct calculated with Comsol

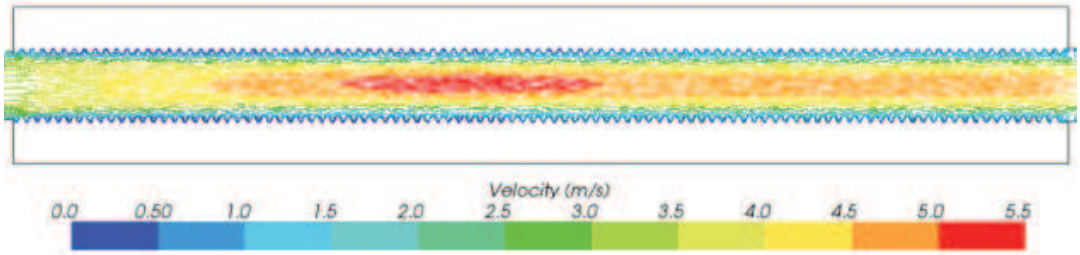

Figure 2.17 Flow distribution on M14 threaded duct calculated with STAR CCM+

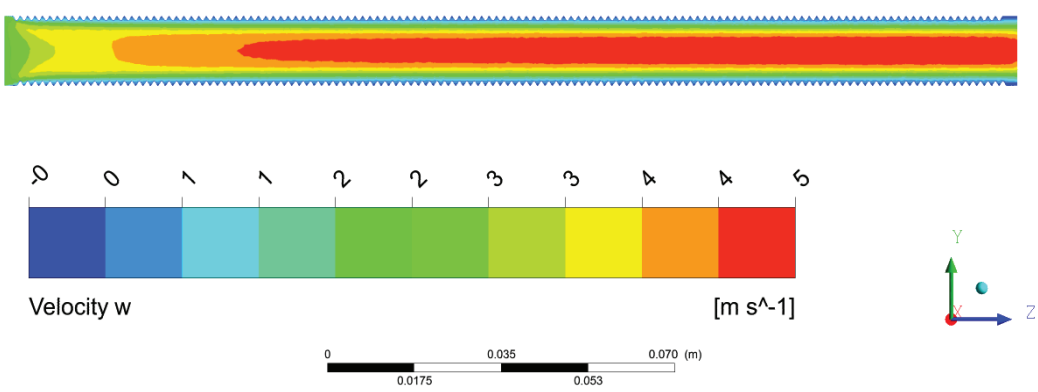

Figure 2.18 Flow distribution on M14 threaded duct calculated with Ansys CFX

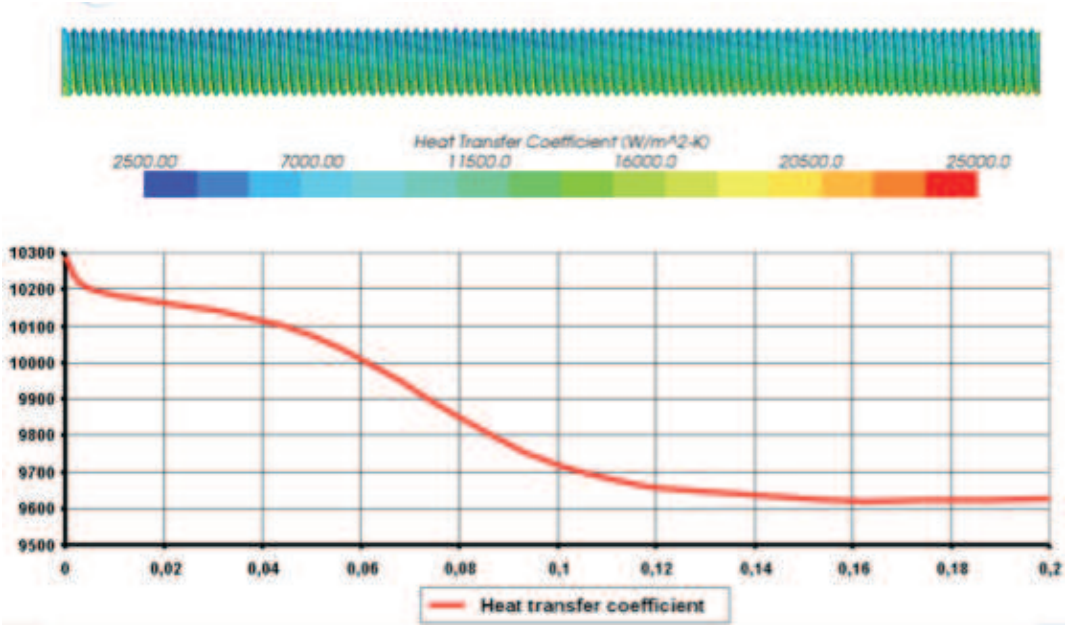

Figure 2.19 Average convective heat transfer coefficient along the threaded duct calculated with STAR CCM+ with a reference temperature of 20.5 °C

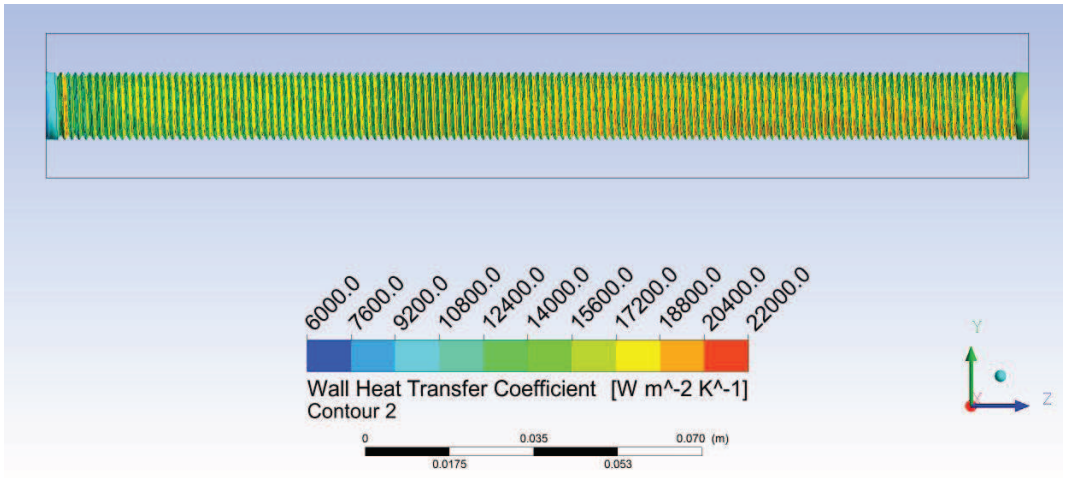

Figure 2.20 Convective heat transfer coefficient along the threaded duct calculated with Ansys with a reference temperature of 20.5 °C

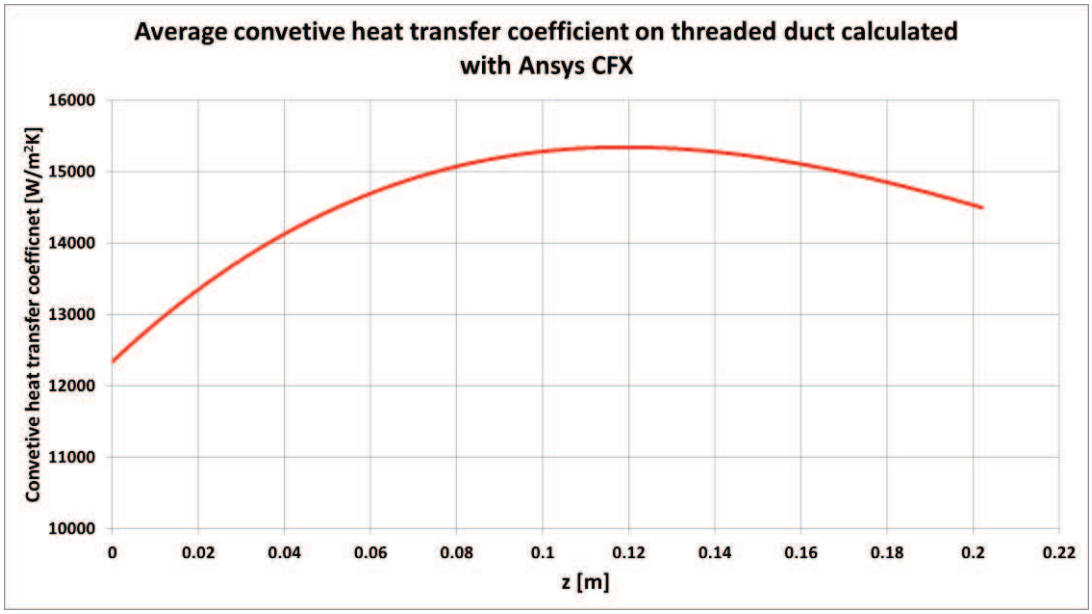

Figure 2.21 Convective heat transfer coefficient along the threaded duct calculated with Ansys CFX with a reference temperature of 20.5 °C

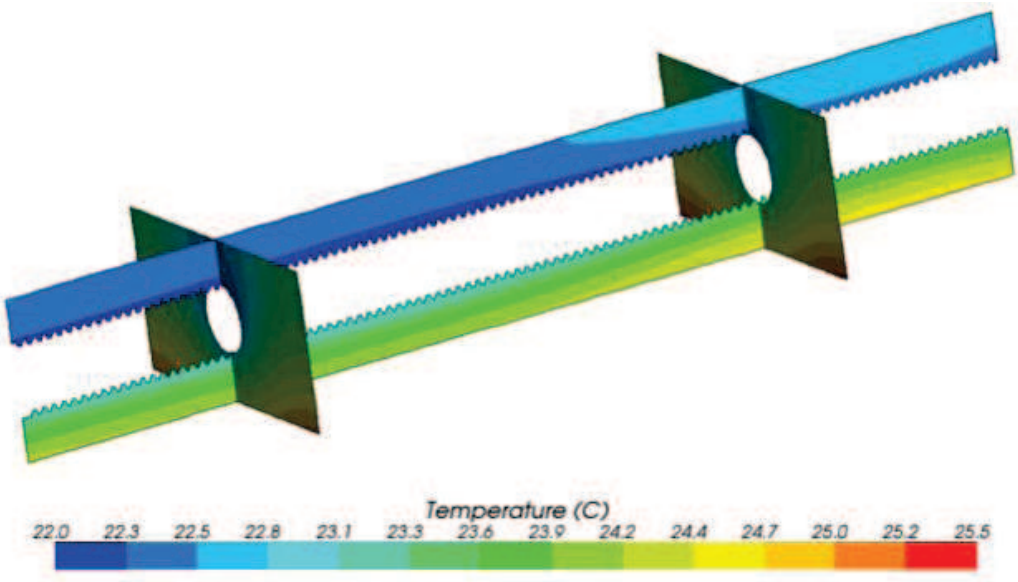

Figure 2.22 Temperature along the threaded duct calculated with STAR CCM+.

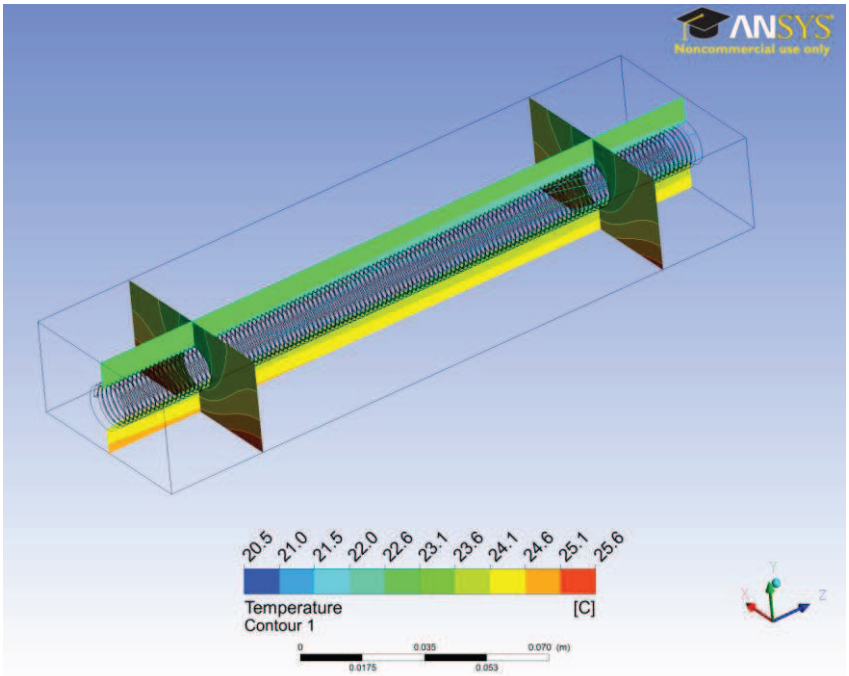

Figure 2.23 Temperature along the threaded duct calculated with Ansys CFX.

On a first analysis the convective heat transfer coefficient is greater for the smooth duct instead the threaded one. But the heat exchange is more efficient on the threaded duct thanks to the increase of the exchanging area.

Although the greater efficiency of the threaded channel, it seams that the flow is much uniform on the smooth one. For the stability of the cavity, a uniform temperature distribution is wanted, the smooth duct seems to be better than threaded one.

Table 2.1 reports the summary of the simulations with the variety of software.

	Smooth duct	**Threaded duct**
Inlet mass flow [kg/s]	0.34	0.34
Inlet velocity [m/s]	4.39	2.62
Contact area [m^2]	0.625e-2	1.28e-2
Heated area [m^2]	1.2e-2	1.2e-2
Heat flux [W/m^2]	4.3e4	4.3e4

Average heat transfer coefficient [W/(m^2*K)]		
Star CCM+	14500	9900
Comsol	12000	Simulation not converged
Ansys CFX	13500	14000

Table 2.1 Summary of the analysis with various softwares.

Comparing the simulation with the different codes, a discrete agreement was found for the case of the smooth cooling duct. Lot of difference was found on the simulation of the threaded cooling duct. For what concerning the smooth cooling duct there is a zone near the inlet of the channel that is characterized for different trends on the heat convective coefficient and it is very variable. Next to this zone the wall heat transfer coefficient becomes stable and small difference were found comparing the three codes.

Moreover on the computation of the temperature of the copper block small differences less than 5% were found.

Quite big differences were found on the simulations of the threaded cooling duct. In fact the trends of the wall heat transfer coefficient along the channel are different. This could be caused of a higher length of the duct to make the flow stable. Although the values of the average wall heat transfer coefficient are not too much different, a consistent difference was found on the temperature calculated on the copper block.

Due to the differences on the results obtained with different packages, an electrode of the second module of the prototype has been utilized to perform an experimental test for the verification of thermo-fluid dynamics simulations and to calculate accurately the heat transfer coefficient for the smooth and threaded cooling ducts. Figure 2.24 shows the apparatus for the input of the power on the electrode. Two couples of plate resistors, one for the vane and one for the vessel, simulated the thermal losses due to voltage on the RFQ. Figure 2.25 reports the layout of the cooling duct of the electrodes, reproducing the configuration of the final modules of figure 2.3. The cooling of the vane is in blue with two parallel Φ 10 mm smooth cooling ducts, while the cooling of the vessel with M14 duct is in green. The channels of the vane does not cover the full length of the electrode: in

fact on the electrode the undercut will be machined, that is a termination zone for the closure of the currents.

For the cooling circuit a centrifugal pump with a maximum flow rate of 40 l/min and a chiller of 6 kW of maximum cooling power were used. Deionized water was pumped into the channels. The inlets of the vane and of the vessel were separated, in order to evaluate independently each contribute. The temperature on the electrode was read by means of a NEC Avio TVS 600 thermal camera (uncertainty of ± 1 ˚C), calibrated with a PT 100 thermocouple. The mass flow rate at the inlet of the vane and the vessel was measured with two helix type flux meters (uncertainty of ± 1 l/min). The surfaces of the electrode cut by the EDM were not with a uniform emissivity: a special was applied on the points of measure. The thermal maps saved on the thermal camera were successively analyzed with PE Professional 3.0 package.

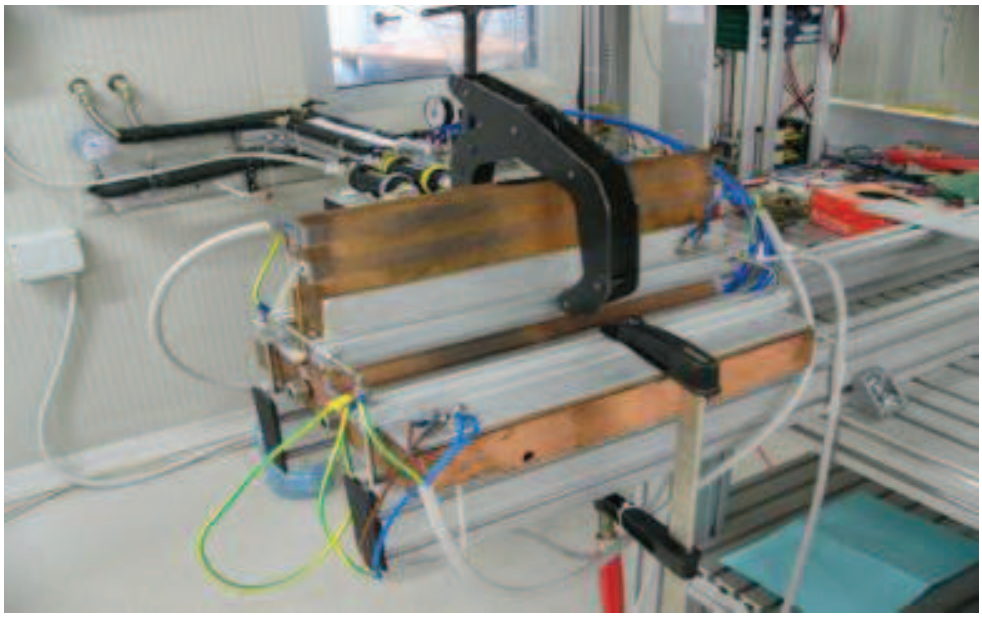

Figure 2.24 Image of the electrode for the cooling test with the resistors on the vane and the vessel

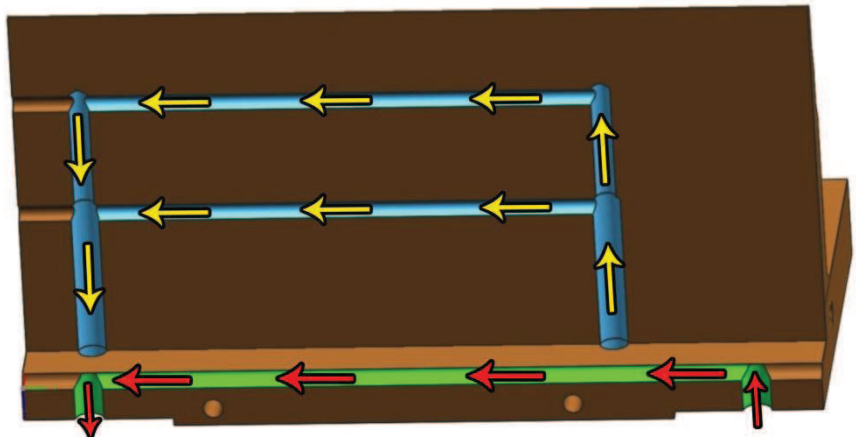

Figure 2.25 CAD section of the electrode that shows the layout of the cooling ducts of the vane (blue) and the vessel (green).

Firstly the cooling of the vessel was analyzed. Water was pumped on the channel of the vessel and power was applied on vessel resistors only. Table 2.2 summarizes the parameters of this experimental test.

Mass flow rate on each channel	15 l/min
Diameter of the cooling ducts	M14
Nominal velocity	2.1 m/s
Inlet temperature	15 °C
Outlet temperature	16.3 °C
ΔT	1.3 °C
Input power of each plate resistor	1350 W

Table 2.2 Parameter of the experimental test of the cooling of the vessel

Figure 2.26 reports the map of temperature in output of the thermal camera. Figures 2.27, 2.28 and 2.30 show the temperature that was extracted on the lines 1, 2 and 3 with the software.

some reflexes were noted on the infrared image, such as the effect of the resistor on the surface of the vane.

For the calculus of the convective heat transfer coefficient FEM analysis with Ansys were done. Considering the symmetry of the problem, half electrode has

been modeled. The cooling duct has been modeled as smooth, considering an equivalent diameter of 14 mm.

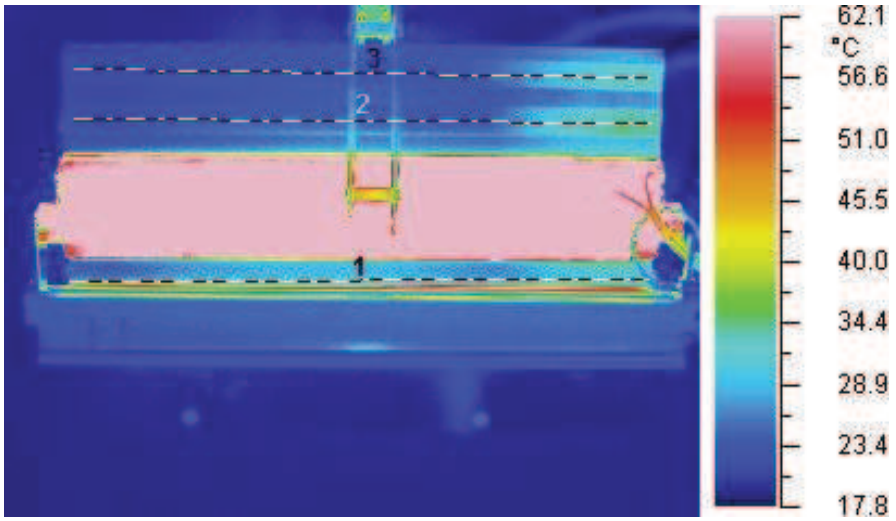

Figure 2.27 Infrared image as output of the thermal camera for the cooling test of the vessel

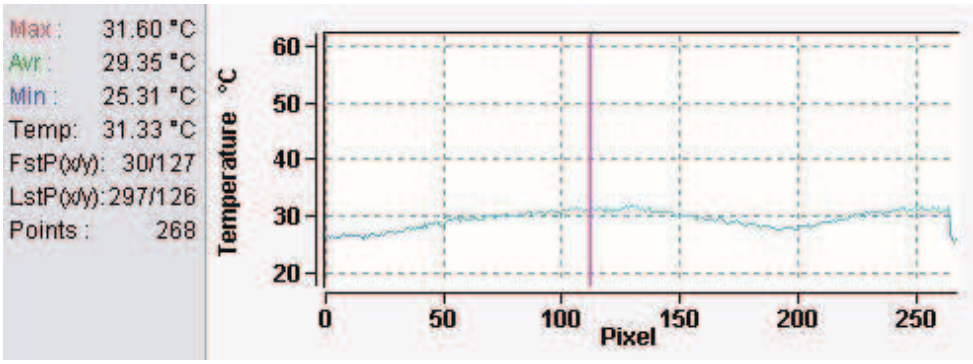

Figure 2.28 Output of the software temperature on line 1 for the cooling of the vessel

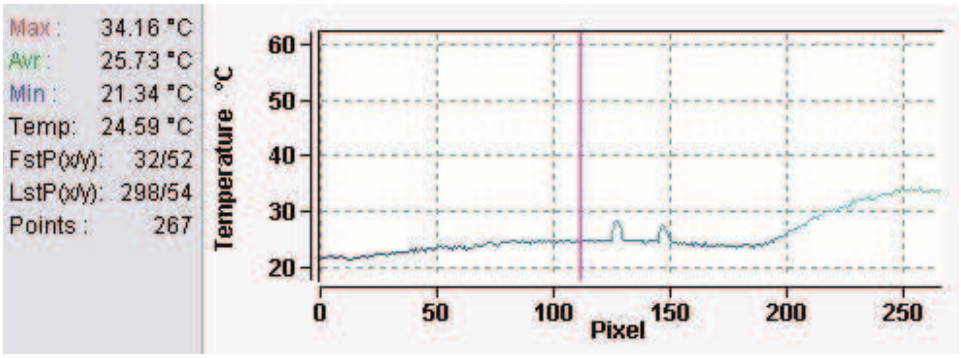

Figure 2.29 Output of the software temperature on line 2 for the cooling of the vessel

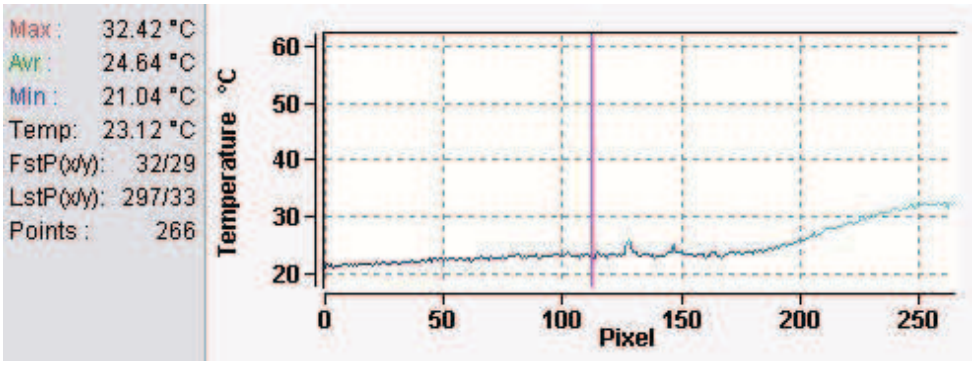

Figure 2.30 Output of the software temperature on line 3 for the cooling of the vessel

The surface of the duct has been subdivided into 4 parts and linear increment of temperature from inlet to outlet was imposed. A thermal heat flux of 31000 $\frac{W}{m^2}$ on the surface of the vessel (figure 2.31). The value of the convective heat transfer coefficient was varied in a such way to fit as much as possible the experimental data. The parameters of the simulations are reported in the table 2.3.

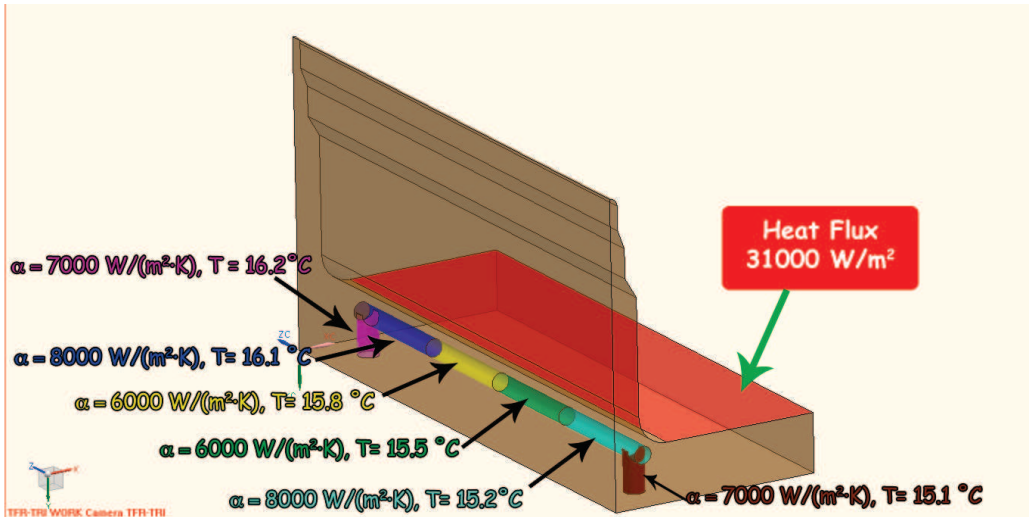

Figure 2.31 Model and boundary conditions for the calculus of the convective heat transfer coefficient for the cooling duct of the vessel

Temperature on the convective surfaces of the cooling duct	Linear increase from 15˚C at the inlet to 16.3 ˚C at the outlet
Thermal heat flux	$31000\ \frac{W}{m^2}$
Element type	Tetrahedral with 4 nodes (Ansys Solid 70)
Number of nodes	About 30000
Solution time	Less than 5 minutes for a PC with 4 GB RAM and dual core processor

Table 2.3 Parameters and boundary conditions for the FEM thermal simulations for the calculus of the heat transfer coefficient of the vessel cooling ducts

Figures 2.32, 2.33 and 2.34 show a comparison between the experimental data and the FEM for the optimal value of the heat transfer coefficient. The agreement between the calculated results and the experimental data is discrete.

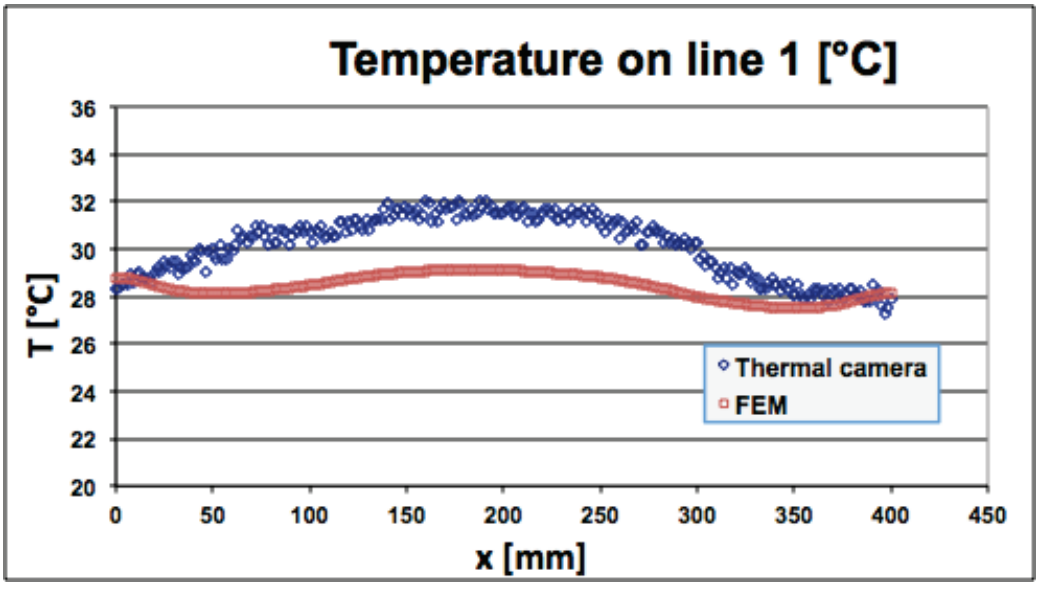

Figure 2.32 FEM and experimental comparison on the line 1 for the vessel cooling

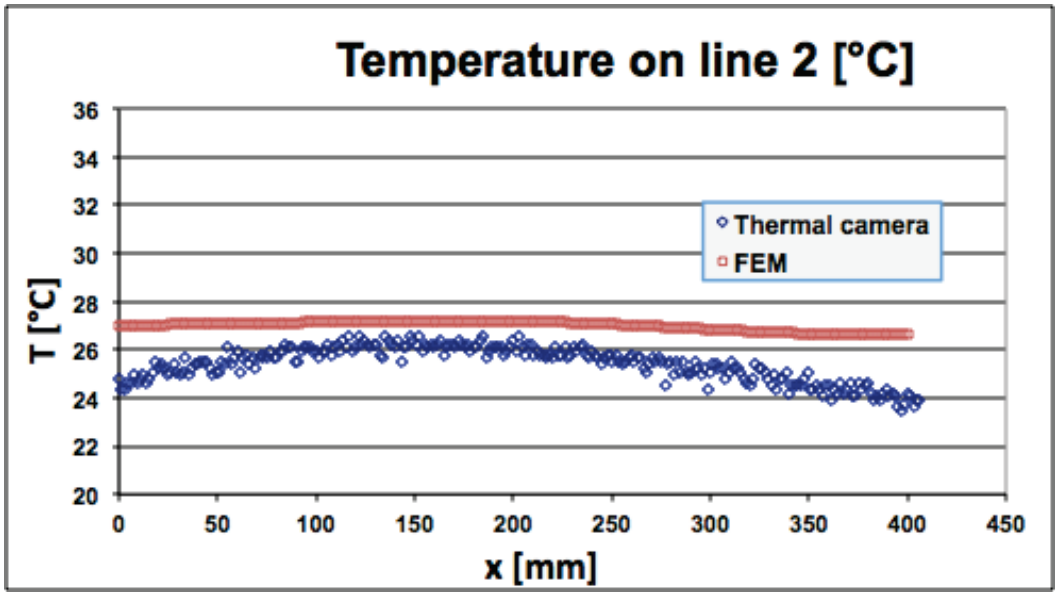

Figure 2.33 FEM and experimental comparison on the line 2 for the vessel cooling

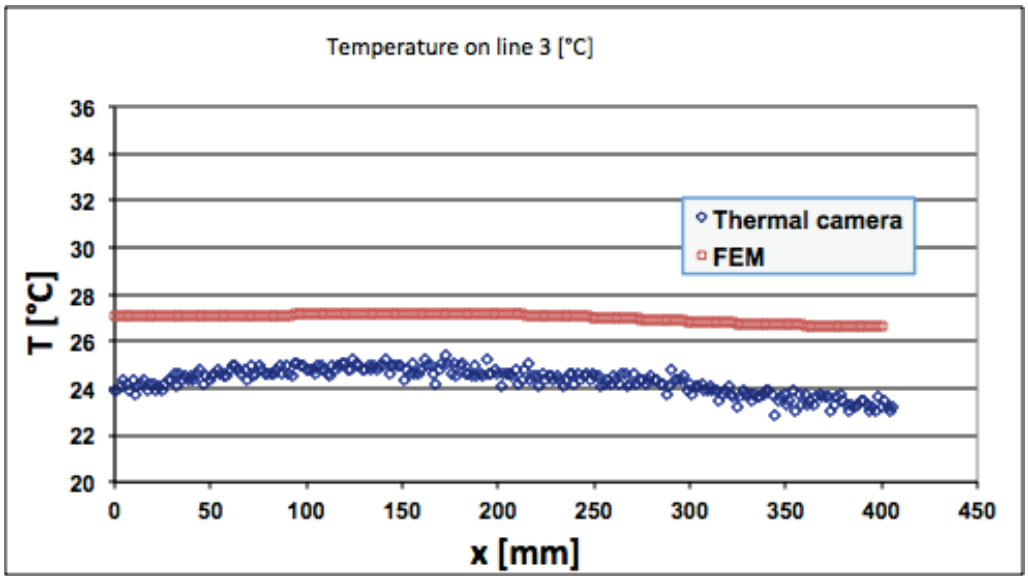

Figure 2.34 FEM and experimental comparison on the line 3 for the vessel cooling

Analyzing the results, the temperature along the electrode is not as uniform as in the case of the smooth duct. The heat transfer coefficient is not constant along the threaded duct as the smooth one. This confirmed the results of the FEM simulations which showed a better uniformity of the flow on the smooth duct.

The cooling of the vane was the second case. As in figure 2.25, the vane is cooled by means of two smooth Φ 10 mm ducts in parallel. Power was put on the two

plate resistors of the vane. The experimental data of the flow used and used for FEM simulation are listed on table 2.4.

Inlet mass flow rate	21 l/min
Diameter of the cooling ducts	φ 10 mm
Nominal velocity on each channel (considering equal distribution of the flow)	2.2 m/s
Inlet temperature	15 °C
Outlet temperature	16.6 °C
ΔT	1.6 °C
Total dissipated power	2475 W

Table 2.4 Experimantal data for the cooling of the vane

Figure 2.35 shows the thermal map of the electrode when the stationary condition was reached. Figures 2.36, 2.37 and 2.38 report the extrapolations via software of the temperature on line 1, 2 and 3.

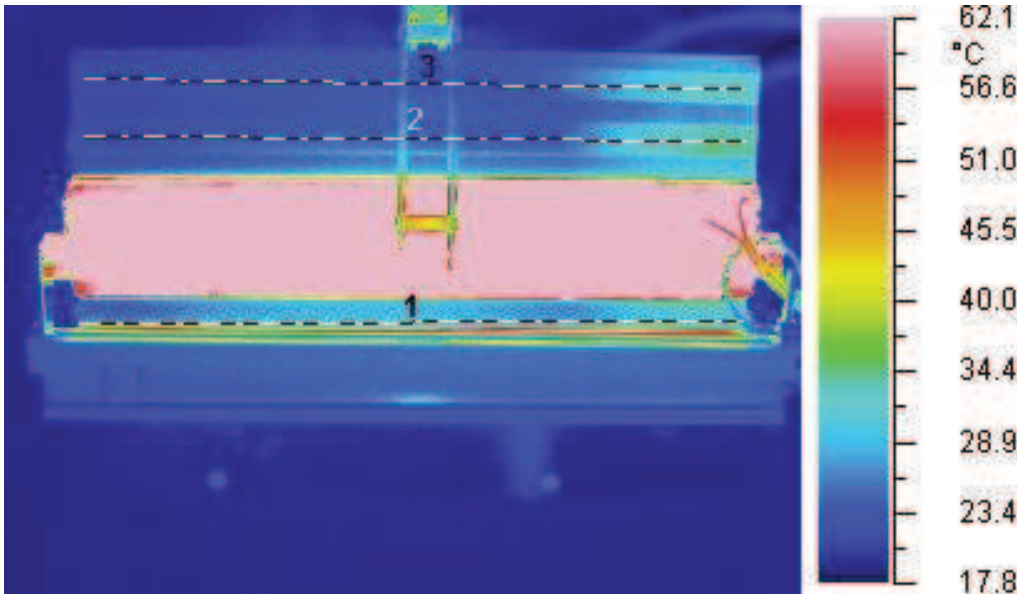

Figure 2.35 Thermal map in output of the thermal camera for the cooling of the vane

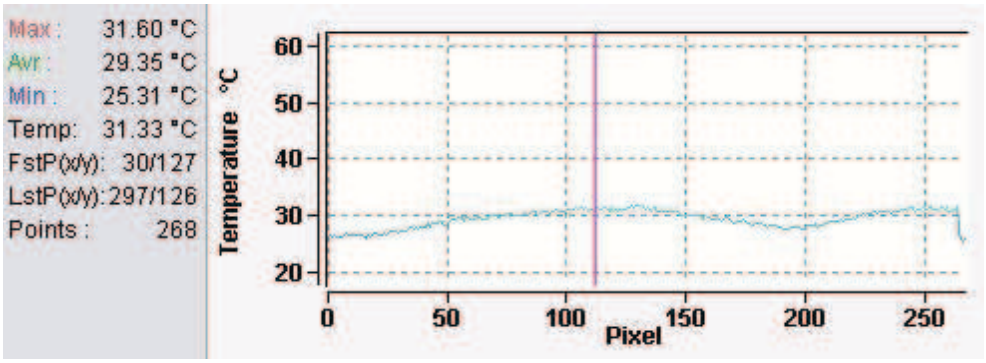

Figure 2.36 Output of the software of the temperature on line 1 for the cooling of the vane

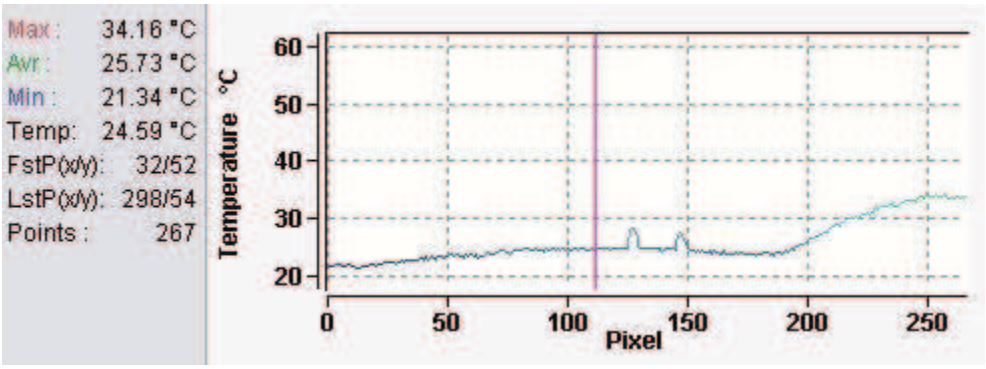

Figure 2.37 Output of the software of the temperature on line 2 for the cooling of the vane

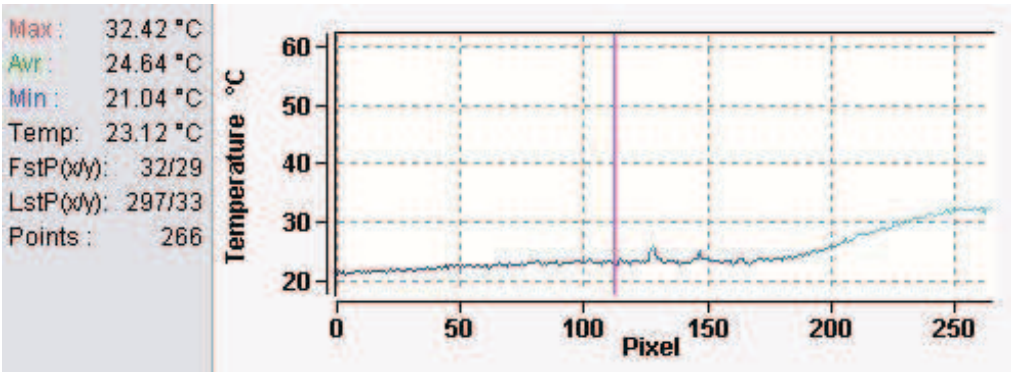

Figure 2.38 Output of the software of the temperature on line 3 for the cooling of the vane

As for the vessel, FEM stationary thermal simulations with Ansys code were used for the calculus of the convective heat transfer coefficient. An equal distribution of the flow and power on the two parallel ducts were hypothesized. A linear increase of the temperature was imposed from the inlet to the outlet, subdividing

into four equal parts the surfaces of the ducts along the length of the electrode. The parameters of the simulations are listed in table 2.5, while the zones of application of the boundary conditions in term of heat flux and the convective heat transfer with the parameters that best fit the experimental data are reported on figures 2.39 and 2.40.

Reference temperature on the surfaces of the cooling ducts	Linear increase from 15˚C at the inlet to 16.6 ˚C at the outlet
Heat flux on the surfaces of the vane	39800 $\frac{W}{m^2}$
Element type	Tetrahedral with 4 nodes (solid 70 Ansys element)
Number of nodes	About 30000
Solution time	Less than 5 minutes for a PC with 4 GB RAM and dual core processor

Table 2.5 Parameters and boundary conditions for the FEM thermal simulations for the calculus of the heat transfer coefficient of the vane cooling ducts

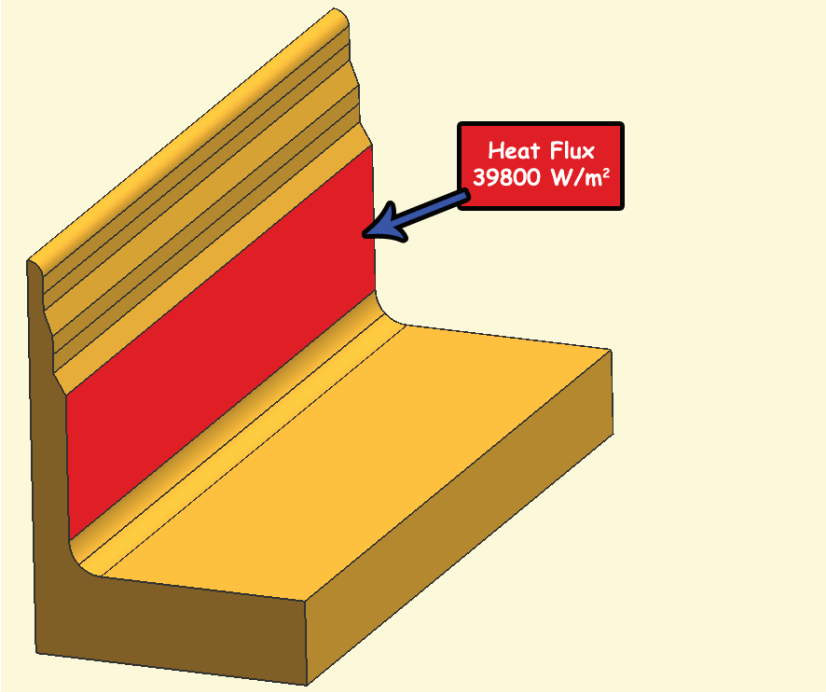

Figure 2.39 Heat Flux boundary condition used on the FEM simulation

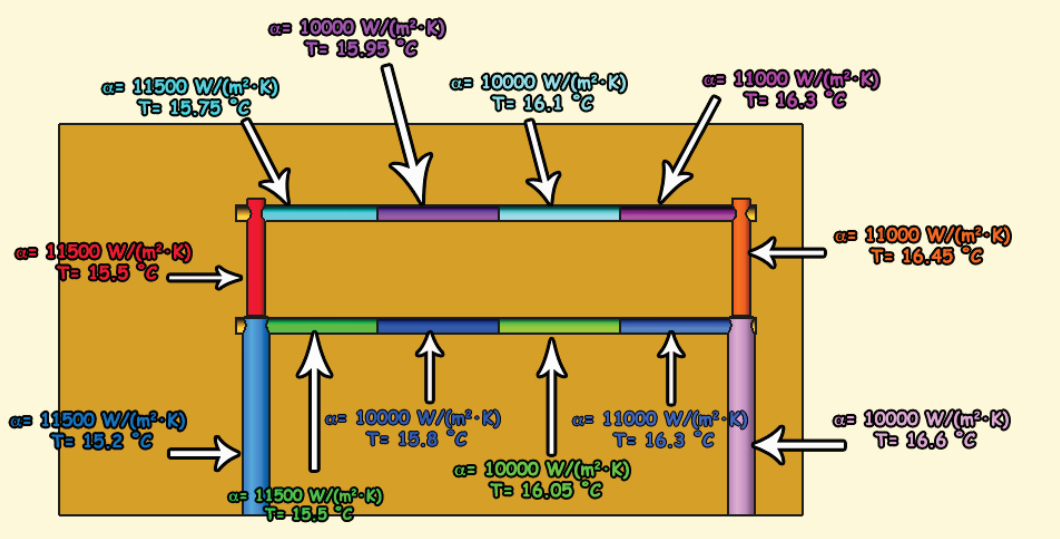

Figure 2.40 Convection boundary condition used to fit the experimental data with FEM

Figures 2.41, 2.42 and 2.43 report the plots of the comparison between the FEM calculated values and the experimental data. To be noticed that the adherence between the FEM and the experimental data is very good, especially on the zones that are directly cooled by the ducts.

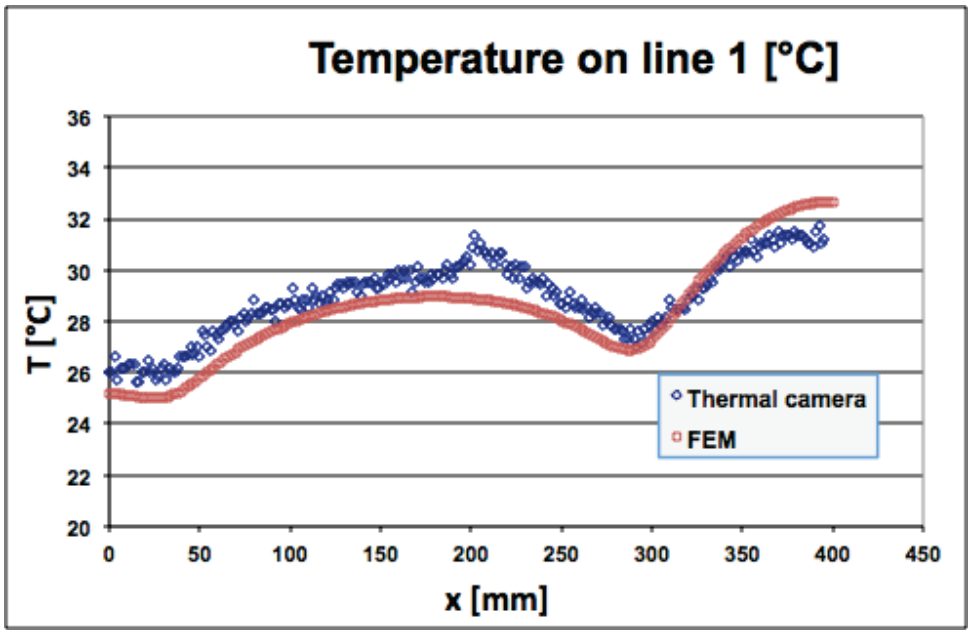

Figure 2.41 FEM and experimental comparison on the line 1 for the vane cooling

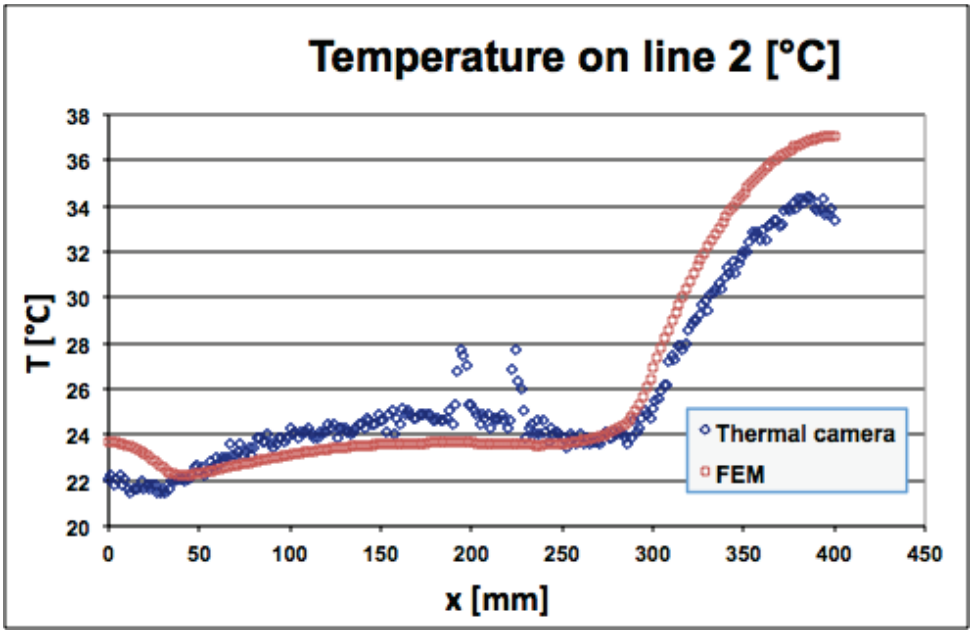

Figure 2.42 FEM and experimental comparison on the line 2 for the vane cooling

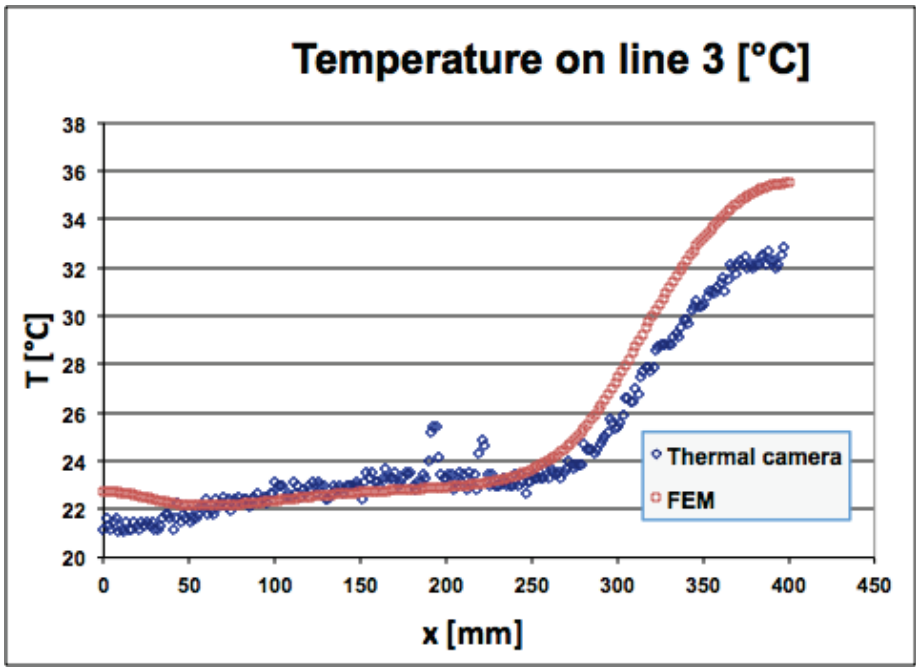

Figure 2.43 FEM and experimental comparison on the line 3 for the vane cooling

The experimental results were also used to verify the accuracy of the thermal fluid analysis with Ansys CFX [5]. It was possible to study only the case of the cooling of the vane. The study of the vessel was also tried, but problems were found. Since the thread was necessary to be modeled, the geometry was created with UG

NX and Parasolid format was imported in Ansys Workbench for the creation of the mesh. For what concerning the Ansys Workbench, the import of the geometry and the generation of the mesh were successful, although it was very difficult to reach a good quality. Different mesh sizes were tried, but problems were encountered to reach the convergence of the solution

Figure 2.44 and 2.45 show the model and the zone of application of the boundary condition used for the thermal fluid dynamics simulations.

The boundary conditions and the parameters of the material used in the simulations are reported in table 2.6.

The parameters of the material are the same of that used on the previous simulations

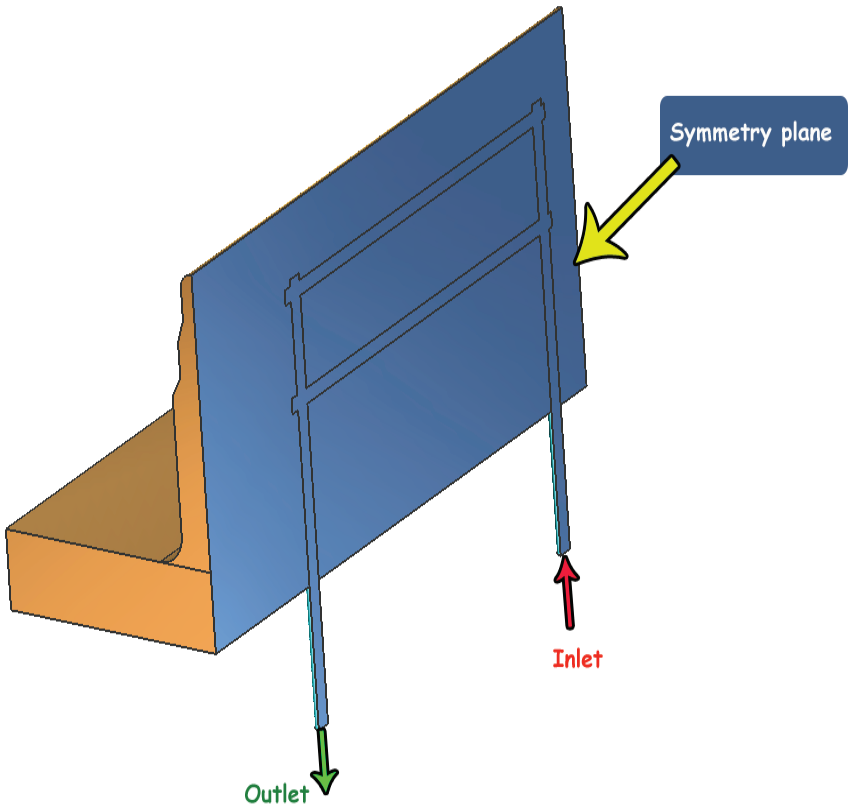

Figure 2.44 Inlet, outlet boundary conditions used on the simulation

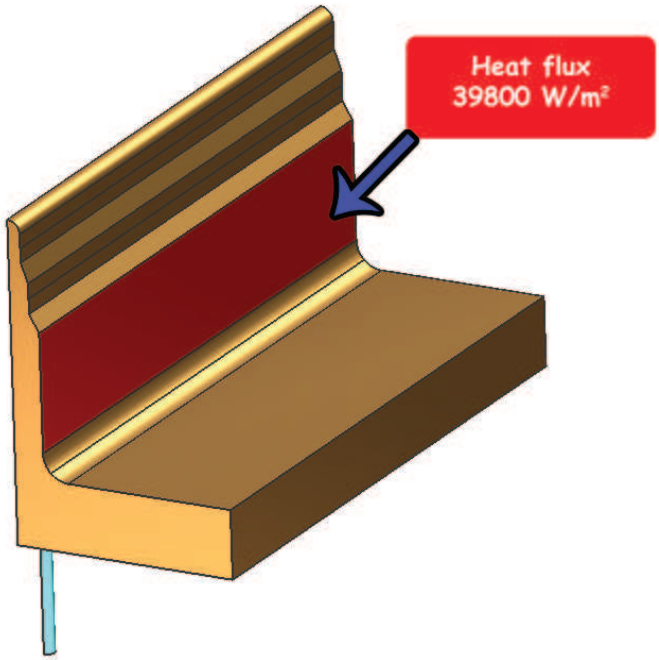

Figure 2.45 Heat flux applied on the model of the simulation

Boundary condition of the fluid domain		
Inlet	**Mass flow rate**	$0.17\frac{kg}{s}$
	Turbulence intensity	5%
	Temperature	15 ˚C
Outlet	**Average relative pressure**	0 Pa
Boundary condition on solid domain (copper)		
Heat flux		$39800\frac{W}{m^2}$
Number of elements		About 400000
Solution time		About 15 minutes on a PC with 4GB RAM and Dual Core Processor for Ansys CFX About

Table 2.6 Parameters and boundary conditions of the thermal fluid dynamics simulations for the comparison of the experimental data

Graphs above (figures 2.46, 2.47 and 2.48) show a comparison between experimental results and the calculated with Ansys CFX considering various turbulence models.

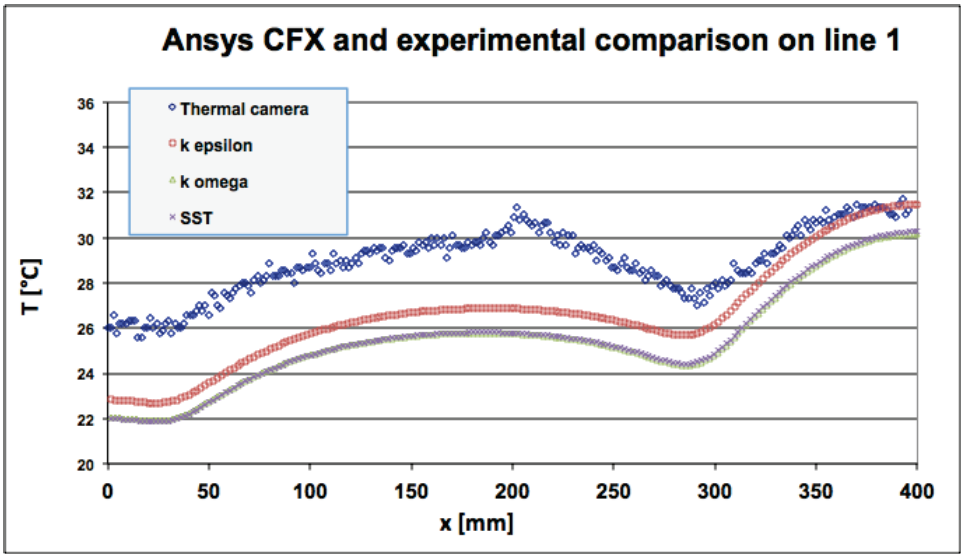

Figure 2.46 Comparison between measured temperature on the electrode and the calculated with Ansys CFX with different turbulence models on line 1.

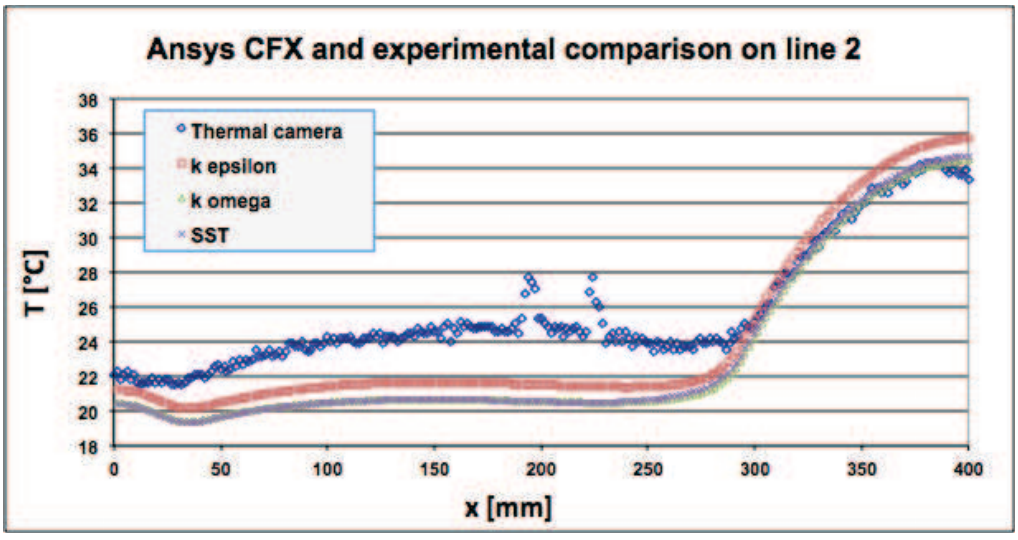

Figure 2.47 Comparison between measured temperature on the electrode and the calculated with Ansys CFX with different turbulence models on line 2.

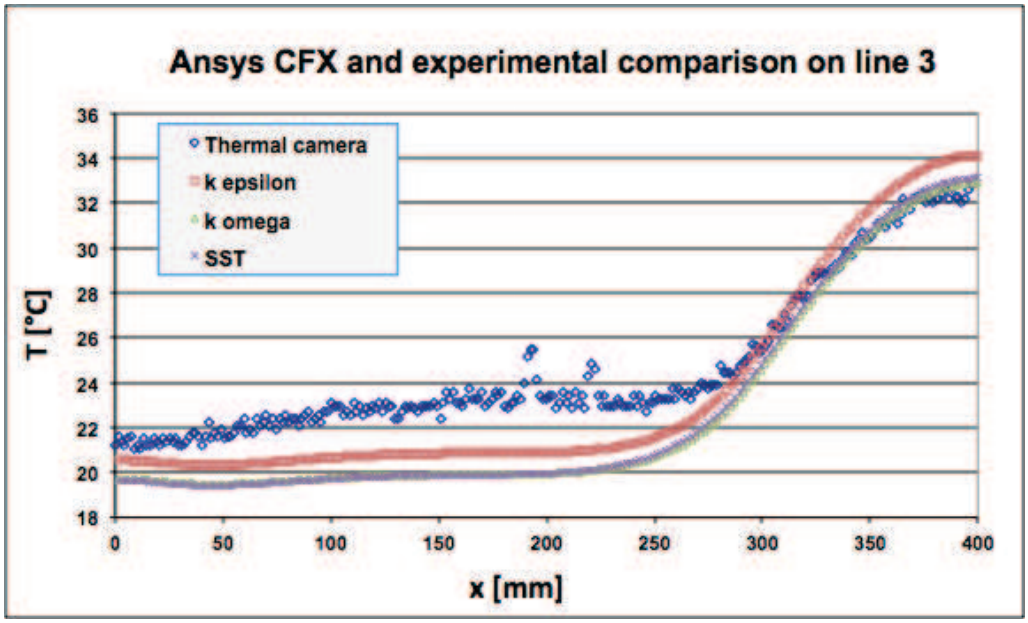

Figure 2.48 Comparison between measured temperature on the electrode and the calculated with Ansys CFX with different turbulence models on line 3.

The accordance with the experimental results is quite discrete. In particular there is a good accordance on the zone that is not cooled, for the value of x in the range 300 - 400 mm. On the zone where there is the presence of the cooling duct the accordance is quite discrete with maximum errors of 15%. The temperature calculated with the k-ω and the SST models is quietly the same. The k-ε model instead shows a better accuracy on the fitting of the experimental results on the cooled zone. In conclusion it seems that with all the models of turbulence there is a overestimation of the wall convective heat transfer coefficient. In particular, it seems that at the entrance the computation is correct, and this fact is demonstrated by the good fitting of the experimental results on the x range of 300 - 400 mm. For the x range of 0 - 300 mm the increase of the wall heat transfer coefficient resulted from the increase of the turbulence on curves seems to be overestimated.
This problem was tried to be corrected considering a thermal resistance at the interface of the cooling duct with the copper electrode. Figures 2.49, 2.50 and 2.51 show the comparison of the experimental results with that calculated with Ansys CFX with different values of the thermal resistance at the interface. The k-ε turbulence model were considered only for the better accuracy of the result demonstrated before.

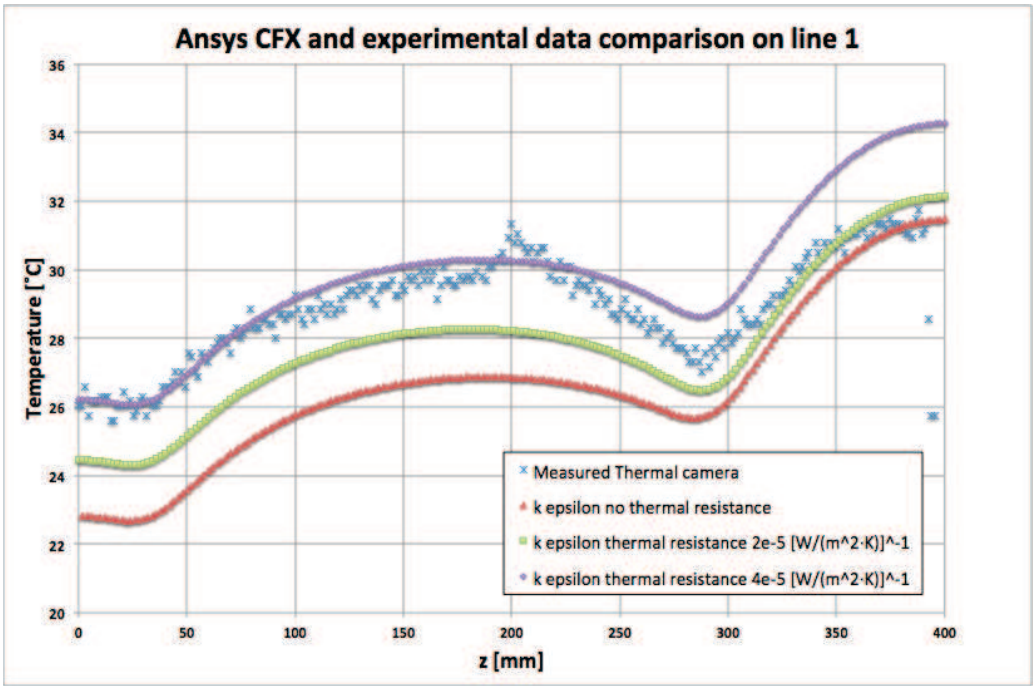

Figure 2.49 Comparison between measured temperature on the electrode and the calculated with Ansys CFX with different turbulence models on line 1 with different values of the thermal resistance at the interface using k-ε to model the turbulence

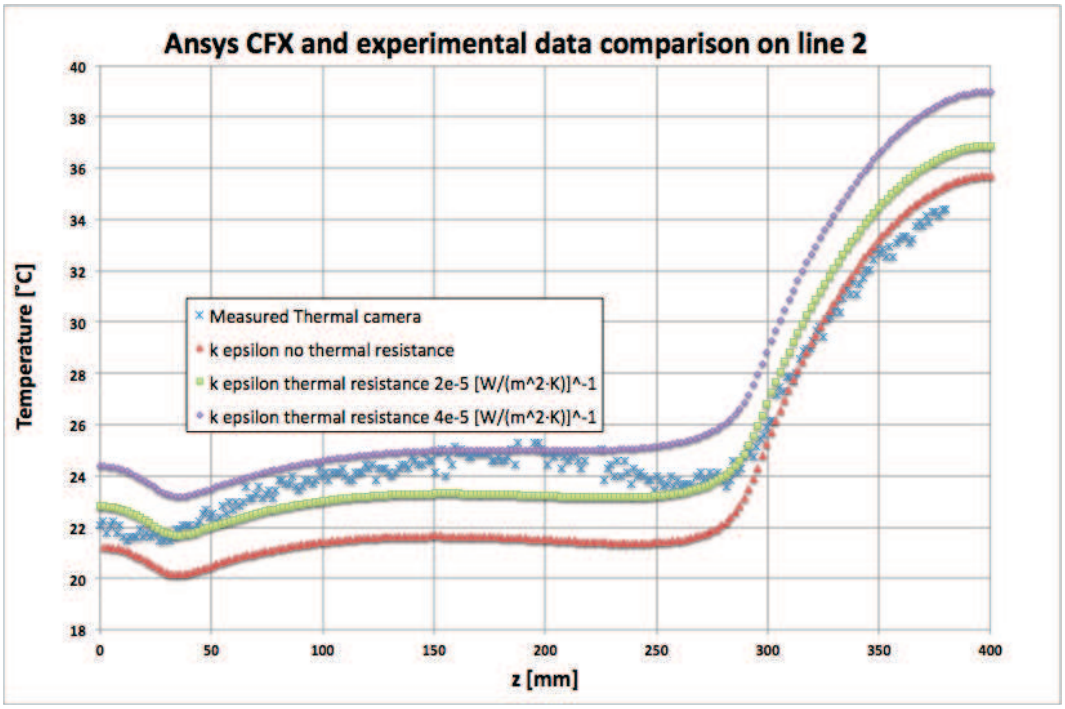

Figure 2.50 Comparison between measured temperature on the electrode and the calculated with Ansys CFX with different turbulence models on line 2 with different values of the thermal resistance at the interface using k-ε to model the turbulence

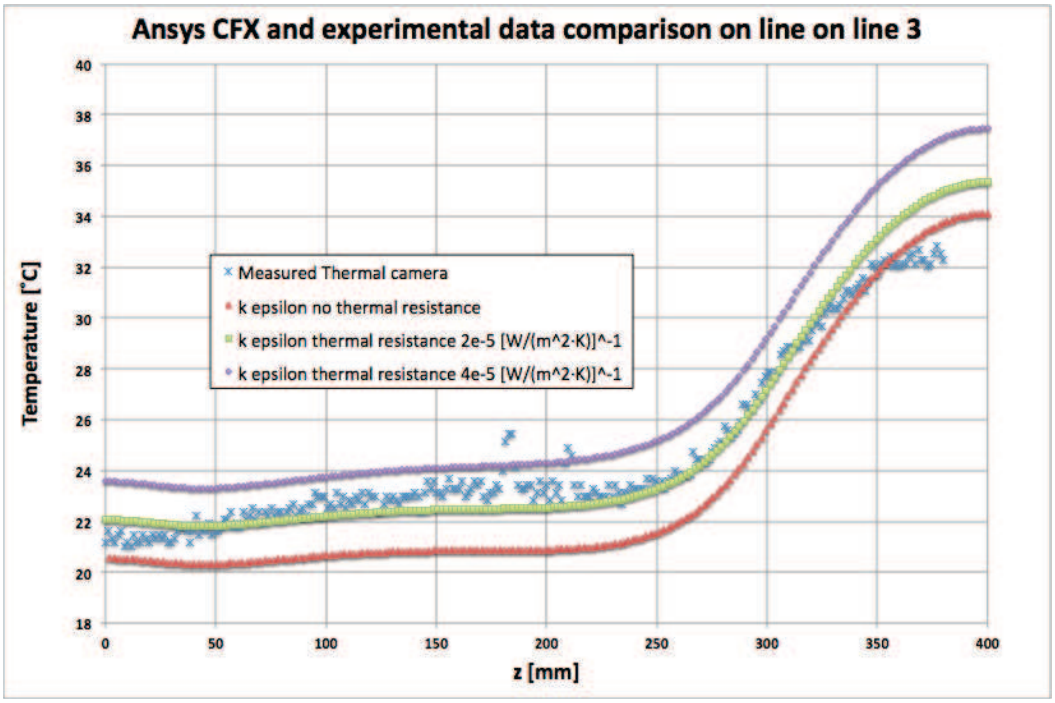

Figure 2.51 Comparison between measured temperature on the electrode and the calculated with Ansys CFX on line 3 with different values of the thermal resistance at the interface using k-ε to model the turbulence

The comparison show that with a value of $2e\square 5\frac{m\times K}{W}$ for the thermal resistance at the interface between copper and water domain the results are fitted with better accuracy, especially on the cooled zones.

Thermal fluid dynamics simulations seem to be preferable to take into account the variations of the heat transfer coefficient induced by the elbow and on the T junctions with the cooling duct with the manifold, although the solution time of the simulation could be major than simple thermal simulations.

What it is important to underline from this experimental test setup, it gave a lot of information on the type of cooling duct to adopt on the final modules. The case of the cooling of the vessel showed that although the higher cooling efficiency, the flow and the temperature along the electrode were not as uniform as demonstrated with the cooling of the vane with smooth ducts. This fact confirmed the results of the simulations of the small copper block of 200 mm length, which highlighted a better uniformity of the flow on the smooth cooling duct. In fact the trend of the

heat transfer coefficient was qualitatively correct (the flow is not as uniform as for the smooth duct), although not quantitatively correct, due to the difference of experimental and simulated results. The final choice was to adopt only smooth ducts for the cooling of the vane and the vessel, because the temperature distribution and the deformations along the beam axis should be as much uniform as possible for the stability of the electric field.

2.4 Design of the cooling system of the RFQ modules [6]

As anticipated on the paragraphs above, the cooling system of each module of the RFQ, in order to keep in control the variation from the nominal frequency induced by deformation of the cavity when the RF power is applied on the electrodes.

Frequency is the main electromagnetic parameter that has to be taken into account on the design of the cooling system. There is an equation, the Slaughter formula [6], that expresses the relation between the shift of frequency and the displacements of particular points of the cavity.

Considering a bi-dimensional sketch of on octave of the RFQ (figure 2.52), the shift of frequency from the nominal value of 175 MHz can be expressed in function of the displacement of the point 1, 2, 3.

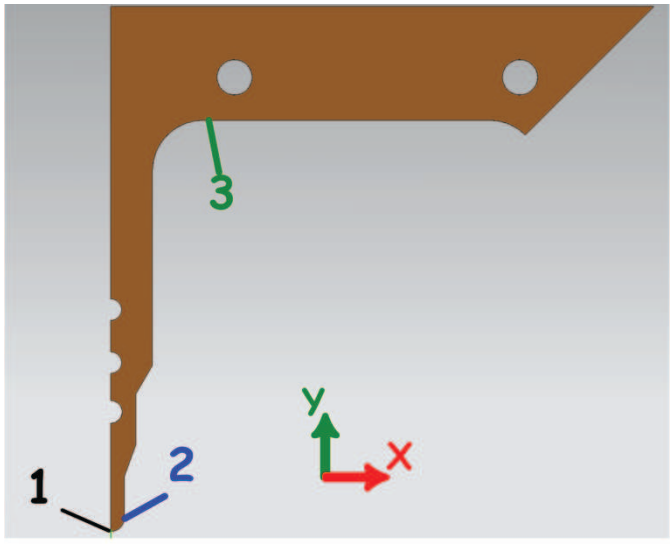

Figure 2.52 Sketch of an octave of the RFQ and the three particular points whose displacements influence the variation of the frequency

The relation that expresses the variation of frequency is:

$$\delta f = \propto_{R_0} \cdot \delta R_0 + \propto_{\rho} \cdot \delta \rho + \propto_{H} \cdot \delta H \qquad (2-30)$$

δR_0 is the y displacement of the pole tip (point 1), $\delta\rho$ is the variation of the pole tip radius (x displacement of the end radius of the pole tip) (point 2) and δH is the y displacement of a point on the vessel in correspondence of the vane. $\propto_{R_0}, \propto_{\rho}, \propto_{H}$ are the sensitivity coefficient that links the displacement of the three point of the cavity to the frequency shift.

The three coefficients are function of the geometry of the cavity. Since the width of the vane and the pole tip radius varies along the beam axis, the coefficients are not constant along the RFQ.

Table 2.7 reports the values of the three coefficient at the begin and at the end of the accelerating line.

	$\propto_{R_0}$ [MHz/mm]	$\propto_{\rho}$ [MHz/mm]	$\propto_{H}$ [MHz/mm]
Modules 1-6	11.6	-5.3	-1.2
Modules 13-18	7.6	-4.1	-0.9

Table 2.7 The $\propto_{R_0}, \propto_{\rho}, \propto_{H}$ coefficients

As result from table 2.7, the effect of a same displacement of the pole tip dominates on the effect od a same displacement on the vessel. The variation of the pole radius, is always very small less than 1 μm and does not contribute to the shift of frequency.

The cooling system on the each module of the RFQ was designed taking into account the (2-10) in a way to satisfy the requests of the RF technician to vary the operational frequency in a range of -/+ 100 kHz.

As anticipated on paragraph 2.2, two separate cooling circuits, one cold and one warm, feed respectively the cooling ducts of the vane and the vessel. The idea was to vary the frequency making the cavity expand or contract considering to vary the inlet temperature of the vessels in a range [15;27] ˚C, maintaining fixed the inlet temperature of the vane to 15 ˚C.

2D thermal structural analyses using Ansys APDL 12 and 3D fluid-thermal-structural analyses with Ansys CFX were performed to study the configuration of the cooling ducts on each module in terms of the dimension and position.

In particular, since there are three modules between an inlet and an outlet, the average frequency of the entire cooling module should be in the range -/+ 100 kHz from the nominal frequency of 175 MHz.

Moreover, the target value of -100 kHz or lower had to be considered on the design of the cooling system with all the inlet on the vessel and the vane at 15 ˚C.

2.5 Design of the cooling system of the high-energy modules (13-18) of the RFQ. [6]

In this paragraph the strategies of the design for the cooling system of the high energy modules will be presented.

Initial bi-dimensional coupled thermal-structural simulations were performed with ANSYS APDL using the SOLID223 element, which has both thermal and structural degrees of freedom. The target of the simulations was to determinate a first preliminary position of the cooling ducts on the modules of the high-energy zones. Figure 2.53 shown the model created and meshed with Ansys APDL. A simplified geometry was used considering only the copper. In this case considering the symmetries only an octave can be modeled.

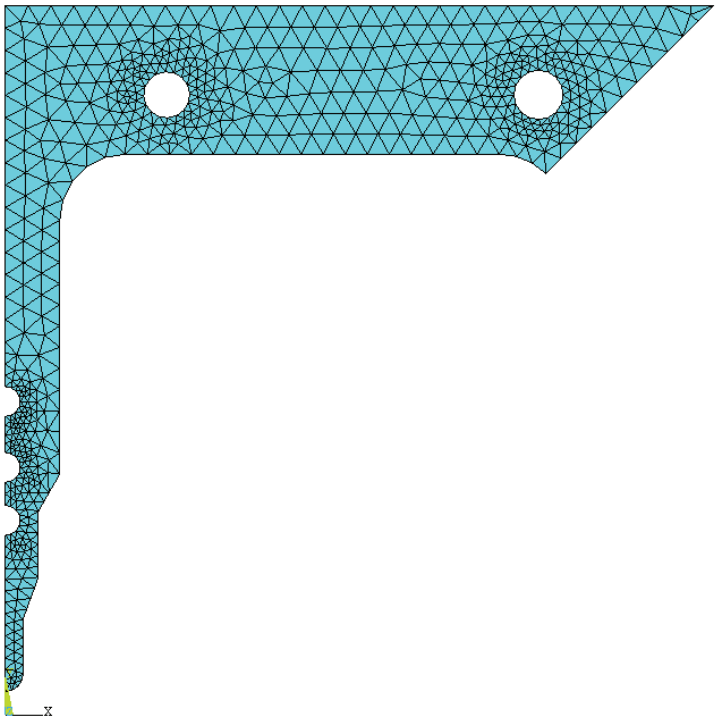

Figure 2.53 Model and mesh on the octave RFQ for the preliminary study of the cooling ducts of the high energy modules

This zone is characterized by modules with the same geometry of the internal cavity and also the RF dissipated power is constant on each module.
This means that the study of only one cooling module is necessary.
A thermal heat flux was applied on the surfaces of the cavity and it was calculated by means of electromagnetic simulations with Ansoft HSS code by the colleague of LNL. On the surfaces of the cooling duct a convective constraint was applied. The reference temperature was the average between inlet and outlet of a duct, considering the thermal cooling module as an extrusion of three modules. Dittus-Boelter equation was used for the convective heat transfer coefficient, considering a nominal velocity of 3 m/s on each cooling duct:

$$Nu = 0.023 \cdot Re^{0.8} \cdot Pr^{0.4} \quad (2-31)$$

where Nu, Re, Pr are respectively the a-dimensional numbers of Nusselt, Reynolds and Prandtl:

$$Re = \frac{\rho \cdot v \cdot d}{\mu} \quad (2-32)$$

$$Pr = \frac{c \cdot \mu}{\lambda} \quad (2-33)$$

$$Nu = \frac{\propto \cdot d}{\lambda} \quad (2-34)$$

ρ is the density of the fluid, v is the nominal velocity on the cooling ducts, d is the diameter of the cooling ducts, μ is the dynamic viscosity of the fluid, c is the specific heat capacity, λ is the thermal conductivity of the fluid and α is the convective heat transfer coefficient.
Table 2.7 summarizes the boundary conditions and material properties used for the preliminary bi-dimesnional thermal structural simulations of the modules of the RFQ.

Material properties of copper C10100	
Thermal conductivity	$400\ \frac{W}{m \cdot K}$
Thermal expansion coefficient	$17e-6\frac{1}{^{\circ}C}$
Young's modulus	114 MPa
Poisson ratio	0.3
Boundary conditions	
Internal faces of the RFQ	Heat flux calculated with Ansoft HSS
Surfaces of the cooling duct	Convective coefficient and reference temperature

Table 2.7 Material properties and boundary conditions of the bi-dimensional simulations

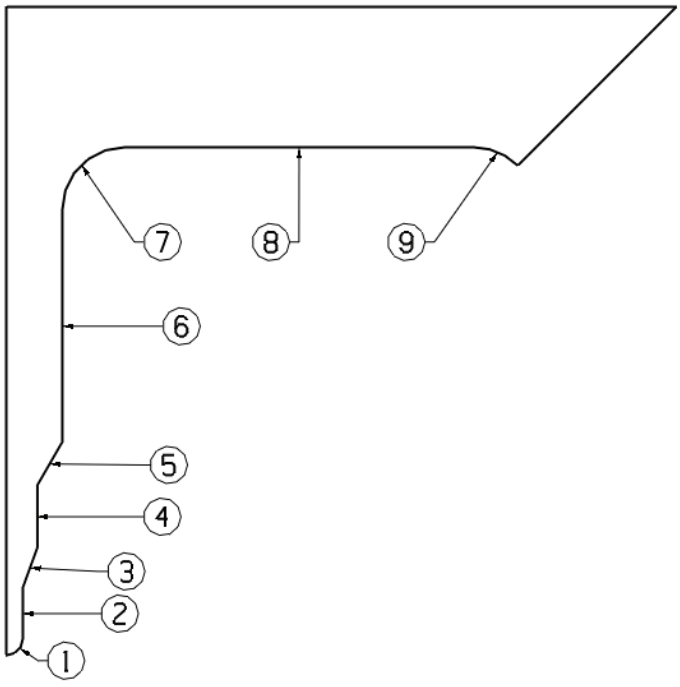

Figure 2.54 Reference location for the thermal loads calculated with Ansoft HSS

Table 2.8 shows the heat fluxes to be applied on the cavity walls as results of Ansoft HFSS results, while figure 2.54 shows their reference location.

Segment	Heat flux [W/m^2]
1	2710
2	14240
3	22050
4	29340
5	33700
6	42800
7	46900
8	48860
9	50370

Table 2.8 Thermal load calculated with Ansoft HSS for the high energy supermodule.

	x [mm]	y [mm]	Diameter [mm]	Convective coefficient [W/(m^2·K)]
Bottom vane duct	0	54	9	12000
Middle vane duct	0	75	9	12000
Top vane duct	0	95	9	12000
Central vessel duct	49	188	14	11000
Angular vessel duct	162	188	14	11000

Table 2.9 Position, dimension and convective coefficient of the cooling ducts

Table 2.9 reports the displacements of the point of the cavity that allow to evaluate the shift of frequency from the nominal as function of the temperature applied on the the ducts of the vessel, while the temperature on the channels of the vane is fixed to 15 ˚C, since the coefficient of the equation (2-10) are:

•α_{R0}: 7.6 kHz/μm;

• α_{ρ}: -1.3 kHz/μm;

• α_{H}: -0.91 kHz/μm.

Vessel Temperature [˚C]	δR_0 [μm]	δρ [μm]	δH [μm]	δf [kHz]
15	-7.8	1	22	-80
22	4.6	1	38.5	-0.7
27	16	1	54	73

Table 2.10 δR_0, δρ and δH displacements and shift of frequency in function of the temperature on the vessel duct.

The shift of frequency δf resulted of -70 kHz with the temperature of all the cooling ducts at 15 ˚C. The initial configuration of the cooling ducts in terms of number, dimension and position seemed to be acceptable, because, since the ΔT between the inlet and the outlet is major on the vane than the vessel, it has been experienced from the three dimensional analyses that there is a decay of the frequency from the first module to each next module of the series of the three modules that constitute the cooling module.

The-bidimensional termo-structural FE analyses do not give the real information on the displacements of the internal cavity. In fact the modules are rich of three dimensional details:

- The steel frames at the ends of each module.
- The bolted side flanges for the connection between each module
- The holes for on the copper for the housing or the tuner
- The vacuum grid on copper for the vacuum pumping
- The steel CF flanges for the connection with the couplers, tuners or the vacuum ports
- The modules are quite short and the effect of the inlet and the outlet cooling ducts of the vane and the vessel.

Thanks to the quite good tuning of the heat transfer coefficient, coupled fluid-thermal analyses were solved with Ansys CFX in Ansys Workbench environment. In particular 3D fluid thermal simulations were performed in

order to include the increase of temperature along the different cooling ducts and the effect of the non uniformities of the flow on the ducts and near the elbows. The temperature map was then imported for the solution of a structural simulation in Ansys Workbench to calculate the displacement of the cavity and the induced stresses.

The study was concentrated on the cooling module formed by the modules 13, 14 and 15. Because the power to be dissipated on the cavity is the same along all the six modules, the deformation and so the shift of frequency would be the same on the modules 16, 17 and 18.

Each of the three modules was studied independently; otherwise the consumption of the computational resources would be too much.

The thermal loads that have been applied on the cavity walls are the same as the 2D study. Moreover, an enhancement of dissipated power was applied on the vacuum grid, according to figure 2.55.

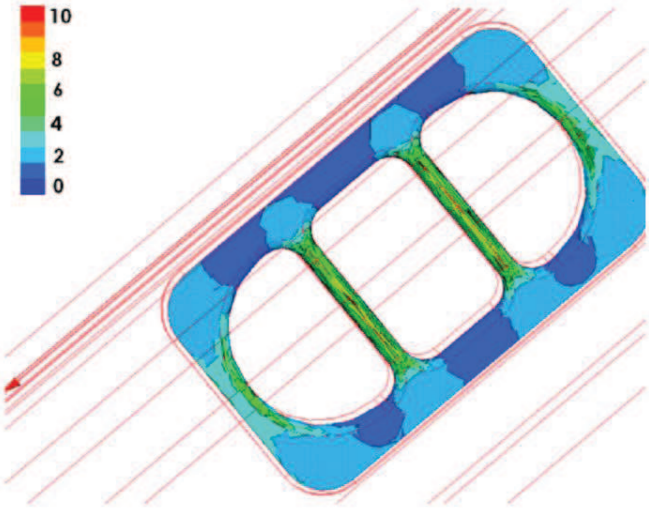

Figure 2.55 Enhancement of power dissipated on the vacuum grid zone

The increase of dissipated power is expressed as the ratio to the nominal power on the cavity wall considered as smooth without any hole.

The cooling duct layout was that of the 2D study. The dimensions of the cooling duct on the vane has been decided by means of fluid dynamics simulations performed with Ansys CFX code. In fact it has been decided to feed the three cooling channels of the vane with a single manifold: the

modules are short, avoiding the introduction of other three dimensional effects.

The dimensions of the manifold and of the cooling ducts has been studied in a way to distribute the mass flow uniformly and to be as close as possible to the nominal velocity of 3 m/s on each cooling duct. Symmetry was considered.

Table 2.11 lists the boundary condition used for the simulation, while the properties of the cooling fluid (water) were the same considered previously.

Boundary conditions		
Inlet	Mass flow	0.18 kg/s
	Turbuent intensity	5%
Outlet	Average relative pressure	0 Pa

Table 2.11 Boundary condition and fluid properties used for the simulation of the design of the manifold and the cooling ducts of the vane.

After some iterations the optimal configuration was found (figure 2.56 and 2.57).

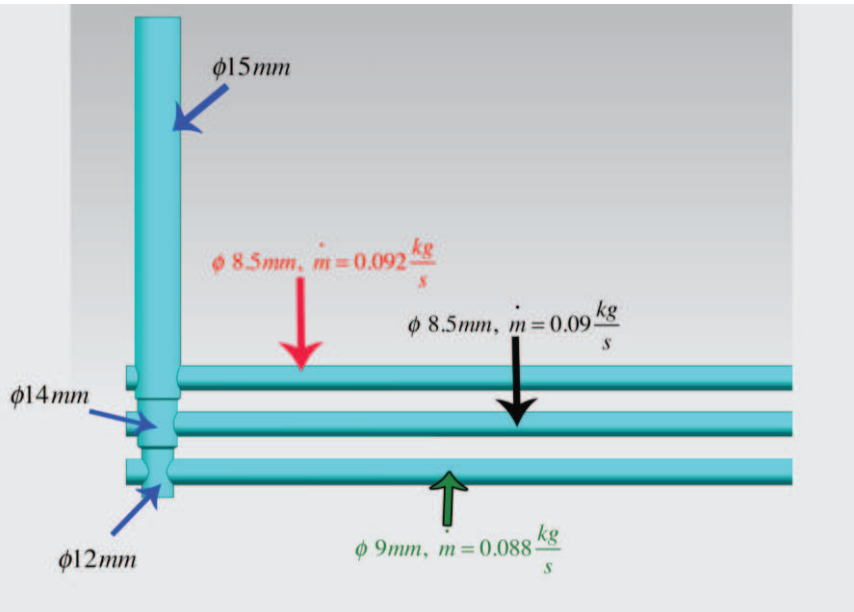

Figure 2.56 Optimized geometry of the manifold and diameters for the cooling duct system of the vane of the high energy modules.

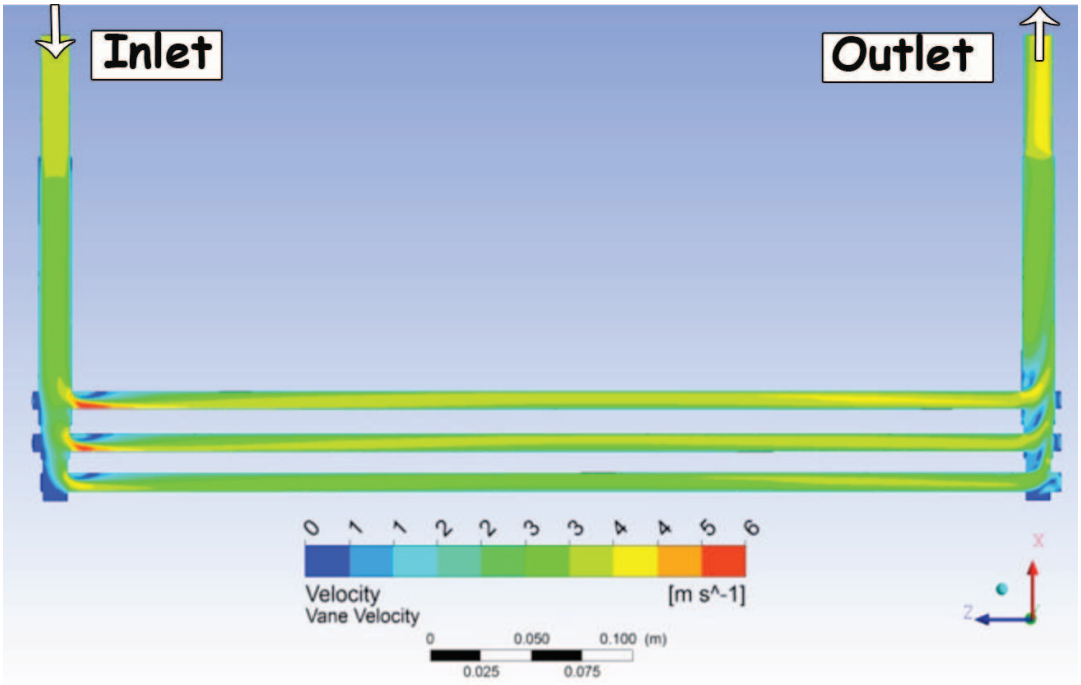

Figure 2.57 Fluid flow on the cooling ducts of the vanes

Once the design of the manifold and the dimensions of the cooling ducts of the vanes for the third supermodule has been decided, fluid thermal structural simulations were performed to evaluate the three dimensional deformation on the modules. Each module of the cooling module ha been simulated separately to save resources of memory, taking into account that the temperature at the inlet of the channel was that at the outlet of the previous module. On each simulations symmetry was considered, modeling only a quarter of module.

The boundary conditions and parameters of the material used for the thermal fluid and thermal simulations are summarized in table 2.11, while figure 2.58 shows an example for the module 13 where the boundary conditions on the fluid have been applied. As for the previous simulations all the material properties were taken from the MPDB (Material Properties DataBase) software. Since the accordance between the experimental and the calculated data from CFX anayses on the cooling test of the vane described previously was good considering a contact resistance of $2e-5\frac{m^2K}{W}$, the same was considered into the analyses.

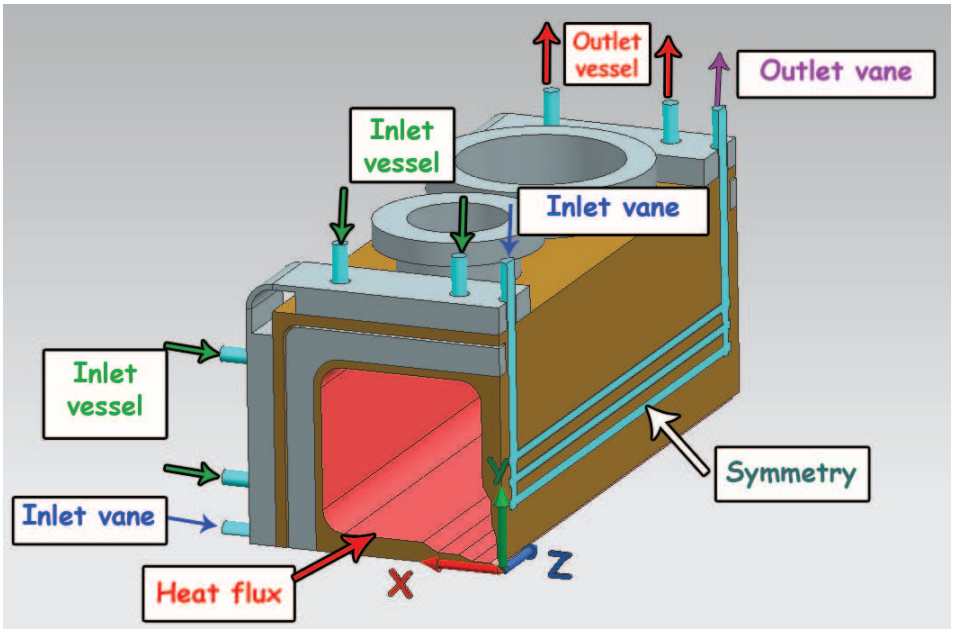

Figure 2.58 Model and boundary conditions of the module 13 for the thermal fluid calculations with Ansys CFX.

Boundary conditions		
Vane inlet	mass flow/2 (symmetry)	$0.27\ \frac{kg}{s}$
	Temperature	15 ˚C
	Turbulence intensity	5%
Vessel inlets	mass flow	$0.47\ \frac{kg}{s}$
	Temperature	from 15 ˚C to 27 ˚C
	Turbulence intensity	5%
Vane and vessel outlets	Average relative pressure	0 Pa
Wall thermal contact resistance		$2e-5\ \frac{m^2K}{W}$
Cavity wall		Heat flux

Boundary conditions		
Material Properties		
Water	Density (ρ)	$998\ \frac{kg}{m^3}$
	Dynamic viscosity (μ)	$1e-3\ Pa \cdot s$
	Specific heat(c)	$4180\ \frac{J}{kg \cdot K}$
	Thermal conductivity (λ)	$0.6\ \frac{W}{m \cdot K}$
Copper C10100	Specific heat (c)	$385\ \frac{J}{kg \cdot K}$
	Thermal conductivity (λ)	$400\ \frac{W}{m \cdot K}$
	Density (ρ)	$8920 \frac{kg}{m^3}$
Stainless Steel AISI 316 LN	Specific heat (c)	$500\ \frac{J}{kg \cdot K}$
	Thermal conductivity (λ)	$16\ \frac{W}{m \cdot K}$
	Density (ρ)	$7960\ \frac{kg}{m^3}$

Table 2.12 Boundary conditions for the fluid thermal Ansys CFX simulations

Once the temperature on the modules were calculated, it was imported for FE structural analyses in Ansys Workbench.

The material properties utilized (from MPDB) for the structural simulations are tabulated in 2.14.

Material Properties used in the Static Structural Analyses		
	Copper C10100	AISI 316 LN
Coefficient of thermal expansion (α)	$1.7e-5\ \frac{1}{°C}$	$1.65e-5\ \frac{1}{°C}$
Young modulus	117 GPa	200 GPa
Poisson ratio	0.34	0.3

Table 2.13 Material properties for the structural simulations

The boundary condition for the structural analyses are schematized on figure 2.59. Only one of the two steel frames was fixed on the z direction, since the modules are free to expand.

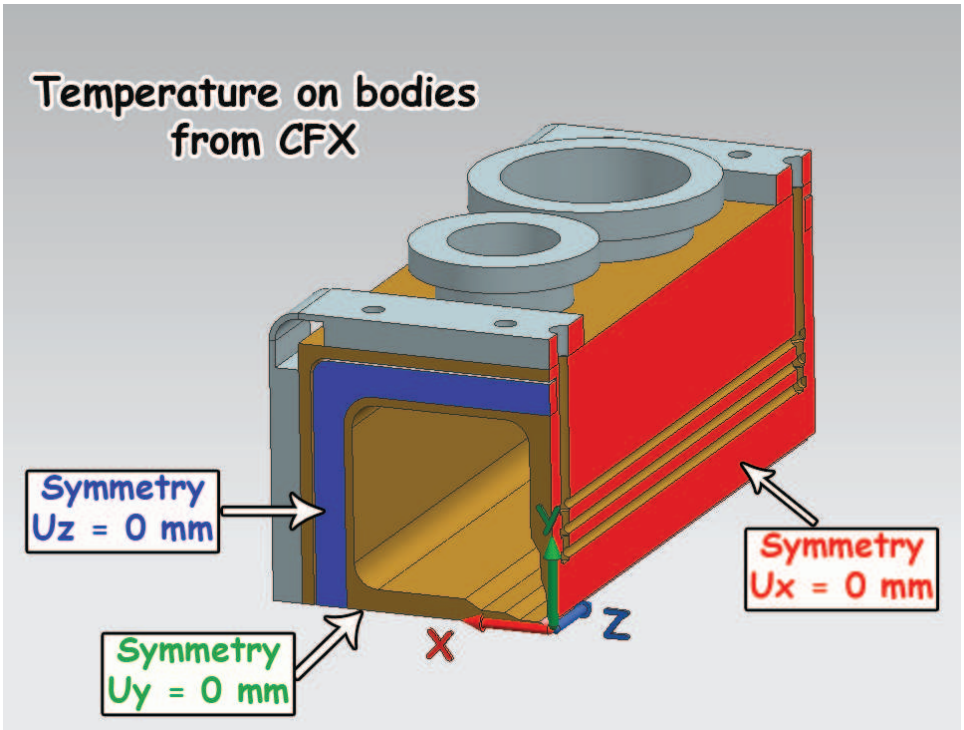

Figure 2.59 Boundary condition for the FE model

The displacements of the same three characteristic points δR_0, $\delta\rho$ and δH considered on the bi-dimensional simulations was taken into account to evaluate the shift of frequency on each module, by means of the coefficient α_{R0}, α_ρ and α_H. The following figures report the results of the displacements along the cooling module of the points mentioned before for the calculus of the frequency (dR0 means δR_0, drho $\delta\rho$ and dH δH) on the cavity for the modules 13, 14 and 15 that

compose the cooling module. The electrode 1 is that with the steel CF flanges, while electrode 2 that without holes. Z is the origin of Z is at the start of the entire cooling module. The positive z is defined from the direction of the beam axis.

For what concern the convention on the positive sign:

- A positive value of δR_0 means an increase of the distance respect to the beam axis
- A positive value of $\delta\rho$ means an increase of the pole tip radius
- A psoitiva value of δH means an increase of distance of the vessel from the beam axis.

The displacements were calculated with the inlet of the cooling ducts of the vessel of the "cooling module" at the different temperatures of 15 ˚C, 22 ˚C and 27 ˚C.

It is possible to have a value of the shift frequency for each point of the beam axis (z).

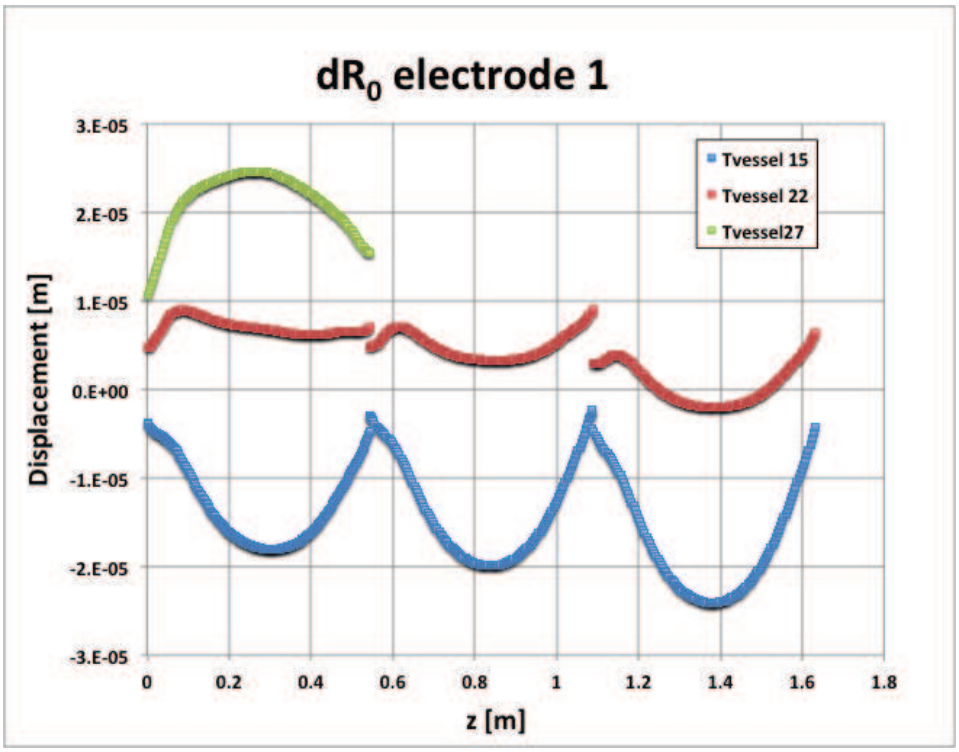

Figure 2.60 δR_0 displacement on the cooling module on electrode 1 for different temperatures at the inlet of the vessel.

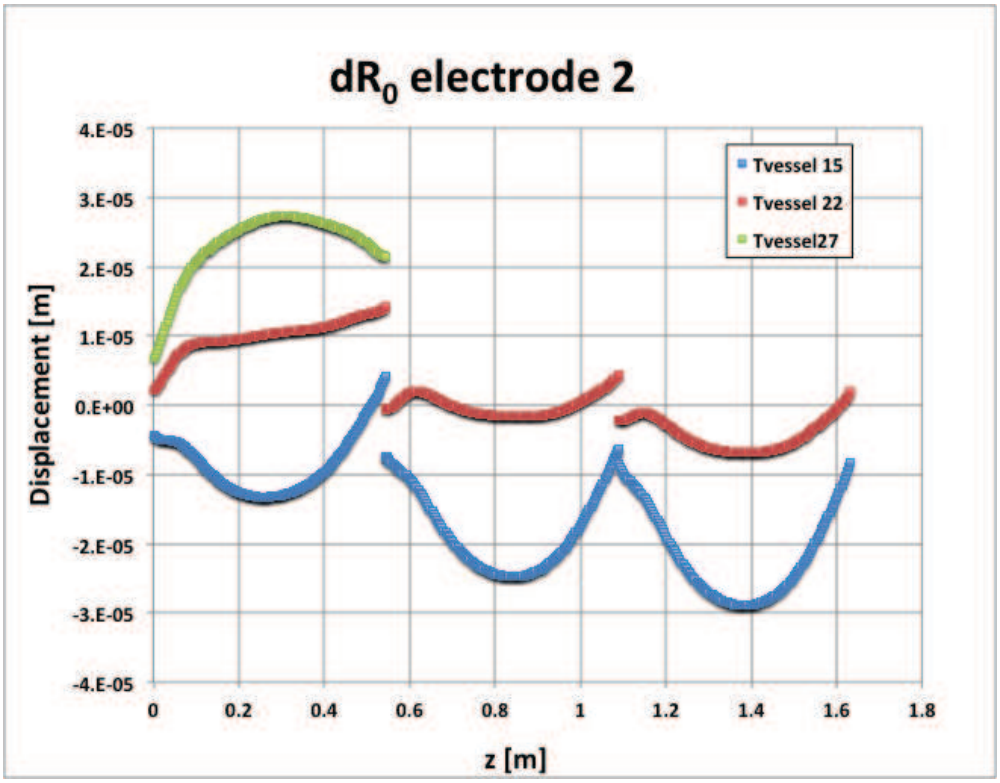

Figure 2.61 δR_0 displacement on the cooling module on electrode 2 for different temperatures at the inlet of the vessel.

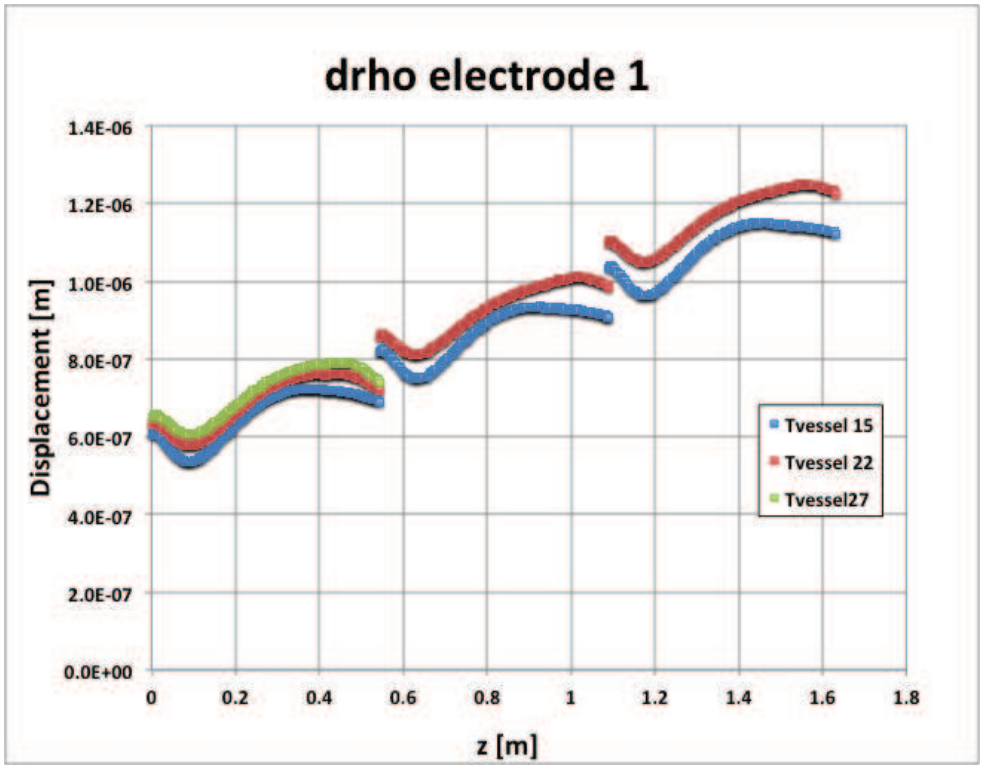

Figure 2.62 $\delta\rho$ displacement on cooling module on electrode 1 for different temperatures at the inlet of the vessel.

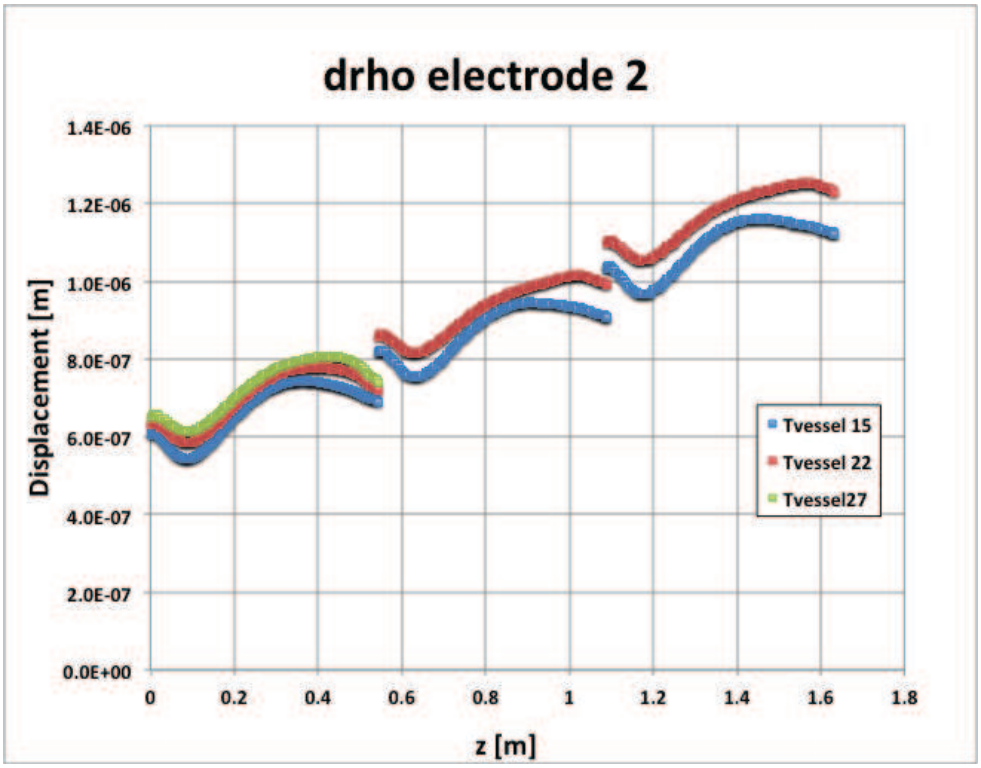

Figure 2.63 δρ displacement on cooling module on electrode 2 for different temperatures at the inlet of the vessel.

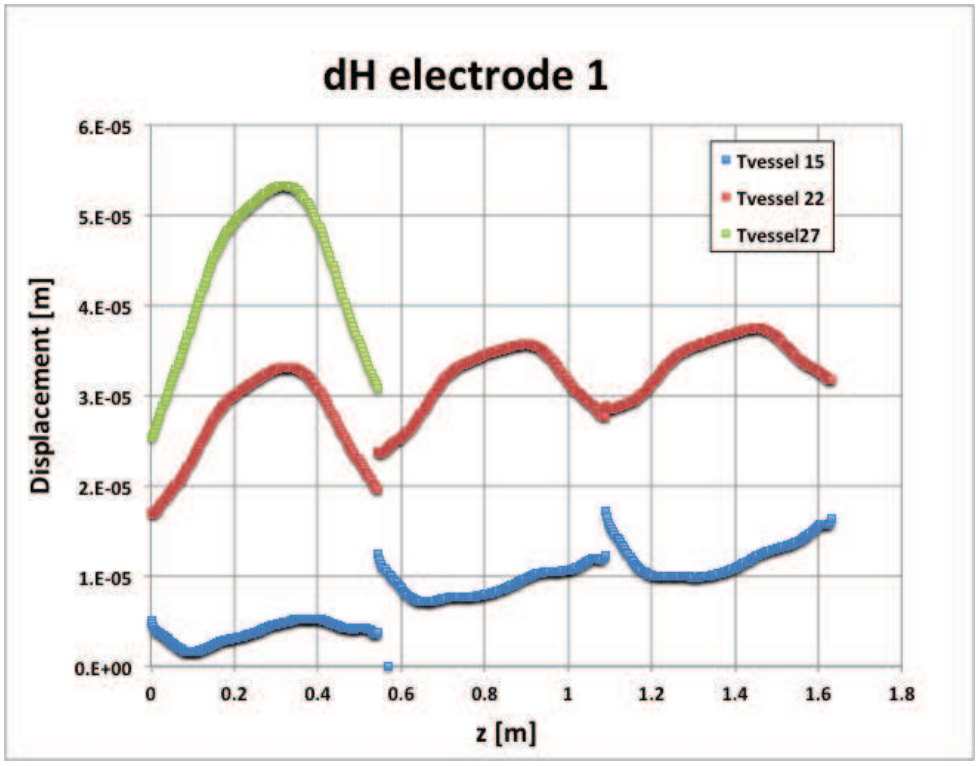

Figure 2.64 δH displacement on cooling module on electrode 1 for different temperatures at the inlet of the vessel.

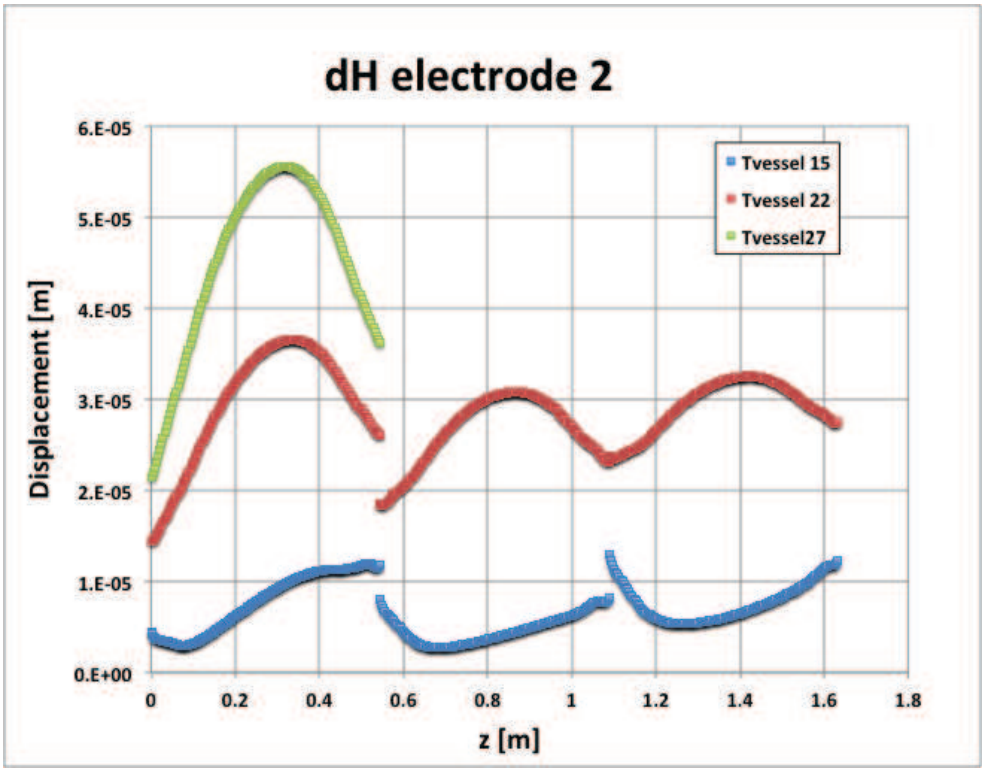

Figure 2.65 δH displacement on cooling module on electrode 2 for different temperatures at the inlet of the vessel.

The calculated displacements were analyzed by the RF experts of LNL to calculate the effect on the shift of frequency induced by the deformation of the cavity and to evaluate the perturbations on the electric field. The deformations of the cavity were acceptable for the electromagnetic targets criteria.

The table below (table 2.14) reports the results of the average shift of frequency calculated by the RF expert of LNL on each module at the different temperature at the inlet of the vessel of module 13. The average frequency for the entire cooling module was -125 kHz with the inlet at 15 ˚C and -3 kHz with the inlet at 22 ˚C.

The module 14 and 15 were not simulated with the inlet at 27 ˚C. In fact considering the decay of frequency from the module 13 to 15 with the inlet at 15 ˚C and 22 ˚C the average frequency for the cooling module is 90 kHz. The target value of +100 kHz can be reached with a small increase of the inlet of the vessel near 28 ˚C.

	δf module 13 [kHz]	δf module 14 [kHz]	δf module 15 [kHz]
Tvessel 15 ˚C	-90	-130	-160
Tvessel 22 ˚C	36	-5	-40
Tvessel 27 ˚C	125	-	-

Table 2.14 Average shift of frequency on the cooling module composed by the modules 13, 14 and 15

Another important point for the design of the modules is the evaluation of the stresses on the vacuum port induced by the enhancement of RF dissipated power, that was previously illustrated on figure 2.55.

The worst case for the vacuum port is that with the inlet of the vessel at 27 ˚C. Moreover the vacuum port on module 16 should be considered, since it is the third in series module of the cooling module. However, since the increase of temperature from the inlet to the outlet of the cooling duct of the vessel is on the order of 1 ˚C, the differences with module 13 are very small.

The maximum temperature on the vacuum grid is 72 ˚C and the maximum equivalent Von Mises stress is 45 MPa. The zone of maximum temperature and maximum stress are evidenced an figures 2.66 and 2.67. The case of such an high temperature was analyzed by the expert on science material of LNL, because the copper could release electrons. The values of temperature was retained acceptable. The maximum stress is acceptable, since the elastic limit of the material is 69 MPa, as mentioned on chapter 1.

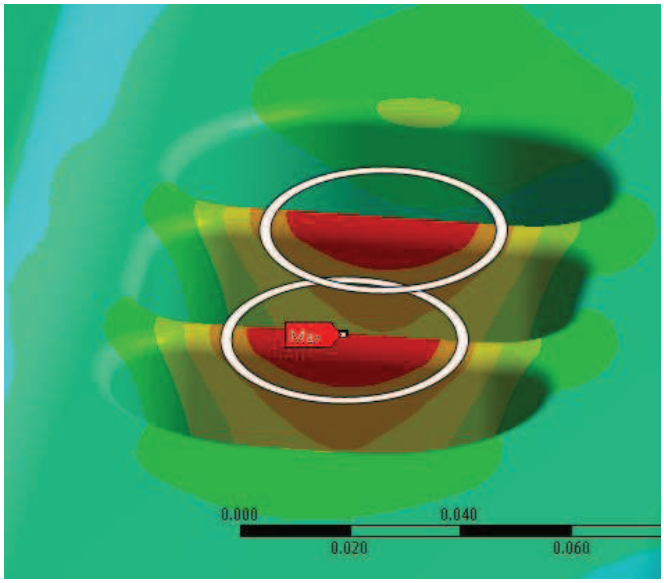

Figure 2.66 Zones of maximum temperature (72 ˚C) on the vacuum grid

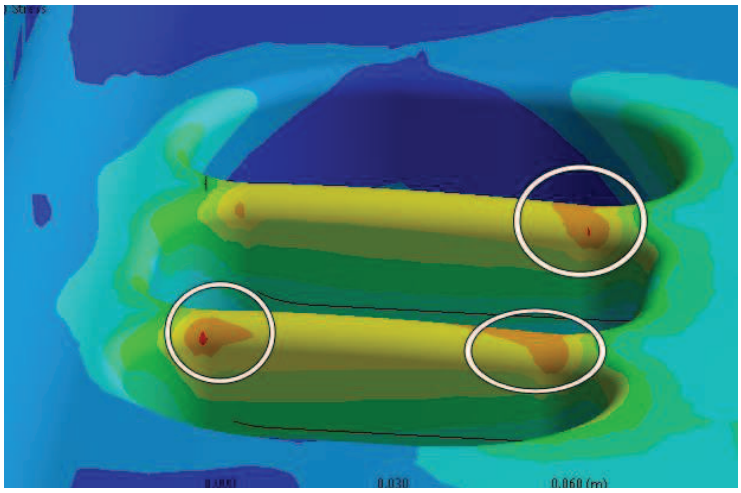

Figure 2.67 Zones of maximum Von Mises stress (45 MPa) on the vacuum grid

2.6 Design of the cooling system of the low energy modules (from 1 to 6)

The first six modules of the RFQ present a variable geometry of the vanes on the first three ones, while on the last three ones the geometry of the vanes can be considered as constant, as described on chapter 1. As for the high energy modules, bi-dimensional thermal structural simulations were performed to calculate a preliminary layout of the cooling ducts for the three dimensional analyses. As the geometry of the vanes is not constant along the six modules, thermal loads that have to be dissipated on the cavity walls are not constant. So the two cases relative to the first (modules 1-3) and the second (modules 4-6) cooling modules were considered.

Table 2.15 report the heat fluxes due to RF power dissipation on the internal cavity of the modules 1-6, according to figure . As for the high energy modules 13-18, they are result of electromagnetic simulations made by the RF experts of LNL.

Segment	Heat flux range [W/m^2]
1	990-1000
2	5660-6380
3	9300-10960
4	12550-14900
5	15244-18940
6	19110-23140
7	20370-24080
8	21090-24830
9	21660-25400

Table 2.14 Thermal load calculated with Ansoft HSS for the low energy modules.

Table 2.14 states that the variation of the RF losses between the module 1 and the modue 6 is on the order of a maximum of 15%. As for the high energy modules preliminary bi-dimensional simulation with Ansys APDL were made to determine a first distribution of the cooling ducts.

Since the variation of the dissipated RF power is low form module 1 to 6, the thermal structural bi-dimensional studies to determine the preliminary layout of the cooling ducts was made on module 6.

Figure 2.68 shows the numerical model and the final optimal preliminary configuration of the cooling ducts layout. As for the simulations of the high energy modules, heat fluxes boundary condition were applied on the surfaces of the cavity and convective flux on the surfaces of the cooling ducts. Also in this case the convective coefficient was calculated by Dittus Boelter equation and the bulk temperature was varied in a range 15-27 ˚C. The solution is quite similar than that one for the high energy modules: the top cooling duct of the vane is

suppressed and the diameter of the cooling ducts of the vessel was reduced from 14 mm to 12 mm (table 2.15)

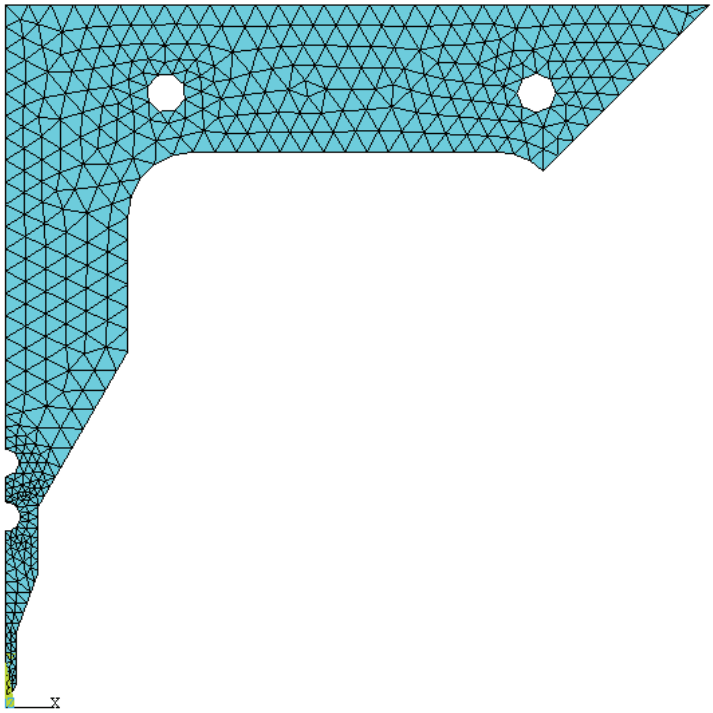

Figure 2.68 Numerical model and final layout of the cooling ducts on module 6

	x [mm]	y [mm]	Diameter [mm]	Convective coefficient [W/(m^2·K)]
Bottom vane duct	0	54	9	12000
Top vane duct	0	75	9	12000
Central vessel duct	49	188	12	11000
Angular vessel duct	162	188	12	11000

Table 2.15 Position, dimension and convective coefficient of the cooling ducts

Table 2.16 report the values of the shift of frequency for the different value of the bulk temperature of the vessel, considering the coefficient of the (2-10):

•α_{R0}: 11.3 kHz/μm;

• α_{ρ}: -5.3 kHz/μm;

• α_{H}: -1.2 kHz/μm

Vessel Temperature [˚C]	δR_0 [µm]	δρ [µm]	δH [µm]	δf [kHz]
15	-8.1	0.3	5	-96
21	4.9	0.3	25	28
27	18	0.4	46	150

Table 2.16 δR_0, δρ and δH displacements and shift of frequency in function of the temperature on the vessel duct.

As for the study of the high energy modules, this configuration of the cooling duct was used for the three dimensional fluid thermal structural simulations for the cooling modules composed by modules 1-3 and modules 4-6.

Table 2.17 lists the boundary condition used for the thermal fluid simulations, according to figure 2.69.

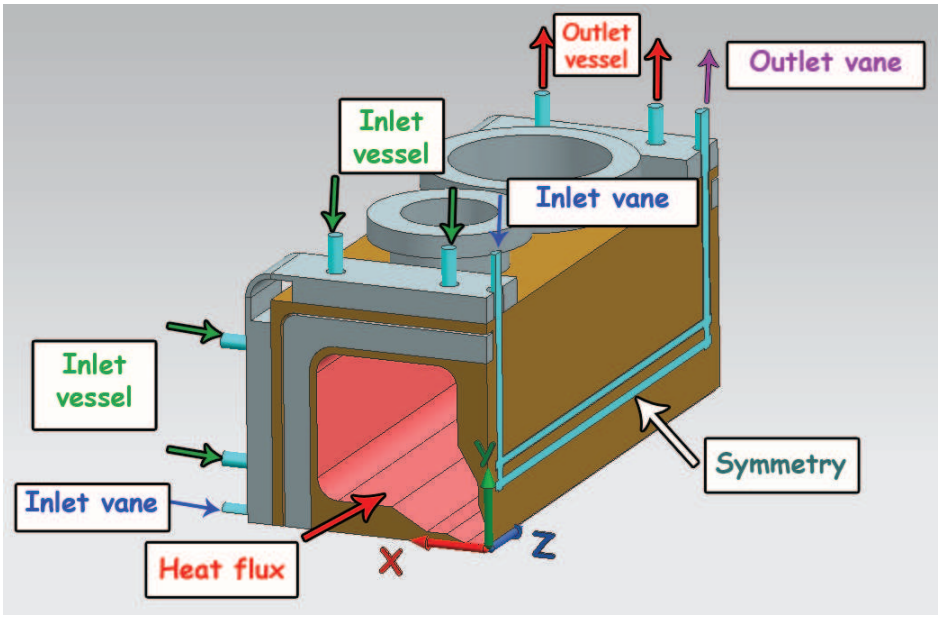

Figure 2.69 Example of boundary conditions applied on the modules of the low energy zone

Boundary conditions		
Vane inlet	mass flow/2 (symmetry)	$0.18\ \frac{kg}{s}$
	Temperature	15 ˚C
	Turbulence intensity	5%

Boundary conditions		
Vessel inlets	mass flow	$0.34\ \frac{kg}{s}$
	Temperature	from 15 ˚C to 27 ˚C
	Turbulence intensity	5%
Vane and vessel outlets	Average relative pressure	0 Pa
Wall thermal contact resistance		$2e-5\ \frac{m^2K}{W}$
Cavity wall		Heat flux

Table 2.18 Boundary conditions for the thermal fluid simulation of the low energy modules

As for the study of the high energy modules, the temperature distribution calculated with CFX analyses was given in input for the structural analyses in Ansys Workbench (figure 2.70). The material properties used on the simulations were the same mentioned on the study of the high energy modules.

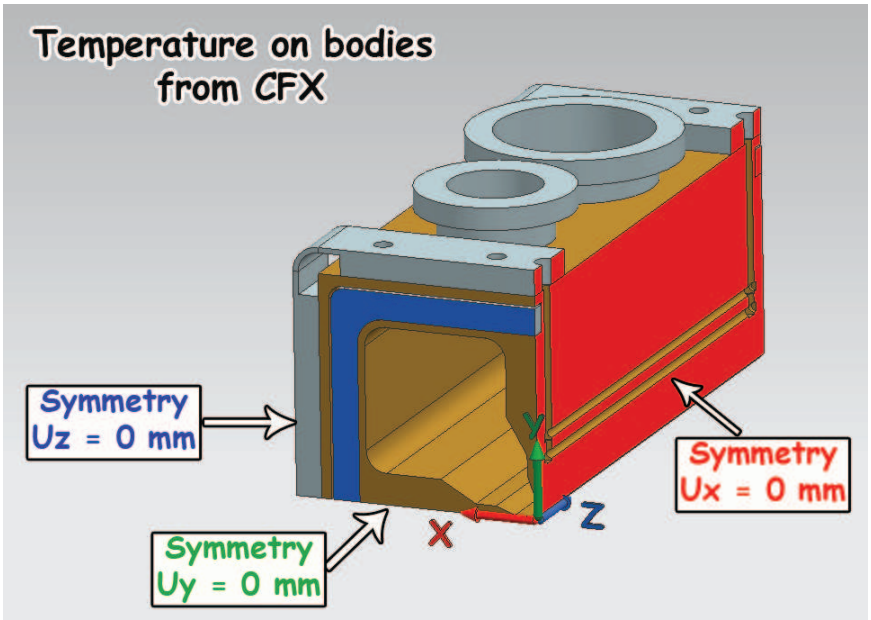

Figure 2.70 Boundary conditions for the structural simulations of the low energy cooling modules.

Figures from 2.71 to 2.76 report the displacements of the points necessary for the calculation of the shift of frequency for the cooling module formed by the modules 1 to 3 for the various temperatures at the inlet of the vessel. The convention on the positive signs for the δR_0, $\delta\rho$ and δH is the same as used on the high energy modules.

The z origin is placed at the start of the first module of the cooling module and positive direction is defined from the inlet to the outlet. The electrode 1 is that with the CF flanges, the electrode 2 is that without holes.

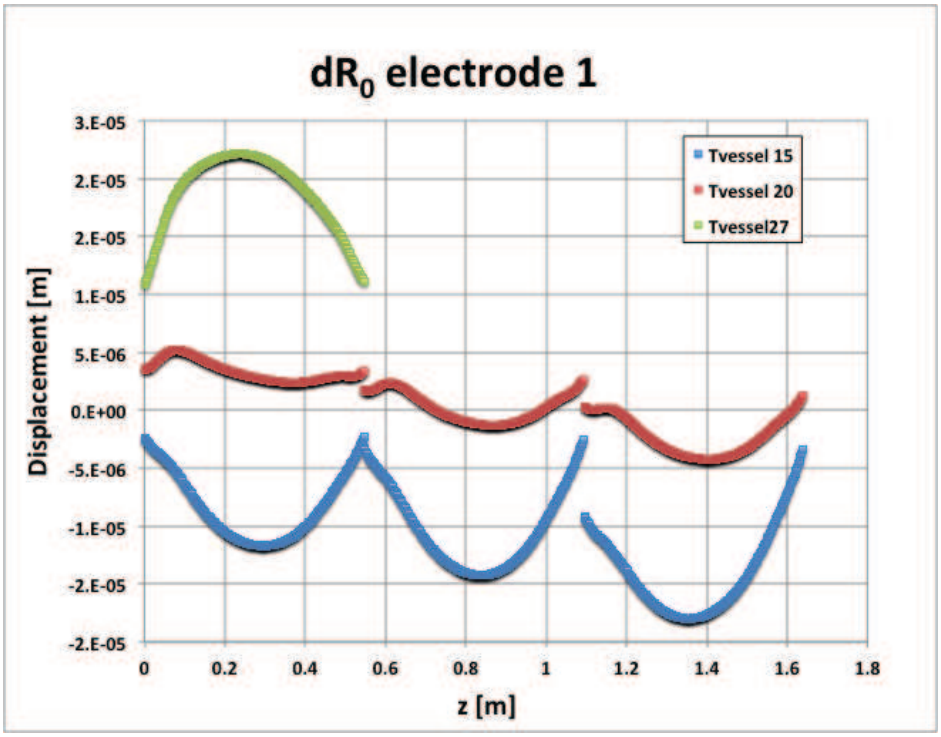

Figure 2.71 δR_0 displacement on the cooling module on electrode 1 for different temperatures at the inlet of the vessel.

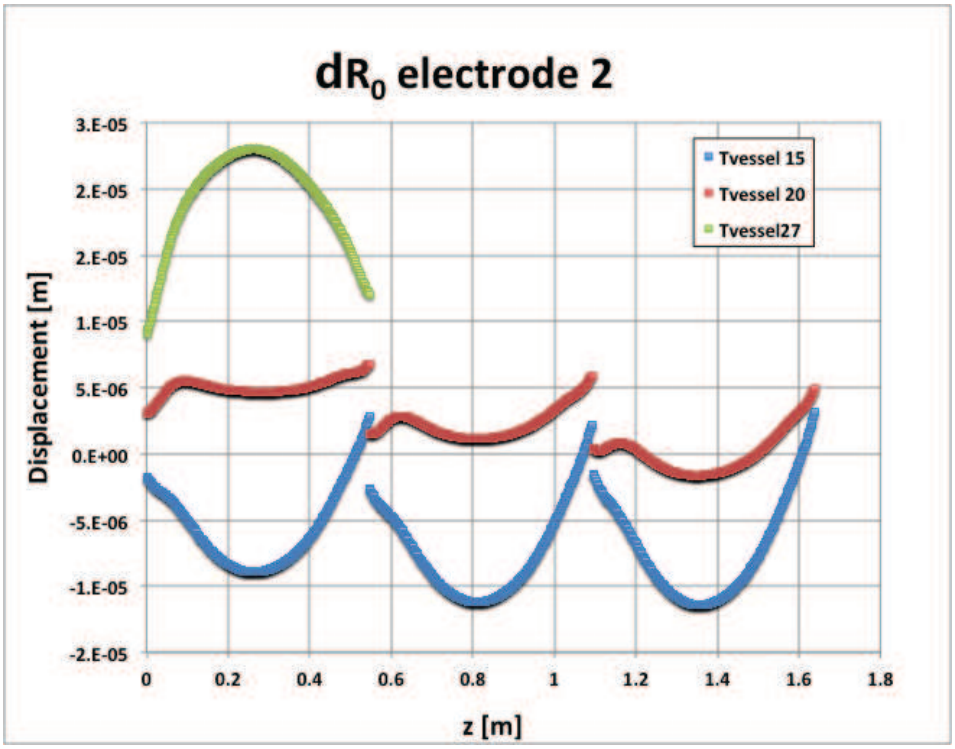

Figure 2.72 δR_0 displacement on the cooling module on electrode 2 for different temperatures at the inlet of the vessel.

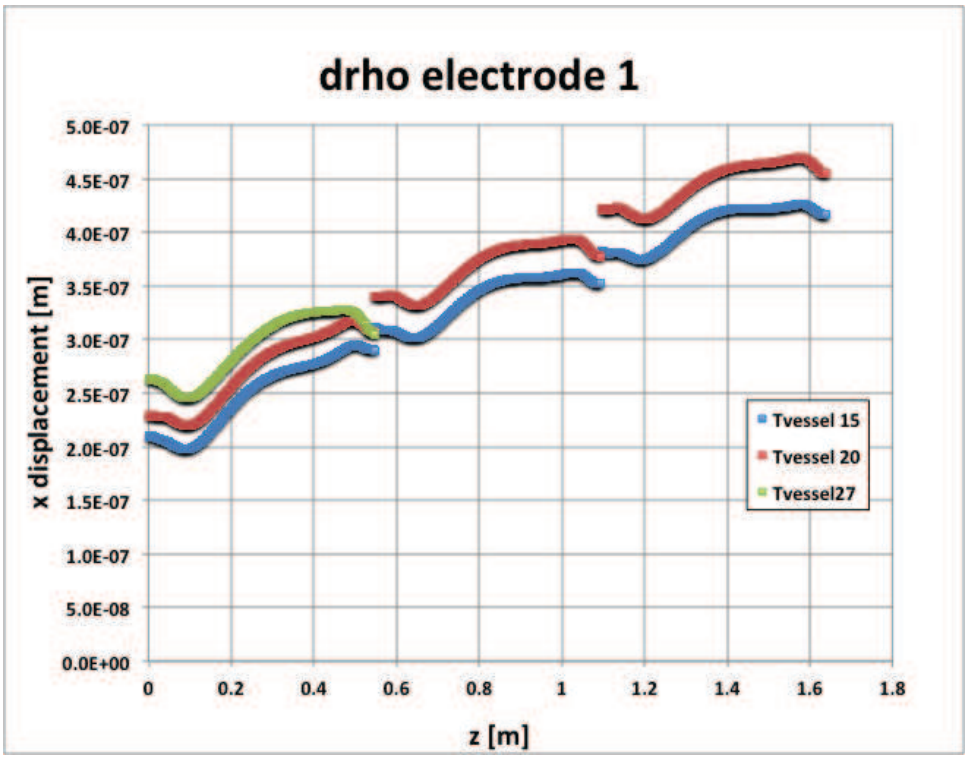

Figure 2.73 $\delta\rho$ displacement on cooling module on electrode 1 for different temperatures at the inlet of the vessel.

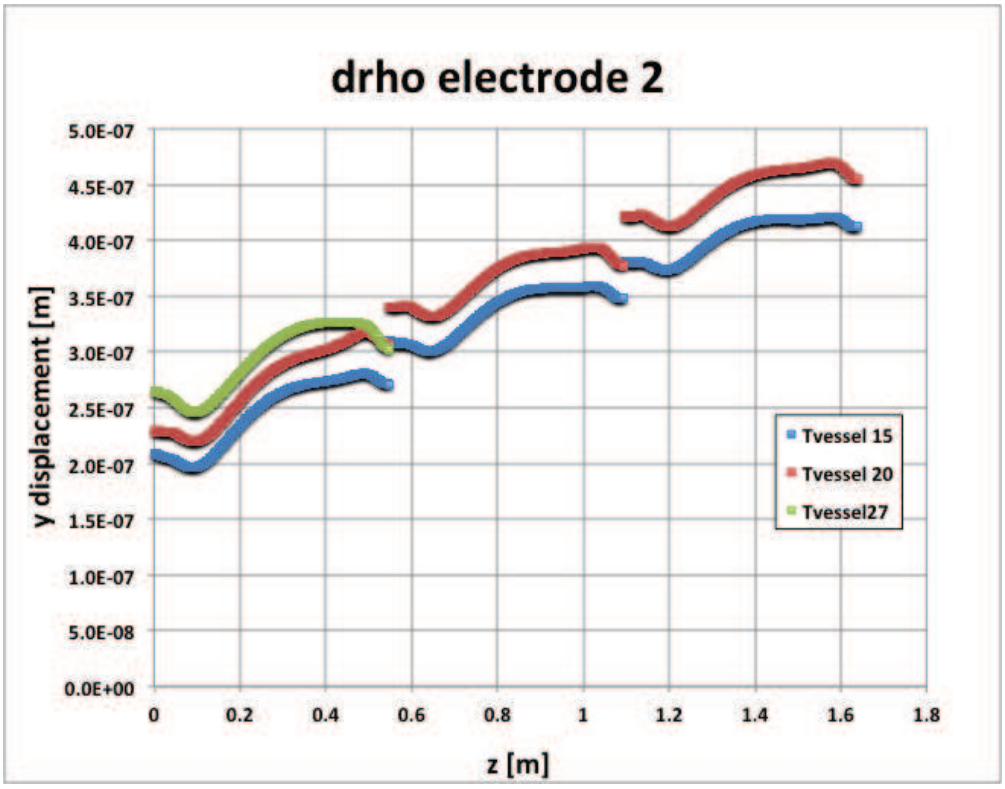

Figure 2.74 δρ displacement on cooling module on electrode 2 for different temperatures at the inlet of the vessel.

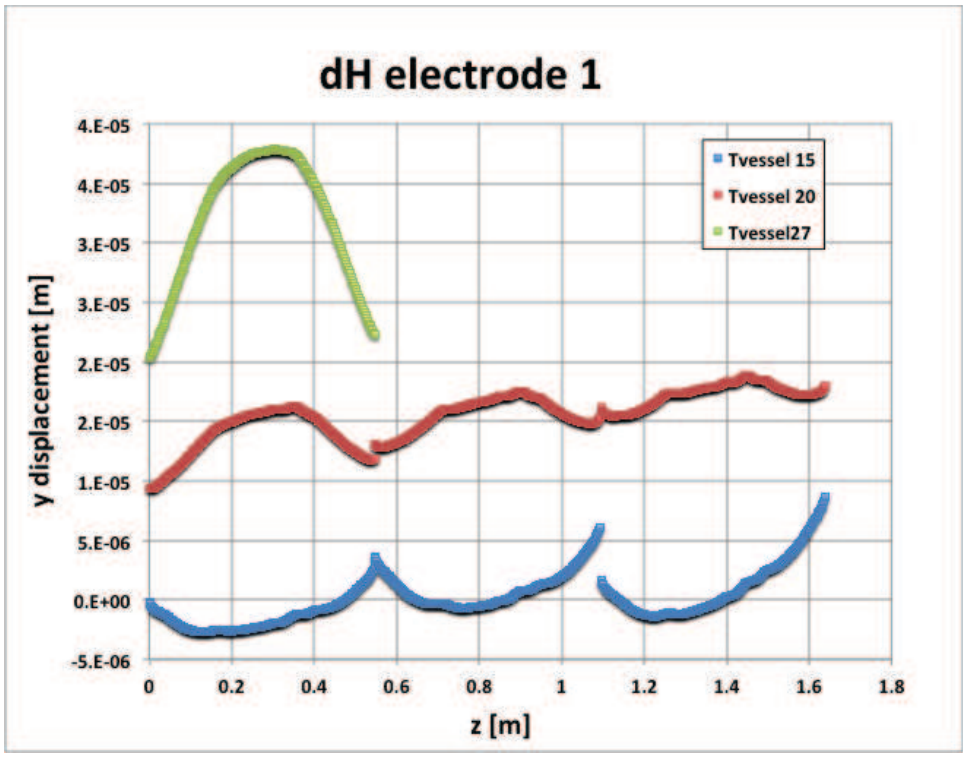

Figure 2.75 δH displacement on cooling module on electrode 1 for different temperatures at the inlet of the vessel.

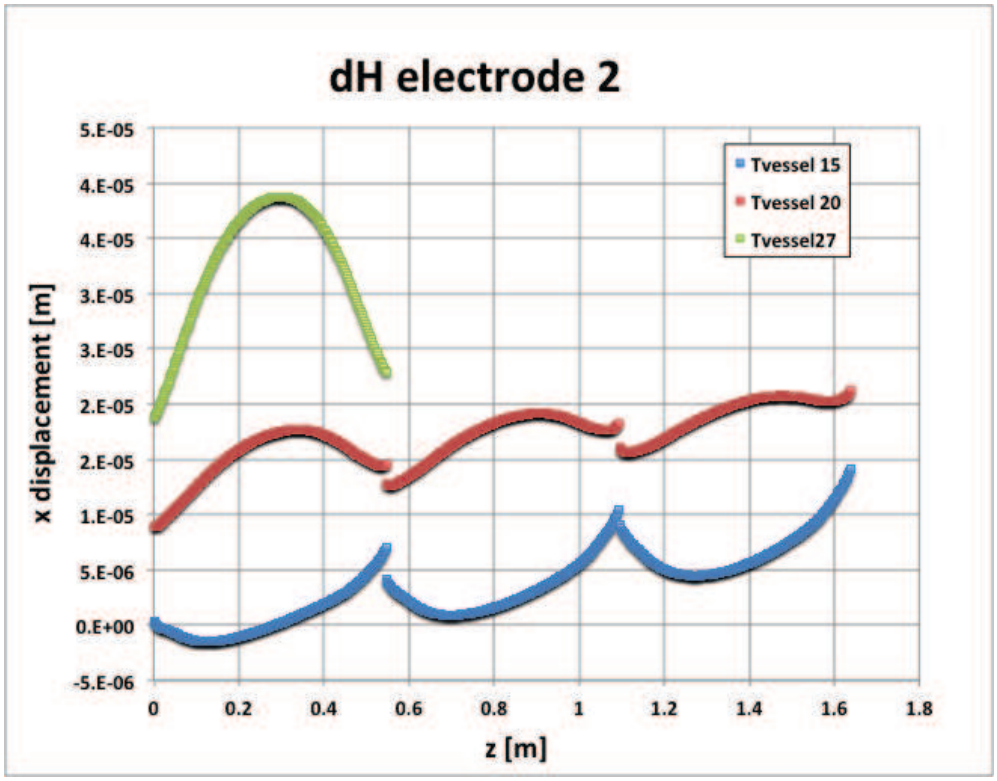

Figure 2.76 δH displacement on cooling module on electrode 2 for different temperatures at the inlet of the vessel.

The RF technician of the LNL analyzed the displacements of the cavity evaluate the effects on the frequency and the perturbation on the electric field. As for the high energy modules, the effect on the perturbation on the electric field is within the design specification. The following table reports the average shift of frequency from the nominal on each module. The tuning target criteria of the tuning range of ± 100 kHz is satisfied. The average frequency is of about -100 kHz with the inlet on the vessel at 15 ˚C. Although the module 2 and 3 were not simulated with inlet temperature of 27 ˚C on the vessel, the average shift of frequency on the cooling module is above +100 kHz considering a decay of 30 kHz on each module.

	δf module 1 [kHz]	δf module 2 [kHz]	δf module 3 [kHz]
Tvessel 15 ˚C	-70	-100	-125
Tvessel 20 ˚C	26	4	-26
Tvessel 27 ˚C	155	-	-

Table 2.19 Average shift of frequency on the cooling module composed by the modules 13, 14 and 15

The result of the simulations of the cooling module composed by the modules 4-6 will not be reported. In fact, since the variation of the dissipated RF load on the internal surfaces of the cavity is limited respect to the previous cooling module, the same deformations of the cavity were registered. The effects on frequency were also the same, since the variation of the coefficient that relates the deformation and the frequency is low.

2.7 Design of the cooling system of the middle energy modules (from 7 to 12)

As described on chapter 1 and on the second paragraph of this chapter, this group of modules present some peculiarities: the geometry of the vanes and the dissipated RF power are variable along the beam axis.

Since the dissipated RF power is intermediate to the low and high energy modules, the cooling system (position, dimension and mass flows on the cooling ducts) of the modules 7-9 was the same as 1-6 and that of 10-12 the same as 13-18. Fluid thermal structural analyses varying the inlet of the vessel on the range 15-27 ˚C has been performed to evaluate the effects on frequency on these modules.

The first cooling module studied was formed by the modules 7-9. According to figure 2.1 the inlet of the cooling module is on module 7.

For what concerning the boundary conditions for the fluid flow are the same of the low energy modules. According to figure 2.54 the heat fluxes are variable along the cooling module.

Segment	Heat flux range [W/m^2]
1	1000-1520
2	6380-8930
3	10960-14840
4	14900-20090
5	18940-24740
6	23140-30830
7	24080-32620
8	24830-33750
9	25400-34620

Table 2.20 Dissipated RF power on the internal cavity on the modules 7-9

The temperature distribution calculated by CFX was passed to the thermal structural simulations.

The displacement of each module with the different inlet temperature on the inlet of the vessel of the module 7 were analyzed by the RF experts of the LNL.

Table 2.21 reports the value of the shift of frequency on each module of the cooling module. The average lower shift of frequency is even below -100 kHz. The average shift of frequency (85 kHz) results below + 100 kHz with the inlet of the vessel at 27 ˚C. This is not a problem, since this value can be compensated by an increase of the inlet temperature on the vessel.

	δf module 7 [kHz]	δf module 8 [kHz]	δf module 9 [kHz]
Tvessel 15 ˚C	-90	-135	-150
Tvessel 22 ˚C	38	11	-27
Tvessel 27 ˚C	130	78	46

Table 2.21 Shift of frequency on the modules 7-9

The second case analyzed was the cooling module composed by modules 10-12. Table 2.22 reports RF dissipated power on the internal surfaces of the cavity that

was applied on the thermal-fluid dynamics analysis. For what concerning the flow boundary condition, the same of the high energy modules were applied.

Segment	Heat flux range [W/m^2]
1	1520-2710
2	8930-14240
3	14840-22050
4	20090-29340
5	24740-33700
6	30830-42800
7	32620-46900
8	33750-48860
9	34620-50370

Table 2.22 Dissipated RF power on the internal cavity on the modules 10-12

The temperature distribution on the modules calculated by CFX were applied for the thermal structural analyses. Table 2.23 reports the average shift of frequency on the modules 10-12 calculated by the RF experts of LNL analyzing the calculated displacements of the cavity. As for the previous cooling module, the lower limit of -100 kHz of the design specification was satisfied. The average upper shift of frequency, although it doesn't satisfy +100 kHz criteria, can be compensated increasing the inlet temperature of the vessel of the module 12.

	δf module 12 [kHz]	δf module 11 [kHz]	δf module 10 [kHz]
Tvessel 15 ˚C	-98	-116	-130
Tvessel 22 ˚C	15	-3	-15
Tvessel 27 ˚C	98	80	68

Table 2.23 Shift of frequency on the modules 10-12

2.7 3D Simulation of the termination cell of the module 18 [7]

Up to now the first and the last modules have been treated as the others. Actually the first and the last module of the RFQ differ from the other because of the termination cell necessary for the closure of the currents and the electric field. Such a design of the termination cell involves some concentration of dissipated RF power. Figure 2.77 shows the dissipated power on the termination cells of module 18 as results of electromagnetic calculation performed by the LNL RF expert.

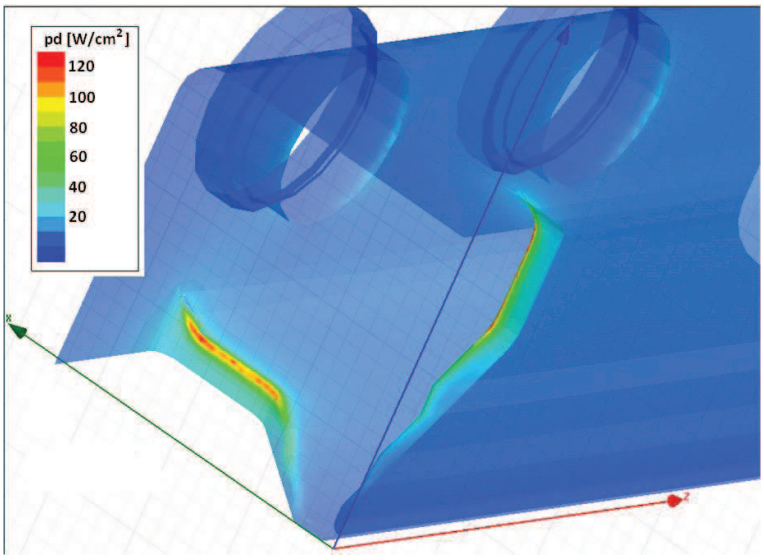

Figure 2.77 Enhancement of dissipated RF power on the termination cell

Moreover a perturbation of the deformation on this zone occurs respect a module without the termination cell.

A strict collaboration with the RF expert of LNL was made in order to optimize the deformation and the cooling system layout on the termination cell of module 18. Module 18 has been studied because of the higher dissipated power and so present the major deformations.

Figure 2.77 shows the optimized geometry of the termination cell of module 18. The dissipated powers were applied for the fluid thermal structural simulation with Ansys in order to verify the maximum deformation of the cell.

Figure 2.78 shows the model used for the fluid thermal structural study, while the geometry of the nose and the cooling duct layout on the vane on figure 2.79 and 2.80.

As on figure 2.80, the position and dimension of the cooling ducts of the vane and the vessel is not changed from that simulated for the high energy modules.

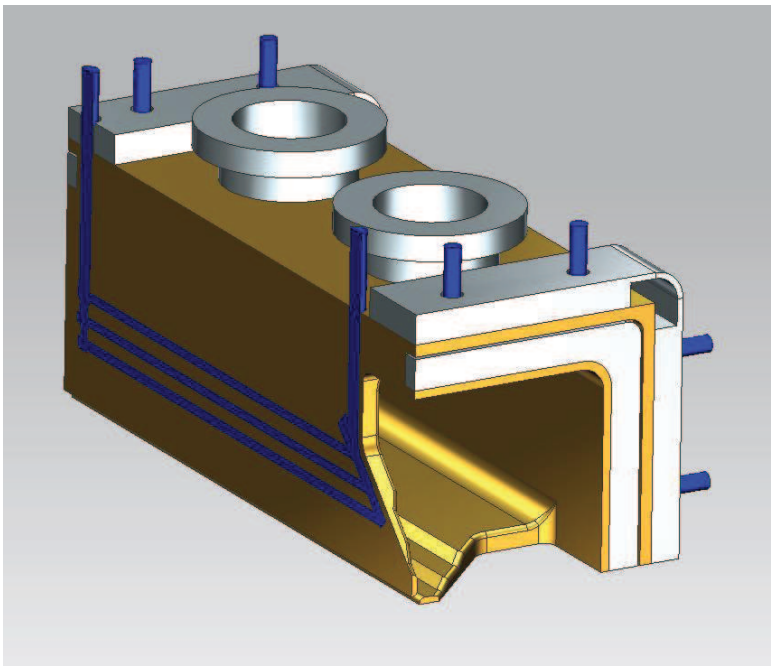

Figure 2.78 Model used for the fluid thermal simulations

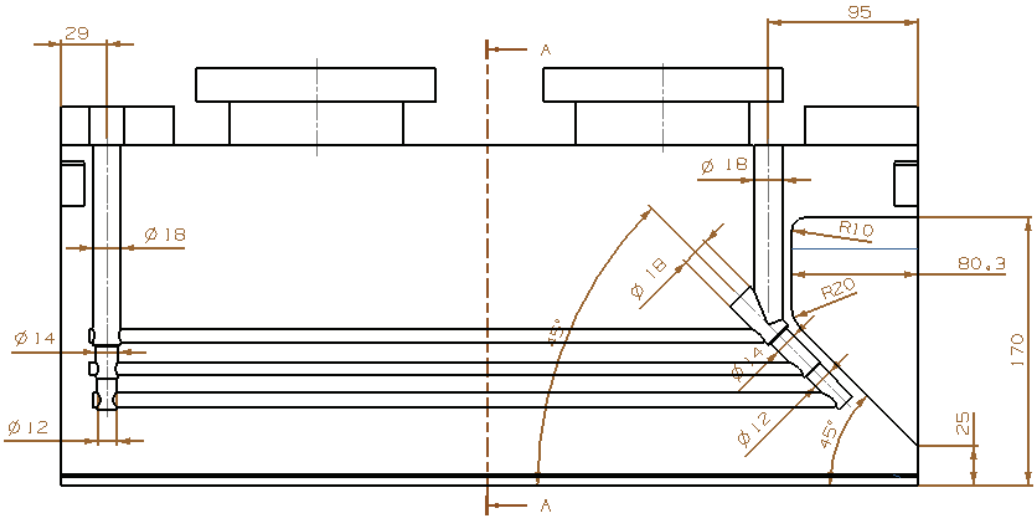

Figure 2.79 Geometry resulted from the optimization of the termination cell

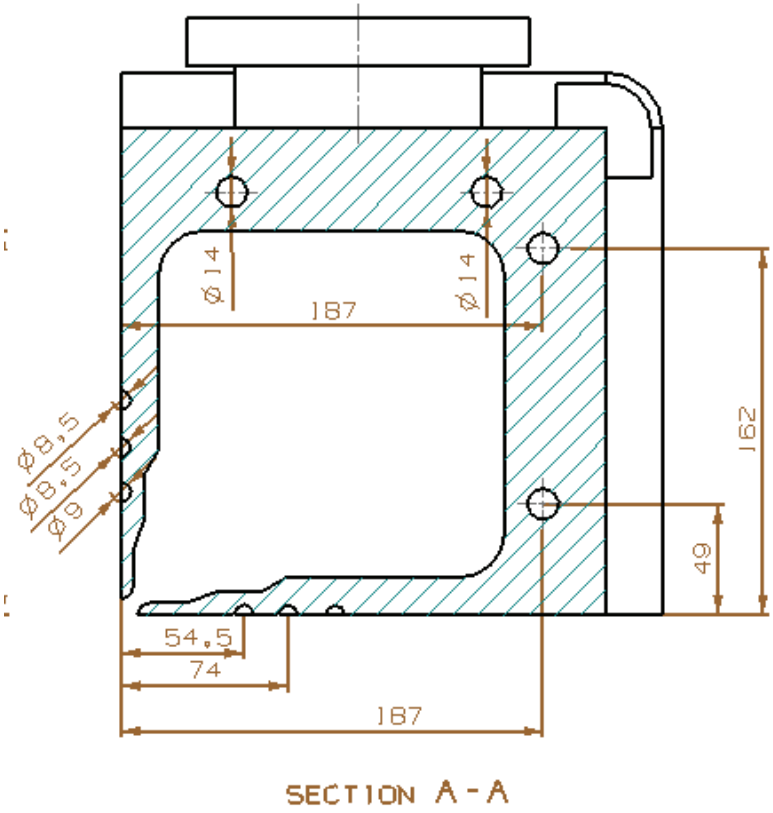

Figure 2.80 Section A-A view according to figure 2.74 showing the position of the cooling duct.

The material properties and boundary condition on the cavity walls and for the fluid flow are the same as for the high energy modules. According to figure 2.2 the inlet are on the termination side.

Due to the particular geometry of the vane cooling ducts, a CFD study was made to evaluate the flow distribution.

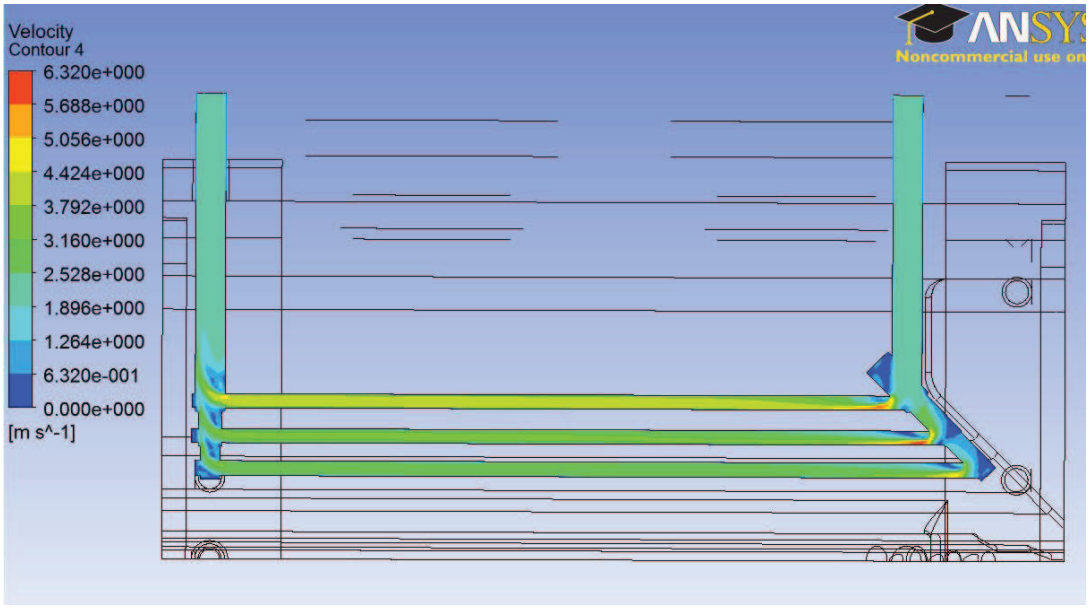

Figure 2.81 Fluid flow distribution on the vane ducts.

Figure 2.81 shows the result of the CFD simulation. The distribution of the fluid flow on the three ducts is quite the same as the high energy module without the termination cell.

The temperature calculated with Ansys CFX was then given in input to structural simulations.

Figure 2.82 shows the plot of the deformation on the module 18 for the tuned case (temperature of 22 ˚C, when the cavity is at the nominal frequency). The maximum deformation of the pole tip is less than 100 μm, that is the acceptance criteria for the stability of the electric field.

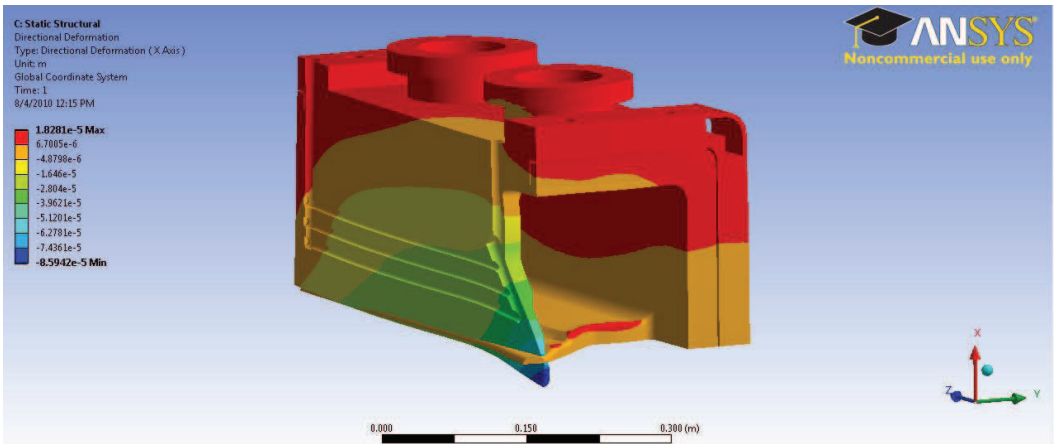

Figure 2.82 Deformation of the pole tip of the termination cell

2.8 Conclusions

Very satisfying results have been reached on the design of the cooling system of the modules of the RFQ. The target specifications in term of frequency tuning range and stability of the electric field can be reached. The experimental tests for the smooth cooling ducts and the threaded cooling ducts was fundamental and a very important phase for the design of the cooling system. In fact, as already mentioned, if a threaded duct was chosen and since the modules are quite short, the temperature profile and the deformation could not be so uniform along the cavity, involving problem on the stability of the electric field.

REFERENCES

[1] Henrique S. De Azevedo et al. “Numerical Simulations of turbulent flow in corrugated pipes”, 12th Brazilian Congress of Thermal Engineering and Science, November 10-14, 2008, Belo Horizonte, MG

[2] Wolverine Tubes Inc., Wolverine tube Heat Transfer Engineering Data Book III, chapter 2, http://www.wlv.com/products/databook/db3/data/db3ch2.pdf

[3] Ansys 12.0 CFX Theory Guide, Ansys help, Ansys Inc.

[4] Quingzhao Wang, “Numerical analysis of cooling effect of a cylinder head water jacket”, Master degree thesis, University of Minnesota Duluth, Department of Mathematics and Staitstics

[5] A. Pepato, R. Dima, F. Scantamburlo, “Engineering design and first prototype tests on the ifmif-eveda rfq”, IPAC 10 (International Particle Accelerator Conference), 2010, Kyoto (Japan), p. 600

[6] F. Scantamburlo, A.Pepato, A. Palmieri, “3d thermo mechanical study on IFMIF-EVEDA RFQ, LINAC 10 (Linear Accelerator Conference), 2010, Tsukuba (Japan), p. 539

[7] A. Palmieri, F.Grespan, F. Scantamburlo, “3d aspects of the IFMIF-EVEDA RFQ: design and optimization of the vacuum grids, of the slug tuners and of the end cell”, LINAC 10 (Linear Accelerator Conference), 2010, Tsukuba (Japan), p. 533

CHAPTER 3: DEVELOPMENT OF THE VERTICAL BRAZING TECHNOLOGY: FIRST BRAZING TEST AT LNL

3.1 Introduction

The IFMIF EVEDA project will confirm the feasibility of the different part of the linear accelerator (EVEDA: Validation and Engineering Design Activities) and one relevant commitment will be to provide a complete and reliable design for all items, allowing for a complete outsourcing of the final IFMIF line, that will be composed by two identical lines to provide the required luminosity and intensity.

The RFQ cavity is composed by eighteen modules and its production is subdivided into three parts. The first six and last six modules will be machined and brazed by external companies on the basis of a common design developed at INFN Padova, to provide reliable and experienced suppliers for the final IFMIF Project. The production of the central six modules will be done in house and will involve four INFN's sections. The rough cut of the CuC2 raw blocks will be performed by EDM at the INFN PD and INFN TO mechanical workshop, while all the finish machining operations and all the dimensional survey of components and modules will be done at the Padova site. The assembly and brazing steps will be done at the LNL with the Padova manpower.

The acquisition, at the INFN PD workshop, of new machines (tailored to the design parameters) as a large EDM, a five axis milling center, a CMM with continuous active scanning and some other tooling (PMMS portable arm, phased array UT scanner, infrared thermal camera etc.) was done in the aim of developing in-house all the critical items of the mechanical design and to provide a feed back production site for any problem arising during the very challenging production schedule.

The choice to produce in-house the mid energy part of the line was done on the basis of the very complex and machining time consuming tridimensional geometry: the width of the vane and the modulation on the pole tip vary largely along the RFQ.

The dimensional results of the first module of the prototype were well in the limits of acceptance both for the single components production and for the final brazed module.

It was decided to perform some brazing tests at the LNL to increase our experience on the vacuum oven of the laboratories and to confirm the feasibility of a completely different design approach of the brazing step, allowing for a single step brazing technology.

This goal nevertheless required to develop vertical assembly of the components, instead of the horizontal one, with a new definition of the grooves geometry and of the brazing tooling.

In this chapter the problems of the brazing of the first module of the prototype will be described and the various phases in terms of production, design of the thermal brazing cycle and quality control of the brazing joints will be described.

3.2 The production, brazing and dimensional inspection of the first module of the prototype

We decided to product two prototypes shorter than the definitive module (400 mm) with almost the same transversal section (420 mm x 420 mm) to validate all the machining phases, the dimensional quality assurance process and the brazing technology. The first module of the prototype was produced in collaboration between the INFN for the machining and CERN for the brazing. The various phases of the production of this module are better described in [1], that is also attached in appendix A of this thesis. The brazing was performed into two steps, accordingly to the well developed and good results in terms of quality of the brazing and the respect of the design specification in terms of displacements of the electrodes during brazing reached by CERN [2,3,4,5]: the first horizontal to join only the copper electrodes (figure 3.1) and the second vertical to join all the AISI 316 LN components, such as vacuum flanges, side flanges for the coupling of the modules, and the seal vacuum flanges (figure 3.2).

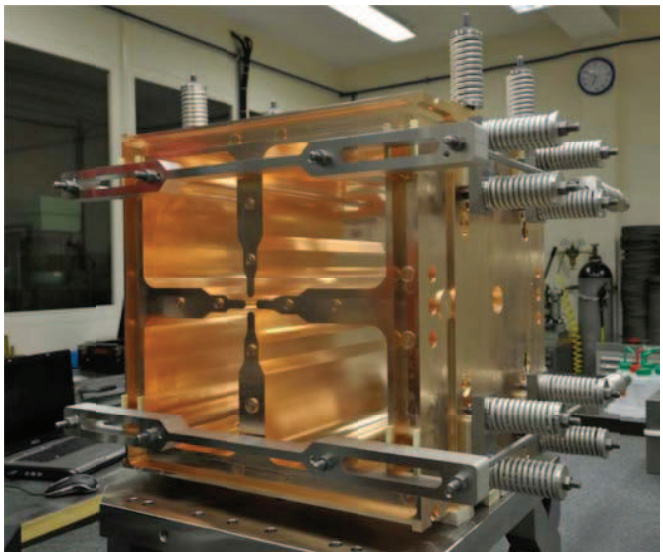

Figure 3.1 Assembly of the first module of the prototype for the horizontal brazing

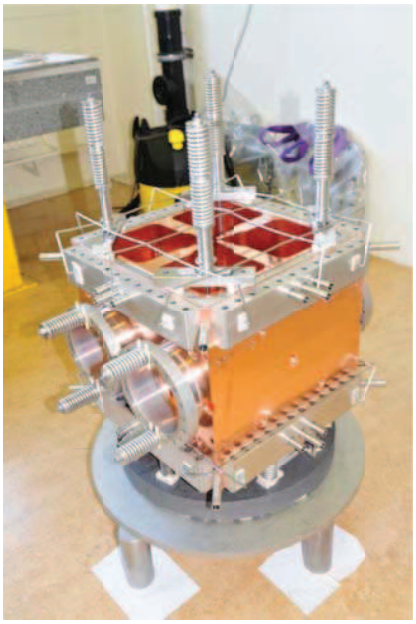

Figure 3.2 Assembly of the first module of the prototype for the second vertical brazing step.

The first module of the prototype was completed at the end of 2010. In May 2010 a new CMM Zeiss Accura (figure 3.3) was acquired by the INFN of Padova, but the skills necessary to perform complex and reliable measures were fulfilled only after the second brazing of the first module of the prototype. The accuracy of the CMM enter on the maximum specification of the constructor of, according on ISO

10360:

$$accuracy = \pm(2\mu m + \frac{1\mu m}{L})$$

where L is the course of the machine expressed in [mm]. When measuring, other factors should be taken into account, such as effect of temperature, humidity, cleaning of the surfaces, etc.

The advantage of a machine with continuous scanning is that in a very few time lot of points can be acquired with higher statistics and accuracy of the measures. Before the measures were performed only by a portable CMM arm Cimcore Infinite 2.0 (figure 3.4) that guarantees an accuracy of measure of 40 μm on a volume of a sphere of 2,4 m.

Although less precise than the CMM machine, the portable arm is very useful to measure workpieces directly on the machines such as milling, lathe, etc. without removing it with the loss of the alignment or, obviously, to measure pieces that cannot be placed on the CMM.

Figure 3.3 ZEISS Accura CMM with active scanning technology [6].

Figure 3.4 Cimcore INFINITE 2.0 portable arm [7].

As reported on the document for the construction of the module, the measures during the construction of the prototype 1, the Zeiss CMM was not available yet, so the measures were performed by means of the portable arm.

The process of measure for the dimensional qualification of the components and of the assemblies before and after the brazing were not clearly understood at all.

After the production o these module and refining the design of the component for the final production of the modules, an increasing experience was done for the process of the qualification of each phase of production. Chapter 5 will describe the progress made on the designs and the qualification of the components and the assemblies of the modules. The qualification of the components and of the brazing assembly was not entirely possible with such an instrument. Moreover, the geometrical tolerances imposed on the drafting were below the accuracy of the portable arm.

For example, the qualification of a component requires determining the position of the modulation. With the portable arm this position cannot be measured.

The usage of an intermittent single probe technique would not be so accurate, because the system cannot detect precisely the direction of the normal of the probing point. In fact since the controller register the measure at the center of the probe and do not detect the direction of probing, the compensation of the probe radius is not possible.

Vain attempts by means of the portable arms were performed to measure a

modulation test (figure 3.5) with scanning techniques sliding the touch probe on the crest, but not affordable results were reached. In fact the encoders of the portable arm are not so stable during the measurements, thus compromising the accuracy of the measures.

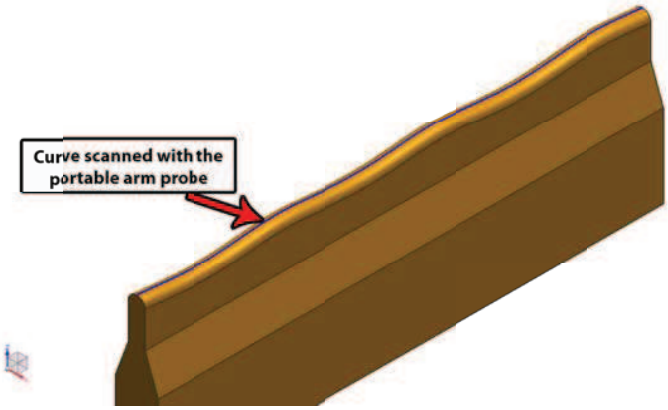

Figure 3.5 Crest of the modulation to be measured for the qualification of each electrode

3.2.1 Signs and advantages of the ZEISS active scanning technology[1]

The ISO 10360-1 standard describes probes as touch probe systems. The standard differentiates between "touch trigger" and "scanning" systems depending on the type of measuring point acquisition.

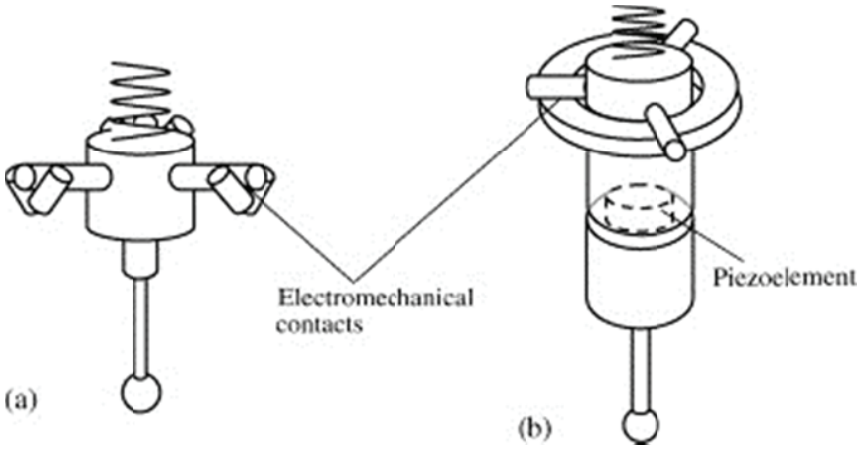

Figure 3.6 Simple scheme of the traditional CMM trigger system [9]

[1] All the information on this paragraph are referenced to [8]

Touch-trigger systems record the measuring point at the moment of contact through a mechanical switch or through an electrical pulse transformer element, e.g. a Piezo sensor or wire strain gages (figure 3.6). The scanning system (figure 3.7) captures the deflection of the probe system when contact is made with the workpiece surface utilizing the integrated measuring system, and determines the deflection. It is used to correct the measuring point coordinates delivered by the measuring system of the axis of motion.

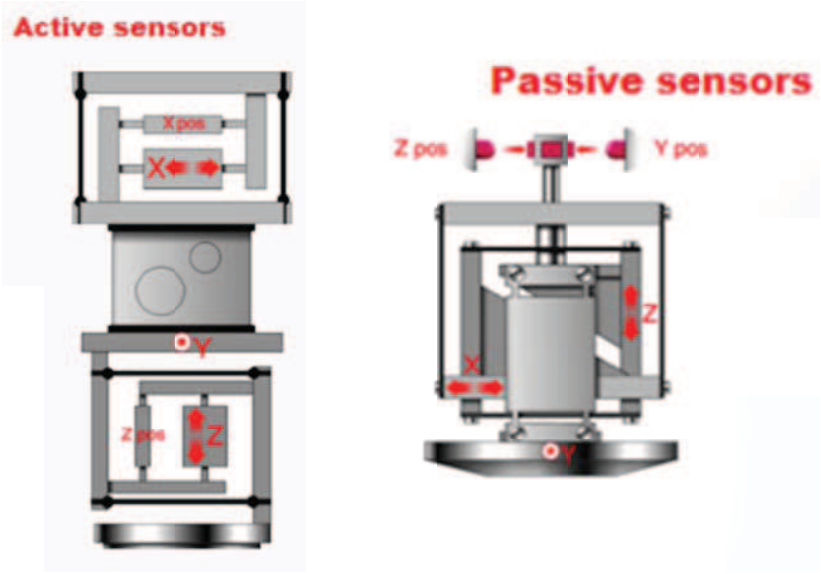

Figure 3.7 Simple scheme of active and passive scanning sensors [10]

The VAST scanning systems from Carl Zeiss use the "sliding determination of mean values" procedure in conjunction with the ZEISS Intelligence Scanning Controller during measuring point acquisition. During this process, the machine is stopped after it registers a probe pulse due to the deflection of the probe. The system then checks if the sum signal from the probe deflection and positional data of the measuring machine axes remain constant. A probing point is accepted if the signal remains constant within a short time interval. The mean value from the deflection signals recorded during this period is used to correct the probe deflection. Sliding determination of mean values automatically dampens noise pulses caused by vibrations, for example.

As a result, the active probes are less affected by electromagnetic interferences than a touch-trigger probe, which have an effect the moment contact is made with

the workpiece.

The advantage of such a solution would be the possibility to capture the possibility of capturing 2D and 3D data maintaining a continuous moving contact with the surface to be measured, and collect much more data than the traditional trigger method, that takes measurements by only intermittent single-point touches.

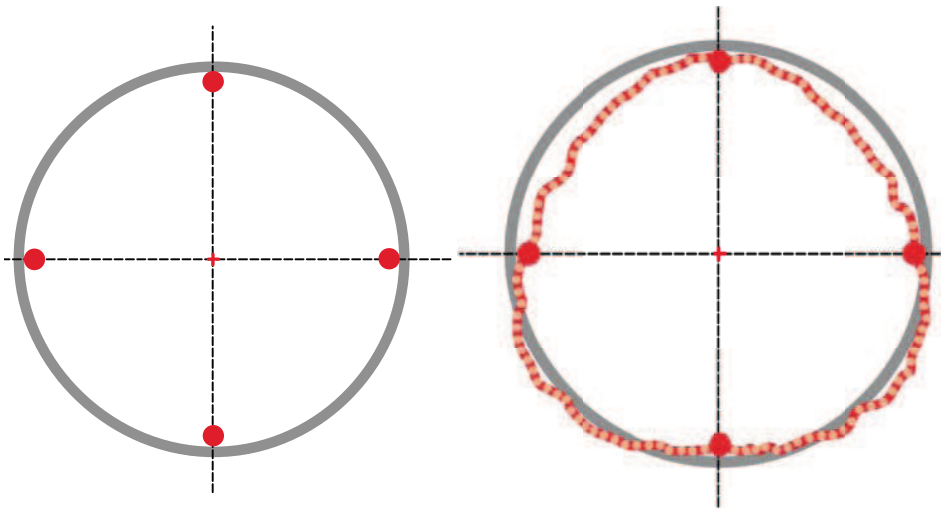

Figure 3.8 Example of a measure of a circle with a traditional touch-trigger system with 4 points (left) and continuous scanning technology with multiple pioints (right) [11]

The advantage of a continuous scanning technique can be seen on figure 3.8, regarding the measure of a circle with traditional trigger probe and a scanning probe.

Scanning systems are distinguished by the type of measuring force generation. With a passive system, the measuring force is generated by a mechanical spring. An active system consists of linear drive that generates the probing force electrically. This is also known as an “electrical spring”. The use of electrical sprigs enable the operator to set the measuring force over a large force range, largely independent of the deflection, thus permitting a larger measuring range which is required for a high scanning speed (figure 3.8).

The measuring range of a passive system is limited by the limited by the linearity range of the mechanical springs in which the force and deflection are

proportional. It is two or four times smaller on a passive system than an active system (figure 3.9).

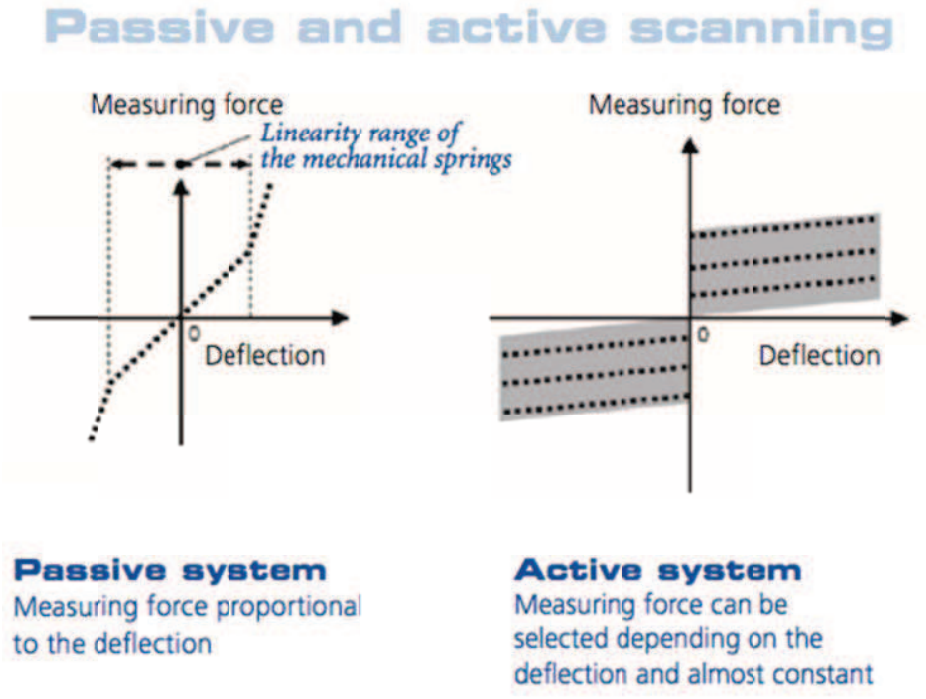

Figure 3.9 Simple scheme of active and passive scanning sensors [8]

Active systems allow significantly high scanning speed, up to 300 mm/s for the Zeiss VAST gold series. For what concerning the Zeiss Accura acquired by the INFN of Padova, it is equipped with a VAST XT probe. Reasonable values of active scanning would be 20 mm/s for feature such as planes circles cylinder, and 3 mm/s for the scanning of surfaces and profiles.

3.2.2 Results of the measures of the first module of the prototype [1, 12]

With the improvements on the skill on the new CMM and on the procedure of measure, the form of the cavity was investigated. Since the pole tips were not accessible with the stylus probe, some assumption had to be taken:

- The good quality of machining, i.e. the modulation of each copper electrode respect the tolerances of -/+10 μm in form and position.
- The good quality of the dry assembly before the first brazing: the respect of the tolerance of positioning of -/+ 20 μm.

The good quality of the machining of the copper electrodes (especially the

position of the modulation) and their positioning on the first brazing assembly were validated by the RF physicians with experimental measures on the cavity. With these hypotheses, the displacements of the pole tips can be the same of those measured on the vessel near the vanes.

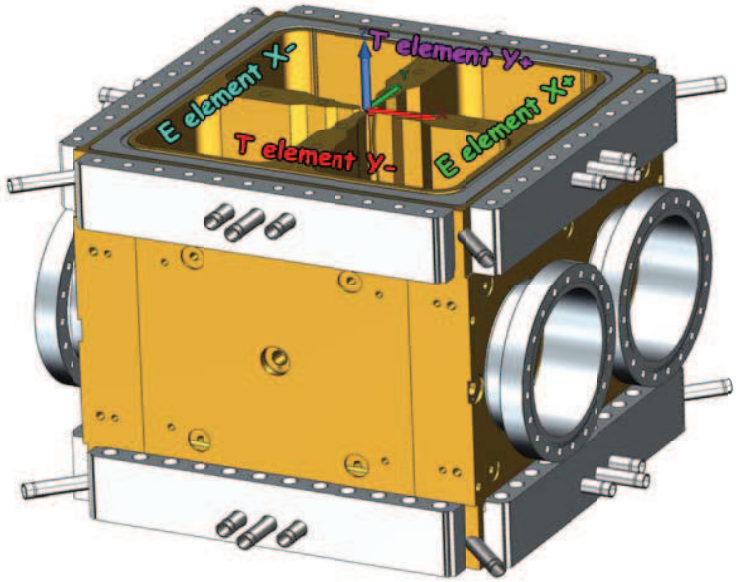

Figure 3.10 Nomenclature of the element and CMM alignment of the cavity.

The CMM alignment was constructed with:

- the references of the machining of the top E element of the assembly of the brazing (E element X- of figure 3.10) , that define a precise plane (0.01 μm of flatness);
- the intersection of the middle planes to the tips of each element.

Figure 3.8 shows the definitions of the elements of the cavity and the coordinate system for the CMM alignment.

Several transversal profiles and longitudinal scans were performed on the cavity, as reported in figure 3.10 and 3.11.

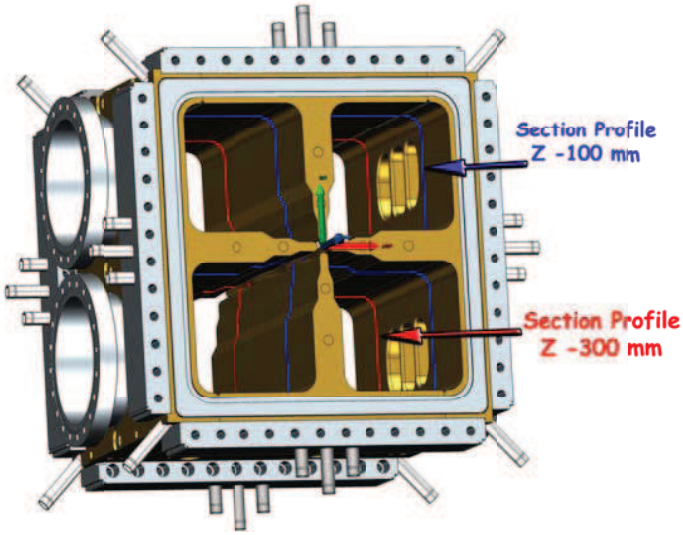

Figure 3.10 Transversal profiles measured on the cavity.

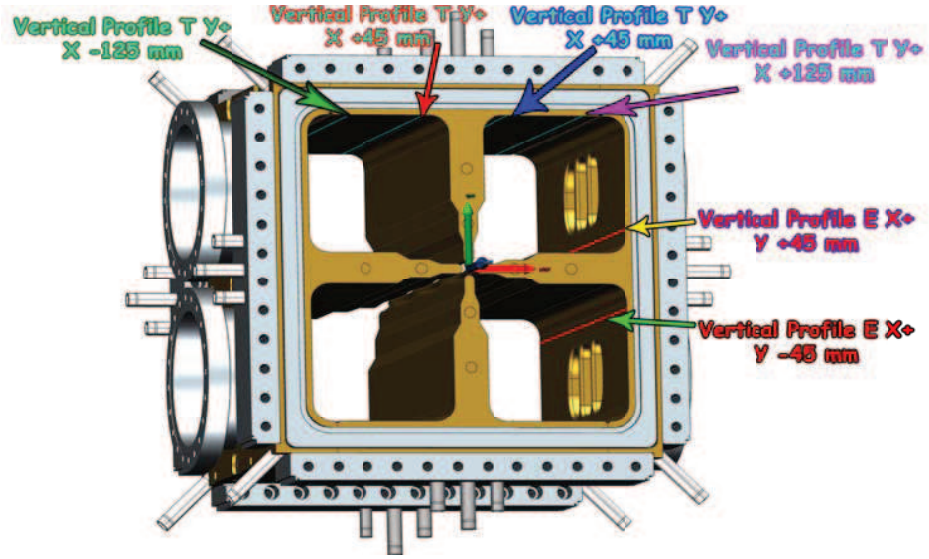

Figure 3.11 Longitudinal profiles measured on the cavity

A simple scheme of the deformation of the cavity is reported figure 3.12, reproducing the position of the copper components and the supports of the first brazing assembly.

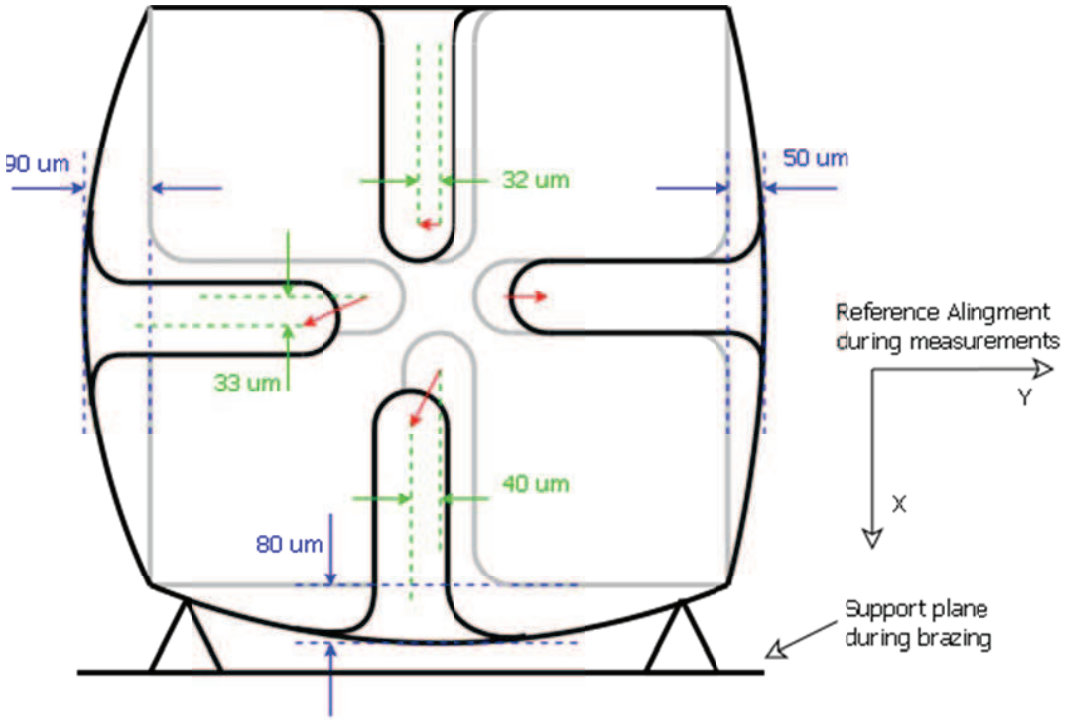

Figure 3.12 Scheme of the deformation measured with the CMM of the cavity of the first module of the prototype

Pole	ΔX	ΔY	ΔR_0
	[μm]	[μm]	[μm]
E X+	-40	-80	89
T Y+	50	0	50
E X-	-32	0	32
T Y-	-90	-33	95
	mean ΔR_0	**[μm]**	**67**
	$\partial f/\partial R_0$	[kHz/□μm]	7.6
	Δf	**[kHz]**	**510**

Table 3.1 Summary of the displacement of the tips of the first module of the prototype.

Taking into account the assumptions described before for what concerning the displacements of the pole tips, table 3.1 summarize the displacement of the tips.

What is important for the physicians is the variation of the resonant Radio

Frequency of the cavity, that is function of the variation of the volume of the cavity. In particular variation of the frequency is more sensible to the variation of the volume near the tips. In fact the same displacement of the tips vary about 7 times higher the frequency than the vessel. As mentioned on chapter 2, the RF physicians call R_0 the distance of the tips respect to the beam axis. Let define ΔR_0 the variation of the distance of the tip from the beam axis and $\partial f/\partial R_0$ the variation of the frequency with ΔR_0.

The shift of frequency Δf calculated from the measures of the deformation of the cavity was about 510 kHz. The value has been confirmed by the RF physicians combining their experimental measures of the frequency of the cavity before the first brazing step and after the second brazing step.

Such a deformation is still acceptable for the single module, but not if all the eighteen modules deforms like this, because the shift of frequency cannot be compensated with the tuners.

Looking another time to figure 3.11, it is difficult to establish precisely the causes of such form of the deformation. Since the deformation is constant along the module, the most probable is the limitation on the expansion of the E element on the bottom induced by a frictional force between the copper element and the supports of alumina during the first brazing. The lack of uniformity of the temperature of the components during the brazing cycles can also be a cause, but the access to the documentation of the thermal brazing cycles made by CERN was not allowed.

The development of a vertical brazing technology was retained mandatory, and some in-house tests were performed involving the mechanical designers and workshop of Padova and the brazing laboratory of LNL.

There are so many advantages of the vertical brazing technology.

First, the increase of uniformity of the heat transfer by radiation, exploiting the symmetry of the beam axis.

Second, all the components, including the copper all the stainless steel components can be brazed in a single brazing step. Less deformation and stresses on the material are induced. Better mechanical properties of the material can be guaranteed, because less annealing brazing cycles. More brazing repairs can be

performed.

Brazing tests were performed to develop the vertical brazing technology, in order to test the vacuum furnace of LNL, the tooling for the brazing and the feasibility of a single step vertical brazing.

3.2 Description of the brazing test

A first brazing test was performed to test the design of new brazing grooves, the coupling of different material as CuC2 and AISI 316 LN and the functionality of the brazing tooling, in particular the Nimonic90 springs used to guarantee a certain pressure on the brazing coupling surfaces. The brazing alloy used was Palcusil 10®[2] in form of 1mm diameter wire. The choice of the such brazing alloy was made to the experience of an external farm that made experience on copper-copper and AISI316-copper joints. Since the experience on the behavior of Palcusil5® and Cusil® was performed by brazings at CERN of many RFQs (TRASCO, IPHI) and the first prototype module of IMIF, we decided to make in-house experience with Palcusil10® by means the LNL oven. Compared to Palcusil5®[3] and Cusil® brazing fillers, the advantages of Palcusil10® are:

- Major viscosity: surfaces with greater clearances can be brazed without the flowing down of the brazing alloy;
- The wettability of the AISI316LN surfaces increases and no nickel plating is required thanks to the higher brazing temperature;
- Considering two step brazing, one with Palcusil 10® and the other with Cusil®, the difference between the solidus temperature of Palcusil10® and the liquidus temperature of Cusil® is higher than considering Palcusil 5®. The probability of eventual damage induced on joint made previously with the high melting alloy is reduced.

On the other side, since difference between the liquidus and the solidus temperatures of the Palcusil10® are considerable compared to the Palcusil5® and the eutectic Cusil® the design of the thermal cycle can be more delicate and the verification of the wetting must be provided.

[2] Palcusil 10 composition: 59 % Ag, 31% Cu, 10% Pd – liquidus: 852 ºC, solidus: 824 ºC

[3] Palcusil 5: composition: 72 % Ag, 28% Cu, melting temperature: 780 ºC (eutectic alloy)

3.2.1 Copper steel joint

The joint between copper and AISI 316 LN stainless steel was tested, reproducing the same condition of the brazing of flanges of a small scale prototype (described on chapter 5). A C-shape of copper was cut by electro-erosion. Then a slot and the grooves for the brazing alloy were milled to allow the coupling of an AISI 316LN flange, in order to test the same condition of the brazing of flanges of a small scale prototype (figure 3.12). The C-shape of copper was then mounted on two layers of ceramics ($Al0_2$) of dimension of 13mm x 30mm x 7 mm to guarantee thermal insulation from the base of AISI 316 LN. A stainless steel tool of AISI 316 LN was then mounted between the copper and the steel flange with a pre-load Nimonic 90 spring to keep the flange in position and to guarantee a certain contact pressure. Between the stainless steel flange, the copper C and the stainless steel tools with the Nimonic 90 spring, ceramics blocks were interposed to guarantee thermal insulation (figure 3.16).

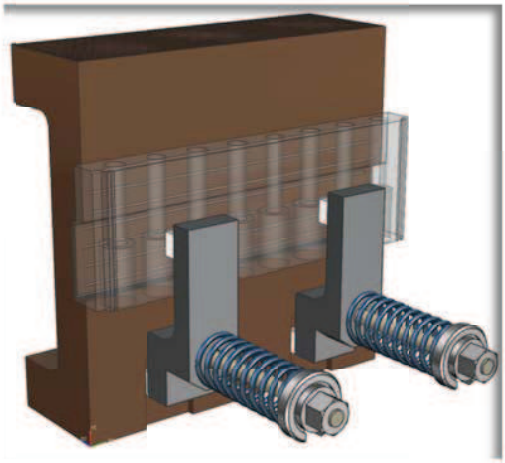

Figure 3.13 Assembly of the test for the coupling the AISI

3.2.2 Copper blocks brazing test

It was also thought to perform three brazing test with simple copper CuC2 parallelepipeds to understand the behavior of the brazing alloy in such cases of different position of the brazing planes (horizontal or vertical) and with different design of the brazing grooves (figure 3.14). The grooves were dimensioned to not entirely filling the gap on the brazing plane, in order to test the effective wetting of the filler.

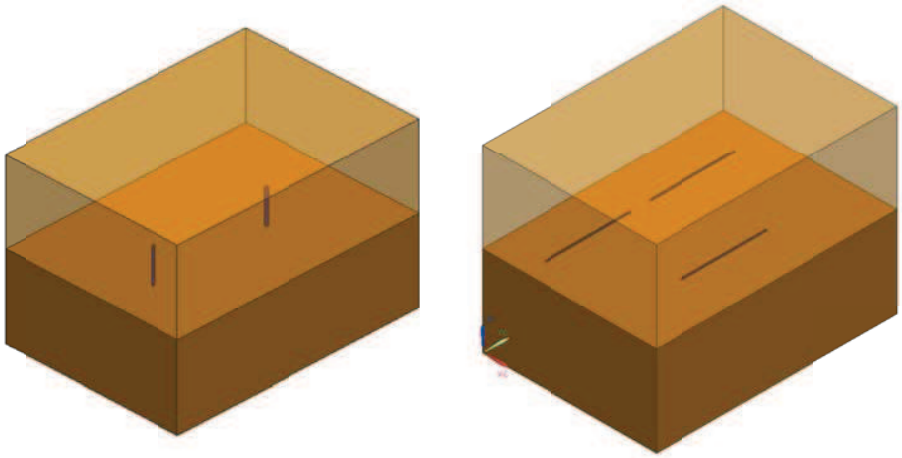

Figure 3.14 Copper blocks for the testing of the wetting of the brazing alloy

Also for this test a layer of alumina was interposed between the copper blocks and the AISI 316 LN base for thermal insulation and a tooling with two Nimonic 90 springs of 150 N of pre-load each was used to keep a contact pressure on the brazing planes (figure 3.16). The copper blocks with interrupted straight grooves were mounted in two different position, horizontal and vertical to test the different wetting. The test with inclined grooves was mounted in vertical position. Figure 3.15 gives the general view of the positioning of the components on the oven.

3.2.3 Copper-copper vertical brazing test

The other test was the vertical brazing of two copper C-shape elements 400 mm height and 120 mm large (figure 3.15). The dimension of the brazing plane was 40 mm x 400 mm in order to be as closest as possible to the real conditions of the definitive modules. In fact, due to gravitational effect, the brazing grooves should not be continuous along the brazing surface, the solution adopted for the first horizontal brazing of the module 1 of the prototype. In such case the brazing alloy could flow down. Two different designs of the grooves for the brazing alloys were tested: vertical interrupted and oblique. The spacing and length of the grooves was made of the assumption of 30 μm of gap on each brazing surface.

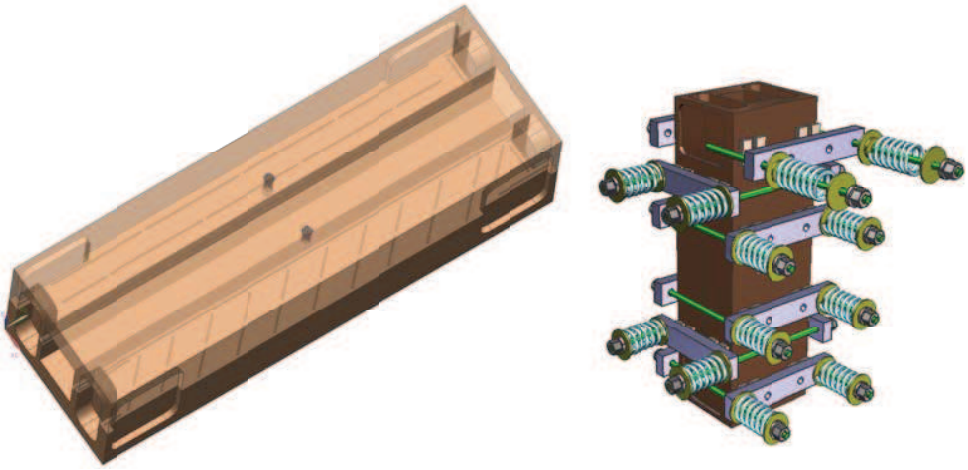

Figure 3.15 C shaped copper of 400 mm length to test the vertical brazing and different kind of grooves (left) and with the tooling to keep all the component together (right)

The components were supported on a 400x400x40 mm stable AISI 316 LN base supported by two layers of alumina, in order to guarantee thermal insulation from the base (figure 3.15). A tooling of stainless steel bars in contact with copper by means of some aluminas, molybdenum rods and Nimonic90 springs with a pre-load of 150-200 N, was mounted (figure 3.15 and 3.16). The scope of the tooling was to keep a certain contact pressure on the brazing surfaces and to keep in position the two copper components avoiding sliding on the brazing plane.

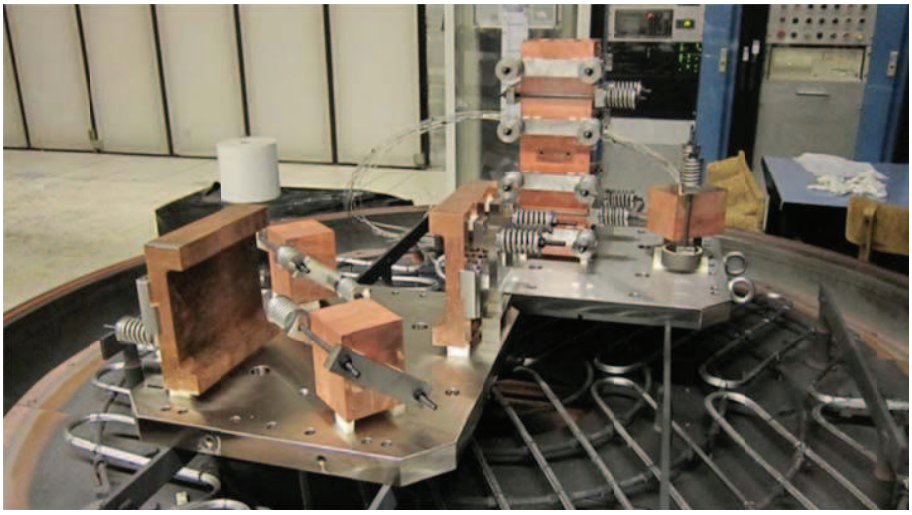

Figure 3.16 Overall view of the components inside the vacuum oven

3.3 Design of the brazing process of the first test of the prototype

In general the brazing experts working on vacuum furnace set up the thermal cycle empirically. Monitoring the temperature of the load they regulate all the various phases of a brazing thermal cycle: the pendency of the pre-heating ramps before, that to guarantee the uniform melting of the brazing alloy and the cooling ramps, eventually inserting intermediate thermalization phases to uniform the temperature of the load avoiding thermal stresses and residual deformations.

We decided to develop an approach based on 1D simulations and FE analyses in order to predict the behavior in terms of temperature distribution of the components during the brazing thermal cycle, avoiding elevated thermal gradients resulting in deformation and thermal stresses. In this paragraph a little description of the vacuum furnace will be described as well as the development of the techniques for the brazing thermal cycle prediction.

3.3.1 The high vacuum oven of the LNL laboratories [12]

Figure 3.17 gives an overall external view of the vacuum furnace located at the LNL laboratories.

The oven is a vertical charging type (figure 3.18). The principal nominal characteristics of the oven are [13]:

- Charge: the maximum allowable load is 1000 kg
- Vacuum: the oven is able to reach a vacuum of the order of 1e-7 mbar (high vacuum)
- Temperature: the maximum allowable temperature is 1300 ˚C
- Maximum utile work dimension: 1300 mm of diameter, 1600 mm of height, for a total volume of 2 m^3. This volume is considering a certain
- distance from the heating resistors in order to guarantee the uniformity of the heat flow on the components during the thermal cycle.

Figure 3.17 External view of the vacuum furnace at LNL

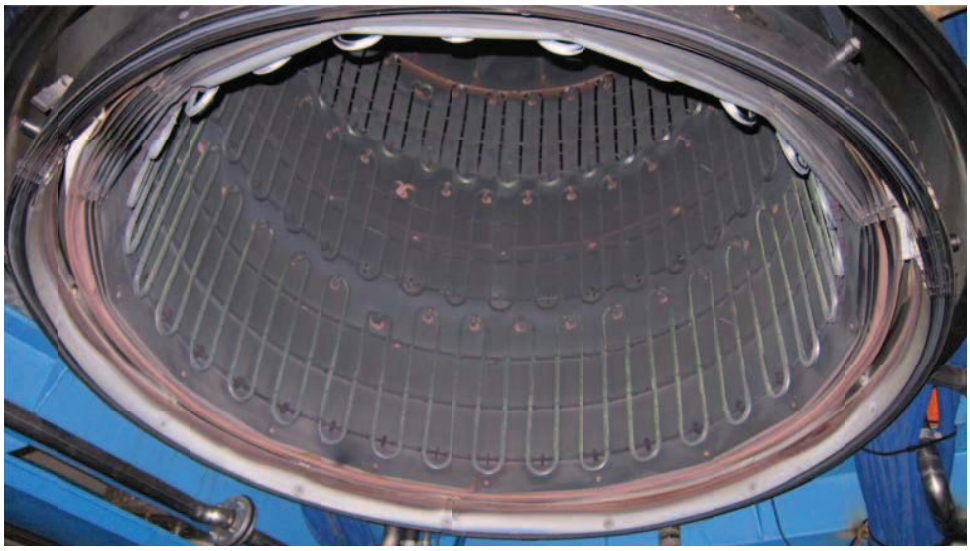

Figure 3.18 Internal view of the oven with the resistors and the Molybdenum reflectors

The oven uses some thermal resistors placed on the internal cylinder and at the bottom plate that heat the walls of the furnace that represent the radiating surfaces (figure 3.18).

A control system manages the current given to the resistor in order to maintain the correct set point temperature on the radiating surfaces.

The temperatures of the radiating walls (hot zone) and on the components of the load are monitored with a set of respectively four and a maximum of twelve thermocouples. The accuracy on the measure of the thermocouples is on the order of ± 2 °C.

The walls are made with various layers of molybdenum in order to resist up to 1300 °C and the temperature is keep controlled and uniform by a cooling system.

In general possibilities of heat exchange are:

- Convection
- Conduction
- Radiation

Since the oven work and he brazes are at high vacuum condition, convection is irrelevant due to the limited number of molecules that can transfer kinetic energy from zones with higher temperatures to lower ones.

Conduction is also negligible, and it can be considered to evaluate the losses to

the external ambient.

The unique possibility to furnish heat to a piece under vacuum condition, like into the oven, is by radiation. The heat transfer energy increase with the fourth power of the temperature, so it becomes very intense at high temperatures.

The managing of the thermal cycle can be done by means of the PLC or a computer with a software linked to the control system of the oven. The software installed on the PC permit also to monitor the principal parameters of the oven, such as vacuum level, the residual gases presents on the cavity and more important the set point temperatures of the oven and the temperatures measured on the components by means of the eleven thermocouples inside.

The set point temperature of the oven can be managed also manually. In this case it is impossible to control the duration of the heating ramp, but the oven will reach the set point temperature as fast as possible with a certain overshoot also, resulting on possible inhomogeneity of temperature on the component that can cause deformations of the geometry.

It has been retained very important to predict and simulate the effect of the component to be brazed, in order to automatize as much as possible and evaluate critical point of this process, such as in homogeneities of temperature on the components that can result in distortion of the geometry.

The brazing test was made to learn better the brazing process, the behavior of the vacuum oven, and to tune the parameters of the simulation, such as the emissivity of the materials of the components. In particular a lumped model with Mathcad has been developed for the prediction of a preliminary thermal cycle and FE analyses has been developed for more accurate calculations.

3.3.2 Analytical solution for the prediction of the brazing thermal cycle

Since the radiation is a strongly non linear effect cause the dependency of the fourth power of the temperature and the transients of the thermal cycle are so long, the develop of the mono-dimensional model is very important for the prediction and the calculation of the thermal cycle.

The fundamental law governing all heat transfer is the first law of thermodynamics, commonly referred to as the principle of conservation of energy. However, internal energy, U, is a rather inconvenient quantity to measure and use

in simulations. The equation that governs heat transfer phenomena per unit of volume on a solid is purely conductive:

$$\rho \cdot c_P \cdot \frac{\partial T}{\partial t} + \nabla \cdot (-k \cdot \nabla \mathrm{T}) = \mathrm{Q} \qquad (3\text{-}1)$$

where

- ρ is the density $\left[\frac{kg}{m^3}\right]$
- c_p is the heat capacity at constant pressure $\left[\frac{J}{kg \cdot K}\right]$
- T is the absolute temperature $[K]$
- k is the thermal conductivity $\left[\frac{W}{m \cdot K}\right]$
- Q is the heat source $\left[\frac{W}{m^3}\right]$

The first term on the left represent the inward heat, the second one the conductive heat transfer.

Since the thermal cycle for the brazing is performed on a high vacuum furnace, there is no convection, but only conductive and radiation heat transfer.

In case of a component inside a cavity, and considering the hypothesis of grey-diffuse surfaces the term Q that describe the heat flux exchanged by radiation of the equation (3-1) is given by the equation:

$$Q = \sigma \cdot \varepsilon \cdot A \cdot (T_{source}^4 - T^4) \quad (3\text{-}2)$$

where

- σ is the Stefan-Boltzmann constant ($\sigma = 5.67 \cdot 10^{-8}\ \frac{W}{m^2 \cdot K^4}$)
- ε is the emissivity of the radiated surface
- A is the effective exposed area of the component to the radiating source $[m^2]$
- T_{source} is the absolute temperature of the surface $[K]$
- T is the absolute temperature of the component $[K]$

Since the melting point of the brazing alloys used for the tests and also for the production of the modules of the accelerating line is near 800 °C, the heat transfer by radiation become dominant, and the second term on the left on the equation (3-1) on a fist approximation can be neglected.

This approximation is also reasonable considering the definition of the thermal diffusivity:

$$a = \frac{k}{\rho \cdot c_P} \quad (3\text{-}3)$$

The thermal diffusivity a can be seen as the ratio between the capacity of a material to conduct heat and the capacity to store energy. The higher value of a, the propagation of energy is faster. In table 3.2 the value of a were considered for the material copper CuC2 and AISI 316 LN at 20°C.

	Copper CuC2	**AISI 316 LN**	**ALUMINA (AL_2O_3)**
$k \left[\frac{W}{m^2K}\right]$	400	16	40
$\rho \left[\frac{kg}{m^3}\right]$	8900	7800	3985
$c_P \left[\frac{J}{kgK}\right]$	385	500	690
$a \left[\frac{m^2}{s}\right]$	1.2e-4	4.1e-6	1.4e-5

Table 3. 2 Different values of the thermal diffusivity a for two different materials at 20°C.

Since copper CuC2 present a value of a of about 3 order higher than AISI 316 LN, the equation 3-1 can be reasonably simplified and in the case of the design of the approximated thermal cycle for the brazing of the copper components.

The lumped equation that govern the heat transfer between the components and the oven for the calculation of the brazing thermal cycle is:

$$m \cdot c \cdot \frac{dT}{dt} = \sigma \cdot A \cdot \varepsilon \cdot (T_{oven}^4 - T^4) \quad (3\text{-}4)$$

where:

- m is the mass of the component that have to be heated
- c is the heat capacity of the material of the component at constant pressure
- σ is the Stefan-Boltzmann constant
- A is the exposed area of the component to the cavity of the oven
- ε is the emissivity of the surface of the component
- T_{oven} is the absolute temperature of the radiating surfaces of the oven
- T is the absolute temperature of the component inside the oven

This equation was implemented in PTC Mathcad R14, with the technique of the

finite difference for the prediction of the thermal brazing cycle, to best-fit the experimental data, calculate and keep into control the parameters of the simulation during the brazing cycle and eventually change the thermal cycle.

The design of the themal-cycle was made in collaboration of a colleague expert in brazing joint of the INFN laboratories of Legnaro, taking into account also the experience of the technicians of the brazing laboratory of CERN for TRASCO.

In general the thermal heat cycle is composed by various phases:

- The heating ramp and thermalization: the oven is heated to a set point of temperature that is somewhat below of about 5-10 ˚C from the solidus temperature of the brazing alloy, following a maximum ramp of 150-200 ˚C per hour, avoiding too big thermal gradients and thermal distortions on the charge components. Cause the thermal inertia of the load, the oven then is maintained to the set point to uniform of the components to that temperature. This first phase should be as fast as possible but not too much avoiding thermal gradients that translates into thermal stresses. Eventual intermediate thermalization steps are possible to allow the temperature to be uniform.
- Heating ramp and thermalization for the brazing: in this phase the temperature of the oven is risen again and then maintained to a certain set point temperature to melt the filler metal which starts flowing into the joints. This step is the most important: the heating ramp, the set point temperature and the duration of this phase are very critical parameters for a good design and quality of the brazing joints. This phase depends on the brazing alloy (solidus and liquidus temperatures) and has to be as faster as possible avoiding interactions between the filler and the base material and avoiding flow off of the alloy from the brazing surfaces. However without generating thermal gradients on the components causing stresses and distortions. In particular, lot of attention must be kept when using non-euctetic brazing alloys and with large differences between the liquidus and solidus temperatures. In fact if the heating is too small, liquation phenomena are possible. The first component to be melted is that with eutectic composition. If the melting of the brazing wires is too slow the

low melting component will flow by capillary actions to the hottest zones (if the clearances between the brazing surface is fine, less than 0.04 mm), thanks also to the minor viscosity respect the higher melting components. The higher melting components will not find a bath of the previous elements around them. In this case the temperature necessary to the melting of the higher melting components can result much more than the solidus temperature. However liquation should not be a problem and the mechanical resistance of the joints should not be affected.

- Controlled cooling: the walls of the oven will cool down. The cooling of the component must be slow enough avoiding non uniformities of temperature on the components, especially until the brazing alloy is not solid.

As anticipated before the thermal cycle has been designed considering Palcusil10 as brazing alloy. The liquidus temperature is 852 ˚C and the solidus one is 824 ˚C.
The equation 3-1 can also be rewritten as:

$$\frac{dT}{dt} = \sigma \frac{A \cdot \varepsilon}{m \cdot c} \cdot (T_{oven}^4 - T^4) \qquad (3\text{-}5)$$

The term $\frac{A \cdot \varepsilon}{m \cdot c}$ can be seen as a thermal inertia of each component. This is a very important parameter for the design of the brazing thermal cycle: the increase of the thermal inertia, the heating of the component will be faster.
For what concerning this brazing test the two C shaped components of 400 mm length present the slowest inertia. For this reason, the thermal cycle was designed for those components.
Firstly a simulation was made with Mathcad for the prediction of a cycle.
The parameters used for the simulation were:

- Mass (m): $42\ kg$
- Exposed area (A): $0.21\ m^2$

In general the heat capacity c and the emissivity ε are function of the temperature. Moreover ε depends also on the state of the surface, which means type of mechanical machining (milling, EDM, etc.) and oxidation.
For the solution of the lumped equation the heat capacity was considered as function of the temperature [14], as reported in figure 3.19.

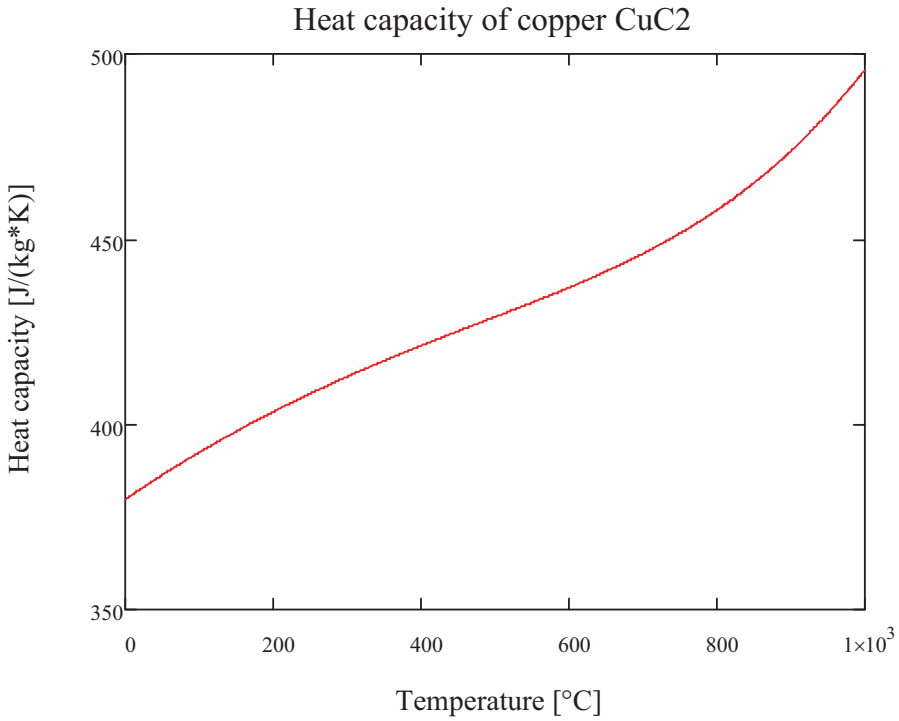

Figure 3.19 Temperature dependency of the specific heat of the copper

Concerning the emissivity instead, it was considered as constant.

The value of the emissivity was that obtained with best-fit calculations on the thermal cycle of annealing of each C shape component.

Figures 3.20 shows the results of the fitting of the experimental mean temperature measured by means of some thermocouples on the copper C during an annealing thermal cycle, for a value of ε of 0.07. The purple curve represents the set point temperature of the oven, the green one is the temperature measured inside the oven by means of thermocouples and the red one is the best-fit curve of the experimental temperatures. The accordance with the experimental results is good at temperatures above 600 °C. At lower temperatures there could be other phenomena such as bad thermal contact with the piece and the thermocouples and conductive effect of the tooling for the support of the component on the vacuum furnace.

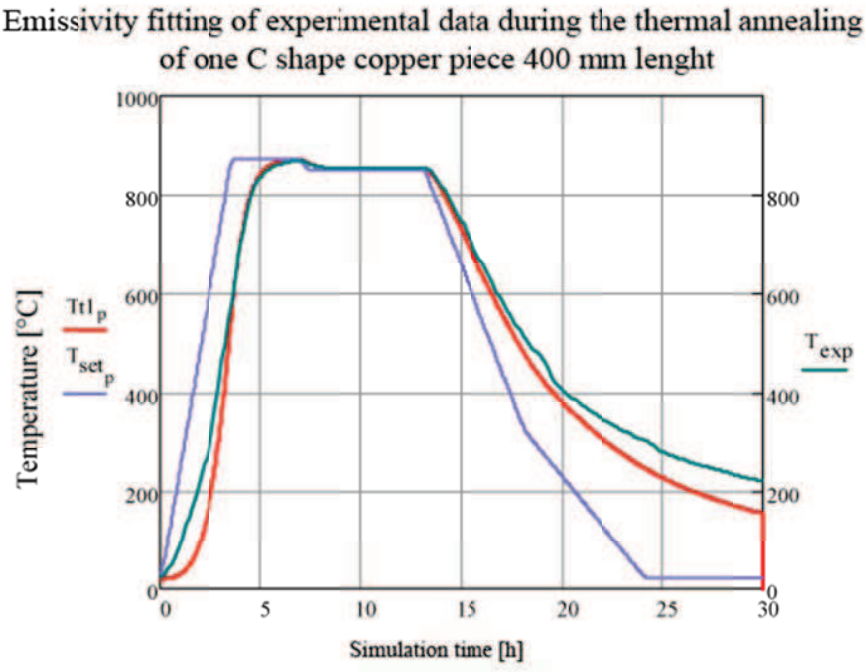

Figure 3.20 Best-fit calculation for the emissivity of the thermal cycle of the annealing of the C shape component of 400 mm length

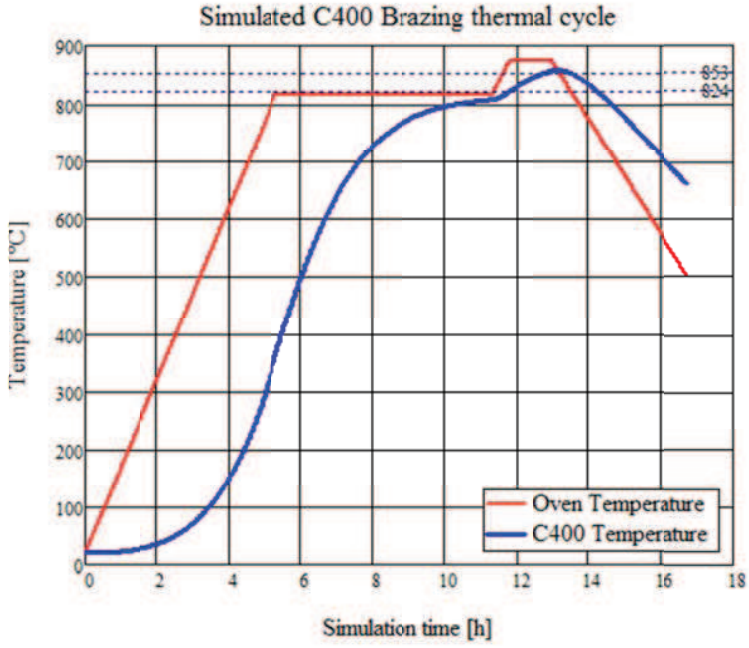

Figure 3.21 Preliminary design of the thermal cycle of the brazing of two C shaped 400 mm lenght

With all the parameters is possible to draft a thermal brazing cycle, as reported in figure 3.21.

A first ramp of 150 °C/h was considered and thermalization at 815 °C. Then ramp of 120 °C/h and a temperature set point of 875 °C for about 1 h were considered for the brazing in order to reach as faster as possible the melting point of the brazing alloy avoiding thermal gradients and to allow the alloy to wet the entire brazing surfaces.

3.3.3 3D FEM simulations of the thermal brazing cycle

Finite Element simulations were performed to design more precisely the thermal cycle, to check the uniformity of distribution of temperature on the components and to evaluate the effects induced by the brazing tooling such as supporting steel plate, the stainless steel bars on which are mounted the Nimonic springs to keep a certain pressure to keep in position the components.

Two different commercial packages were used, Comsol 4.1 and Ansys APDL 12.1 to test the reliability of the simulations with the two different packages. A transient thermal simulation was defined giving in input the thermal cycle calculated solving the lumped equation by Mathcad R14.

Coupled conduction/radiation heat transfer phenomena are solved by means of sequential method considering the equilibrium between the heat transfers by radiation and the diffusion by conduction [15]. Radiative heat transfer fluxes deliver boundary conditions for the diffusion whereas surface temperature distribution provides boundary data for radiation.

Figure 3.21 summarizes the general heat transfer phenomena. The problem consider conductive (diffusion) heat transfer on the solid domain D. On the external surfaces of the domain D temperatures, heat fluxes and convective heat transfer and surface to ambient radiation can be assigned.

Surface to surface radiative heat transfer is considered between the surfaces forming the radiation enclosure S_{enc}.

The equation that govern the heat transfer problem on a solid domain is the (3-1) reported above.

Initial conditions and boundary condition must be provided to solve the equation (3-1).

Initial condition specify the temperature field T(x,y,z,t) on the solid domain D at the initial time:

$$T(x,y,z,0) = T_i(x,y,z) \qquad \forall (x,y,z) \epsilon D \qquad (3\text{-}6)$$

Boundary condition describe the status of the surface S of the domain D. They can be expressed on the following way:

$$T(x,y,z,t) = T_{assign}(x,y,z,t) \qquad \forall (x,y,z) \epsilon S_{T-assign} \qquad (3\text{-}7)$$

$$-k\frac{\partial T}{\partial n}(x,y,z,t) = q_{assign} + q_{conv} + q_{rad}$$

$$\forall (x,y,z) \epsilon (S_{q-assign} \cup S_{conv} \cup S_{rad}) \qquad (3\text{-}8)$$

$$-k\frac{\partial T}{\partial n}(x,y,z,t) = q_{enc} \qquad \forall (x,y,z) \epsilon (S_{enc}) \qquad (3\text{-}9)$$

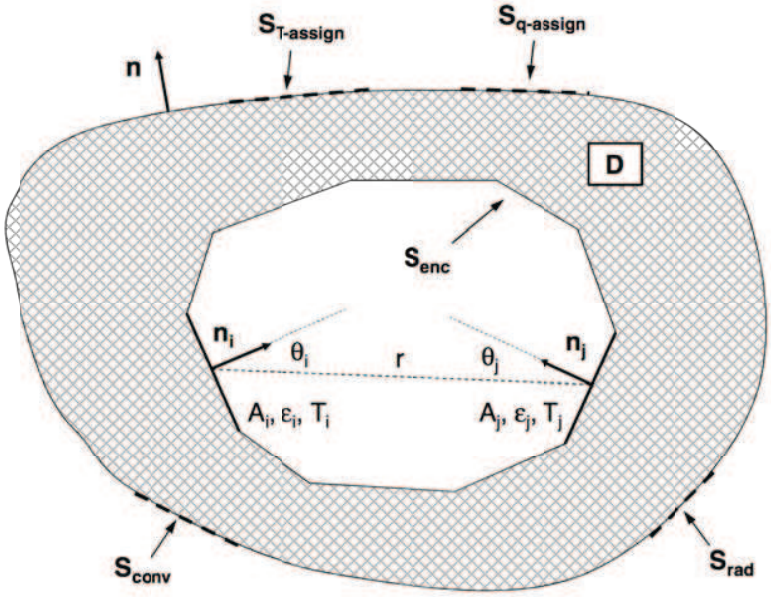

Figure 3.21 Schematic representation of a heat transfer problem [15]

Equation 3-6 expresses an explicit temperature constraint, the normal derivatives (3-8) and (3-9) are computed with the respect of the external versor **n** normal to the boundary S (with $S = S_{T-assign} \cup S_{q-assign} \cup S_{conv} \cup S_{rad} \cup S_{enc}$). The terms q_{assign}, q_{conv}, q_{rad} and q_{enc} are positive when directed along the positive **n**-direction. In particular q_{conv} and q_{rad} indicate the convective and far-field radiative components of the heat flux on the portion of boundary S_{conv} and S_{rad}. They are described by the following expressions [15]:

$$q_{conv} = \alpha \cdot (T - T_c) \qquad (3\text{-}10)$$

$$q_{rad} = \varepsilon \cdot \sigma \cdot (T^4 - T_{amb}^4) \quad (3\text{-}11)$$

In equation (3-10) α is the convective heat transfer coefficient, T_c is the temperature of the fluid surrounding the surface S_{conv}. In equation (3-11) ε is the hemispherical total emissivity of the supposed gray diffuse boundary surface Srad, σ is the Stefan-Boltzmann constant and T_r is the environment absolute temperature of the isothermal surface (much larger than S) that completely surrounds the external boundary of the domain of figure 3.21. On the surfaces A_i belonging to enclosure S_{enc}, boundary conditions are governed by equation (3-9), where q_{enc} is the net radiative loss from A_i. According to (3-9), since convective heat transfer is absent on surface S_{enc}, q_{enc} is equal to the conductive heat flux through the boundary surface S_{enc} inside the domain D.

The solution of the radiative problem, i.e. the determination of q_{enc}, is obtained by considering the following expression and assuming that the N surfaces involved in the radiative heat transfer are grey and diffuse and that each one is characterized by a uniform value both for the temperature and the net radiative heat flux [15]:

$$\sum_{i=1}^{N} \left[\frac{\delta_{ji}}{\varepsilon_i} - F_{j-i}\left(\frac{1-\varepsilon_i}{\varepsilon_i}\right)\right] \cdot q_{enc,i} = \sum_{i=1}^{N} \left(\delta_{ji} - F_{j-i}\right) \cdot \sigma \cdot T_i^4 \qquad (3\text{-}12)$$

where δ_{ji} is the Kronecker delta (δ_{ji}=1 if i=j, δ_{ji}=0 otherwise), ε_i is the hemispherical total emissivity of the surface i, $F_{j\text{-}i}$ is the radiation view factor, $q_{enc,i}$ is the rate of the radiative energy loss per unit area (net flux) of the surface i, σ is the Stefan-Boltzmann constant and T_i is the absolute temperature of the surface i. The view factor $F_{j\text{-}i}$ is defined as the fraction of the total radiant energy leaving the surface j which impacts directly the surface I; it can be expressed as [15]:

$$F_{j-i} = \frac{1}{A_i} \iint_{A_j A_i} \frac{\cos\theta_j \cdot \cos\theta_i}{\pi \cdot r^2} dA_i dA_j \qquad (3\text{-}13)$$

where the geometric quantities are defined in figure 3.21.

Since the radiative heat transfer problem is highly non-linear, to save computational resources symmetry was considered, modeling only a quarter of the geometry, as in figure 3.22. All the springs, bar and small geometrical details were eliminated to save resources of computing and avoiding calculus errors. The oven was modeled as a cylinder with a spherical cap, as shown in figure 3.23.

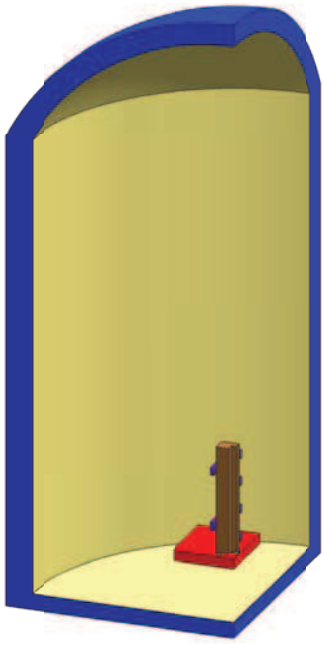

Figure 3.22 Geometrical model for FEM analyses

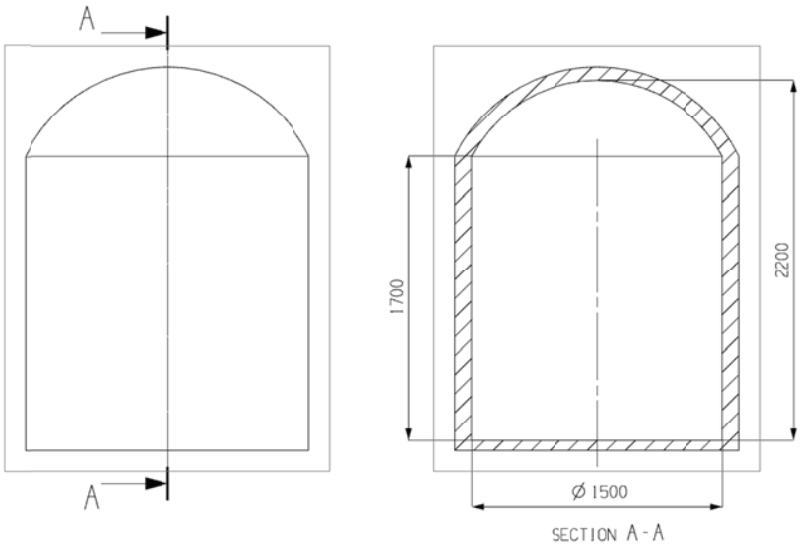

Figure 3.23 Overall dimension of the cavity of the oven for the FEM analysis

Figure 3.24 reports an exploded view of the simplified model of the assembly used for FE analyses. The CAD model was generated with Siemens UGS NX and imported with Parasolid format on both Ansys and Comsol packages.

For what concerning the simulations performed via Ansys APDL, the Radiosity solver permit with RSYM command to define a symmetry condition for radiation on a plane and Ansys consider a mirror on the imaginary plane.
On the other hand, in Comsol it is not possible to define an imaginary symmetry plane, and the mirror planes have to be modeled physically (figure 3.25).

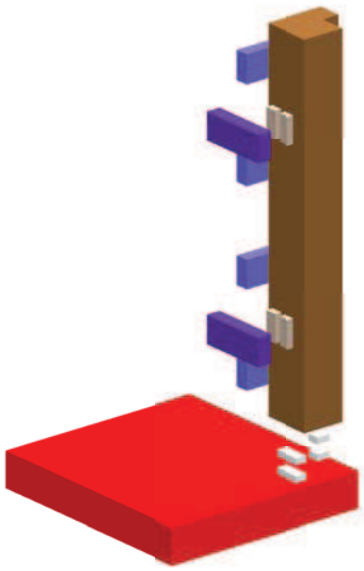

Figure 3.24 Exploded view of the assembly of the copper component with the tooling and the positioning on the stainless steel support

Figure 3.15 Model used in Comsol for the simulation of the thermal cycle with the presence of the modeled mirror planes

Table 3.3 reports the material properties used for the simulation. All the material properties were exported from the software MPDB (Material Properties DataBase)

Material	Property	Reference	Value
Copper CuC2	Thermal conductivity	[16]	Range (400 $\left[\frac{W}{m^2K}\right]$ @ 200 K, 324 $\left[\frac{W}{m^2K}\right]$ @ 1300 K)
	Specific heat	[14]	Range (355 $\left[\frac{J}{kgK}\right]$ @ 200 K, 500 $\left[\frac{J}{kgK}\right]$ @ 1300 K)
	Density	[17]	Range (8980 $\left[\frac{W}{m^2K}\right]$ @ 200 K, 8690 $\left[\frac{W}{m^2K}\right]$ @ 800 K)

Stainless steel AISI 316 LN	Thermal conductivity	[18]	Range (12 $\left[\frac{W}{m^2K}\right]$ @ 200 K, 25 $\left[\frac{W}{m^2K}\right]$ @ 1200 K)
	Heat Capacity	[19]	Range (432 $\left[\frac{J}{kgK}\right]$ @ 200 K, 632 $\left[\frac{J}{kgK}\right]$ @ 1200 K)
	Density	[20]	Range (7970 $\left[\frac{W}{m^2K}\right]$ @ 273 K, 7685 $\left[\frac{W}{m^2K}\right]$ @ 920 K)
Alumina Al_20_3 99%	Thermal conductivity	[21]	Range (54 $\left[\frac{W}{m^2K}\right]$ @ 200 K, 6.5 $\left[\frac{W}{m^2K}\right]$ @ 1300 K)
	Specific heat	[22]	Range (535 $\left[\frac{J}{kgK}\right]$ @ 200 K, 1270 $\left[\frac{J}{kgK}\right]$ @ 1200 K)
	Density	[23]	Range (3994 $\left[\frac{W}{m^2K}\right]$ @ 220 K, 3900 $\left[\frac{W}{m^2K}\right]$ @ 1220 K)
Molybdenum	Thermal conductivity	[24]	Range (128 $\left[\frac{W}{m^2K}\right]$ @ 273K, 102 $\left[\frac{W}{m^2K}\right]$ @ 1273K)
	Specific heat	[24]	Range (278 $\left[\frac{J}{kgK}\right]$ @ 200 K, 310 $\left[\frac{J}{kgK}\right]$ @ 1200 K)
	Density	[24]	Range (10160 $\left[\frac{W}{m^2K}\right]$ @ 293 K, 10015 $\left[\frac{W}{m^2K}\right]$ @ 1193 K)

Table 3.2 Material properties used for the simulation

The boundary conditions of the simulation were:

- Temperature on the inner faces of the oven (yellow surfaces on figure 3.21): the temperature of the oven function of time of the thermal cycle calculated by means of 1D simulations was considered (figure 3.21)
- Surface to surface radiation was applied on the surfaces of the base stainless steel, of the copper C and the stainless steel tooling. The value of the emissivity of copper and stainless steel was based on best-fit calculations of the materials during the previous annealing thermal cycles. The emissivity of copper was the same of that considered for the 1D simulation: 0.07. The emissivity of steel was considered to be 0.2.
- A thermal resistance has been considered at each contact interface.

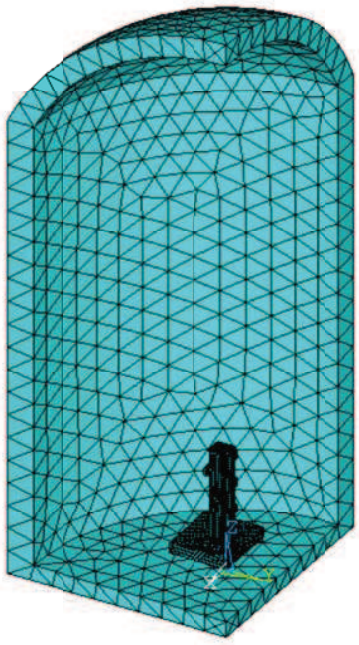

Figure 3.26 Overall view of the mesh generated in Ansys

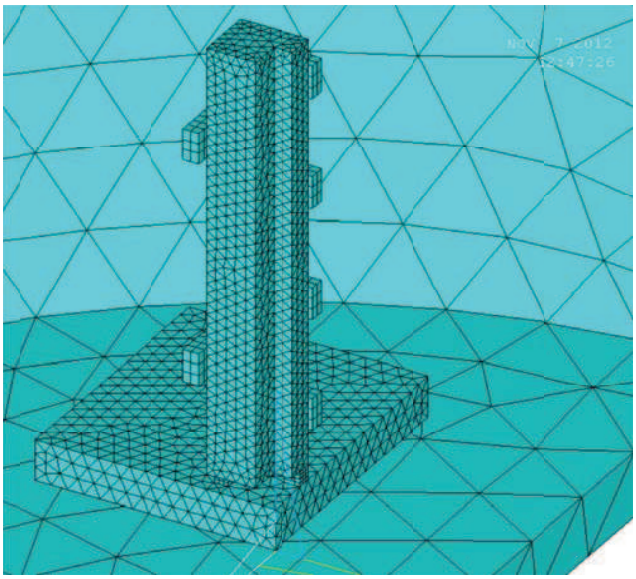

Figure 3.27 Detailed view of the mesh of the copper components, the stainless steel base, and the tooling of the brazing generated in Ansys

Figures 3.26 and 3.27 show the overall image and a detailed image of the discretization constructed for the Ansys APDL simulation used for the more detailed simulation with the also the steels of the tooling. Thermal solid 70 linear element was used and the total mesh consists of about 25000 elements.

Figure 3.28 Overall view of the mesh generated in Comsol

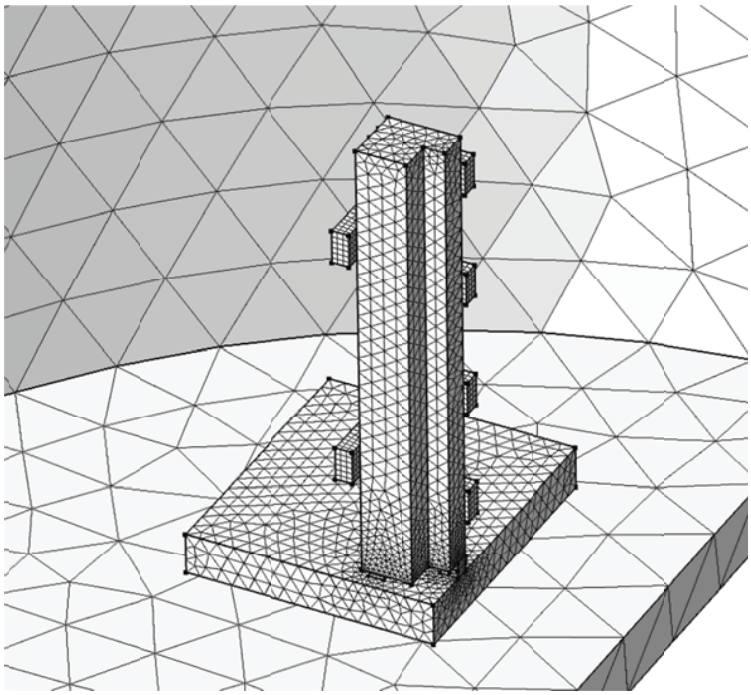

Figure 3.29 Detailed view of the mesh of the copper components, the stainless steel base, and the tooling of the brazing generated in Comsol

Figures 3.28 and 3.29 show a general view and a detailed view of the discretization of the physical domains in Comsol with all the brazing tooling. The mesh consist of about 30000 elements. Differently from Ansys, the type of discretization, (linear, quadratic, cubic,etc.) can be defined after the generation of the mesh, just before the solution and the code automatically inserts the nodes in the middle of the edges of the elements.

The presence of a thermal contact resistance at each surface at the interface of the contact has been considered.

For what concerning the contact resistance, a possibility would be to model physically a layer between the contact surfaces and assigning a material with a certain thermal conductivity.

Another strategy to model thermal resistance on the two FEM codes Ansys and Comsol is to create contact pairs and it is possible to define the thermal contact resistance and it is the strategy that has been adopted.

ANSYS APDL requires the definition of a contact and a target on the surfaces.

The surfaces must be meshed with target and contact elements. For the simulation, linear contact element TARE170 and CONTA173 has been defined.
In Comsol it is sufficient to define the master (target) and the slave (contact) surfaces, and the software automatically treat the contact problem.
Depending on the condition of the contact of the surfaces, the heat transfer between the target surface and the contact surface can be conductive, convective or radiating.
Setting the contact condition to bonded, the heat transfer between the target and the contact can be only conductive.
Then the possibility to define the thermal resistance with a conductance value.
The heat flux of conduction between the two contact surfaces is governed by the equation [25]:

$$q = TCC \cdot (T_T - T_C) \quad (3\text{-}14)$$

where:

- TCC is the thermal contact conductance coefficient to be defined in the real constants of the contact pair and has the dimension of $\frac{HEAT}{TIME \cdot TEMPERATURE \cdot AREA}$
- T_T and T_C are the temperature on the contact points on the target and the contact points.

The value of TCC must be defined on the real constants of the contact pair, and can also be a tabular value function of the average temperature between the target and the contact.
Small values of TCC lead to high temperature discontinuities at the contact interfaces, while high value of TCC tend to the perfect contact approach.
In Comsol the imperfect contact was modeled with considering "Pair thin thermally resistive layer".
It is possible to define the thermal resistance by means the definition of an ideal resistive layer at the interface defining the thermal conductivity and the thickness.
The heat flux across the thermally resistive layer is defined as [26]:

$$-n_d \cdot (-k_d \cdot \nabla T_d) = -k_s \cdot \frac{T_u - T_d}{d_s} \quad (3\text{-}15)$$

$$-n_u \cdot (-k_u \cdot \nabla T_u) = -k_s \cdot \frac{T_d - T_u}{d_s} \quad (3\text{-}16)$$

where:

- d and u refers to the upside and downside of the surface of the contact pair
- n is the normal direction of the surface
- k is the thermal conductivity of the downside material (with subscript d), the upside material (subscript u), and of the contact resistance (subscript s)
- T are the temperatures of the downside material (with subscript d) and the upside material (subscript u)
- d_s is the thickness considered modeling of the resistive layer.

It is obvious that, considering the equation 3-14:

$$TCC = \frac{k_s}{d_s} \qquad (3\text{-}17)$$

In literature can be found different studies of the phenomena of the heat transfer between two contact bodies. Different equations for the calculus of the heat conductance were developed from experimental studies. In general the heat conductance depends on geometrical properties of the contacting surfaces and the mechanical and thermal properties of the contacting materials.

An analytical equation [27], developed from experimental results was used to estimate the contact resistance between two contacting surfaces:

$$hc = 1.55 \cdot k_s \left(\frac{m}{\sigma}\right) \cdot \left(\frac{\sqrt{2} \cdot p}{m \cdot E'}\right)^{0.94} \qquad (3\text{-}18)$$

where:

- hc is the thermal conductance in $\left[\frac{W}{m^2 \cdot K}\right]$.
- k_s is the harmonic mean of the thermal conductivity in $\left[\frac{W}{m \cdot K}\right]$ of the materials of the two contacting bodies:

$$k_s = \left[\frac{1}{2} \cdot \left(\frac{1}{k_1} + \frac{1}{k_2}\right)\right]^{-1} (3 - 19).$$

- m is the mean absolute asperity slope at the contact interface:

$$m = \sqrt{m_1^2 + m_2^2} \qquad (3\text{-}20).$$

- σ is the RMS surface roughness in [m] of the contact asperities (figure 3.30):

$$\sigma = \sqrt{\sigma_1^2 + \sigma_2^2} \quad (3\text{-}21)$$

- p is the contact pressure in $\left[\frac{N}{m^2}\right]$considering the nominal area
- E' is the effective Young's modulus $\left[\frac{N}{m^2}\right]$ of the two contacting materials:

$$E' = \left(\frac{1-\nu_1^2}{E_1} + \frac{1-\nu_2^2}{E_2}\right)^{-1} \quad (3\text{-}22)$$

The subscripts 1 and two on the equations (3-19), (3-20), (3-21) and (3-22) refers respectively to material 1 and 2 of the contact bodies.

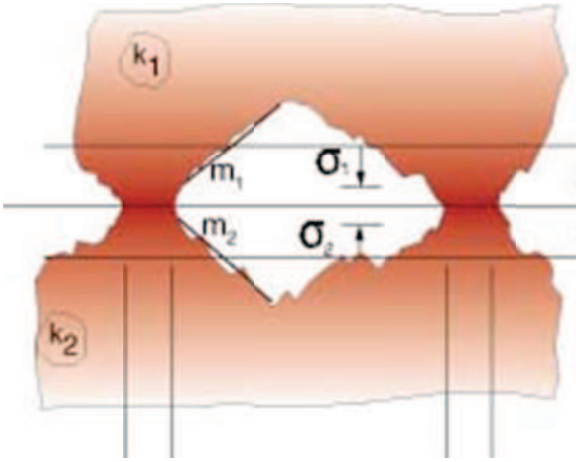

Figure 3.30 Scheme of the localized contact between two surfaces and representation of the geometrical parameters [28]

The surface asperity slope is frequently not given. It can be approximated by the correlation equation proposed by Antonetti [29]:

$$m = 0.125 \cdot (\sigma \cdot 10^6)^{0.402} \quad (3\text{-}23)$$

The relation expressed in 3-22 is valid for $0.216 \leq \sigma \leq 9.6\ \mu m$.

The first case considered was the heating of the copper C supported on the stainless steel base only. The tooling for the fixation and to avoid relative displacements of the two Cs was added later, in order to evaluate separately each contribution.

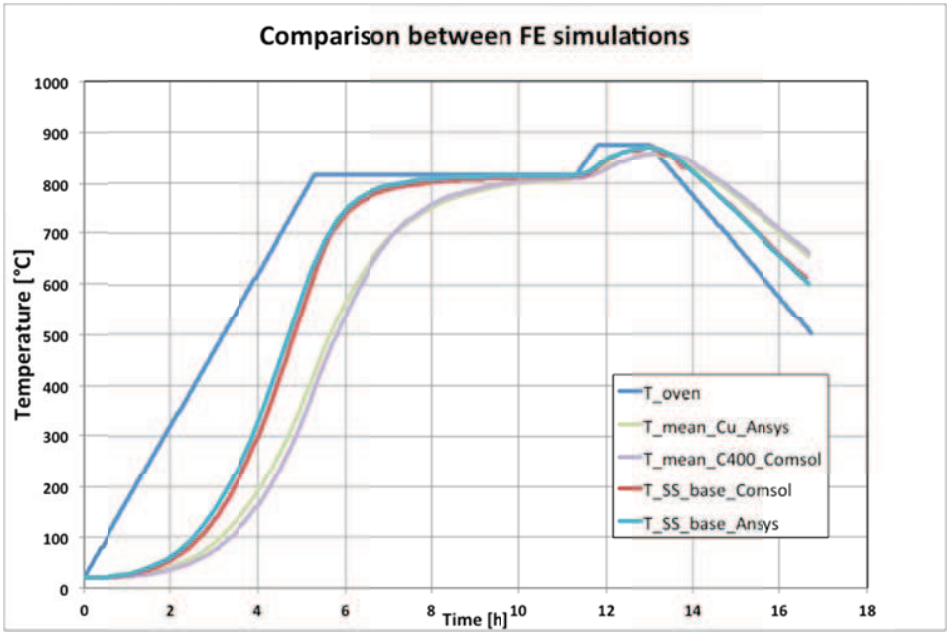

Figure 3.31 Comparison between Ansys and Comsol FE analysis on the temperature calculated on the copper C400 and a point on the stainless steel base near the copper component.

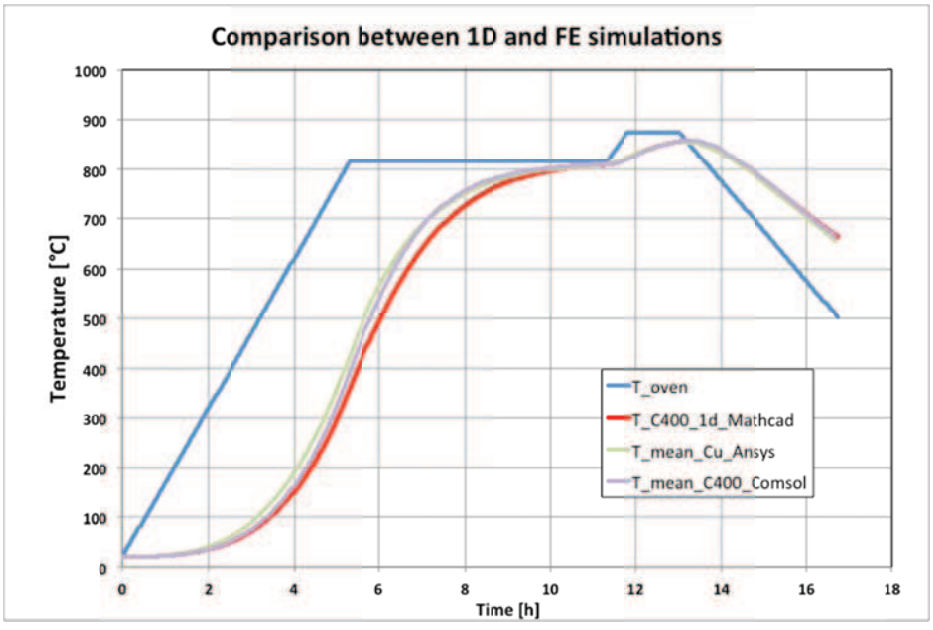

Figure 3.32 Comparison between 1D finite differences solution by Mathcad and Ansys and Comsol FE analyses on Copper C400 temperature.

The accordance between Comsol and Ansys is quite good, with some differences at the initial of the heat ramp, with maximum errors less than 10% (figure 3.31). The accordance between the FE analyses and the 1D simulation is quite good: some differences are present during the ramp to the thermalization phase, with maximum differences of about 50 °C, due to the conductive effects between the copper C and the base (figure 3.32). In fact, since the ratio $\frac{A \cdot \varepsilon}{m \cdot c}$ of the base steel is higher than the copper C, the base is hotter than the C.

Figure 3.33 shows the total balance of heat flow on copper, considering the net radiative heat on copper surfaces and the conductive heat from the lower alumina. The plot shows a maximum small amount of about 25 W (about 10% to the total heat on copper) coming from the alumina. The most important thing is that the conductive heat from alumina became practically zero during the brazing phase, so the copper component is well insulated and no thermal gradient are induced by conductive effects during this phase.

To be noticed that noise without physical significance is present at about t=14h for the calculation of heat from alumina and the mean values should be considered.

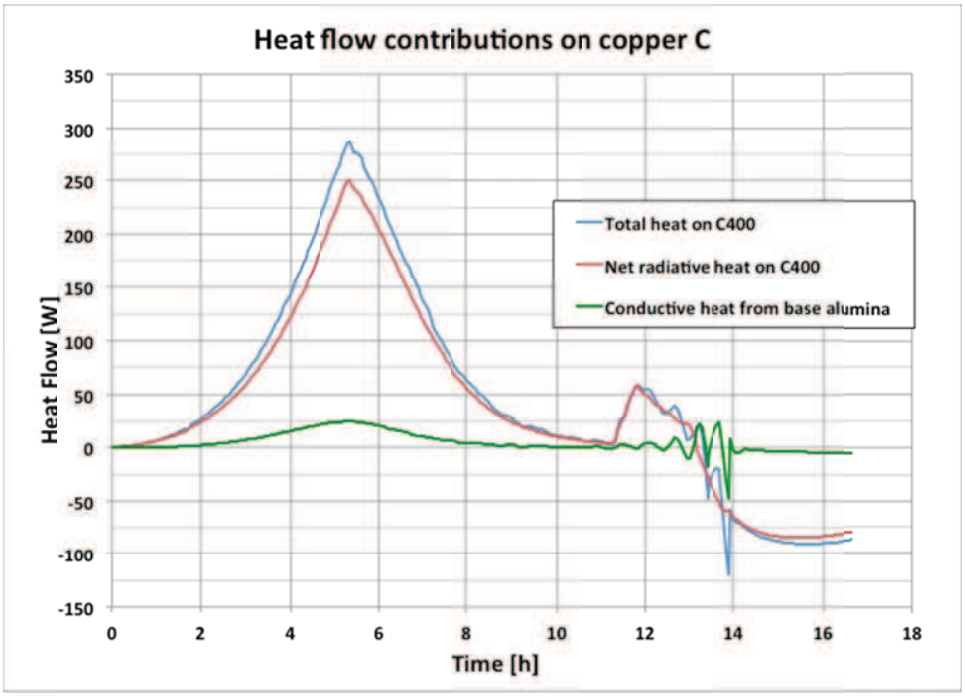

Figure 3.33 Heat balance on copper component

In fact, the heating curves of the copper resulting from the 1D and the FE simulations are overlapped on the heating for the brazing, so the exposed heating area of the copper used for 1D simulation is correct and the contribution of the base steel is still negligible.

Analyzing Comsol and Ansys FE simulations, small thermal gradients on the Copper C develop at the bottom in correspondence the interface with the alumina during the thermalization ramp phase. Figures 3.34 and 3.35 show the temperature plot of Ansys and Comsol calculations at the instant when maximum gradient is registered time on the copper C (time = 5h, according to figure 3.32 and 3.33). The accordance of the two simulations is good with a maximum difference of about 5 °C between the top and the bottom, as confirmed also by the graph of figure 3.36.

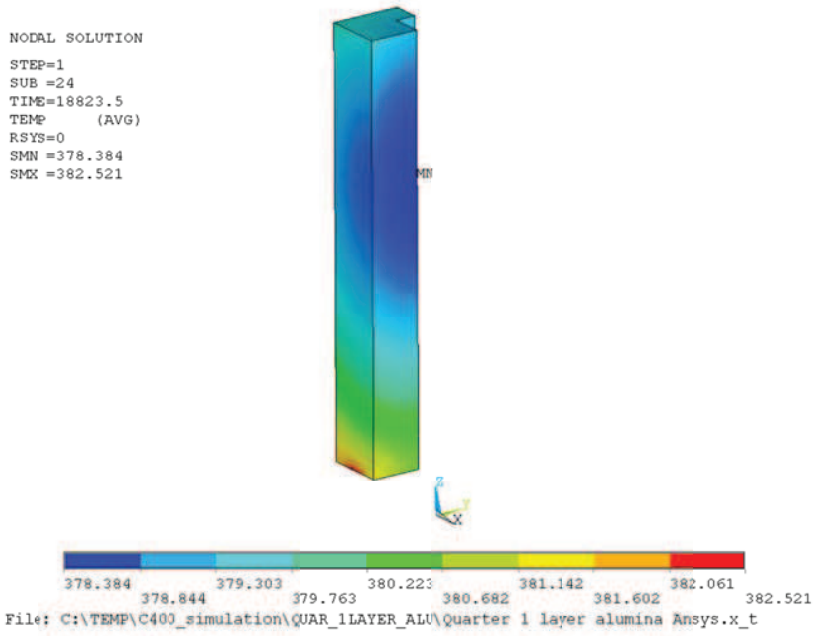

Figure 3.34 Ansys temperature [°C] on the copper C plot at about 5h from the start of the simulation

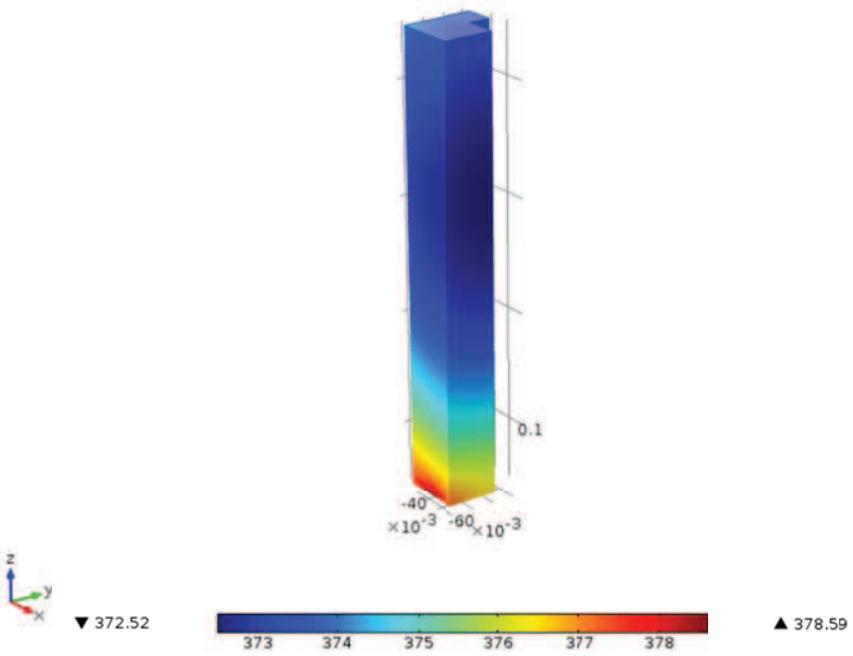

Figure 3.35 Comsol temperature [°C] on the copper C plot at about 5h from the start of the simulation

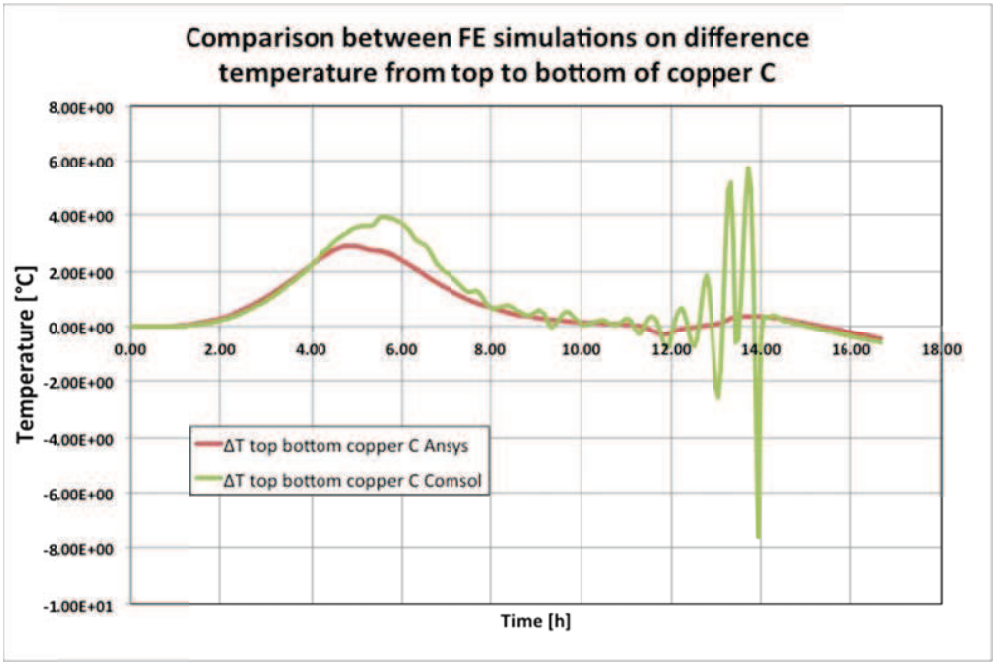

Figure 3.36 Differences between the top and the bottom temperature as results from Ansys and Comsol calculation. The bottom point is the hottest point, while the top is the coolest.

On the thermalization phase, Comsol presents some noise and instability, but the calculations do not have physical significance and the mean values should be considered. The thermal gradient is acceptable: structural calculations were performed on the copper C giving in input the temperature map calculated at the instant of maximum difference between the top and the bottom. Very low thermal stresses on the piece and relative displacements less than 3 μm were registered.

Once analyzed accurately the conductive effect of the stainless steel base on the copper C, attention was paid on the effect of the fixation tooling. Also for the tooling thermal contact resistance between the tools-alumina and copper-alumina contact faces.

In this case, surface to surface radiation boundary condition was applied to the faces of the tools of the fixation facing those of the oven with the same emissivity value of the base mentioned above. The surface to surface boundary condition on copper C was not applied to all the surfaces. In fact, for a more conservative study, to maximize the masking effect of the tools surface to surface boundary condition was not applied to the faces of the copper C below the tools. Moreover, those areas exposed to the stainless steel tool are small compared to the total area of the copper C exposed to the oven radiating surfaces.

Figure 3.37 shows a comparison between the 1D and the 3D FE analyses. The accordance between Ansys and Comsol is good. Marked differences are between 1D and 3D simulations. In fact, considering also the tooling components, considerable heat comes from the fixture stainless steel components (figure 3.38).

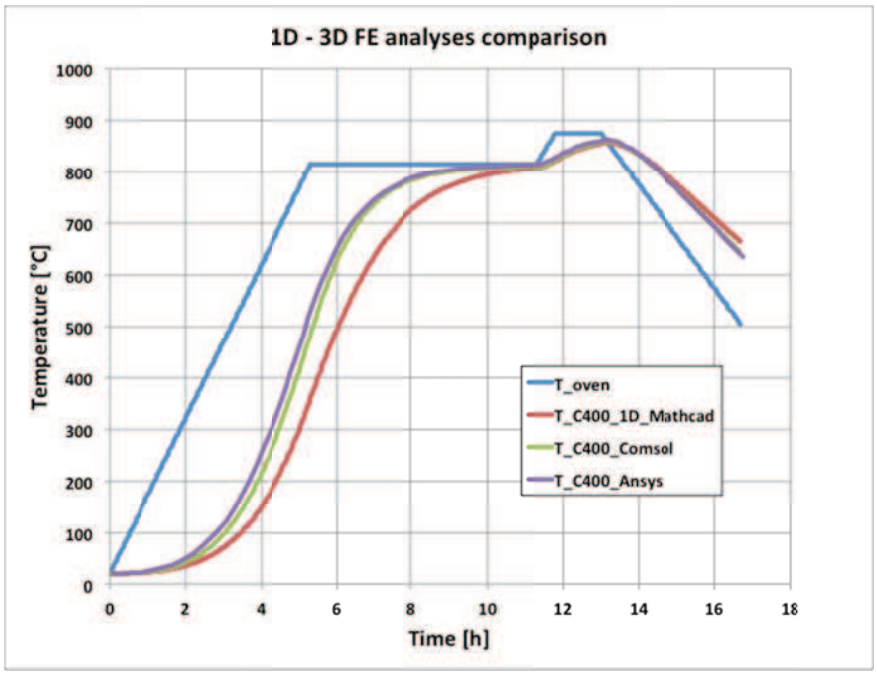

Figure 3.37 Comparison between 1D and 3D FE analyses on the calculated temperature on the C400 component.

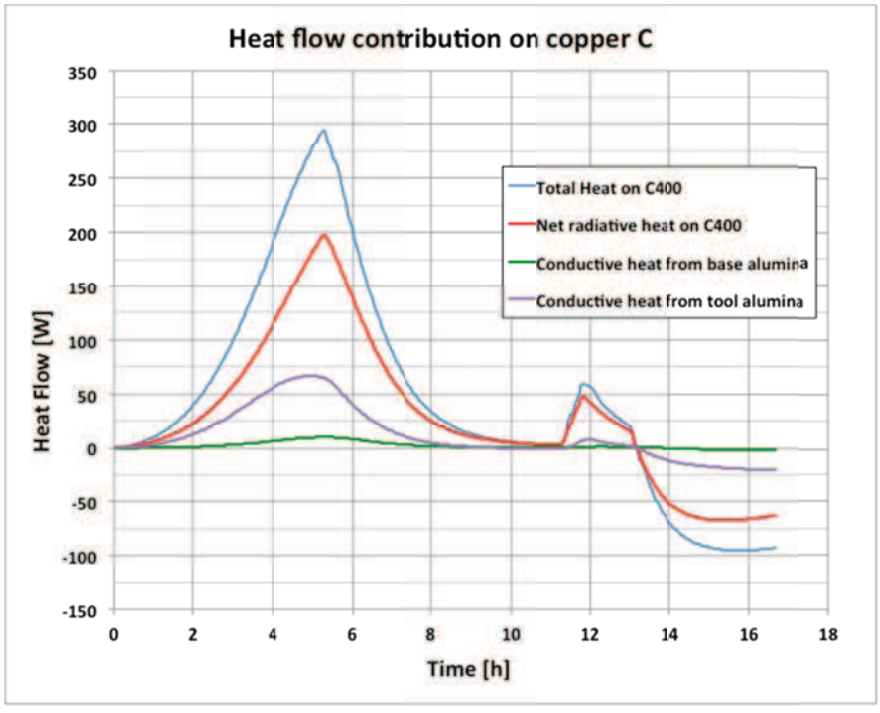

Figure 3.38 Heat flow contribution on copper C considering the fixture tooling also.

However, the temperature distribution inside the copper is quite uniform for all the thermal cycle with difference of maximum 2 °C between the hottest and the coldest points. As shown in figures 3.37 and 3.38 the tooling does not influence so much the temperature distribution on copper during the brazing phase. In fact the heating curves of the copper calculated by 1D and 3D FEA are practically overlapped, and the piece is well insulated. In fact during the brazing phase the conductive contributions from the tooling and the base are negligible (figure 3.38). Since the thermalization of the copper occurs before than 1D and the FE analyses without considering the tooling, the brazing step can be anticipated of about two hours. Let now consider the effects of the thermal cycle for the joining of the copper C to the AISI 316 LN flange, reproducing the same type of junction of the small prototype.

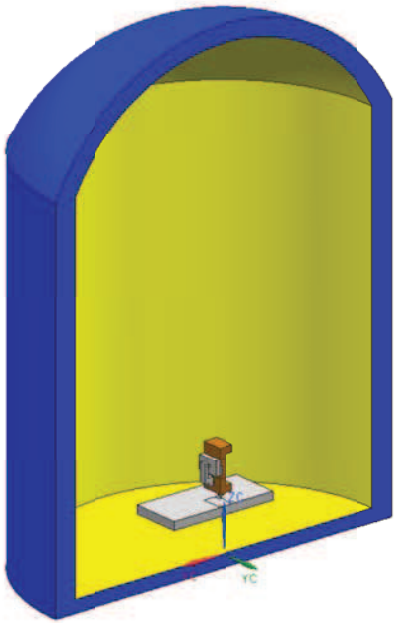

Figure 3.39 Overall CAD view of the assembly for the simulation of the AISI 316 LN flange to the copper C.

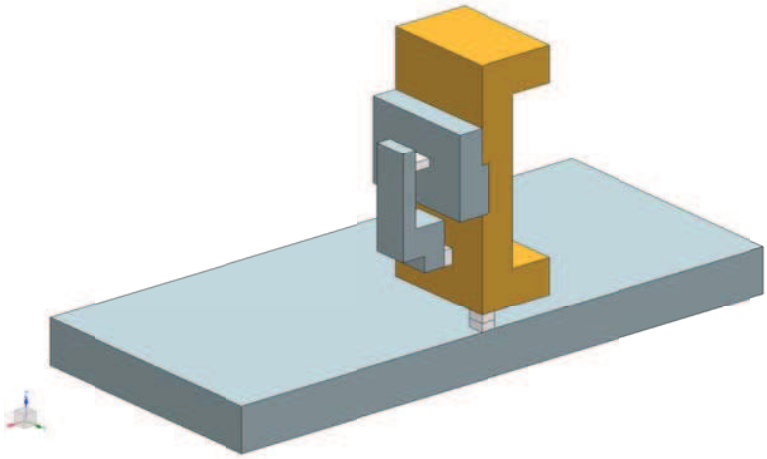

Figure 3.40 Detailed view of the assembly used for FEA

Also in this case the model was simplified, and symmetry was considered to save computational time (figure 3.39). Also in this case Ansys and Comsol commercial codes were used. Figure 3.39 shows the CAD view of the assembly used for the FE analyses. The assembly of the copper C is considered coupled to the stainless steel base by means of a layer of alumina (figure 3.40). The AISI 316 LN tool for the fixation and maintain in position the stainless steel flange respect to the copper C was considered. Two ceramics were interposed between the fixation tool and the copper on one side and the flange on the other side to guarantee thermal insulation.

The material properties are the same used for the previous simulations. The thermal cycle and the surface to surface radiation applied on the oven internal surfaces are also the same applied on the previous simulation.

As for the design of the design of the "C400" brazing cycle, thermal contact has been considered between the base alumina and the copper, the stainless steel tool and the copper and the stainless steel flange and the copper and the stainless steel flange.

But perfect thermal contact has been taken into account between the AISI 316LN flange and the copper when the temperature overtakes 823 °C, that is the liquidus temperature of the brazing alloy Palcusil 10. At this temperature the alloy starts to flow by capillary actions and wets the surfaces of the joint.

Surface to surface radiation boundary conditions were applied on the surfaces

facing to the oven of the copper C, the stainless steel flange, the fixture tool and the base. The surface to surface radiation between the fixture tool and the stainless steel flange and the copper was neglected because its contribution is very small and to not introduce errors and save computational time on the view factor calculation. Figures 3.41 and 3.42 show the discretization on the assembly used respectively in Ansys and Comsol (the mesh of the oven part is the same of the previous case): linear elements were created and the number is about 30000 for both cases.

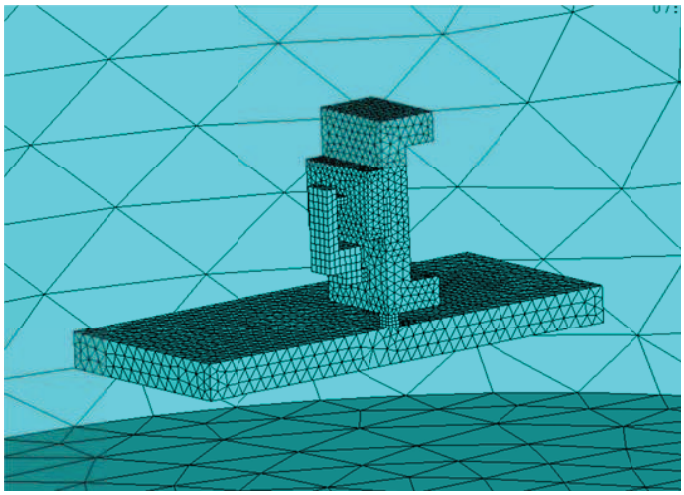

Figure 3.41 Ansys discratization of the assmebly for the study of effect on the copper-stainless steel flange join during the brazing cycle

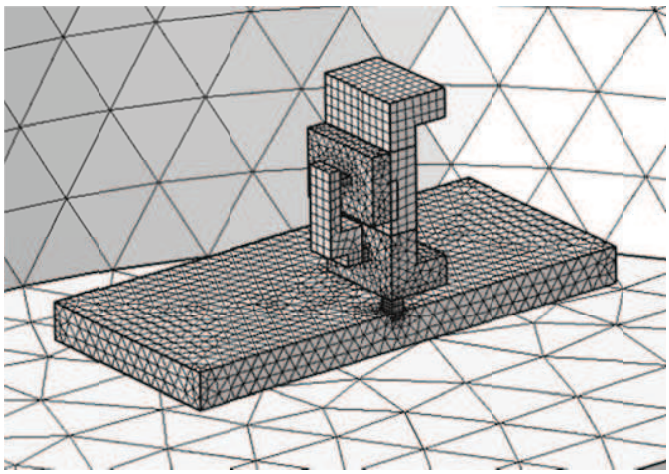

Figure 3.67 Comsol discratization of the assmebly for the study of effect on the copper-stainless steel flange join during the brazing cycle

Figure 3.43 plots the temperature calculated on copper by means Ansys and Comol FE analyses. The accordance of the results is good. Small differences are present on the first heating ramp, while on the brazing step and on the cooling ramp the two Ansys and Comsol curves are pratically overlapped. What is important is that the temperature on copper is uniform with differences less than 1°C during the entire thermal cycle on both Ansys and Comsol calculation.

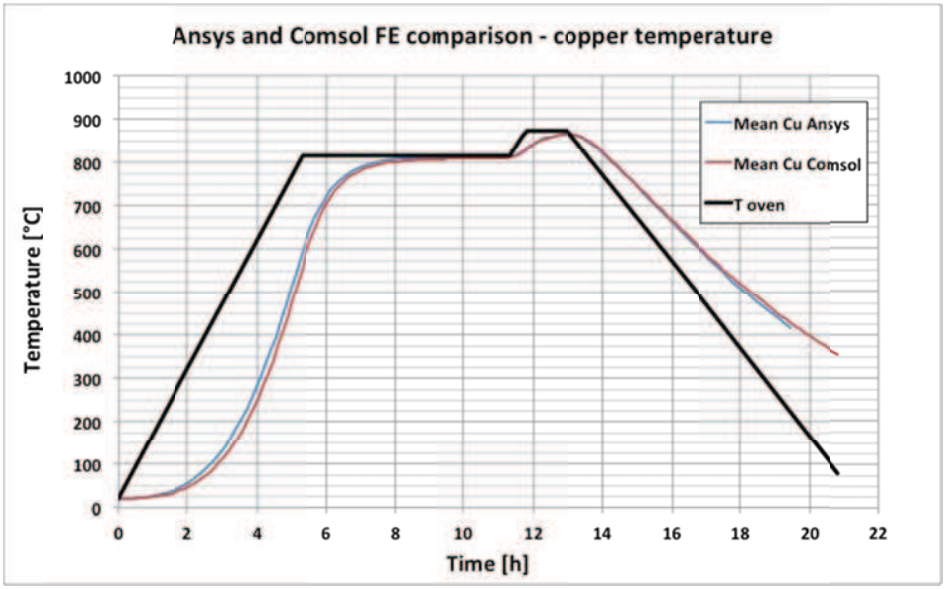

Figure 3.43 Comparison on calculated temperature on copper by Comsol and Ansys FE analyses

However, what is important is that the temperature on the copper is uniform during all the thermal cycle and no thermal stresses are induced by the thermal cycle.

Figure 3.44 and 3.45 show a comparison of the the minumum and maximum temperatures calculated with Ansys and Comsol on the steel flange. Also in this case the accordance between Ansys and Comsol calculation is good.

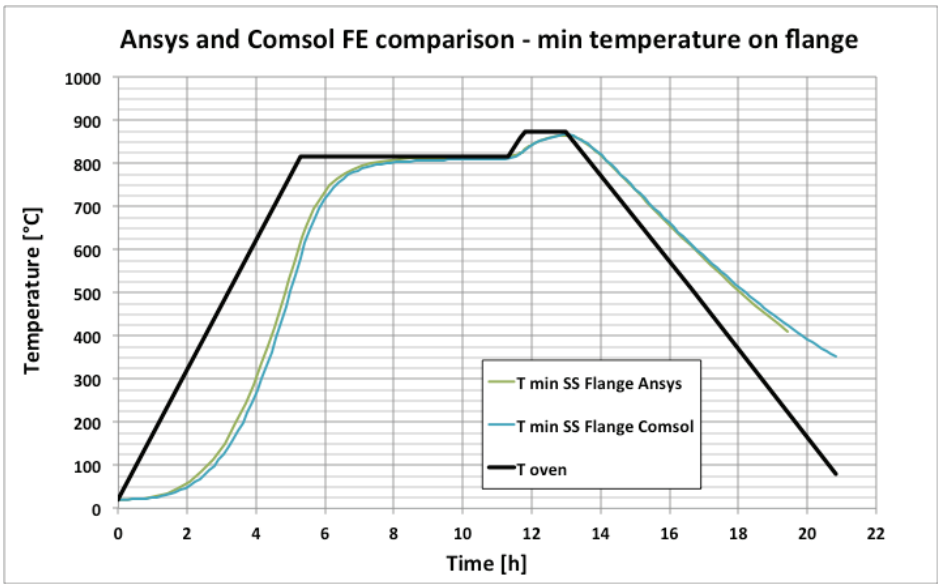

Figure 3.44 Comparsion between Ansys and Comsol calculation on minimum temperature on flange

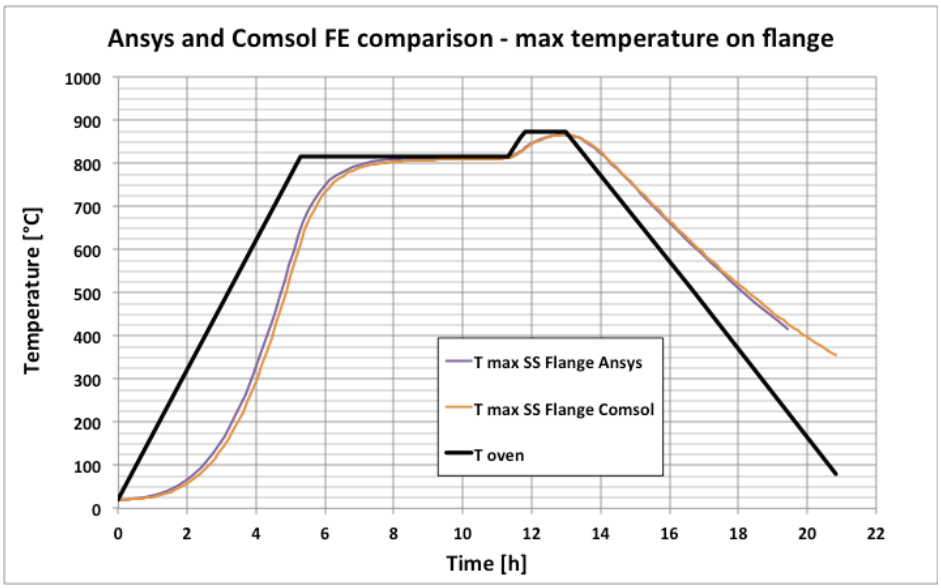

Figure 3.45 Comparsion between Ansys and Comsol calculation on maximum temperature on flange

Figure 3.46 plots the difference between the copper tempearture and the maximum temperature on the surfaces of the flange coupling to the groove on on the copper C. The evaluation of this difference is very important to evaluate thermal stresses induced during the thermal cycle.

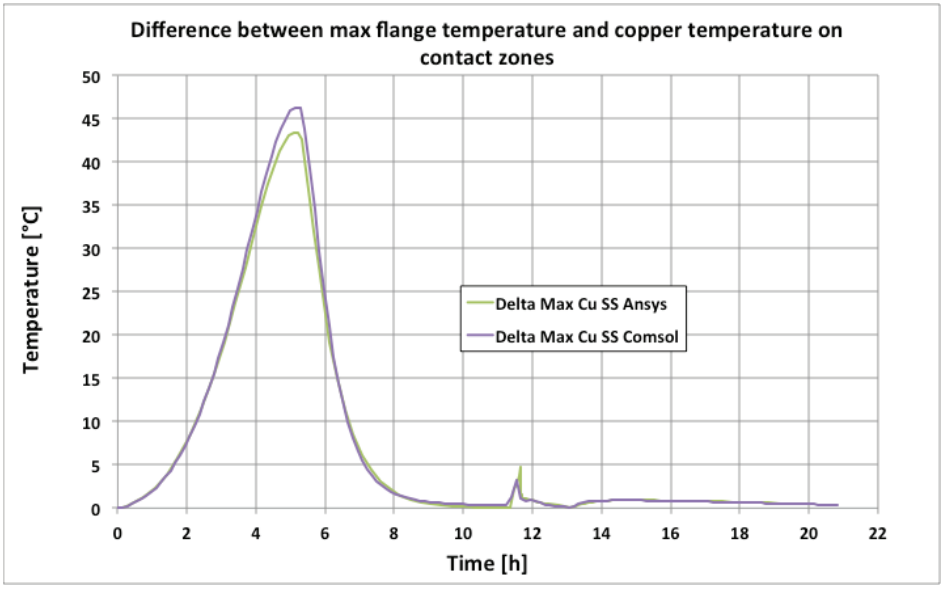

Figure 3.46 Maximum difference of temperature between the flange and the copper on contact zone

The accordance between Ansys and Comsol calculation is very good and a maximum difference of about 40 °C can be noticed on the heating ramp. Considering the differential thermal expansion (figures 3.47 and 3.48) between the copper and the AISI 316 [30], the part of the flange that couples to the copper groove expands of a maximum 0.04 mm more than the copper groove. This value is acceptable, compared to the 0.05 mm of clearance on the coupling of the flange to the copper groove.

For what concerning the cooling ramp, the temperature between the copper and the flange becomes uniform with difference less than 3 °C, considering a perfect contact. Thermal stresses are induced on the junction are very low, according to the integral thermal expansion coefficient considered before.

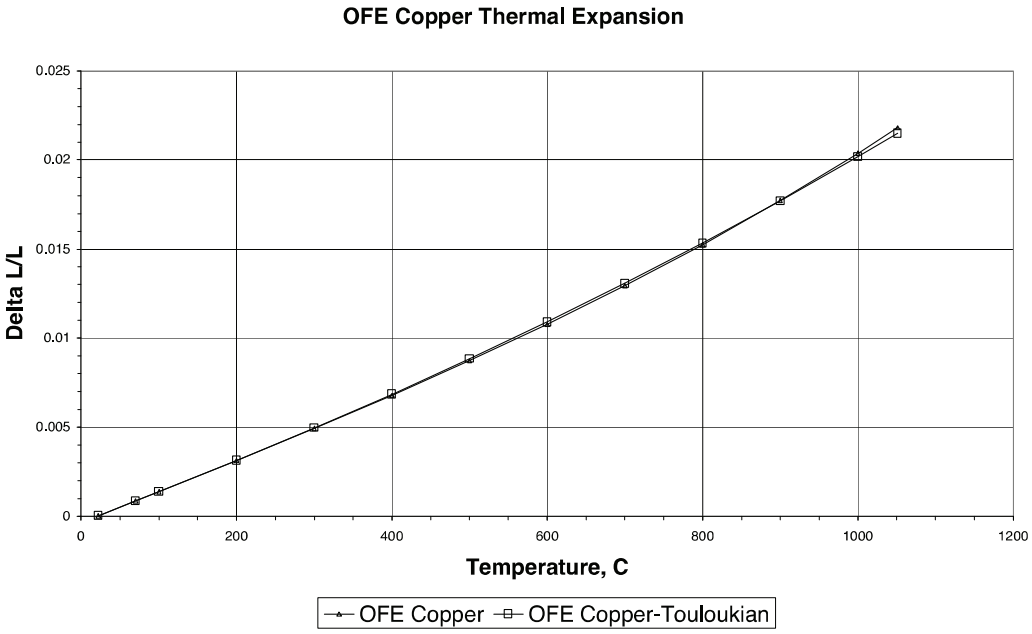

Figure 3.47 Experimental resuslts of the thermal expansion of copper [30]

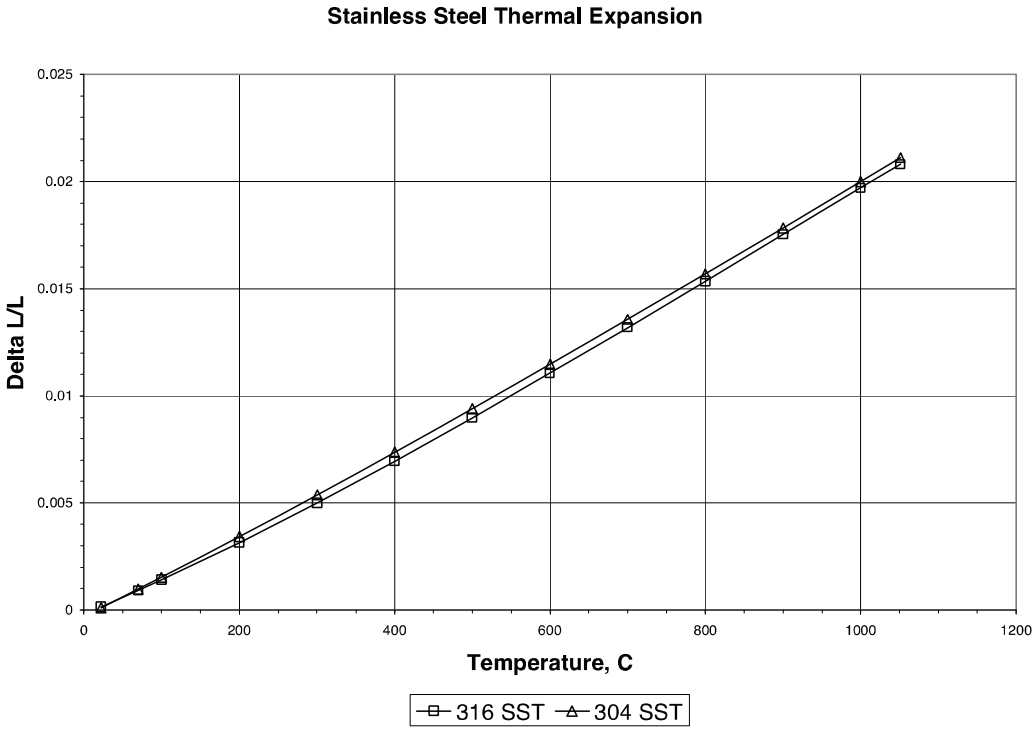

Figure 3.48 Experimental results of the stainless steel expansion [30]

3.3.4 Real brazing thermal cycle and comparison between the experimental results and FE analyses.

The curve of temperature of the radiating surfaces of the oven calculated by means the of the solution of (3-2) with Mathcad and with the FEA approach, was then implemented to the controller of the vacuum furnace.

Figure 3.49 sketches a top view of the positioning of the thermocouples on the different part of the load. Four thermocouples were placed on assembly of the two copper C 400 mm length near the brazing planes in order to control the flow of the brazing alloy: two on the top and two on the bottom of the assembly in order to capture non-uniformities of temperature.

Two thermocouples were placed on each assembly of the brazing of the flanges to the copper Cs. Also in this case they were placed near the brazing surfaces.

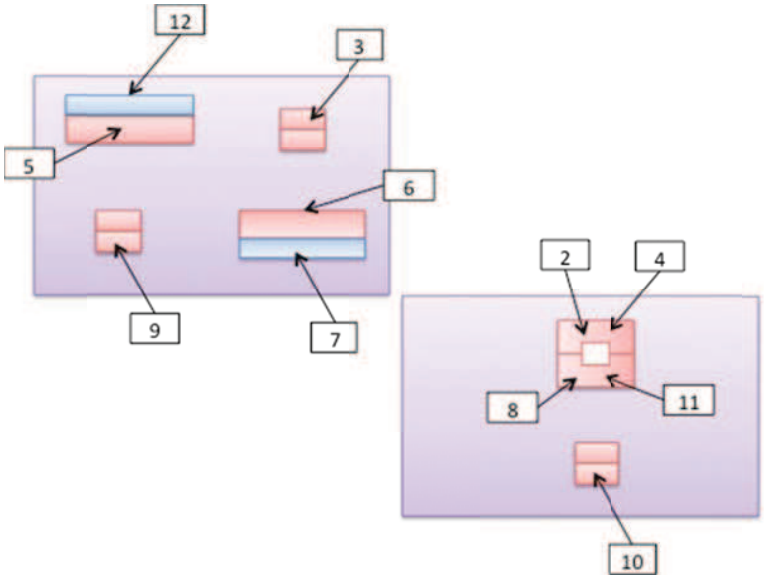

Figure 3.49 Top view sketch of the positioning of the thermocouples on the component of the load.

The brazing thermal cycle was operated by the expert technician and responsible of the brazings of the LNL brazing lab.

Figure 3.50 shows the temperature plot measured by the thermocouples on the load and set point imposed to the hot zones of the furnace.

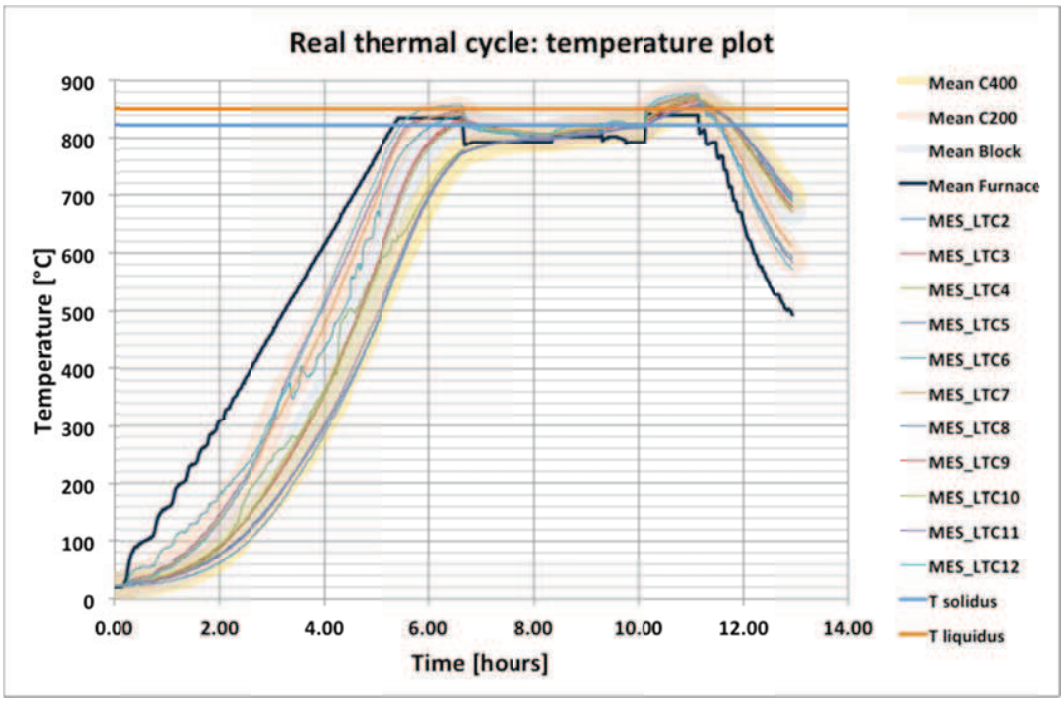

Figure 3.50 Plot of the temperatures measured by the thermocouples on the component of the load and the hot zone of the oven

There is an evident problem since the temperature measured on the copper blocks and the steels of the copper-steel flange assembly are major than the set point temperature of the furnace. The offset is not constant and varies from 10 °C and 28 °C. The problem can be on the control system of the oven or errors on the measures of the temperature on the hot zone of the oven.

The copper block crossed two times the solidus-liquidus interval of the brazing alloy and probably underwent double brazing. For what concerning the copper-steel flange assembly the brazing wire underwent to partial melting oat the end of the first thermalization ramp since the solidus temperature was overtaken.

The two copper Cs for the vertical brazing test did not overtakes the solidus temperature of the brazing alloy during the first thermalization ramp.

The thermal cycle has been redesigned and the oven switched to manual mode. Since FE analyses cannot be performed to calculate a new thermal cycle because too much time (30 min) is required for the solution, 1D simulations performed by the expert technician of the LNL were used to fit the experimental data and to calculate a new thermal cycle. However, with this system it was possible to

recreate the same temperature profile based on the thermal cycle prediction.

Another problem seems to be the accurate measure of the temperature on the component of the load, especially at the low temperature. In fact the thermal contact between the thermocouples and the pieces seem to be very low especially on the first heating ramp. This means that the uniformity of the temperature measured on the copper assembly of the vertical brazing and the difference between the copper and the flange on the copper-stainless steel flange assembly are difficult to evaluate precisely.

The measure of the temperature becomes more accurate at high temperature (above 700 °C). Analyzing the experimental results the temperatures remain uniform with maximum deltas of 2 °C and 5 °C during the brazing step respectively on the two Cs of the vertical brazing test and the copper-flange assembly.

For what concerning the comparison between the experimental results and the FE calculation, a new thermal cycle has been implemented on FE analyses: the set point temperature on the control system of the oven and the offset between the set point temperature and the real measured temperature was considered.

Figure 3.51 shows a comparison of the experimental and FE simulations.

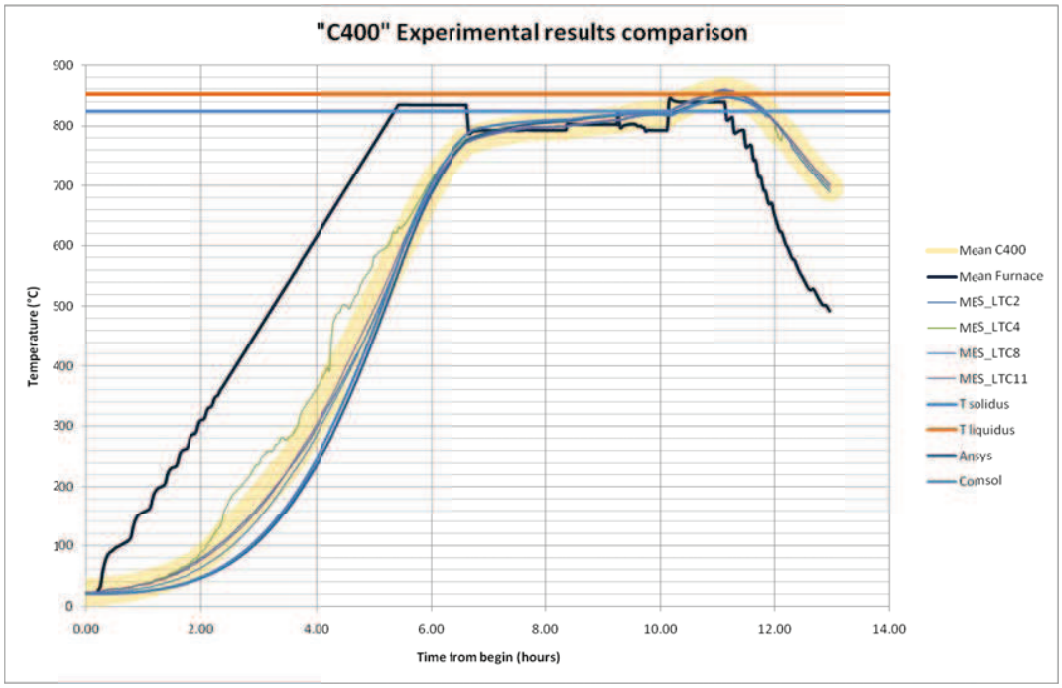

Figure 3.51 Comparison between FE simulations and the experimental results

The plot of figure 3.51 shows a very good accordance between the experimental results and the FE simulations at temperatures above 500 °C. The real cycle shows that the component underwent to an initially faster heating than the simulation. This fact can be attributed to: conductive effects between the stainless steel base and the copper and the stainless steel and the support of the oven and eventual imperfect contact of the thermocouples.

Figure 3.52 displays the comparison between the FE simulations and experimental results. The accordance is very good, but the value of the emissivity of copper and stainless steel were recalculated with 1D simulations during the real brazing cycle. The new value of the emissivity copper was 0.2 and 0.3 for the stainless steel. This fact is due to the different status of the surface of the copper.

Also in this case the components seem to heat faster than the prevision of the simulation.

However the value of the thermal contact resistance seems to be good, especially between the copper and the stainless steel flange.

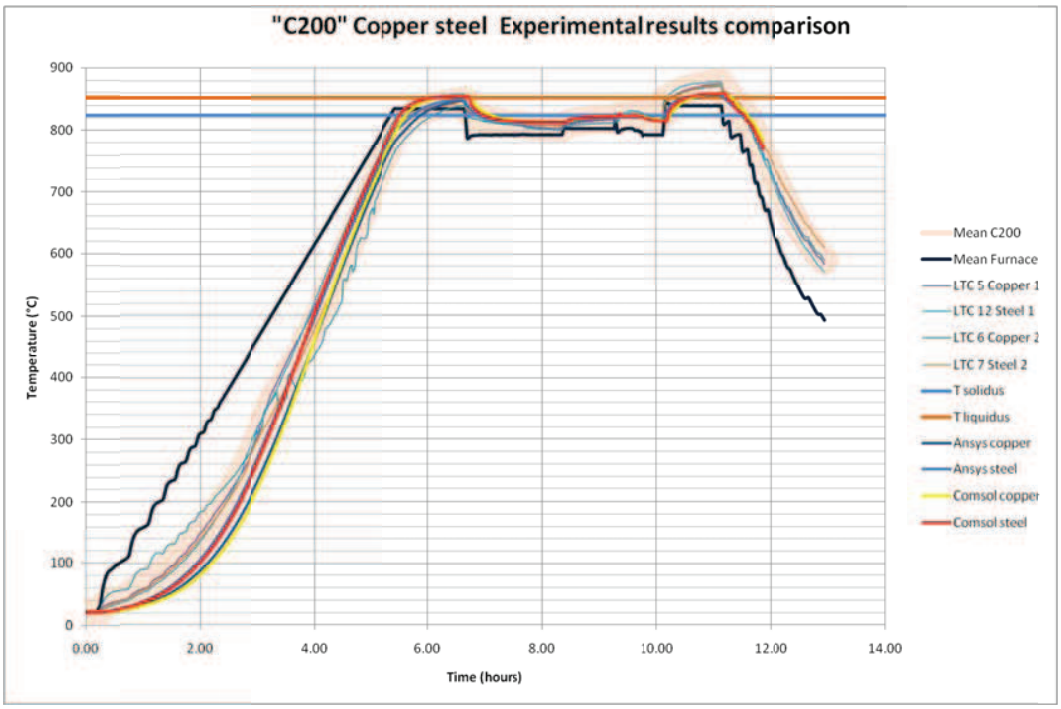

Figure 3.52 Comparison between experimental results and the FE simulations on the brazing of the copper-stainless steel flange

3.3.5 Conclusions

Good instrumentations were developed for the control, prediction and implementation of the brazing cycle. 1D simulations are very useful for a first prediction of the thermal cycle and to manage the real thermal cycle. In fact 1D simulations are fast and reliable to predict the preliminary thermal cycle, fit the experimental data during the brazing cycle in order to eventually modify in real time the thermal cycle. 3D FE analyses are also a good instrument and complementary to the 1D simulations. They are an important instrument to evaluate the effect of the brazing tooling, the supporting base and the thermal stresses induced during the thermal cycle.

However, the thermal brazing cycle cannot be fully automatized at the moment and a very skilled expert is necessary to keep in control what happening during the thermal cycle.

3.4 Inspection and quality assurance of the brazed joints

Since this test was very important for the improvement in terms of the design the grooves on the brazing surfaces that would be adopted for the definitive modules, the development of some methods to guarantee the quality assurance of the brazing surfaces was retained fundamental. Up to now the brazing surfaces of the RadioFrequency cavities were controlled prevalently only by optical inspection and under vacuum conditions. In other words if the meniscus of the flow of the brazing alloy was visible by human eyes on the joint and the vacuum tightness of the cavity was satisfied, the couplings were retained good.

The development of other techniques was retained mandatory to test the performances in terms to have an accurate image of the wetting of the brazing alloy in order to collect more information on the acceptability of a brazed joint.

Non-destructive controls by means of ultrasonic technique were introduced.

3.4.1 Optical inspection of the brazing tests

All the components of the brazing tests were firstly optically inspected. The figure 3.53 shows a detailed of the brazing of the copper C 400 mm height. Figure 3.54 shows instead a detail of the coupling between copper and copper CuC2 and an AISI 316LN flange.

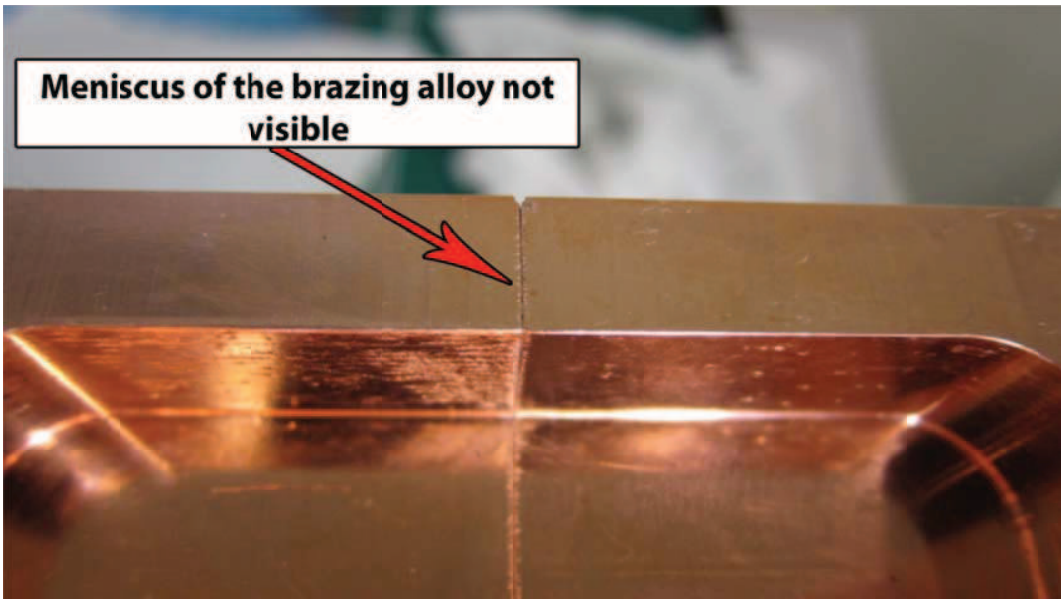

Figure 3.53 Detail of the brazing line on the copper C400

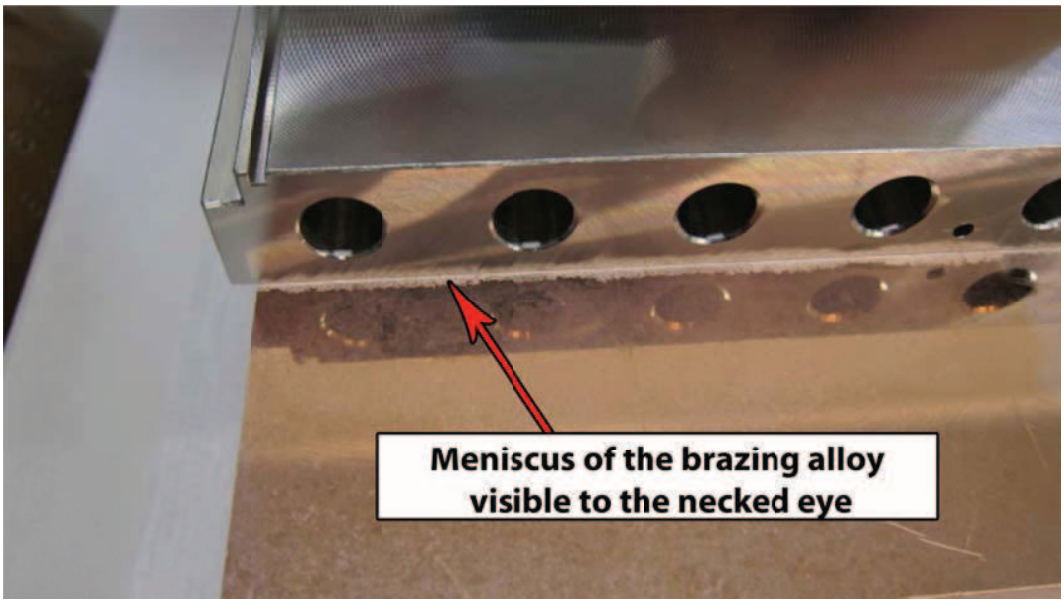

Figure 3.54 Detail of the copper-stainless steel flange brazed joint

The brazing joints were also controlled by means of a lens system capable up to 300x of zoom mounted on the column of a small CMM available at the laboratories of Legnaro. Unfortunately, this kind of system was not allowing the saving of images.

Such a control permit to view and understand with more precision the flowing of

the brazing close to the external surfaces of the joint. In fact, if the brazing filler was not visible as in the case of the figure 3.53, the microscopic control confirmed the presence of the meniscus close to the external surfaces of the joint.
However, microscopic control by means the instrumentation of the Laboratories of Legnaro allow the control only on small pieces such these, not for the final modules. Moreover, the manipulation of the final module is extremely delicate, and any damage on the internal surfaces of the cavity would compromise the functionality.
To understand better the flowing and the filling capability of the brazing alloy, destructive and non-destructive technique by means of ultrasonic scan were introduced.

3.4.2 Theory frame of the ultrasonic waves and inspection[4]

By definition, the non-destructive testing is the testing of the material, for surface or internal flaws or metallurgical conditions, without interfering in any way the integrity of the material or its suitably for service.
The main techniques used for the non-destructive controls can be subdivided in:

- Magnetic Particle Crack Detection
- Dye Penetrant Testing
- Eddy Current and Eectro-magnetic testing
- Radiography
- Ultrasonic Flaw Detection

Other techniques can be electrical potential drop, sonics, infra-red, acoustic emission, spectrography.
The Magnetic Particle Crack Detection, Dye Penetrant Testing and the Eddy Current and Electro-magnetic testing are restricted on the detection of superficial defects, while the defects on the brazing joints are flaws on a volume.
Also the radiography cannot be used for the control of the brazings of a module, because of the impossibility to investigate thick sections.
The Ultrasonic Flaw Detection technique is suitable for the control of brazing

[4] All the arguments, formulas and images on the following paragraph are taken from [31, 32]

alloy.

The advantages of this method are:

- The depth of penetration for flaw detection or measurement is superior to other
  NDT methods.
- It is sensitive to both surface and subsurface discontinuities.
- Only single-sided access is needed when the pulse-echo technique is used.
- It is highly accurate in determining reflector position and estimating size and
  shape.
- Minimal part preparation is required.
- It provides instantaneous results.
- Detailed images can be produced with automated systems.
- It is nonhazardous to operators or nearby personnel and does not affect the material being tested.
- It has other uses, such as thickness measurement, in addition to flaw detection.
- Its equipment can be highly portable or highly automated. The depth of penetration for flaw detection or measurement is superior to other

The disadvantages of this technique are:

Surface must be accessible to transmit ultrasound.

- Skill and training is more extensive than with some other methods.
- It normally requires a coupling medium to promote the transfer of sound energy
  into the test specimen.
- Materials that are rough, irregular in shape, very small, exceptionally thin or not
  homogeneous are difficult to inspect.
- Cast iron and other coarse grained materials are difficult to inspect due to low
  sound transmission and high signal noise.
- Linear defects oriented parallel to the sound beam may go undetected.

Reference standards are required for both equipment calibration and the characterization of flaws.

The propagation of the sound on a component is transmitted by means of elastic vibrations of the atoms and molecules of its constitution. The velocity of propagation depends on the mechanical properties of the crossed material.

The presence of imperfections or non-homogeneities on the component, lead to phenomena such as scattering, showed with the presence of spurious echoes, reverbs and, in general, attenuation of the sound wave.

The Non-Destructive controls with the ultrasonic method (UT) are based on these principles.

When a component is perturbed on a surface, the perturbation propagates in a certain finite time as a sound wave that origins from the vibration of the molecules and atoms which constitute the material.

As all the wave propagation phenomena, also for the sound waves it is possible to define a length wave λ, a period T and a frequency f, linked together by the following relations (figure 3.55):

$$f = \frac{1}{T}, \lambda = \frac{C}{f}, \lambda = c \cdot T \text{ (3-24)}$$

where c is the velocity of the sound of the material.

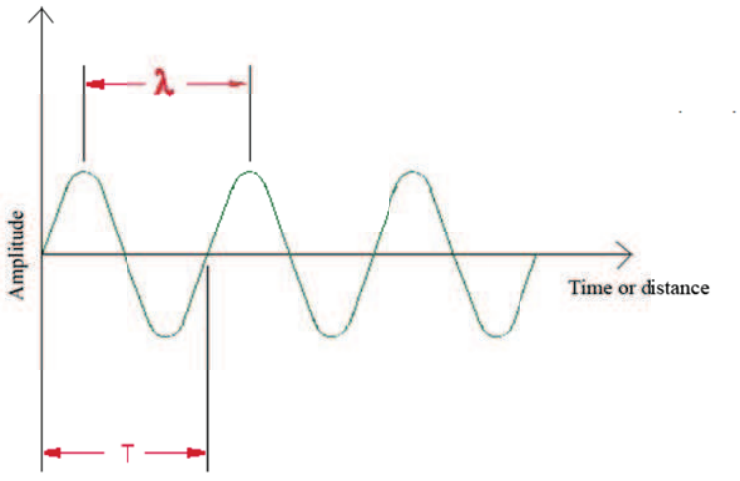

Figure 3.55 Parameters of the propagation of an ultrasonic wave [31]

Differencing from light waves, sound waves need an elastic material to propagate.

They not propagate under vacuum.

It is spoken about audible sounds when the frequency of those waves is on the range 20-20000 Hz, while it is spoken about ultrasounds when the frequency is major than 20 kHz.

The propagation of the acoustic waves (audible or ultrasonic waves) can be of different modalities (figure 3.56).

The longitudinal waves are present when the oscillation of the particles of the material is parallel to the direction of the propagation of the waves.

The transversal waves are those when the wave front moves orthogonally to the direction of the excited particles.

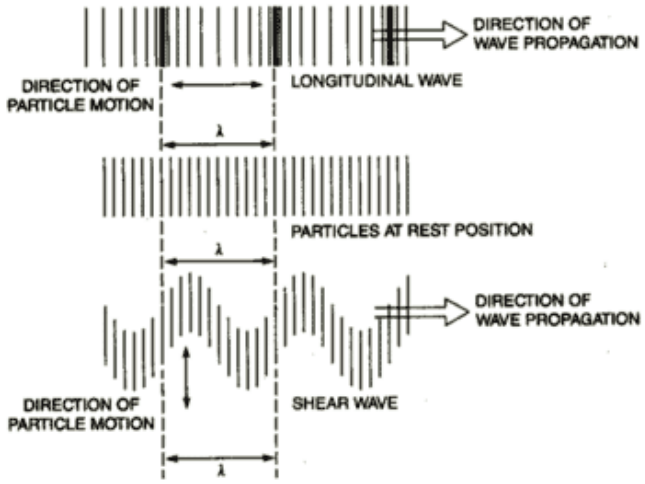

Figure 3.56 Different types of wave propagation: longitudinal waves (top) and transversal waves (bottom) [32]

The sound waves (independently on their frequency) propagate on a material under the influence of a locale pressure P defined "sonic pressure" that represent the overpressure that invest the atoms and molecules respect to the standard atmospheric pressure.

Since the atoms and molecules are linked together elastically, the overpressure propagate on the entire body and, if Q is the particle velocity of the particles, the acoustic stiffness Z of the mean can be defined as:

$$Z = \frac{P}{Q} = \frac{acoustic\ pressure}{particle\ velocity} \qquad (3-25)$$

The acoustic stiffness characterize the behavior of the sound on determined material and it is linked to the physical properties of the material:

$$Z = \rho \cdot V \quad (3\text{-}26)$$

where ρ is the density and V is the velocity of the propagation.

When an ultrasonic wave records a separation surface of two mediums with different material and acoustic stiffness, reflected and transmitted waves are generated (figure 3.57). The incidental wave (V_{L1}) and the reflected one ($V_{L1'}$) are inclined by the same angle α_1, in general different from α_2, the angle of the propagation of the transmitted wave. Angles α_1 and α_2 are expressed by Snell's law:

$$\frac{sen\ \theta_1}{sen\ \theta_2} = \frac{V_{L1}}{V_{L2}} \quad (3\text{-}27)$$

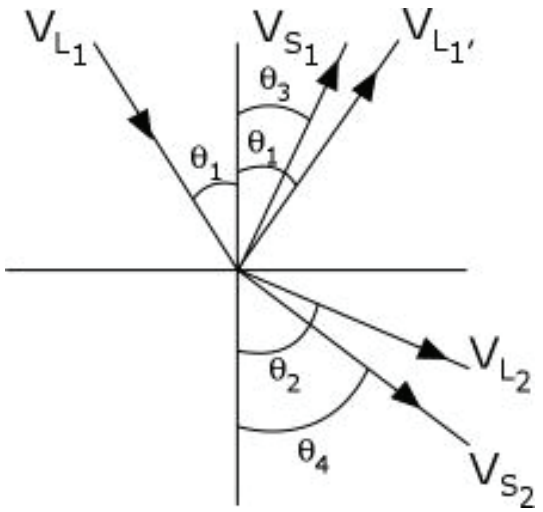

Figure 3.57 Transmission of longitudinal and transversal waves on two different mediums when a longitudinal wave hit the interface between medium I and II.[32]

When an ultrasonic wave (V_{L1}) hit the separation surface of two different mediums, a component of the longitudinal wave is converted to a reflected transversal wave on the medium 1 (V_{S1}) and a transmitted transversal wave on medium 2 (V_{S2}). Also the angles of the propagation of those waves θ_3, θ_4 are regulated by Snell's law, considering the velocities of propagation of the transversal waves on the material.

The ultrasonic control is based on the analyses of the variation of the

characteristics of the reflected and transmitted waves when the acoustic beam encounters a flaw. Poisson formulated the relation that governs the reflection of an ultrasonic wave of two mediums of different acoustic stiffness Z1 and Z2 [31]:

$$R = \frac{Z_2 - Z_1}{Z_2 + Z_1} \qquad (3-28)$$

On the same way the relation concerning the transmission coefficient:

$$T = \frac{4 \cdot Z_2}{(Z_2 + Z_1)^2} \qquad (3-29)$$

Medium	**Velocity** $\left[\frac{m}{s}\right]$	**Density** $\left[\frac{kg}{m^3}\right]$	**Acoustic Impendance Z** $\left[\frac{kg}{m^2 \cdot s}\right]$
Iron	5900	7860	4.64e7
Aluminum	6320	2700	1.7e7
Copper	4700	8920	4.2e7
Gold	3200	19300	6.2e7
Rubber	1800	1200	2.16e6
Plexiglas	2700	1190	3.2e6
Air	330	1.2	396

Table 3.4 Velocity of longitudinal waves, density and acoustic impedance of some common materials

Table 3.4 reports the velocity of propagation of longitudinal acoustic waves, density and impedance of some common materials. It is interesting to observe that the acoustic impendence is very low on gasses (about four order minor than solids), resulting on very high reflection coefficients on the separation surface between the gas and the solid. In other words, the acoustic sounds are not capable to propagate on the air after they passed a solid material. In order to execute efficiently the control, it is necessary to interpose an opportune layer of a solid, liquid or viscous substance (called “couplant”) in order to execute efficiently the control.

The ultrasonic beam, generated by a transducer, as explained later, is divergent, thus involving a progressive reduction of its energy and an increase of the dimensions of the illuminated zone. Moreover, during the propagation on the

material, the ultrasonic waves endure to attenuation, caused by absorption and scattering dissipating phenomena.

In general, the reduction of intensity for a certain length x on a certain material can be expressed by the following relation [31]:

$$I_x = I_0 \cdot e^{-\mu x} \qquad (3-30)$$

The coefficient of absorption μ can be expressed ideally on the sum of two contributions.

$$\mu = \mu_\tau + \mu_s \qquad (3-31)$$

μ_τ is linked to the "real" absorption and it is function of the frequency of the incident wave and result of the energetic dissipation of the molecular friction. μ_s is derived from scattering, and it is function of the dimension of the particles that compose the crossed medium.

The ultrasonic waves are produced exploiting the piezoelectricity, generating an initial deformation of the transducer. In fact applying a difference of potential on the crystal of the transducer, the material expands or contracts. On the other way a deformation of the crystal, generate a difference of potential.

Figure 3.58 General structure of an ultrasonic transducer [32]

This phenomenon allows the transducers to be used as emitter and receiver.

Generally, an ultrasonic transducer is composed by (figure 3.58):

- An oscillating disc (sensible element that generates and receives the ultrasonic impulse).
- A protective layer, to avoid accidental damages and contamination with solids or liquids.

- A damping block
- An external rigid metallic case.
- Electrical connections to the system of acquisition and control

The intensity of the ultrasonic waves of the beam generated by a traditional transducer is not constant, but varies with the dimension of the source that causes phenomena of diffraction (figure 3.59).

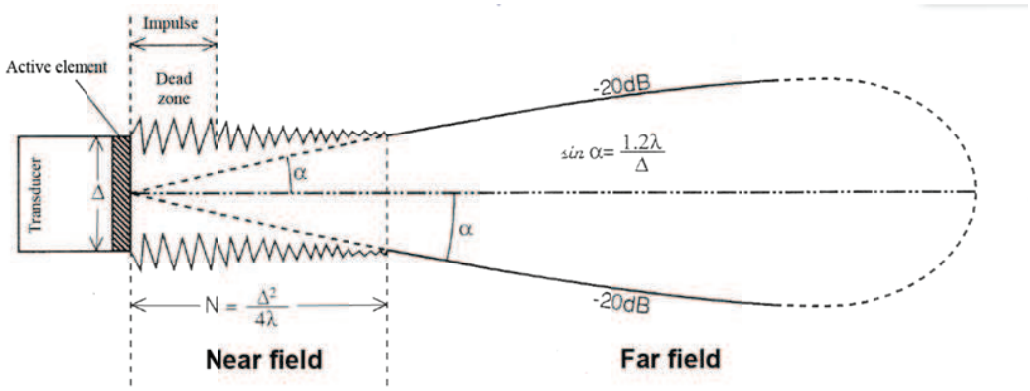

Figure 3.59 Propagation of the ultrasonic inside a medium [31]

In the proximal zone, the intensity fluctuates between a minimum and a maximum value. In this zone, the distance correspondent to the duration of the impulse is defined “dead zone”.

The higher the frequency of the transducer, the lengthier of the proximal zone, on the same material.

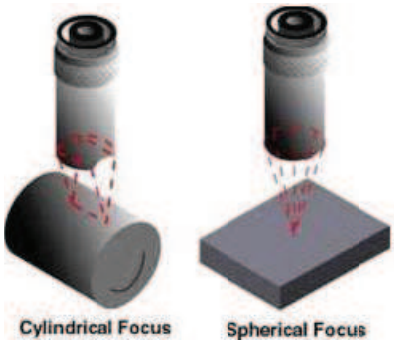

Figure 3.60 Different types of focalization: cylindrical (left) and punctual (right) [32]

After, the beam tends to a major stability, and the beam diverges.

For what concerning the focalized transducers, the acoustic beams are directed by means of opportune systems of “acoustic lenses” or modeling the surface of the

radiating element in a such way that the emission is concentrated on a virtual line (cylindrical focalization) or on a point (spherical focalization) (figure 3.60).
The focalized transducers are essentially used on controls under immersion and allow high levels of resolution, that are requested on automatic scans of specimens even with lots of geometric complexities.

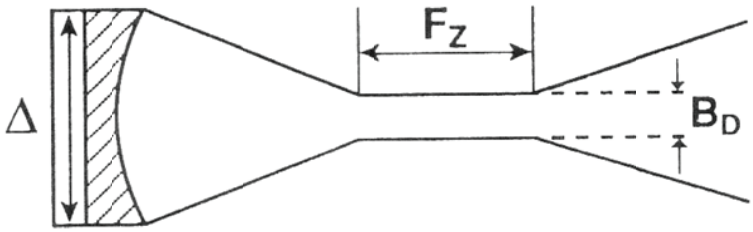

Figure 3.61 Schematic view of the main parameters for focalized transducers [31]

The focalized transducers are distinguished by means of the following parameters (figure 3.61):

- The focalized diameter BD at -6 dB (reduction of the amplitude of the signal of 50 %).
- The length of the focal zone Fz, that expresses the dimension of the spatial zone within the beam maintains a constant section of diameter BD.

Figure 3.62 General operating conditions of a contact tranducer (left) and different types of contact transducers (right) [31]

Contact Transducers (figure 3.62) are made of a single crystal emitting longitudinal waves, designed for the direct contact with the with the test workpiece. Typical applications are the detection of defects and cracks, measures

of thickness, inspections of plates, billets, etc.

They differentiate by the diameter of the crystal and the frequency of the generated impulse.

The angled transducers (figure 3.63) are constituted by a single crystal oriented in order to produce longitudinal ultrasonic waves or shear waves for oblique inspections. This kind of transducers are used for the detection of defects non parallel to the surface of the workpiece. Typical applications are the detection of defects and cracks and the inspection of plates, billets, etc. or workpiece for structural verifications or weld joints verification.

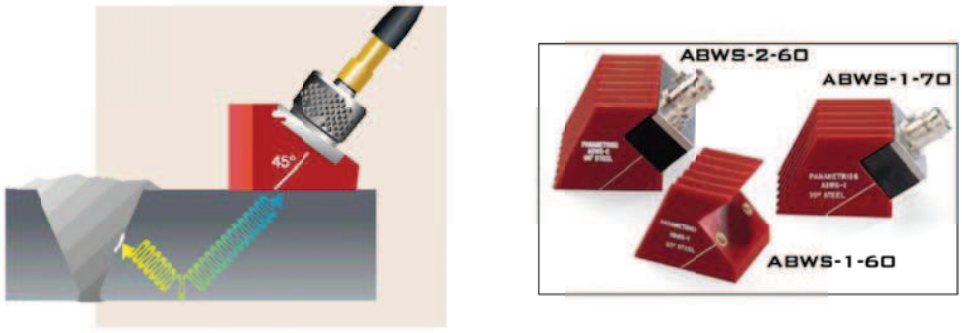

Figure 3.63 Typical operation condition (welding inspection) with an angled transducer (left) and different types of angled transducers (right). [31]

They differentiate by the dimension of the crystal, the frequency and the angle of emission of the waves. The angle is always referred to the propagation of the ultrasonic waves on steel. The angle is between the direction of propagation of the longitudinal wave and the normal to the surface where the transducer is positioned. The most used refraction angles for fixed angle transducers are 45°, 60° and 70° and generally marked on the transducer itself.

The inclination of the sound waves on different materials from steel can be calculated by means Snell's law.

Other types of contact transducers are available on a variety of configurations to improve their usefulness for a variety of applications. If near surface resolution is important, one of the special contact transducer listed below might be used.

Dual element transducers (figure 3.64) contain two independently operated elements in a single housing. One of the elements transmit, the other receives the ultrasonic signal. Dual element transducers are especially well suited for making

measurements in application where reflectors are very near the transducer since the design eliminates the ring down effect that single-element transducer experience (when single-element transducers are operating in pulse echo mode, the element cannot start receiving reflected signals until the element has stopped ringing from its transmit function).

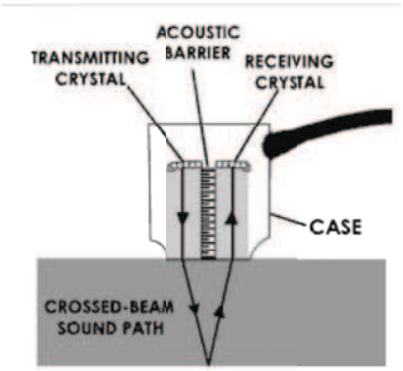

Figure 3.64 Operational principle of a dual element pulse-receiver transducer [32]

Delay line transducers (figure 3.65) provide versatility with a variety of replaceable options. Removable delay line, surface conforming membrane and protective wear cap options can make a single transducer effective for a wide range of applications. As the name implies, the primary function of a delay line transducer is to introduce a time delay between the generation of sound wave and the arrival of any reflected waves. This allows the transducer to complete it "sending" function before it starts the "receiving" function so that near surface resolution is improved. They are designed for use in applications such as high precision thickness gauging of thin materials and delamination checks in composite materials.

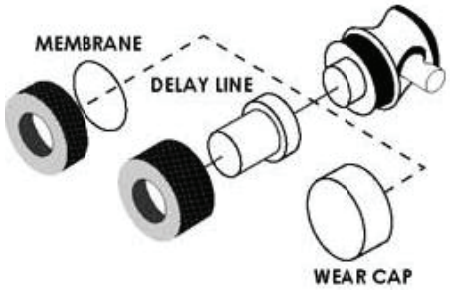

Figure 3.65 Schematic view of a delay line transducer [32]

Paint brush transducers (also called phased array transducers) are used to scan wide areas. These long and narrow transducers are made up of an array of small crystals and that make possible to scan a larger area more rapidly for discontinuities.

The selection of the optimal transducer depends above all from the characteristics of the material to be tested and, in particular, from the capability of attenuation of the ultrasonic beam. In general, high frequency ultrasonic waves guarantee better resolutions, while low frequency waves are capable to pass higher thicknesses or allow the inspection on materials with high attenuation, like rubbers, plastics, etc.

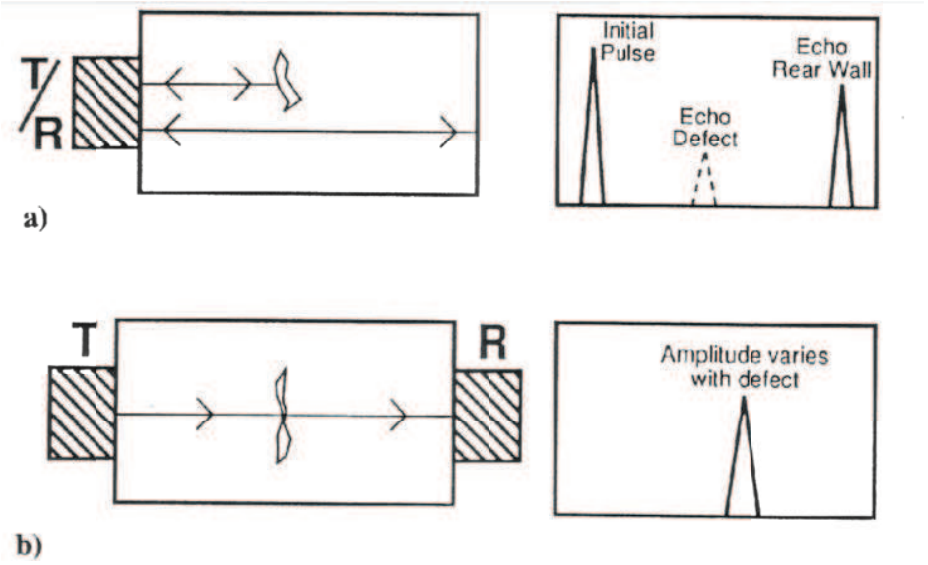

Figure 3.66 Schematic view of the pulse/echo and through transmission techniques [31]

The ultrasonic controls subdivide into two main groups:

- "Pulse-echo" techniques (P/E): the ultrasonic waves invest the workpiece to be tested, penetrate, are reflected and refracted from the surfaces that delimitates the component itself. The internal reflections (echoes) are examined and give information on the presence of flaws on the workpiece. The scheme a) of figure 3.66 sketches a P/E control by means a single transducer with both function of pulser and receiver. The sound wave is emitted by the transducer, passes the material and is reflected by the opposite surface and by a flaw on the material. The ultrasonic signal shows three different peaks that can be detected easily.

- "Through-transmission" technique (T/R): the ultrasonic wave that pass the component is examined, without taking into account reflected echoes. The scheme b) of figure 3.66 shows a typical example of a T/R control with two different transducers: one is emitter of ultrasonic waves, the other is positioned on the opposite surface and collects the waves after they pass the component and eventually some are reflected by the discontinuities on the component.

Figure 3.67 describes a scheme of the set-up for the P/E technique. The T/R technique will not be described, but it is similar, with the difference that there is another transducer that receives the ultrasonic waves.

The transducer emits ultrasonic waves as impulses that are reflected from the opposite surface of the component or by internal flaws. The reflected waves are collected by the same transducer. The impulses are transmitted at regular times (more comprehensive) and the time necessary for the waves to cover the distance between two opposite surfaces is displayed on a oscilloscope. The presence of a defect origins a signal displayed on the time scale of the oscilloscope before the echo of the opposite surface. The amplitude of the reflected waves which allow to characterize the dimension of the discontinuities depends on three parameters:

- The characteristics of the reflector (defect);
- The characteristics of the ultrasonic beam;
- The characteristics of the surfaces of the component to be inspected.

The characteristics of the reflector are:

- conformation (geometry of the boundaries);
- orientation (reflectors that are orthogonal to the beam are visible, reflectors parallel to the beam are practically invisible);
- roughness (the higher the roughness, the higher prevalence of scattering);
- area of the defect.

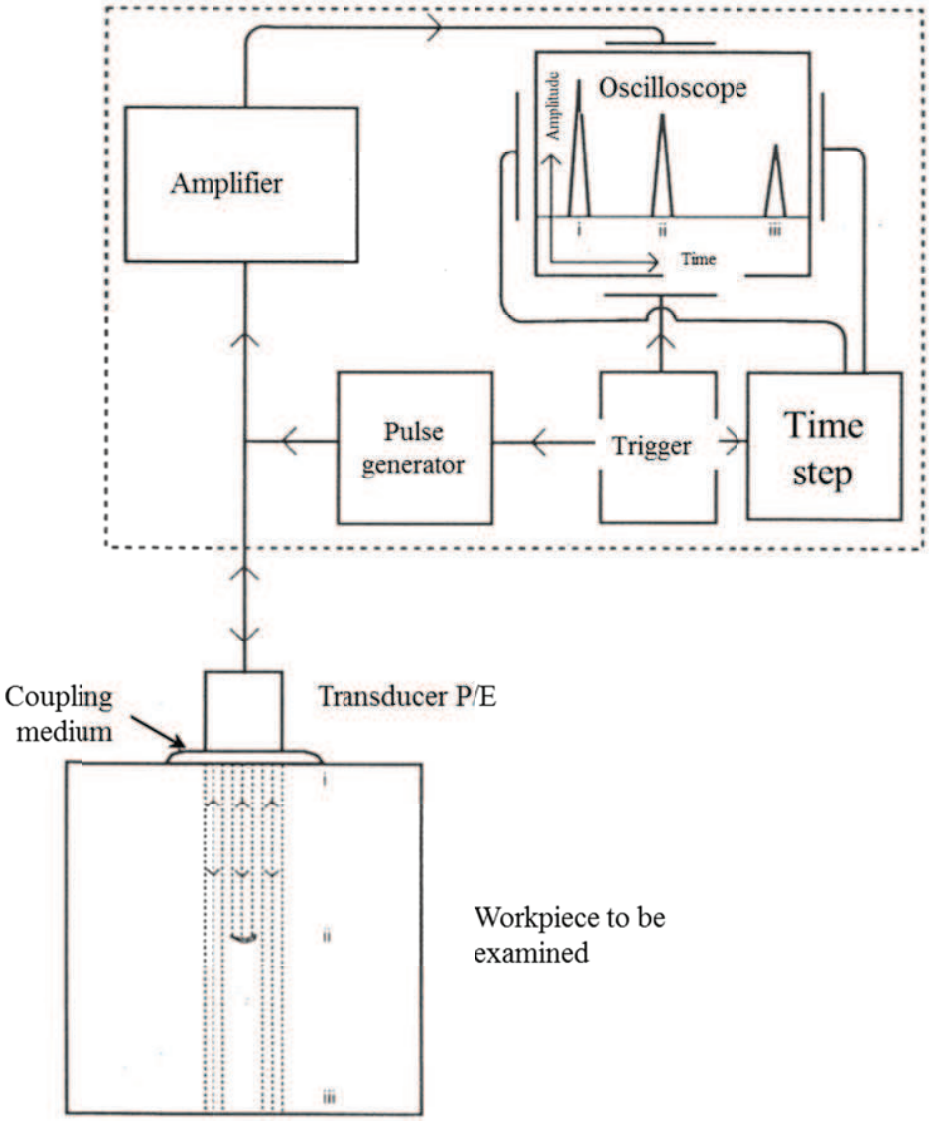

Figure 3.67 General scheme of the measure system for a P/E setup [31]

The characteristics of the ultrasonic beam influence the amplitude of the reflected echo with the distance between the reflecting area and the transducer. Different behaviors are registered with different position of the reflector if it is inside the proximal or the far zone. For what concerning focalized transducers, the response varies if the reflector is on the focalized zone or not.

Dealing with the characteristics of the component, roughness can influence the transmission of the beam at the transducer/material interface; the other important factor is the attenuation of the material.

As anticipated before, when the beam encounters a flaw, a signal is displayed on the oscilloscope before the signal relative the opposite surface of the component.
In other words, the flaw represents an obstacle to the propagation of the ultrasonic waves inside the component. Such disturb, physically, results the variation of the acoustic properties of the materials that are invested by the ultrasonic beam.
Two different cases can be distinguished from different beam dimension to dimension of the flaw ratios.

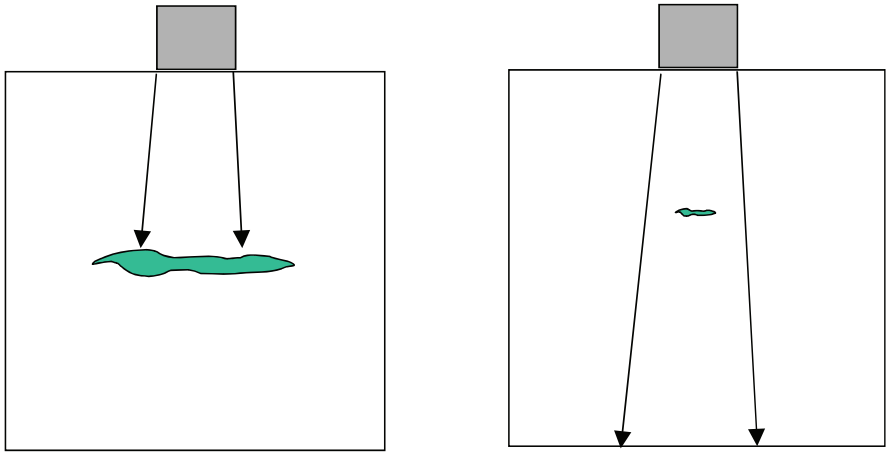

Figure 3.68 Two different types of flaws: a big reflector on left and small reflector on right.[31]

A "big reflector" (figure 3.68, left side) is defined when the dimensions of the flaws are bigger than those of the beam. The propagation of the beam is prevented by the presence of the discontinuity. The signal on the display of the oscilloscope shows the peaks relative to the emission of the ultrasonic beam and the discontinuity only. There can be no significant variation of the signal, depending on the ratio of the dimension of the beam and the flaw.
Considering an emitter of longitudinal waves, the amplitude of the reflected echoes depends on the position of the reflector. If the reflector is on the proximal zone, the amplitude corresponds to that of the echo of the incident beam. If the reflector is on the far zone, the amplitude decreases linearly with its distance.
For focalized transducers, the beam is totally reflected, because its small dimensions.
The dimensions of "big reflectors" are determined with the "contour technique":

1) The transducer is placed at the center of the discontinuity and the gain is regulated in a way that the signal amplitude is 80% of the total height of the screen.
2) The transducer is moved firstly along one axis and secondly on an orthogonal axis to determine 4 points where the amplitude of the echo is halved (-6 dB).
3) Measuring the distances between the four points the dimensions of the reflector are determined.

When the dimensions of the flaws are smaller than the transducer, the discontinuities are called "small reflectors" (figure 3.68, right side). Only a small portion of the incident beam is reflected. The remaining part of the beam is reflected from the bottom surface of the component. The signal on the monitor of the oscilloscope presents one peak at time proportional the depth of the flaw between the echoes relative to the emission of the beam and the opposite surface.

The evaluation of the dimension of the small reflectors is based on the comparison with reference signals coming from well-known reflectors. Distance-Amplitude curves (DAC – Distance Amplitude Correction) or AVG curves are used for the estimation of the equivalent diameter of the defects. The equivalent diameter is intended as the diameter of a circular reflector at the same depth that reflects the same acoustic pressure to the transducer. The amplitude of the signal of the real and the equivalent reflectors is the same.

Considering an emitter of longitudinal waves, the amplitude of the reflected echo will be:

- Proportional to the area of the reflector (intended as the section normal to the beam) and independent on its distance, if the reflector is on the proximal zone;
- Proportional to the area of the reflector and it diminishes with the square of the distance transducer-reflector, because of the divergence of the beam.

Dealing the case of focalized transducers, the maximum amplitude of the reflected echo will be in correspondence of the focus of the probe; attenuation will occur far from the focus.

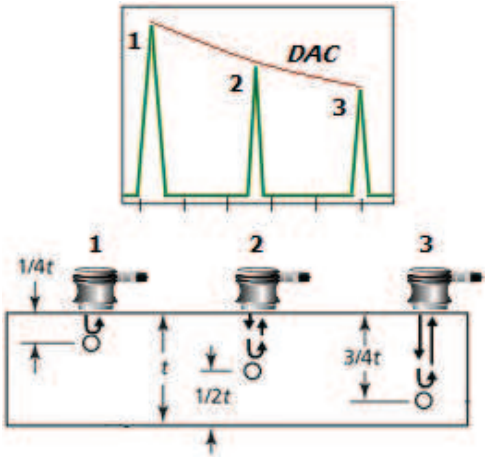

Figure 3.69 Example of calculation of a DAC curve by means of a block with side drilled holes at different depths

DAC curves (figure 3.69) are constructed by means of calibrated blocks with flat holes of certain diameter at the bottom or localized defects on the component. The transducer is positioned on the shortest block and the amplitude of the signal is regulated at 80% of the height of the screen; then the transducer is positioned on the other blocks registering the amplitudes of each reflection.

Once explained how to detect and estimate the dimension of the different types of flaws, let conclude this paragraph with some words on the ultrasonic inspection under immersion condition and the different techniques to present the signal of the response of the ultrasonic beam when encounters a flaw or for example the opposite surface.

A fundamental problem of the ultrasonic inspections is the assurance of the quality of the coupling between the transducer and the component: in fact the emission and the reflection energy flux are transmitted through the coupling.

With the immersion inspection the problem is solved: the component and the transducer are immersed on water or other appropriate liquid. The ultrasonic beam is initially transmitted through water on a certain path; after it reaches the liquid-component interface and the path on the component begins.

Such technique can be very advantageous:

- The coupling between the probe and the component is uniform, involving uniformities on the sensitivity and stability of the signal.

- Component with many complexities can be inspected.
- Automatic processes can be performed.
- The possibility to use focused probes increase the resolution and the sensitivity of the system.

Figure 3.70 exhibits an example of a simple system for the immersion inspections. A bathtub can be equipped with guides to allow the movement of a crane on the plane (X and Y axis). The crane is provided with a slide where a manipulator moves vertically the transducer (Z axis). On a immersion inspection the movements are function of the type of inspection: for example a round rod will be tilted on her axis while the transducer advances.

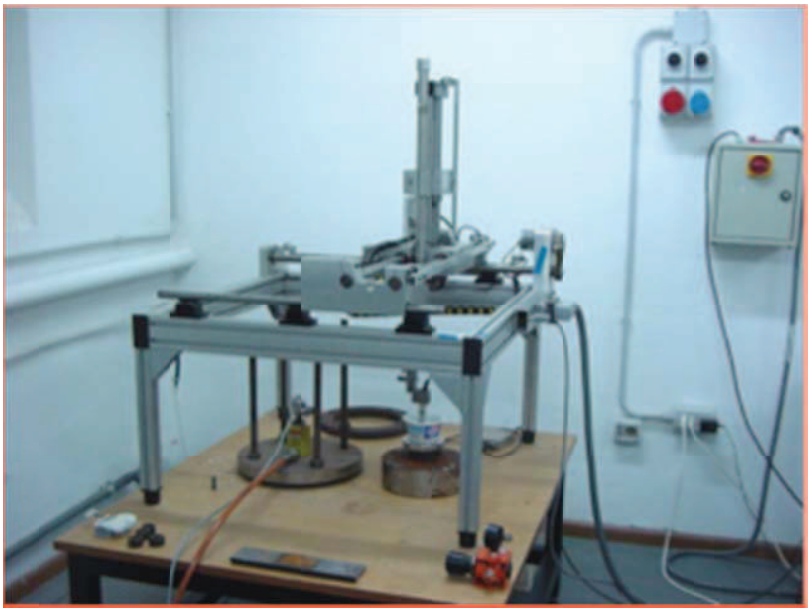

3.70 Example of an automatized system for the ultrasonic control under immersion [31]

When the components reach considerable dimensions and the immersion on a bathtub is impossible, the coupling with a water jet or by means of squirter is used. (figure 3.71).

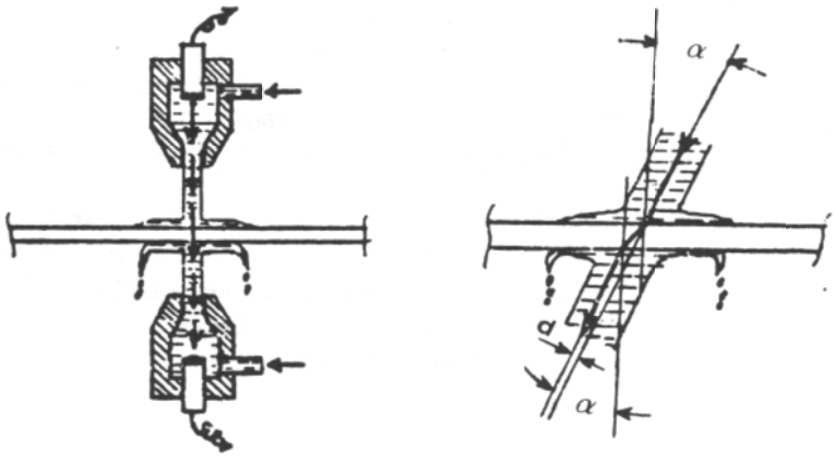

3.71 Example of an ultrasonic inspection by means of some squirters [31]

Figure 3.72 shows an example of a simple control of a specimen under immersion condition.

For what concerning the signals, the oscilloscope displays a first peak of the emission of the transducer, and a peak of minor amplitude that is the reflection of the liquid-solid interface.

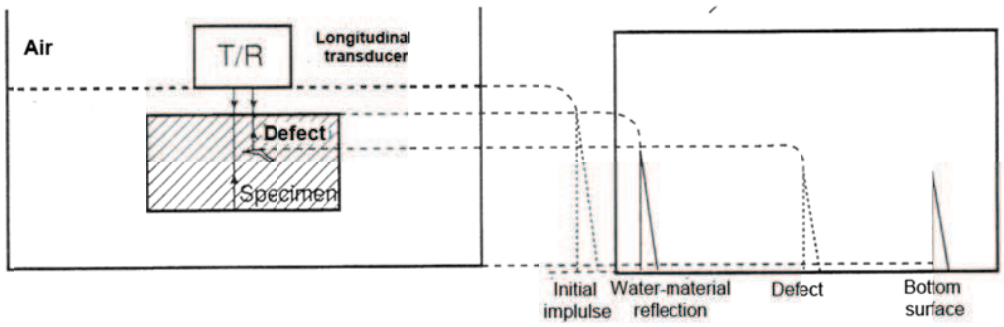

Figure 3.72 Example of control of a specimen under immersion [31]

The beam is partially transmitted inside the component and propagates to the opposite surface, eventually encountering a flaw. Figure 3.72 shows the case of a "small reflector". The reflection evidences a third peak that appears when the ultrasonic beam engraves the flaw, while the last echo is caused by the reflection of the opposite surface.

Despite of the inspection by means of contact transducers, phenomena of attenuation of the water and multiple reflections at multiple water-material

interfaces must be considered.

Before starting the immersion control, the path of the ultrasonic waves from the transducer to the water-material interface must be greater than inside the workpiece.

If such a condition is not satisfied, the echo of the interface can interpose between the peaks of the water-material interface and the opposite surface (zone of potential presence of defects).

When inspecting the component with focuses lens, it is necessary to consider that the beam propagates on two mediums with different acoustic impendence, influencing the focal length (figure 3.73):

$$W_p + \left(\frac{V_M}{V_A}\right) \cdot M_d = f \qquad (3-32)$$

From (3-1) the position of the focal point on the material can be calculated.

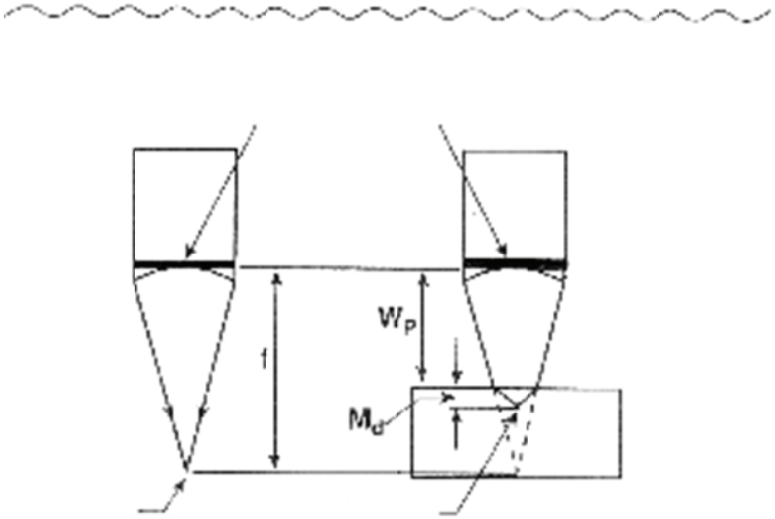

Figure 3.73 Different propagation on water and inside another material of the ultrasonic beam from a focalized transducer [31]

Up to now, it was written that the presence of a flaw results on a peak of reflection on the display of an oscilloscope. Such representation is called A-scan. It is typically used for manual inspections and it is the most diffuse way to present the ultrasonic signal. The transducer inspects punctual zones only and the amplitude of the signal is showed as function of time. At each position of the transducer

corresponds a inspected “column” of material (figure 3.74).

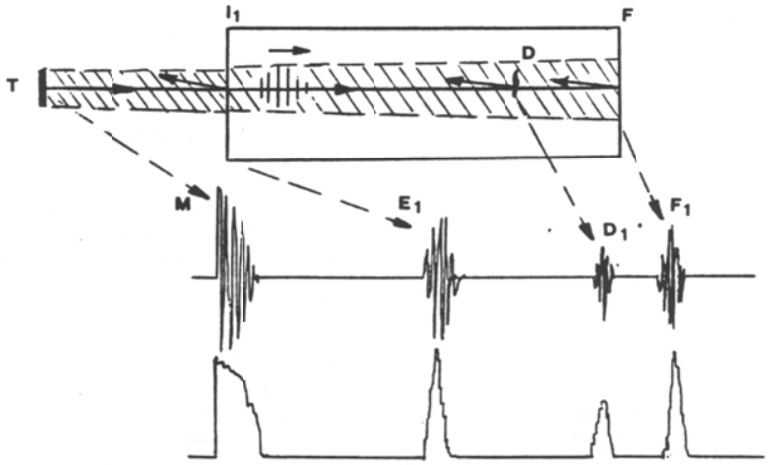

Figure 3.74 A-scan representation of the ultrasonic response [31]

If the transducer is moved on the x axis by an automated system and the revealed signal is coupled to the position of each monitored echo, the representation is called B-scan (figure 3.75).

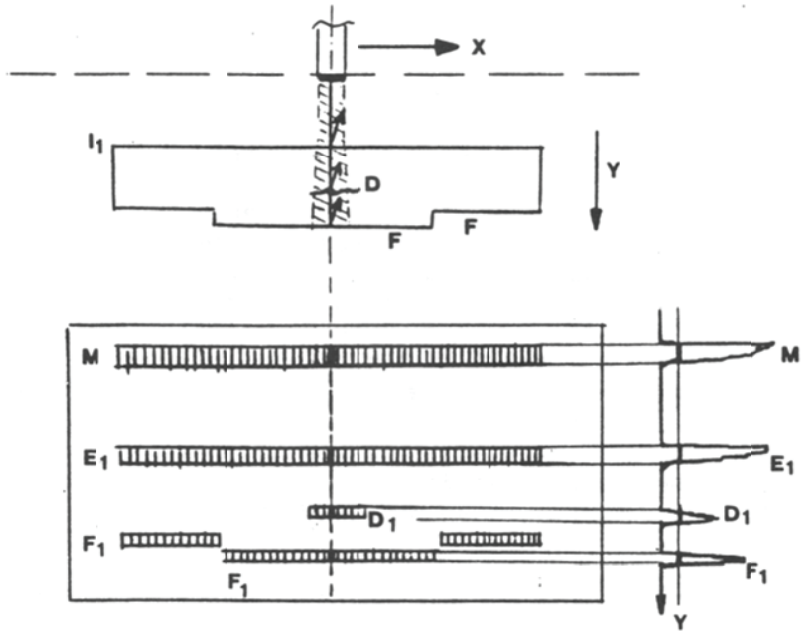

Figure 3.75 B-scan representation of the ultrasonic response [31]

If the transducer is moved on the XY plane by means of an automated system, and associating at each coordinate of the measured echo by the transducer a grey or color tonality, the representation is called C-scan (figure 3.76).

In this way it is possible to evaluate the real extension of the defect, but no information is given on the depth where the defect is located, as for A-scan representation.

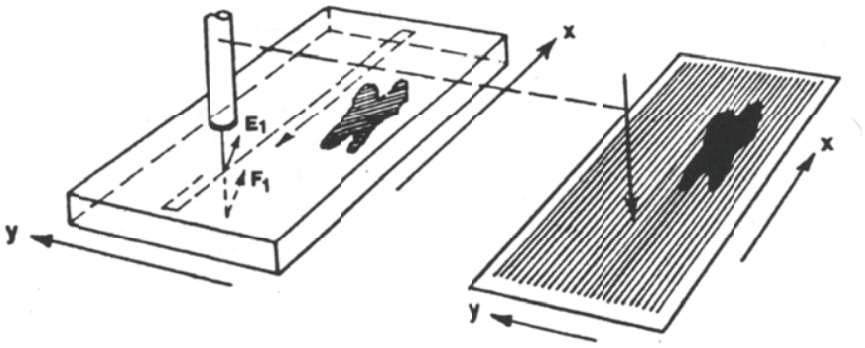

Figure 3.76 C-scan representation of the ultrasonic signal [31]

3.4.3 Ultrasonic inspection of the joints of the brazing test

Ultrasonic inspection has been conducted on the brazed joint of the two C shaped component of 400 mm length and the two blocks brazed vertically with the different geometry of the grooves for the brazing [12]. For each component, slices of 4 mm parallel to the brazing plane were cut by EDM in order to conduct better analyses, reducing attenuation and scattering induced by the material. The ultrasonic scan under water immersion technique was used, in order to reach more detailed information than the traditional contact technique. As reported on the above paragraph relative the theory of ultrasound controls, ultrasonic scans with focalized transducers allow better resolution.

The first case analyzed was relative to the brazing of the two C components.

Two different techniques were used:

- the “pulse-echo” technique with a focalized transducer with a frequency of the pulse of 5 MHz.
- the “through transmission technique”: the pulse frequency of the transducer was 5 MHz and the diameter of 0.5”.

Figures 3.77 and 3.79 report the results of the C scans of the joint using the “pulse-echo” technique using the focalized transducer

Figures 3.78 and 3.80 report the results of the C scans of the joint using the through-transmission technique.

Figure 3.81 exhibits the scale of the amplitude of the ultrasonic signal. For the "echo-pulse" technique, 0 % means no reflection of the signal, while 100 % means total reflection of the signal.

Conversely, for the "through transmission" technique, 0% means that the signal does not pass on the back surface, while 100% means that the entire signal pass to the back surface.

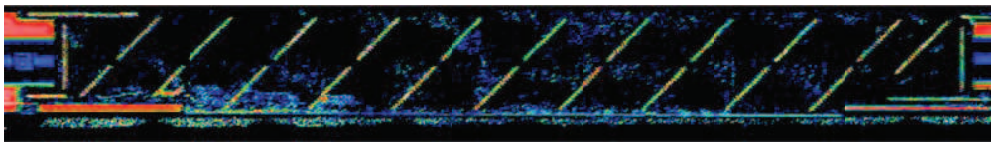

Figure 3.77 C-scan of the joint with inclined grooves of the ultrasonic inspection with the focalized transducer and pulse/echo techinque

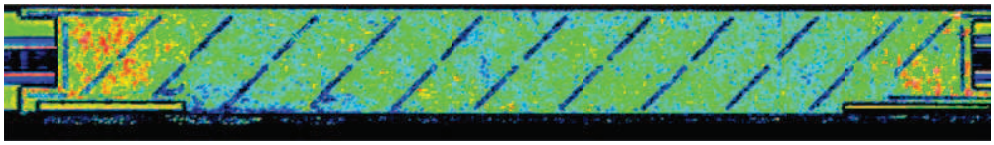

Figure 3.78 C-scan of the joint with inclined grooves of the ultrasonic inspection with through transmission technique

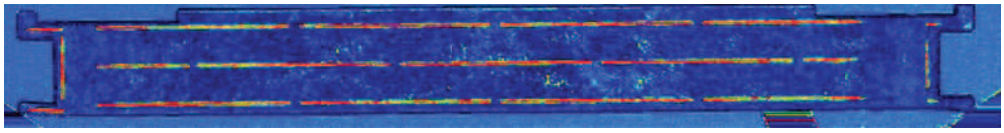

Figure 3.79 C-scan of the joint with vertical interrupted grooves of the ultrasonic inspection with the focalized transducer

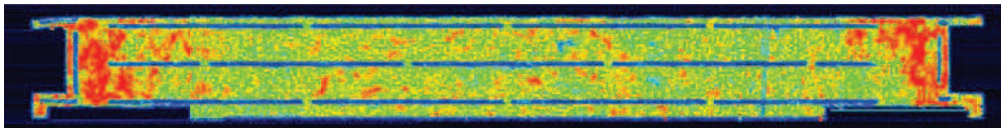

Figure 3.80 C-scan of the joint with with vertical interrupted grooves of the ultrasonic inspection with the focalized transducer

Figure 3.81 Scale of the intenstity of the signal for the C-scan repesentation of the ultrasonic inspection of the C 400 mm lenght copper joint

Both types of inspection demonstrated that the brazing grooves are almost empty. In fact for both cases, the inclined grooves and the vertical interrupted grooves, the peaks of the reflection in correspondence of the groove are very intense and the ultrasonic beam cannot pass to the back surface. For what concerning the "pulse-echo" inspection, the brazed surfaces show very low echoes uniform distributed. Thus the deduction of a good brazing for both surfaces.

The "though transmission inspection" confirm the good brazing of the surfaces. More information can be deducted on the homogeneity of the brazing. The extremities of the component, especially for the case of the vertical interrupted grooves, result in major transparency to the ultrasonic beam and suggest a better quality of the coupling.

For what concerning the interrupted vertical grooves, the grooves are not empty at all (right zone of figure 3.79 and 3.80), according to the figure 3.15. This fact can be attributed to an accumulation at the bottom zones of the brazing joint due to gravitational effects.

The second case analyzed was relative the brazing of the two copper blocks.

Figures 3.82 and 3.83 report the results of the C-scan inspection with "pulse-echo" and "through transmission" techniques of the two slices of the two brazed copper blocks with straight brazing grooves, one brazed horizontal, vertical the other.

The pulse frequency was 6 MHz for both the "Pulse-echo" and "through transmission".

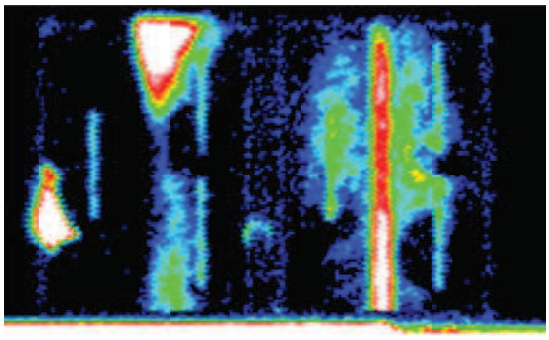

Figure 3.82 C-scan results of the inspection of the block brazed horizontally (left) and vertically (right) by "Pulse-echo" technique

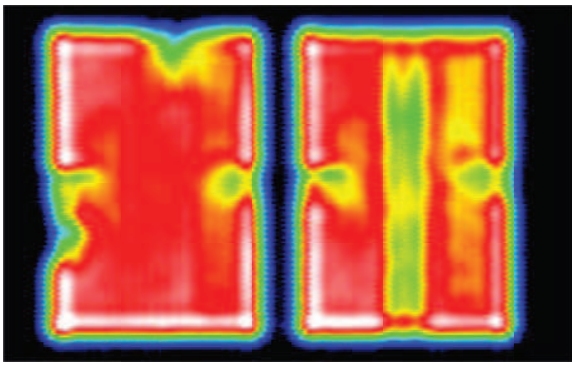

Figure 3.83 C-scan results of the inspection of the block brazed horizontally (left) and vertically (right) by "Through transmission" technique

The scale of the intensity of the signal is the same of figure 3.81. The brazing grooves are visible only by "pulse-echo" inspection at the brazing interface, thanks to a better resolution. The left block shows high peaks of reflection on the higher and left zones. The left block shows high peaks of reflection on the central zone.

The "through transmission" analysis shows some contradictions on the results for the block brazed horizontally, while for the one brazed vertically confirmed a poor mechanical coupling on the central zones. The brazing defects seem to be less extended for the left block, and the defect detected at the bottom with the "pulse-echo" technique is not displayed.

Figure 3.108 shows some attenuation in correspondence to the flanks of both blocks, those are due to the presence of the holes for the thermocouples.

Overlapping the C-scan image of the right block with its drafting, the brazing alloy wet the copper for an extension of 10 mm before flowing down vertically.

3.4.4 Conclusions

Although only optical inspections and vacuum testing evaluated the functionality of the brazing joint up to now, the ultrasonic inspection gave much more detailed information on the quality of the mechanical coupling and the distribution of the brazing alloy at the brazing interface. More information were acquired for the design of the brazing grooves on the definitive modules. For what concerning the brazing of the two C shape copper components, both the vertical and the inclined grooves demonstrated a good mechanical coupling. The inclined grooves seem to

demonstrate a much more uniform distribution of the brazing alloy, while the straight grooves seem to be more sensitive to gravitational effects (the grooves on the right of figures 3.79 and 3.80 are not totally empty as mentioned on the paragraph above).
As a result, the chose to adopt inclined grooves for the modules of the final production.

3.5 Conclusions

In this chapter good progresses has been demonstrated for the development of in-house brazings. Good skills has been developed for the design of the thermal brazing cycle by means of 1D and FE simulations. Lot of experience has been gained on the brazing technique with very good results on the copper-copper joint and copper-stainless steel joint. Good skills has been developed also on the quality control of the brazing, through the introduction of the optical inspection by lenses and the ultrasonic inspection.
What is important to underline is that thanks to the good quality of the copper-copper to test the vertical brazing and the copper-AISI 316LN brazing, an important step to the vertical on one single step has been completed. The next chapter will describe the results obtained on a small scale prototype of RFQ to test the one single step vertical brazing.

REFERENCES

[1] A. Pisent, A. Pepato, F. Scantamburlo et al., “RFQ Module Technological Prototype”, IFMIF DMS (Data Management System), 2011

[2] S. Mathot , “RFQ Brazing at CERN”, EPAC08, 2008, Genova (Italy), p. 1494

[3] S. Mathot et al., “Mechanical Design, Assembly and Brazing Procedures of the LINAC4 RFQ”, IPAC10 (International Particle Accelerator Conference), 2010, Kyoto (Japan), 807

[4] C. Rossi et al., “Progress in the fabrication for the RFQ accelerator for the CERN LINAC4”, LINAC10 (Linear Accelerator Conference), 2010, Tsukuba (Japan) , p. 497

[5] A.Pisent et al, “The TRASCO-SPES RFQ”, LINAC04 (Linear Accelerator Conference), 2004, Lübeck (Germany), p. 69

[6] Inspection engineering:
http://www.inspectionengineering.com/Zeiss_Accura.htm

[7] Promech Engineering: http://www.promech-eg.com/Cimcore

[8] D. Inkamp, K. Schepperle, “The application determines the sensor: VAST scanning probe systems”,
http://www.zeiss.fr/C12568E80026F83C/EmbedTitelIntern/Techno_VAST/$File/innovation_vast_line.pdf

[9] M. Dobosz, A. Wozniac, “CMM touch trigger probes testing using a reference axis”, Precision Engineering, Volume 29, Issue 3, July 2005, Pages 281–289

[10] Coord3 Metrology: http://www.coord3-cmm.com/passive-v-active-cmm-scanning-technique/

[11] TSQ (Total Quality System)
http://www.tqscorp.com/docs/zeiss/probing/ScanningBrochureDL.pdf

[12] F. Scantamburlo, A. Pepato, R. Dima, “PRODUCTION AND QUALITY CONTROL OF THE FIRST MODULES OF THE IFMIF-EVEDA RFA”, LINAC 12 (Linear Accelerator Conference), 9-14 September 2012, Tel Aviv, Israel, on proceeding

[13] P. Modanese, “Preparazione di un manuale di utilizzo di un forno ad alto vuoto per brasature e trattamenti termici”, Master Thesis on “Surface Treatment on Innovative mechanical technologies for the industry”, 2004.

[14] G.K. White and S.J. Collocott, J. Phys. Chem. Ref. Data, vol 13, no 4, p1251 (1984)

[15] G. Meneghetti, M. Manzolaro, A. Andrighetto, “Thermal–electric numerical simulation of a target for the production of radioactive ion beams”, Finite Elements in Analysis and Design, 47, 2011, pp. 559-570.

[16] C.Y. Ho, R.W. Powell and P.E. Liley, J. Phys. Chem. Ref. Data, v1, p279 (1972).

[17] T.A. Hahn, J. Applied Physics, v41, p5096 (1970).

[18] C.F. Lucks, C.F., Thompson, H.B., Smith, A.R., Curry, F.P., Deem, H.W. and Bing, G.F., USAF TR 6145, I, p1-127, 1951 [ATI 117 715]

[19] C.F. Lucks, J. Matolich, J.A. Van Valzor, USAF TR 6145, p1-71, 1954.

[20] SSINA (Speciality Steel Industry of North America): Washington DC http://www.ssina.com/composition/chemical.html

[21] B. M. Caruta, “New developments on material science research” (2007)

[22] B. M. Caruta, “New developments on material science research”, p. 114 (2007)

[23] B. M. Caruta, “New developments on material science research”, p. 110 (2007)

[24] Plansee-group, http://www.plansee.com

[25] Ansys Inc., Ansys® Contact Tecnology Guide

[26] Comsol Heat Transfer User Guide, pp. 95-96

[27] A. Dall’Occhio, A. Bertarelli et al., “LHC Collimators: un modello agli elementi finiti per l’analisi termostrutturale”, Associazione italiana per l’analisi delle sollecitazioni (AIAS), XXXVI Convegno Nazionale

[28] Electronic cooling magazine:
: http://www.electronics-cooling.com/1997/05/calculating-interface-resistance

[29] V.W. Antonetti, T.D. Whittle, and R.E. Simons, An Approximate Thermal Contact Conductance Correlation, HTD-Vol. 170,Experimental/Numerical Heat Transfer in Combustion and Phase Change, 1991, pp.35-42.

[30] R. Valdivez et al., “The thermal expansion of some common LINAC materials”, LINAC 2002 (Linear Accelerator Conference), 2002, Gyeongiu (Korea), pp 769

[31] Ing. Pau Massimiliano, university of Cagliary, Department of Mechanical Engineering: http://dimeca.unica.it/didattica/materie/pau/prove/ultrasuoni.pdf,
[32] NDT Technical Resource:
http://www.ndt-ed.org/EducationResources/CommunityCollege/Ultrasonics/

CHAPTER 4: ONE STEP VERTICAL BRAZING TEST

4.1 Introduction

Chapter 3 described the developments on the process of the vertical brazing. As anticipated on chapter 3, vertical brazing would allow to join all the components on a single step, thus reducing the number of the thermal cycle of annealing on the copper and save the mechanical properties of the material, in terms of minor dimension of the grains and better mechanical strength of the material.

Since not enough rough material was available to reproduce a full scale module, two small scale prototypes on the transversal dimensions respect to the final modules were constructed using a vertical single brazing step.

One brazing was performed at the LNL, while the other at an external company CINEL, who has in charge also the production of the last six modules of the accelerating line.

The test was thought to reproduce as close as possible the real condition of the brazing of the definitive modules to test the fixation tooling to keep in position the electrodes and the steel side flange and the steel ring.

This chapter will describe the assembly of the test, the design of the brazing thermal cycle and the results of the dimensional quality control of the brazing process.

4.2 Description of the components of the test

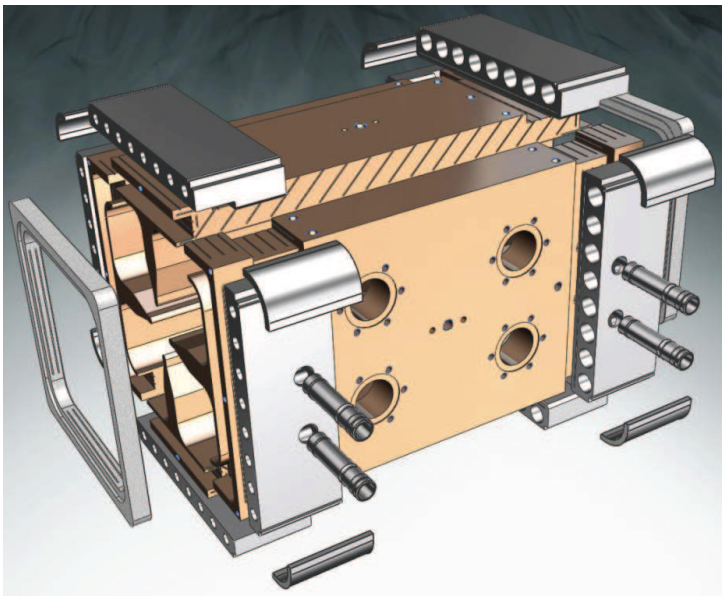

Figure 4.1 Exploded view of the small scale prototype RFQ for vertical one step brazing test

The small RFQ (figure 4.1) was composed by four copper electrodes; two “E” and two “T” form (figures 4.2 and 4.3). The longitudinal dimension is the same of the prototypes of the RFQ (400 mm) and the lateral dimension (about 230x230 mm) are half of those the final RFQ modules (430x430 mm).

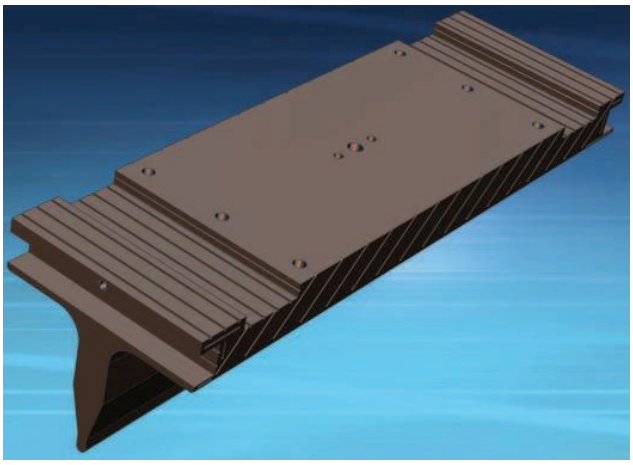

Figure 4.2 T-shaped copper electrode

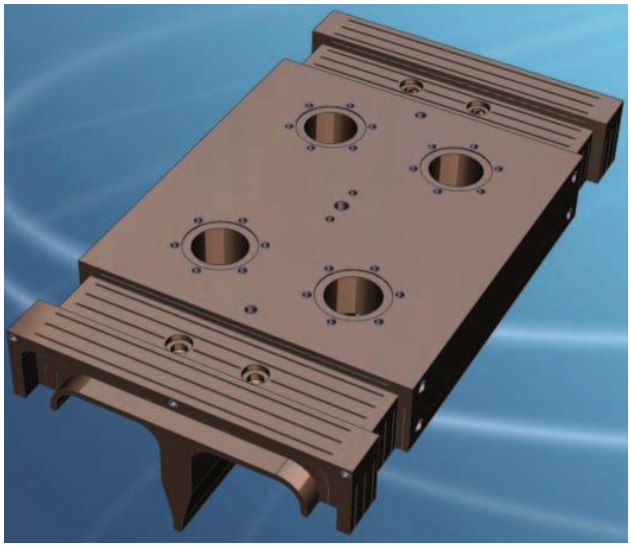

Figure 4.3 E-shaped copper electrode

The external surfaces exposed to the oven of the copper electrodes are finished by EDM cut. The brazing surfaces for the copper-copper and copper-steel are instead milled, because the EDM introduce porosities on the surfaces causing problems on the flow and the wetting of the brazing filler.

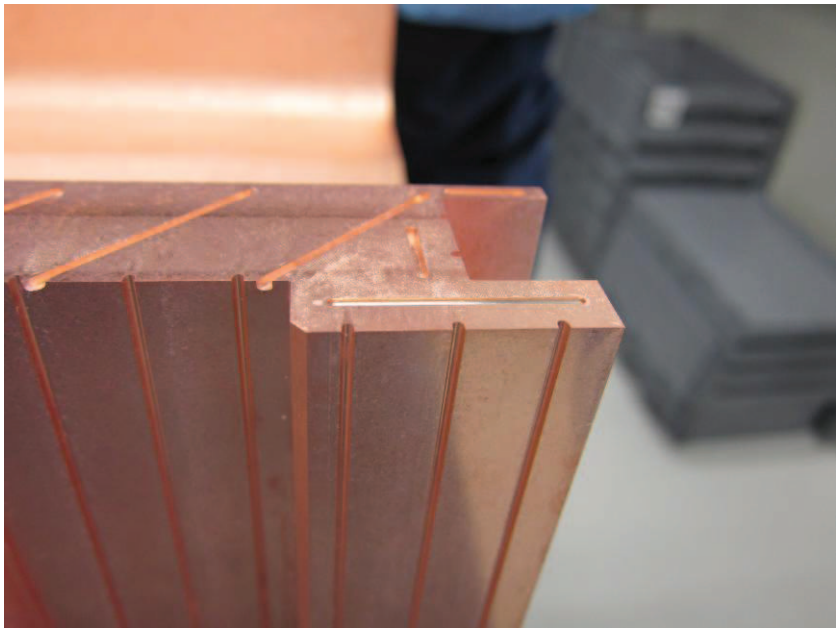

Figure 4.4 Detail of the brazing groove on the T shaped electrode

In order to reproduce similar details between this small RFQ and the final modules of the accelerator, it was equipped with all the stainless steel lateral flanges and frontal frames. In particular:

- A new solution for the lateral flanges was tried: a groove of 5 mm was machined in order to facilitate the coupling and the keeping in position the stainless steel flange to the copper during the brazing thermal cycle (avoid rotation of the flange) and to guarantee better function by the tightening of the bolts of the flanges to close the vacuum seal.
- It was consider to braze the steel frame to the copper on the bottom and on the internal side of the frame.
- A new design of the brazing grooves of the E to T electrodes joints was introduced: they were open to the extern in order to monitor the melting of the filler (figure 4.4). Moreover with such solution we thought to the possibility to insert on the grooves more brazing filler in case a repair of the joint was necessary.

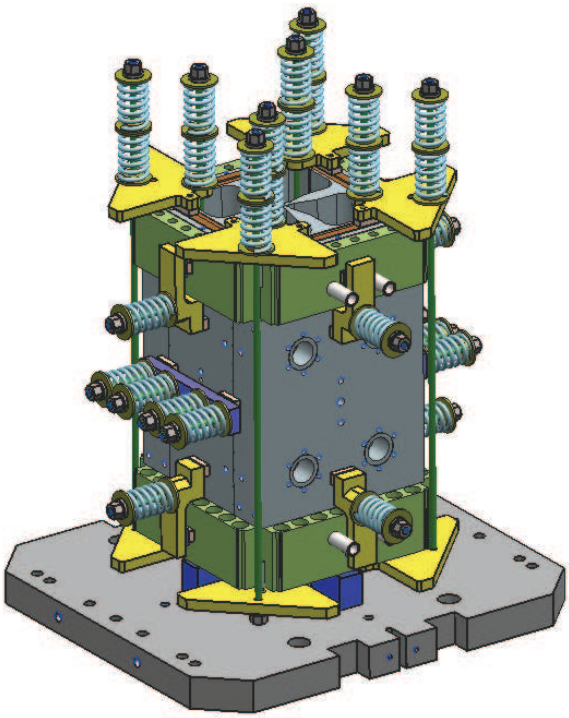

Figure 4.5 Isometric view of the brazing assembly

Figure 4.5 shows a isometric view of the brazing assembly with the tooling and the assembly positioned on the LNL vacuum furnace. Several tools made of AISI 316 LN were mounted on the prototype by means of Molybdenum TZM bars and

Nimonic 90 springs to keep in position the AISI 316 LN lateral flanges and frames. All the springs were pre-load with 200 N. Al_2O_3 ceramics were interposed to guarantee a certain thermal insulation between the tools and the copper and steel parts of the assembly.

This kind of tooling was very similar to the definitive solution adopted on the final modules in order to investigate the masking or conductive thermal effects and if the force of the springs was sufficient to keep in contact the steel frames and flanges to the copper the copper electrodes.

The assembly was supported on a 400x450x38 mm base made of AISI 316 LN by means of some AISI 316 LN supports and a layer of alumina to improve the thermal insulation between the base and the module. Figure 4.6 shows the view of the brazing assembly with the placement of the thermocouples inside the oven.

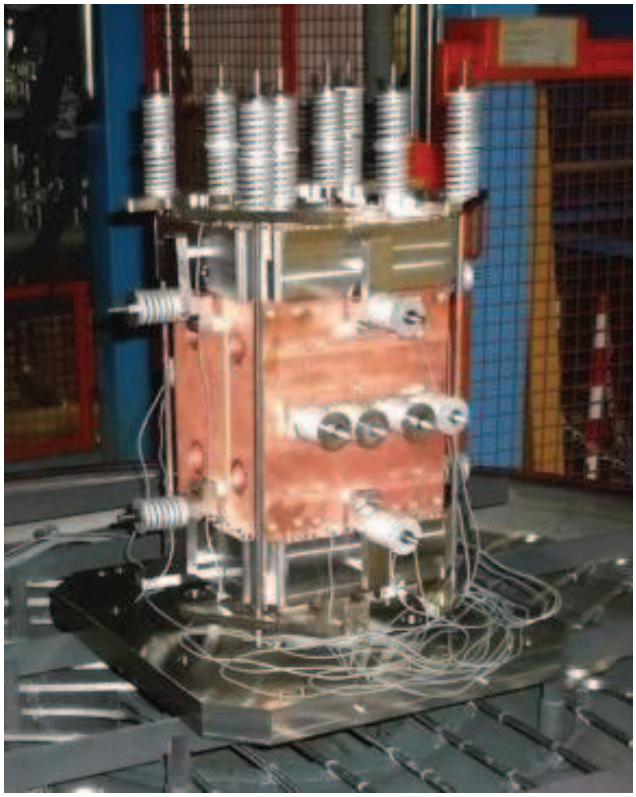

Figure 4.6 Assembly of the prototype on the LNL vacuum furnace

4.3 Definition of the brazing cycle

In this chapter it will be described the procedure for the determination of the brazing cycle of the miniprototype brazed at the LNL. The external company decided the brazing cycle for the other prototype.

As for the brazing tests described on chapter 3, a preliminary thermal brazing cycle was designed by means of 1D simulations and FE analyses, in order to evaluate the uniformity of the temperatures and avoid stresses on the components.

As for the tests described on chapter 3, the design of the thermal cycle was detailed in collaboration with the person in charge of the brazing lab at LNL. 1D simulation gives an idea of the trend temperature on the copper components. In fact, as demonstrated on chapter 3, the copper has a massive behavior and the temperature is quite uniform during the entire thermal cycle. However, since the assembly is very complex with many components of different materials, 3D FE simulations are mandatory.

The equation for the design of the thermal cycle by means of 1D analyses was the same (3-2). The material properties used for the 1D and 3D FE simulations were the same as reported on chapter 3.

Since, as demonstrated on chapter 3, the accordance with the experimental data of the 1D and the 3D FE analyses was good only at high temperatures (above 600 ˚C), the simulations were concentrated on the brazing step.

The equation (3-2) was used only to have an estimation of the heating time of the assembly. A reasonable heating ramp of 150 ˚C/hour up to 815˚C was considered in order to avoid excessive stresses on the assembly.

As follow the parameter used for the 1D simulation:

- $m = 90kg$
- $A = 0.32m^2$
- $\varepsilon = 0.07$

where m is the mass of the copper to be heated, A is the exposed area to the oven and ε is the emissivity of the copper.

As a first approximation, the calculation of the copper exposed area to the oven was done assuming the external surfaces of copper and the surfaces covered by the steel flanges. The value of the emissivity comes from best fit calculations on

the thermal cycle for the annealing of the copper elements made by the expert of LNL who have in charge the management of the oven, the annealing and brazing cycles.

Figure 4.7 plots the predicted thermal cycle and figure 4.8 shows the detail on the brazing step. The two lines at 824 ˚C and 852 ˚C represent the solidus and the liquidus temperatures of the Palcusil 10 brazing alloy.

Figure 4.9 shows a comparison between the brazing steps for the “miniprototype” and the experimental results on copper C400. The same temperature profile was reproduced.

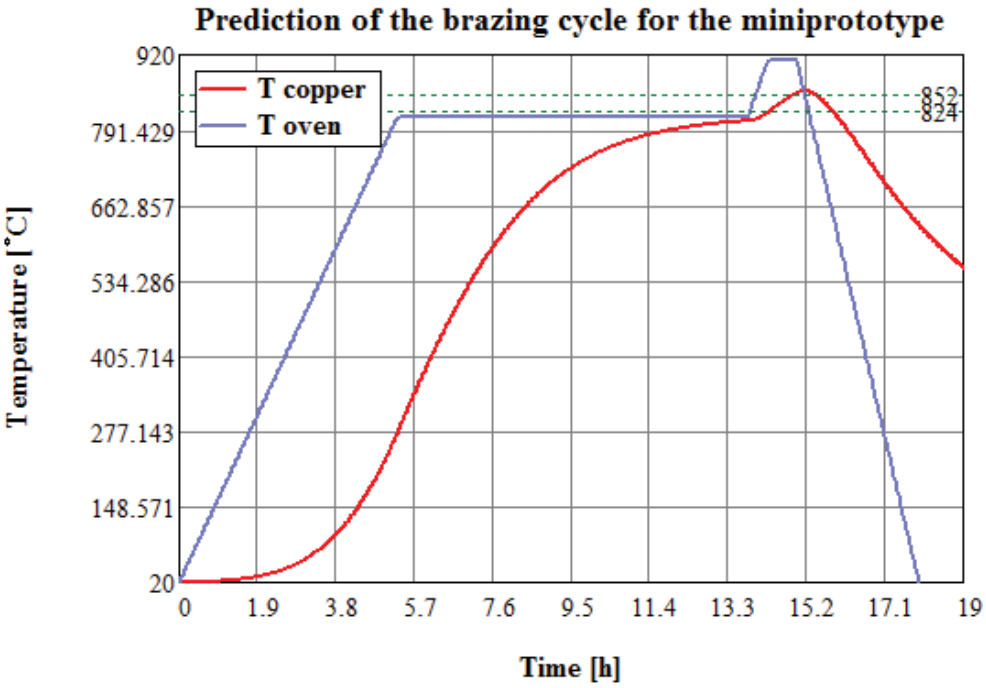

Figure 4.7 Thermal cycle prediction by means of 1D Mathcad simulations

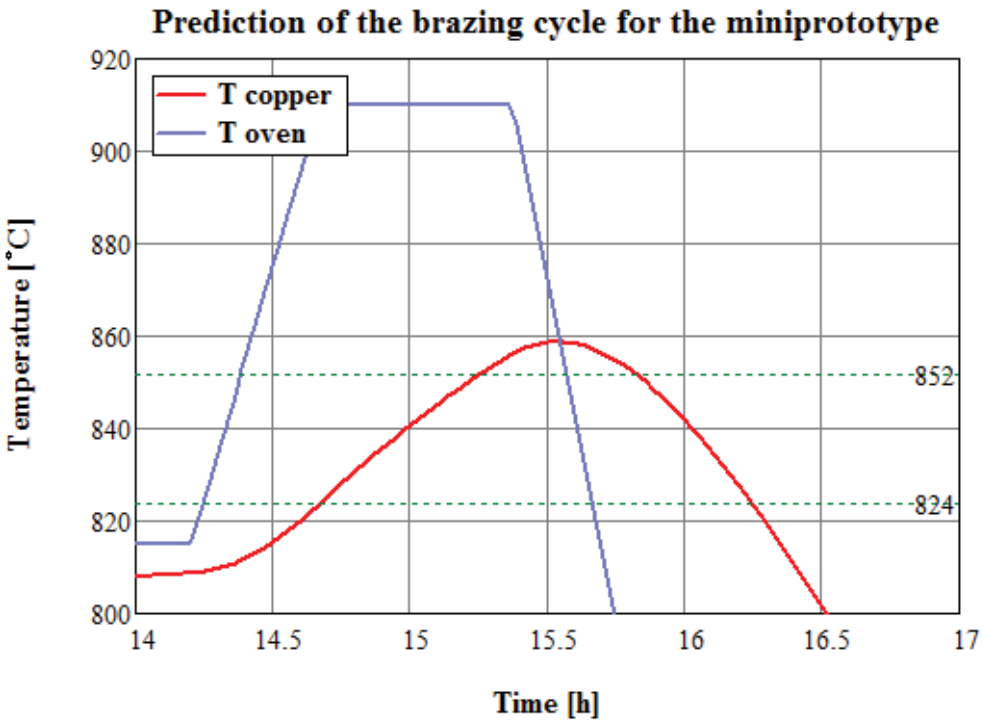

Figure 4.8 Detail of the calculated brazing thermal cycle at the brazing phase

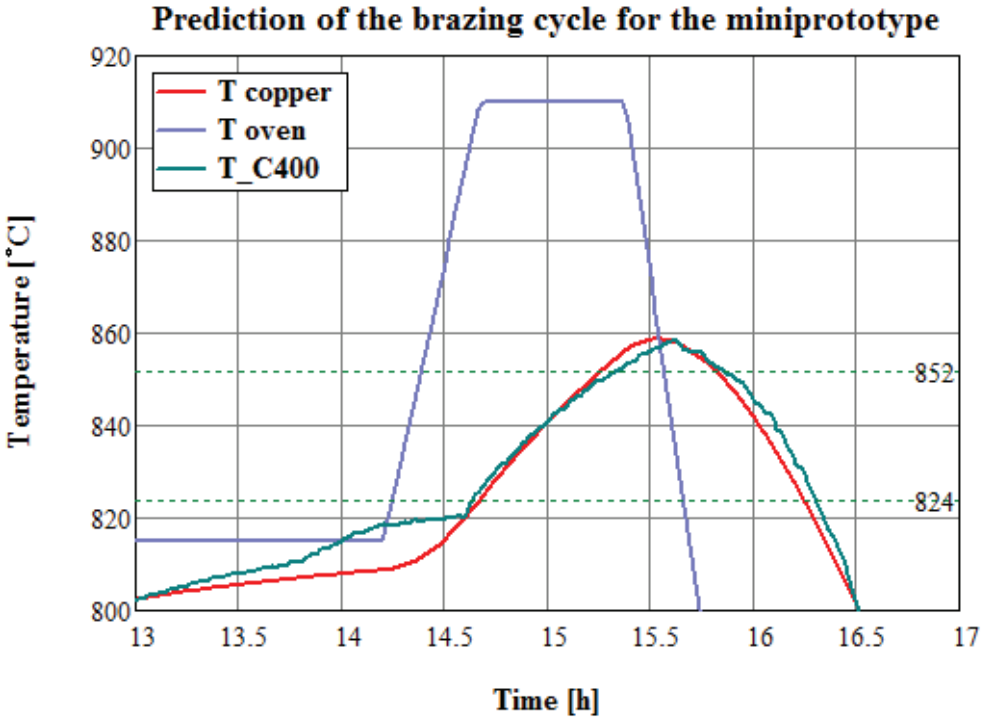

Figure 4.9 Comparison between the calculated brazing cycle for the "miniprototype" and the experimental brazing cycle on the copper "C400"

Since this brazing involves the junction of many components of different materials and several tools are used to keep in position the components, FE analyses with Ansys and Comsol were performed to evaluate the effect of the brazing cycle on the copper components and the steel flanges.

As mentioned before, only the brazing step was simulated, because the accordance between the experimental data and the values calculated by FE is good only above 600 ˚C. This fact was demonstrated by the brazing tests described on chapter 3 with the differences between the experimental data and the FE calculated values at the initial ramp. In fact, especially at the begin of the heating ramp, conductive effects takes place between the base of the oven and the base steel and the contact of the thermocouples on the components could not be good. In this phase it is important that the expert of the LNL brazing lab set a reasonably heating ramp in order to avoid nonuniformities of the temperature on the different part of the assembly that can cause stresses and deformations.

The model for the FE simulations was created with Siemens NX 7 (figure 4.10) and then imported as Parasolid in Comsol Thanks to symmetry, only a quarter could be modeled, saving computational resources. The two symmetric wall are not shown here but were created. The fixation tooling were not considered, because lot of computational time end errors can occur on the estimation of the view factors.

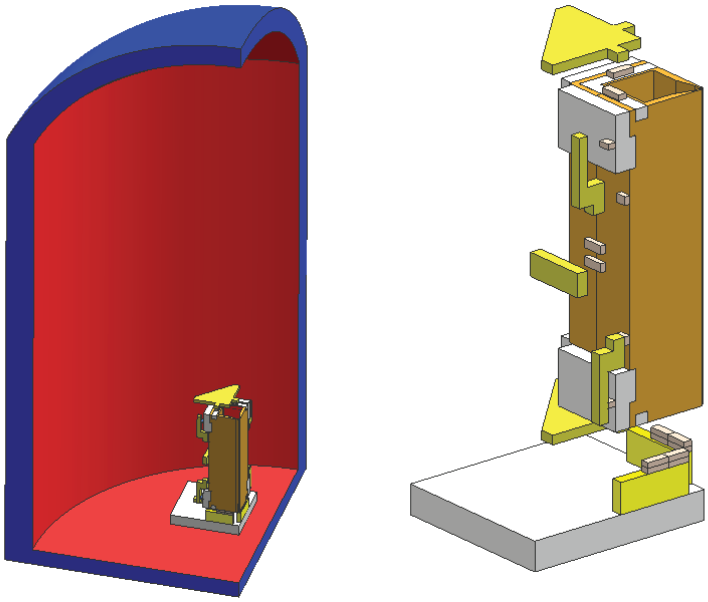

Figure 4.10 Overall and exploded views of the CAD model

The material properties used for the simulation were the same as used in chapter 3. The temperature of the oven as results of the prediction of the 1D simulations was applied on the internal surfaces of the oven (red faces on left figure 4.10). Surface to surface radiation has been applied on the faces of the copper electrodes, the steel flanges, frame and tooling exposed to the oven. An emissivity of 0.07 was applied on copper and 0.2 to the steel parts.

As in chapter 3, a thermal contact resistance function of the pressure induced by the pre-loaded spring were considered on the contact interfaces between the tooling, the base steel, the steel supports and the miniprotoype, Thermal contact resistance was taken into account between the two copper electrodes and the copper and the steel flanges and frames.

Since the brazing alloy melts completely at 853 ˚C, perfect contact was considered between the copper electrodes and the steel flanges and frames at this temperature at the interfaces.

Figure 4.11 shows a comparison between the values calculated by means of 1D simulations (red curve) and the average temperature on copper electrodes calculated with the 3D FE analyses.

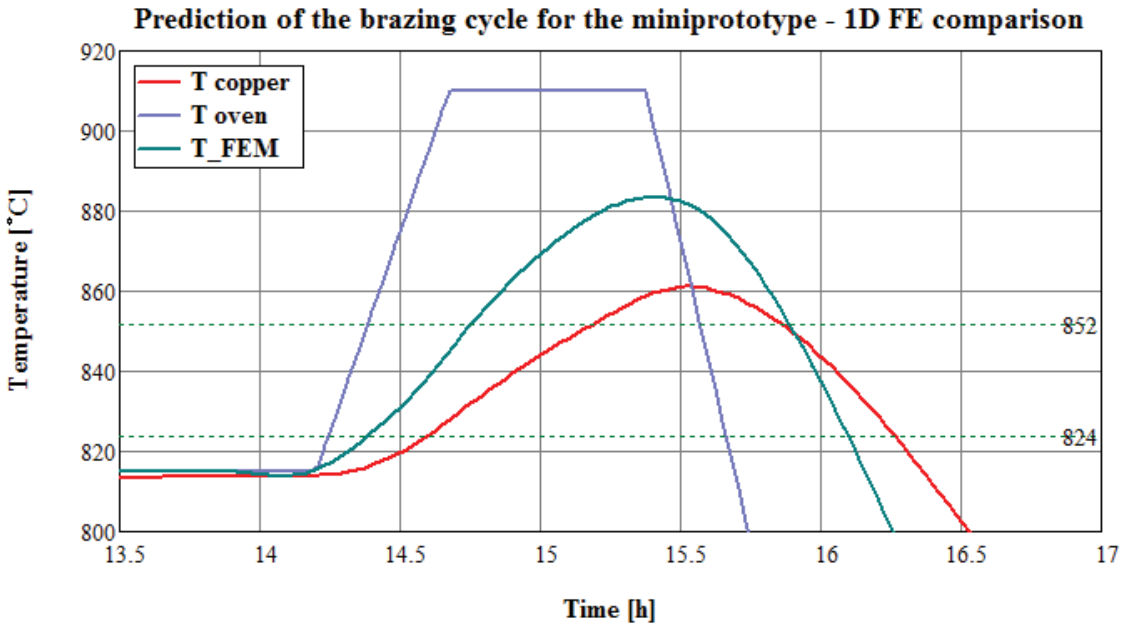

Figure 4.11 Comparison between 1D simulation and the 3D FE analyses

The plot of figure 4.11 shows that the copper heats faster than the preview of 1D simulations. The cause can be the difficulties on the estimation of the correct

exposed area (view factors) because of many components of different materials of the assembly (different material properties and emissivity of the surfaces).

The temperature on all the components of the assembly of the prototype (copper electrodes, steel flanges and frames) is quite uniform, within a range of 10 ˚C.

Figure 4.12 shows the heat flow contributions on the copper calculated with the equation (3-2) for the 1D simulations (red curve), the net radiative heat flux (blue curve) and the total heat flow on the copper calculated by 3D FE analyses. Lot of heat flow comes to the copper by conductive effects of the steel side flanges and the frames.

It seems that the 1D simulations is a poor instrument to predict the brazing thermal cycle. But 3D FE analyses take long time to solve, at least 30 minutes. A solution was found: it is possible to fit the FE data considering an equivalent exposed area.

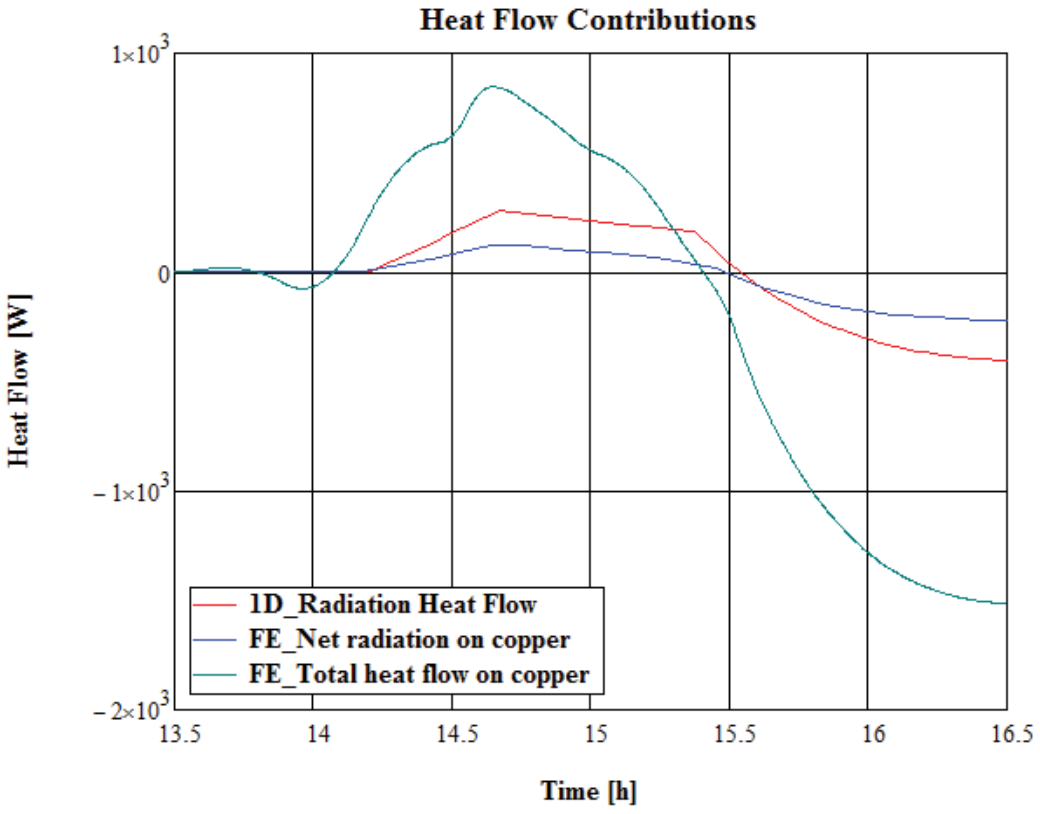

Figure 4.12 Heat flow balance comparison between 1D simulations and 3D FE analyses

With a value of A= 0.6 m^2 the two curves are overlapped, as shown in figure 4.12.

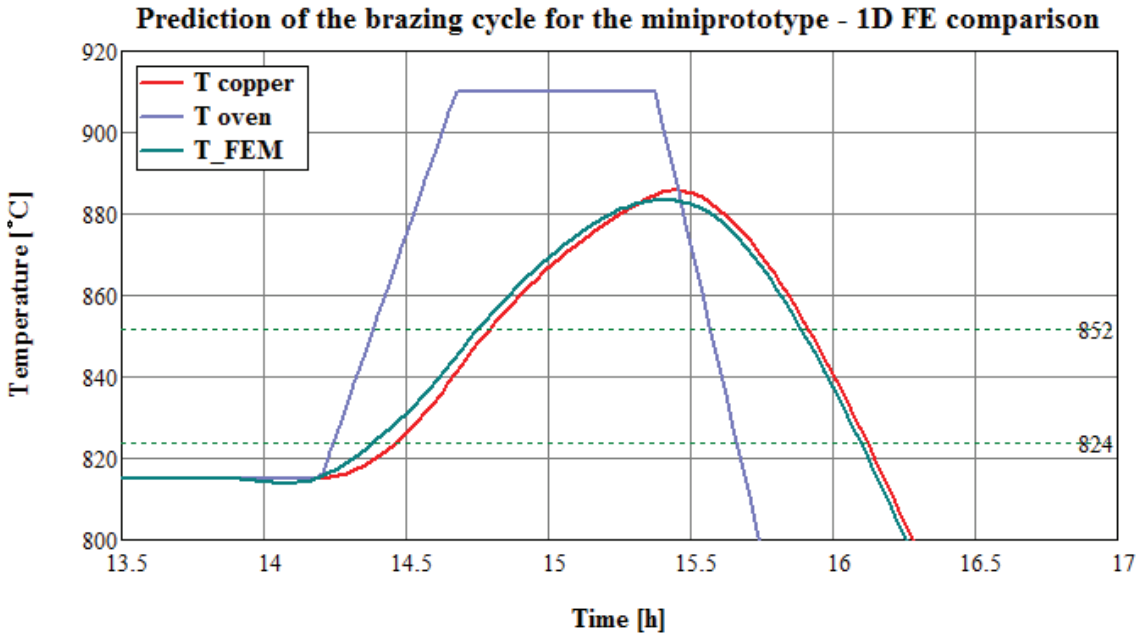

Figure 4.13 Comparison between the 1D and 3D FE analyses with the variation of the exposed area for the 1D analyses.

The brazing step of the thermal cycle of figure 4.13 was redesigned in collaboration of the expert of the brazing lab of the LNL, since an excessive maximum temperature and time above the melting point of the brazing alloy could cause an excessive flow. Figure 4.13 shows the new thermal cycle. Also in this case curves relative to the 1D simulations and the 3D simulations are quite overlapped. This means that the brazing step of thermal cycle can be designed in term of duration with 1D simulations, after the tuning with 3D FE simulations in order to estimate an equivalent exposed area.

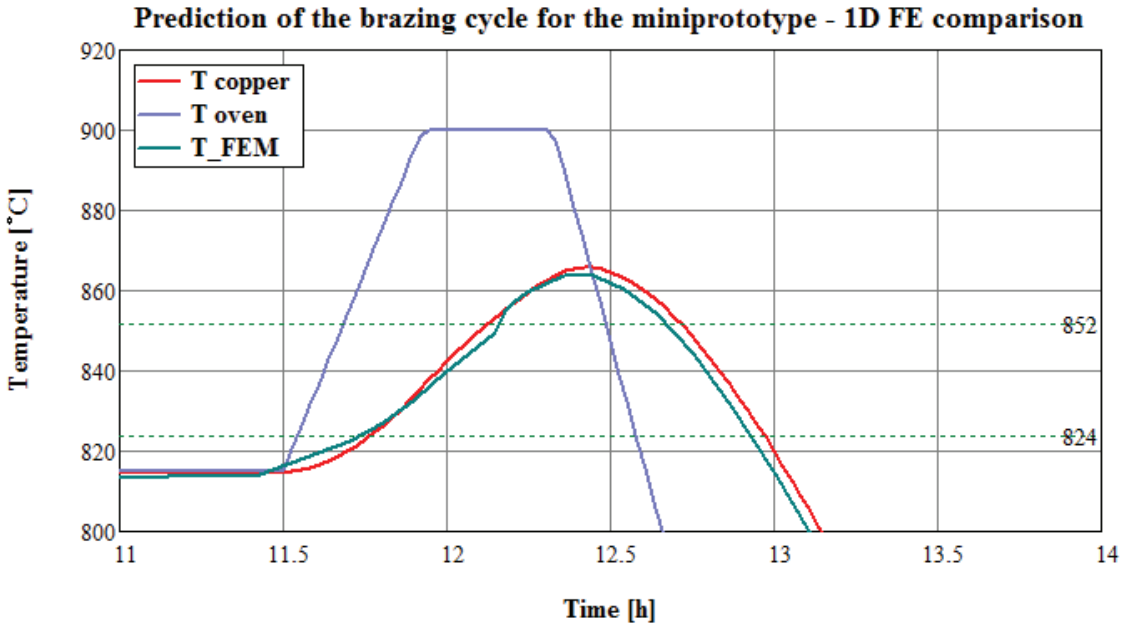

Figure 4.14 New design of the brazing step of the thermal cycle

However, 3D FE analyses are mandatory to evaluate the uniformity of the distribution of the temperature on the components of the miniprotoype. In this case the uniformity of the temperature on the components is contained on less than 10 ˚C.

The correction made on the exposed area for the 1D simulations is useful also to estimate the value of the emissivity of the copper by fitting the temperatures measured by the thermocouples during the thermal cycle: 3D FE analyses take long time to solve (30 minutes) while 1D simulations give instantaneous results. Moreover, if the estimation of the emissivity changes from that used on the predicted cycle, 1D simulations can be used in order to predict in real time the correct brazing step.

This fact happened on the real cycle for the brazing of the prototype. Best fit calculation were performed by the expert of the LNL brazing lab by1D simulations during the last phase of the heating ramp, when the temperature of the components of the assembly is above 650 ˚C, since the simulations start to be accurate above this temperature. Figure 4.15 shows the result obtained on the design of the thermal cycle by 1D simulations, showing the average temperature on the steel parts and on the copper parts.

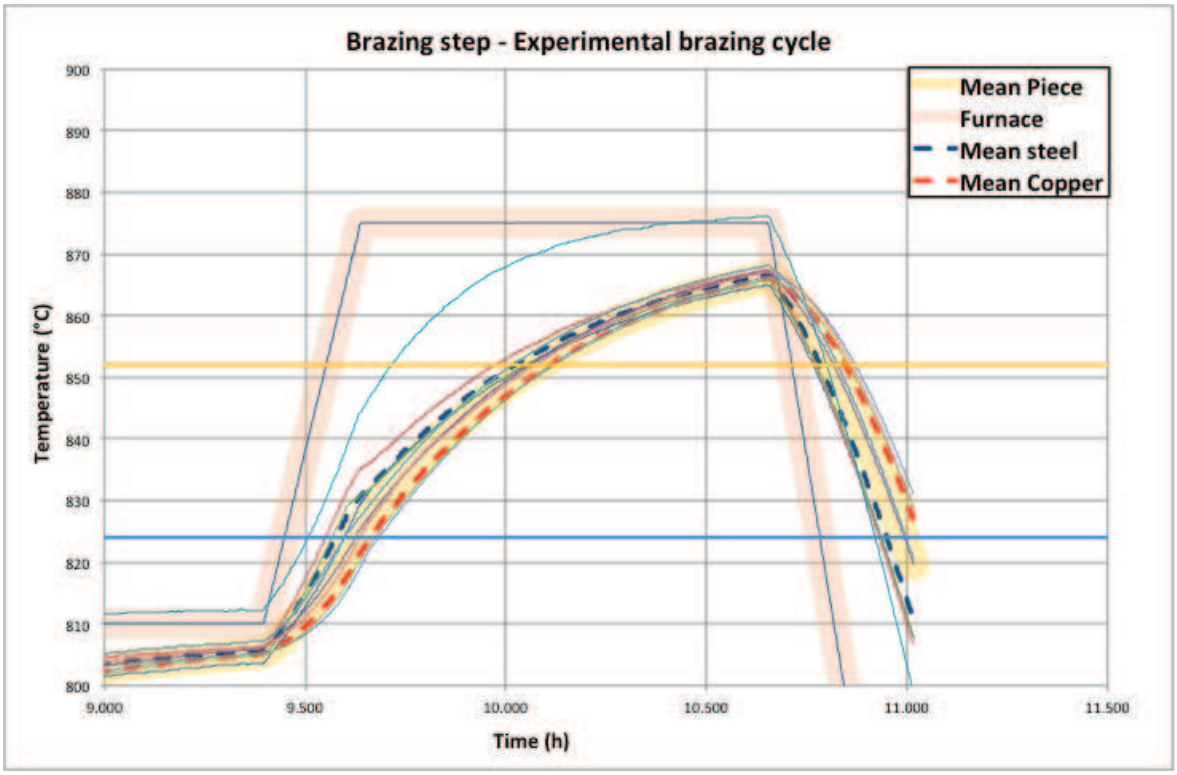

Figure 4.15 The real brazing cycle of the miniprototype

4.4 Consideration on the brazing of the two prototypes, vacuum test and ultrasonic results

The brazing lines of the two prototypes were optically inspected at first. The preliminary impression was that of a very good quality, since the meniscus due to the flowing of the brazing alloy was visible an all the brazing lines, as confirmed on some details provided on the following figures (4.16 – 4.19).

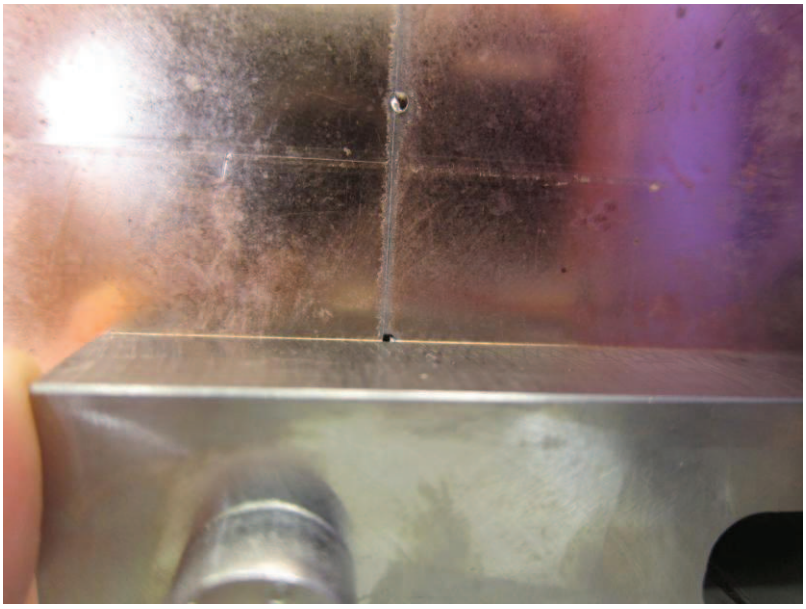

Figure 4.16 Detail of the copper-copper and copper-steel side flange brazing on the miniprototypes brazed at LNL

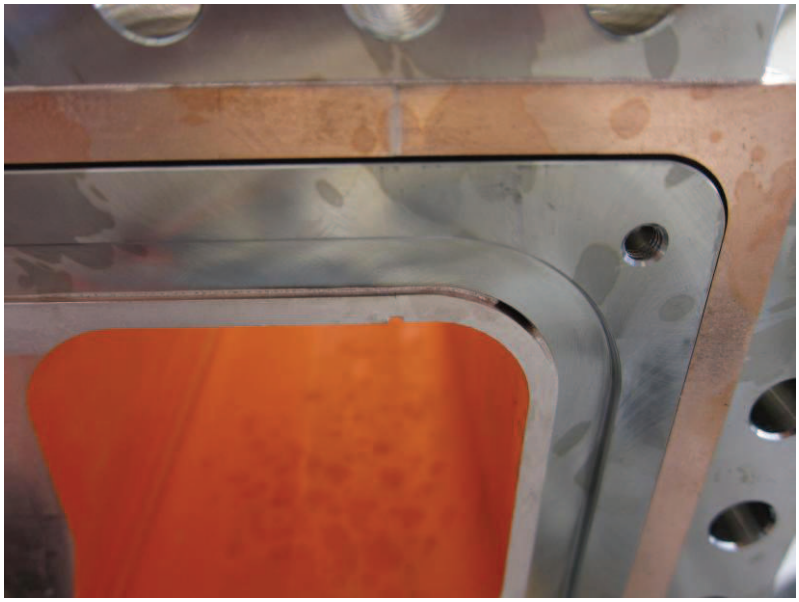

Figure 4.17 Detail of the copper-steel frame brazing on the miniprototypes brazed at LNL

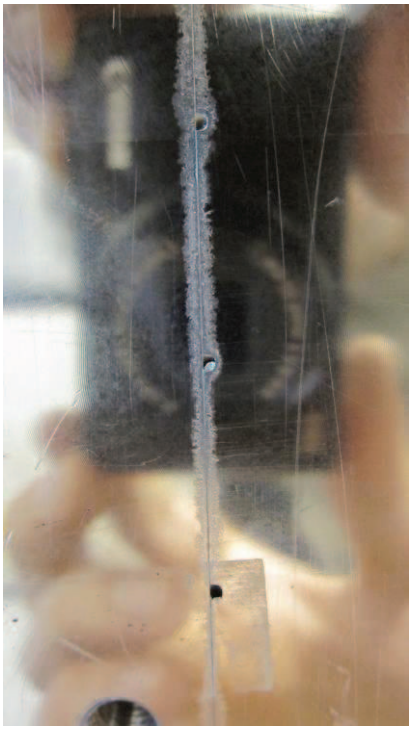

Figure 4.18 Detail of the copper-copper brazing on the miniprototypes brazed at CINEL

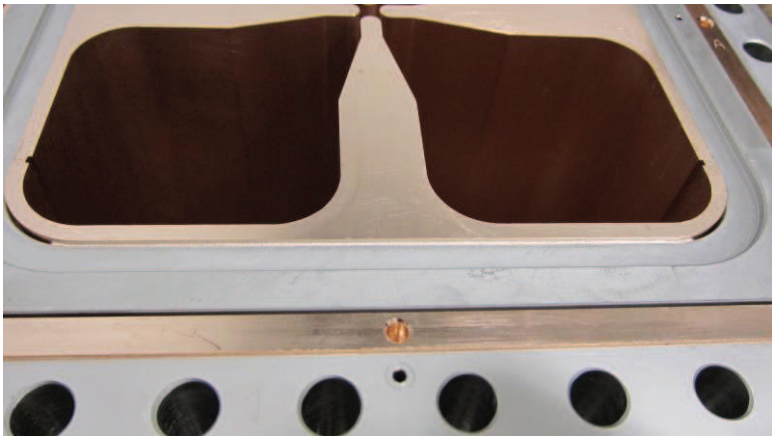

Figure 4.19 Detail of the copper-steel side flange and frame brazing on the miniprototypes brazed at CINEL

Both the modules were ultrasonically inspected with a phased array technique. The measures were performed with the collaboration of an external company, (BYTEST) since we didn't have an adequate instrumentation for the ultrasonic inspection of the brazing surfaces. The results demonstrated an excellent quality

of the brazing joints: the brazing alloy was uniformly distributed on all the joints and the majority of the grooves for the housing of the brazing are empty.

4.5 Measures of the displacements on the two prototypes

The main scope of the production of the two prototypes was to determine the feasibility of a single step brazing. The attention was initially given to the quality of the brazing joints, in term of the flowing of the brazing alloy. As already mentioned on the previous paragraph, this objectives were fully satisfied.

Another important aspect to validate the single brazing process and the appropriateness of the fixture tooling is given from the measure of the displacement of each electrode after the brazing process.

Unfortunately, since lot of attention was given to the quality of the joints, only one prototype was measured. All the measures were performed by our portable Cimcore CMM (figure 4.20) (anthropomorphous arm).

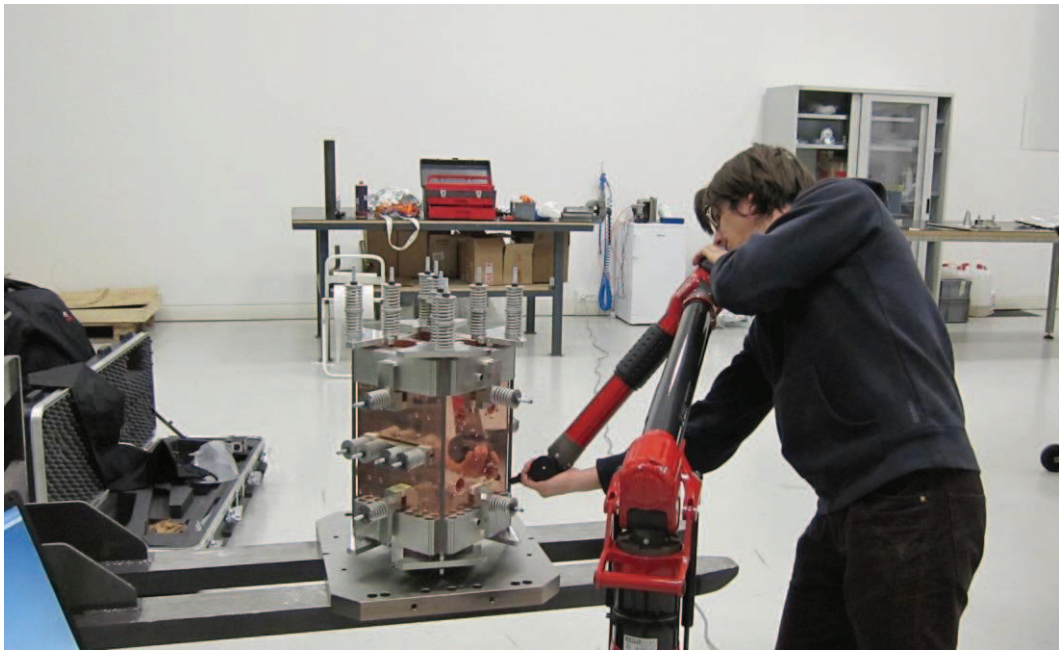

Figure 4.20 A prototype under dimensional inspection by means the PCMM.

Although the arm is not as much accurate as a automatic CMM, we used it because the modules could be measured directly when it is placed on the base plane of the oven. In fact the assembly could undergoes to severe handlings before the placement on the plane of the oven.

However, the measure of the prototype was little bit tricky.

Due to the presence of the fixation tooling very few elements were measure. In fact the access on the internal cavity of the assembly was impossible, only relative displacement between E and T element measured on the external faces were measured. Specific zones were in fact machined on each element in order to measure precisely the displacements before and after the brazing.

Figure 4.21 shows the nomenclature and the alignment coordinate system used on the measures of the two miniprototypes. Table 4.1 reports the relative shift between the various electrodes.

Maximum displacements of 0.025 mm were measured.

The results are quite encouraging, since maximum displacements of 0.025 mm were measured.

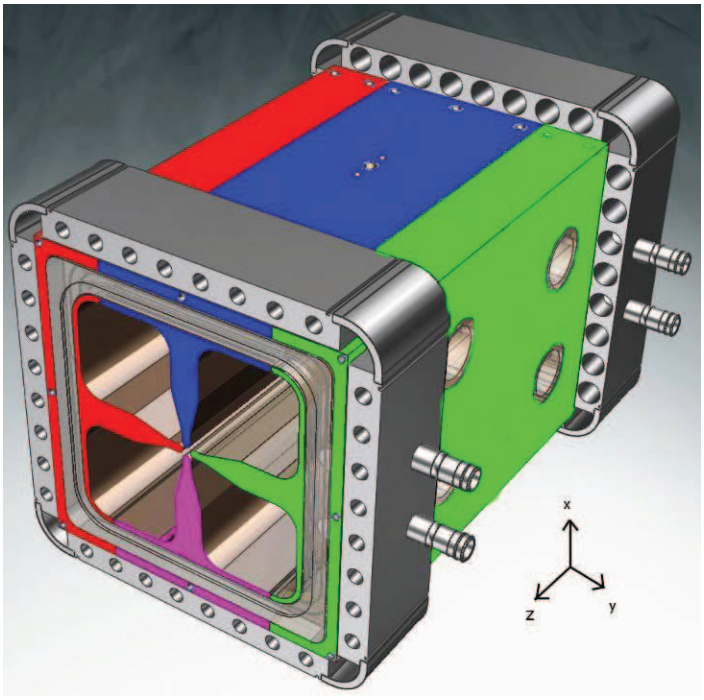

Figure 4.21 Nomenclature of the electrodes used for the measure before and after the measure of the prototype

	Before	After	Delta
Shift (along X)	mm	mm	mm
Red with Blue	0.026	0.001	-0.025
Green with Blue	0.013	0.006	-0.007
Red with Pink	0.003	0.013	0.010
Green with Pink	0.020	0.013	-0.007
Shift (along Z)	mm	mm	mm
Blue with Green	0.015	0.001	-0.014
Blue with Red	0.004	0.027	0.023
Blue with Pink	0.006	0.031	0.025

Table 4.1 Shifts between the various element from the single brazing step

4.6 Conclusions

From this test we had very important outputs for the design and the production for the final modules of the RFQ.

The first reason is the for the feasibility single step brazing that was not no obvious to joint such a number of components of different material. The ultrasonic scans made in collaboration of the external company BYTEST underlined the good quality of the joints.

The second reason is for the successful validation of the tooling for the fixation of the various components of the assembly, although still on a development phase.

For what concerning the brazing grooves, although the vacuum leak test was passed successfully by both the modules, the idea of the refill the brazing alloy in case of a vacuum leak was abandoned. We retained dangerous such design because a small defect in near a groove can affect the vacuum tightness of the cavity. We returned to the old solution for the definitive modules of the inclined grooves already tested on the C400 vertical brazing.

(This page is left intentionally blank)

CHAPTER 5: QUALITY CONTROL AND IMPROVEMENTS FROM THE PRODUCTION OF THE FIRST MODULES OF THE IFMIF RFQ[1]

5.1 Introduction

Chapter 3 and chapter 4 described the tests performed at LNL laboratories and on the external company CINEL for the improvements on the vertical brazing with successful results.

The subdivision of the production of the final accelerating line of the IFMIF/EVEDA was already discussed on chapter 3.

The production of the final modules started from April 2011 with the "supermodule" 3 (high energy zone, composed by the last six modules).

This chapter will describe the various phases of the production of a module of the RFQ with the particular solutions on the mechanical design and the quality assurance aspects (especially dimensional and ultrasonic inspection), since I was involved on these aspects.

A strict collaboration has been established with the expert of the brazing lab of the LNL, our technical office and mechanical workshop.

Since the design geometrical tolerances for the production of the modules are tight and the brazing assemblies need lot of care, the development of quality inspections on the modules was retained mandatory. In fact, quality assurance is mandatory for the feedback on changes and improvements on the design of the modules as well the tuning of the parameters of the mills for the various phases of production.

For what concerning the dimensional quality control, as described on chapter 3, up to now only traditional metrology was used to control the production processes of the accelerators, and the modules were certified only by electromagnetic RF measurement of the resonant frequency.

---

[1] [1] Ref. F. Scantamburlo, A. Pepato, R.Dima et al. "PRODUCTION AND QUALITY CONTROL OF THE FIRTS MODULES OF THE IFMIF-EVEDA RFQ',LINAC 12 (Linear Accelerator Conference), 9-14 September 2012, Tel Aviv, Israel

RF measurements are important for the qualification of the modules, since the electromagnetic specifications has to be satisfied. Unfortunately, they give an average value on the quality of a module. If a problem occurs, it is difficult to localize it.

The use of the metrology allows evaluating the effects on the frequency of the module, using the Slater formula (see chapter 2). In this way a crosscheck between geometrical and the electromagnetic measurements is possible.

This is one of the main aspect that justifies the acquisition of a CMM with active scanning technology.

Since the form and the position of the modulation can be measured by means of our CMM with active scanning, lot of improvements can be achieved: the optimization of the milling parameters, the optimal positioning of the electrodes on the dry assembly, the evaluation of the frequency of the module, the measurements of the deformation of the cavity after each brazing step, etc.

In addition, the scanning technology can give very important feedbacks on the mechanical design.

An example is the result of the measurement of the deformation of the module 1 of the prototype, presented on the first paragraphs of the chapter 3, giving important indications for the development of the vertical brazing.

Up to now, a part the production of the module 1 of the prototype mentioned before, the module 2 of the prototype is completed and the two final modules (16 and 17) are also completed. The production phases of these modules paying attention on the choices for the mechanical design, the inspections for the quality assurance of these modules will be described in this chapter. Unfortunately, some problems were encountered on the production process of the module 16 and the module 2 of the prototype. All in this case accurate dimensional or UT inspection gave lot of information for the solution, as it will be described in this chapter.

The improvements were tested on the module 17 with very successful results.

5.2 “Phase 1” of production: the copper blocks and deep drilling

The production of the modules starts from CuC2 blocks provided from an external company that are firstly hot and then cold forged and then milled to provide the reference faces for the next production phases (figure 5.1).

This phase is defined “phase 0” of the production of the modules since the blocks are provided from the external farm and are the base for the production of each module.

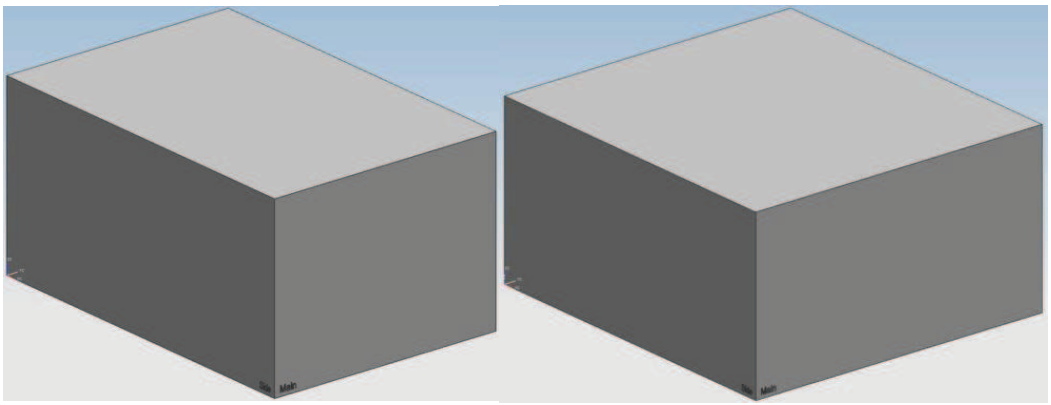

Figure 5.1 The small (left) and the big (right) copper blocks

The copper blocks are of two type: one small (280 x 370 x 550 mm) and one big (280 x 510 x 550 mm). From each copper block two T-shaped and two E-shaped elements are obtained. The different dimensions are because of the different dimension of the T-shaped and E-shaped elements.

After the milling phase, each copper block is ultrasonically inspected for the acceptance test by CERN technician in order to detect eventual void on the blocks and to test the uniformity of the grains. Some specimens of materials were analyzed with SEM technique at CERN metallurgical division to control the respect of the acceptance criteria in term of the dimension of the grains.

Once the copper blocks pass the acceptance criteria, they production of the modules can start with the deep drilling of the cooling ducts and the drilling of some service holes (figure 5.2). This phase is performed by external farms specialized on deep drilling machining.

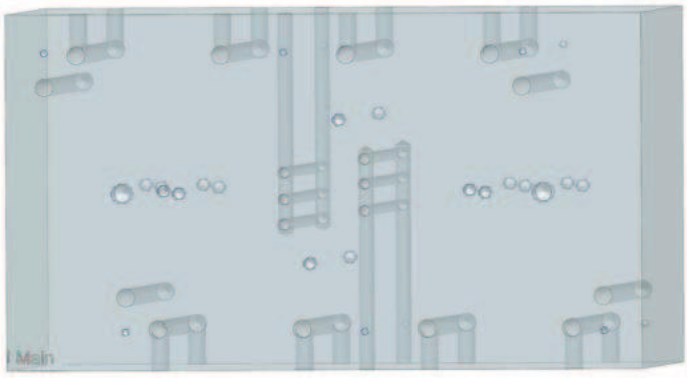

Figure 5.2 Example of deep drilling on a copper block for the E-shaped elements of the high energy module

5.2 "Phase II-III" of production: the EDM cut, the rough milling and the annealing heat treatment of the copper electrodes

In this phase the E and T-shaped elements are obtained from the copper blocks by EDM cut.

The decision to use the EDM cut is based on the previous experience of the LNL with the production of the TRASCO RFQ. The machining of the large copper blocks needed to obtain the net shaped electrodes of TRASCO, induced internal stresses not completely removed by the annealing processes. Moreover deformations occurred during the brazing of the modules.

Since the transversal dimension of the IFMIF are increased of a factor 2 respect to TRASCO, are very large compared to the cavities built up to now and the mechanical tolerances on the modules are tight, we decided to pre-cut the electrodes with EDM. We decided to leave less stock material as possible in order to minimize the energy transferred by milling operations.

During the EDM cut the energy is transmitted on a very limited volume, since the blocks are maintained on a water bath at constant temperature. The INFN of Padova and then the INFN of Torino also purchased a Sodick electro erosion able to cut at 600 mm of maximum height (figure 5.3). Such a height value is the maximum that can cut the EDM machine that are in commerce.

The longitudinal dimension of the copper block (550 mm) comes from the limitation of the EDM machines.

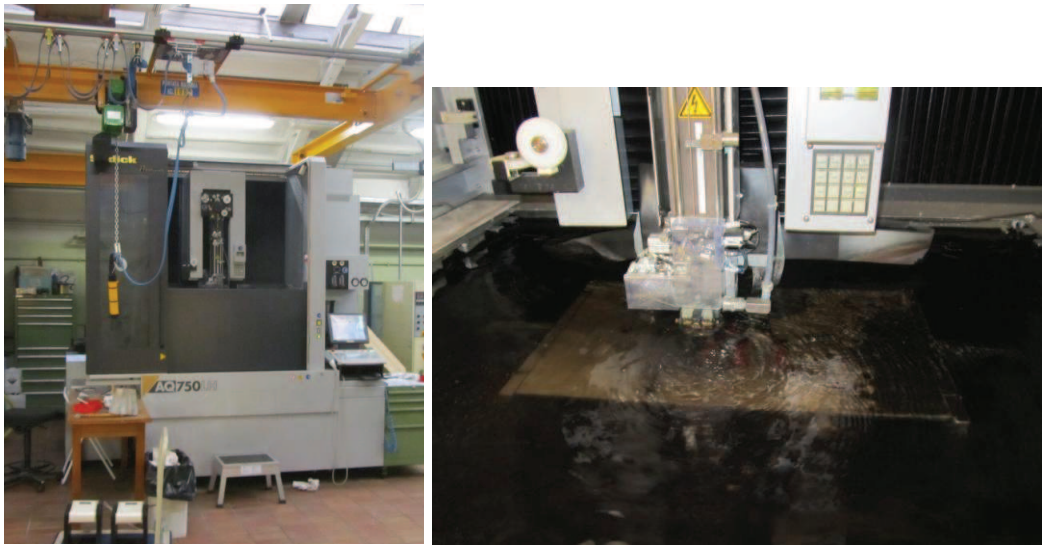

Figure 5.3 Overall view of the EDM in the INFN of Padova mechanical workshop (left) and the EDM during the EDM cut of an electrode from a copper block (right)

As mentioned on the previous paragraph two T and two E –shaped elements can be obtained for each copper electrode, according to figure 5.4, while figure 5.5 shows the electrodes after the EDM cut.

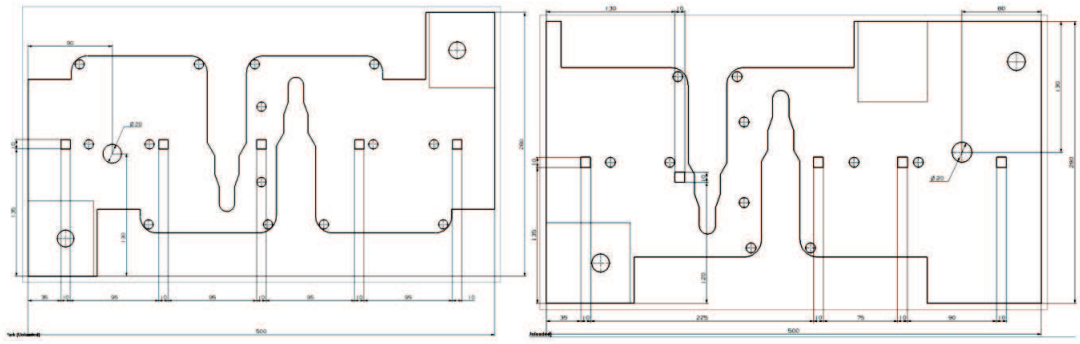

Figure 5.4 Nesting Scheme by EDM cutting of the raw blocks

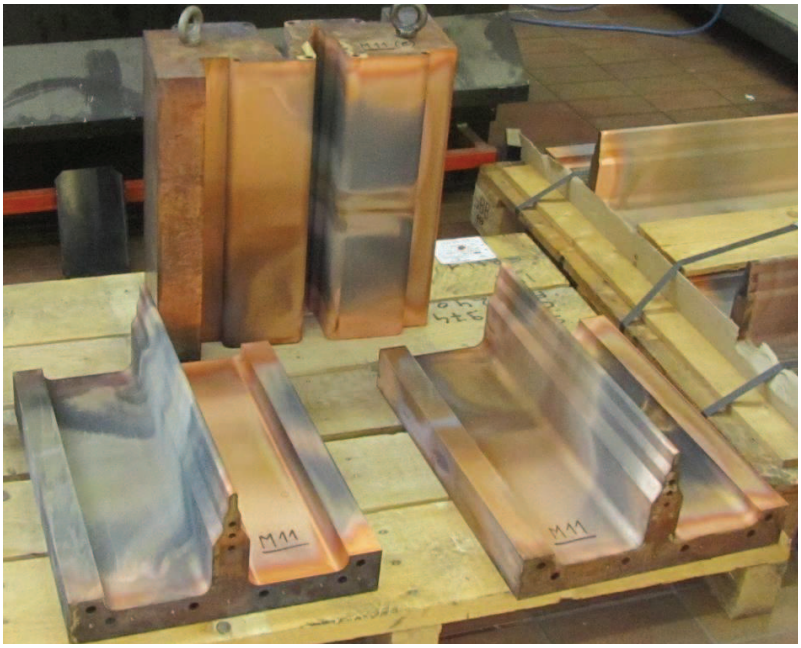

Figure 5.5 Two electrodes after the EDM cut

The annealing heat treatments increase the grain size and reduce the mechanical properties of the material such as the yield strength. A research on the determination of the minimum stock material and the minimization of the number of the annealing processes were performed during the production of the prototype 1, as described on the document of the construction of the technological prototype attached in the appendix of the thesis. Measurements of the deviation of the shape (such as flatness, parallelism, etc. according to ISO 1101) before and after each annealing cycle and EDM/milling operations. Since small deviations were measured, it was decided to leave only 1.5 mm of stock material from the EDM cut and to perform only one annealing cycle after the EDM cut and a first rough milling of the electrodes.

This operation consists on the milling of the identifier code on each element and the aperture of the vacuum ports or the holes for the tuner and the housing of the CF flanges on the E-shaped electrodes (figure 5.6). The back of the electrodes is eventually milled to restore the stock material of 1.5 mm on this side, since the EDM phase leaves more.

The following tables (5.1, 5.2, 5.3 and 5.4) show the results of the dimensional control by means the Zeiss CMM and the variation of the shape from the annealing thermal cycle of the electrodes of the two T-shaped and the two E-

shaped electrodes of the module 16, the two Es of module 15 and 17. Flat. Perp. and Parall. are the abbreviations for flatness, perpendicularity and parallelism.

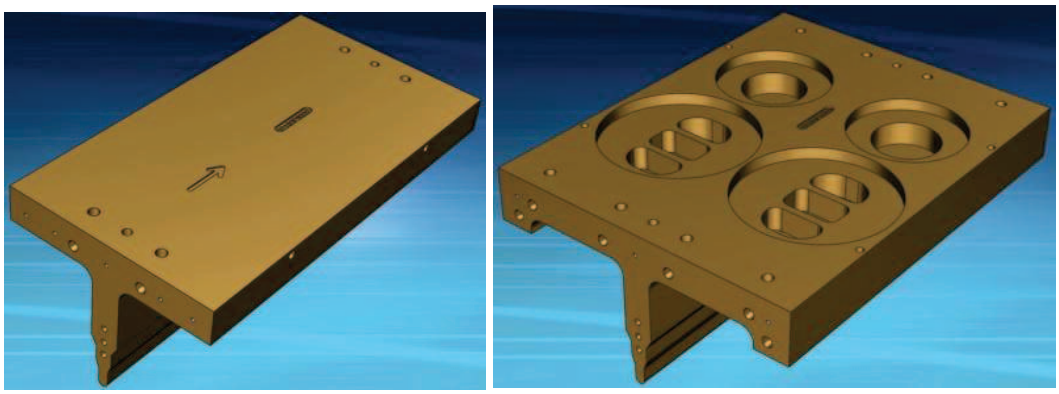

Figure 5.6 The T-shaped electrode (left) and on a E-shaped electrode (right) after the rough milling

The base plane is constructed from the points measured on Base Plane X- and Base Plane X+. The measurements of the perpendicularities of the planes of the vanes and the parallelism of the brazing planes are all calculated considering the Base Plane as datum.

The thermal annealing are performed on the vacuum furnace of LNL, and consist of a heating to 800 ˚C with a ramp of 200 ˚C/hr., a permanence for 2 hours to 800 ˚C and a slow cooling.

Figure 5.7, 5.8, 5.9 and 5.10 show the nomenclature of the measured elements of each electrode and the CMM alignment system.

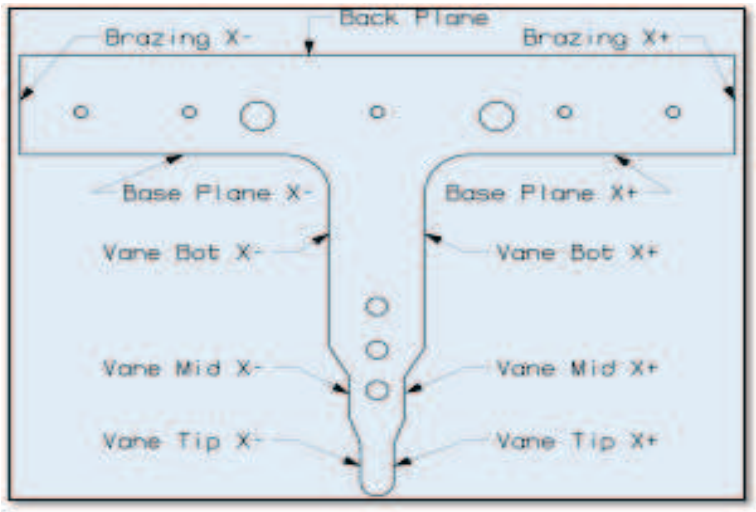

Figure 5.7 Nomenclature of the measured elements on the T-shaped electrodes

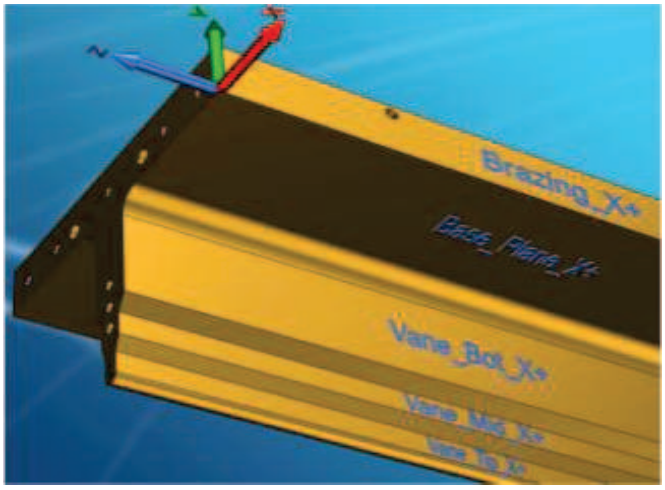

Figure 5.8 Reference CMM alignment for the T-shaped electrode

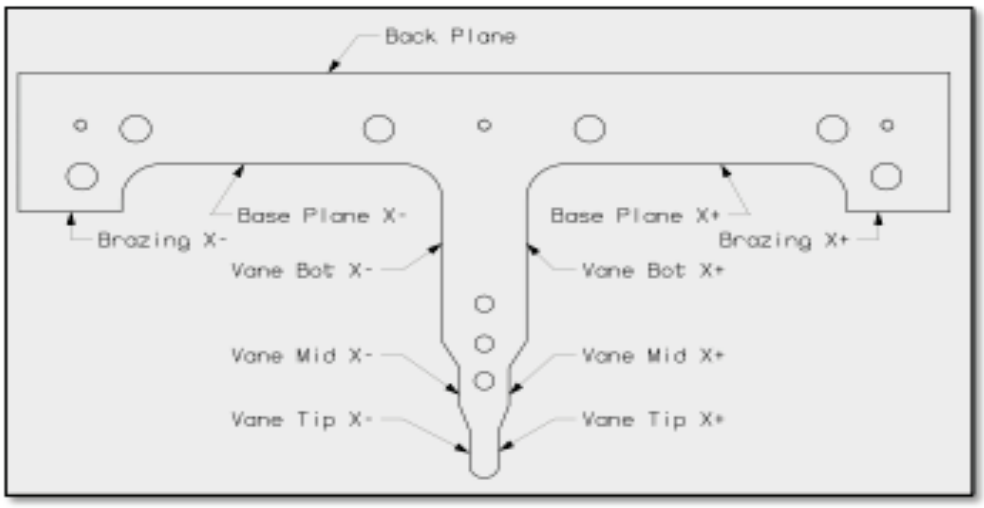

Figure 5.9 Nomenclature of the measured elements on the E-shaped electrodes

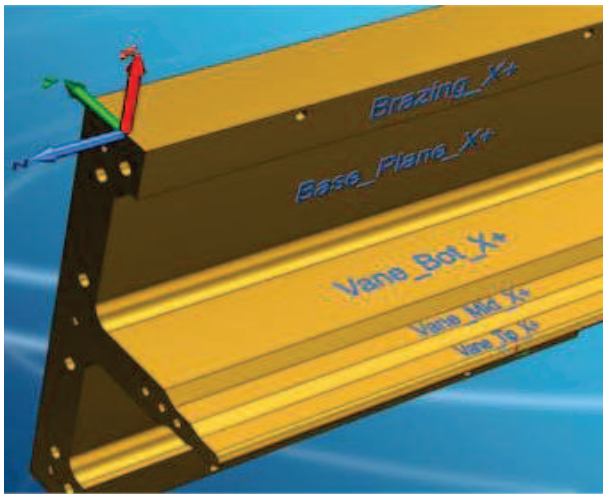

Figure 5.10 Reference CMM alignment for the E-shaped electrode

Module 16	T electrode 1			T electrode 2		
	Before H.T.	After H.T.	Delta	Before H.T.	After H.T.	Delta
Flat. Base_Plane	0.070	0.072	0.002	0.102	0.123	0.021
Flat. Brazing_X-	0.005	0.010	0.005	0.005	0.011	0.006
Flat. Vane_Bot_X-	0.044	0.058	0.014	0.033	0.037	0.004
Flat. Vane_Mid_X-	0.047	0.067	0.020	0.040	0.048	0.008
Flat. Vane_Tip_X-	0.047	0.074	0.027	0.038	0.051	0.013
Flat. Vane_Bot_X+	0.055	0.072	0.017	0.031	0.037	0.006
Flat. Vane_Mid_X+	0.064	0.083	0.019	0.038	0.048	0.010
Flat. Vane_Tip_X+	0.064	0.087	0.023	0.044	0.056	0.012
Flat. Brazing_X+	0.037	0.037	0.000	0.104	0.101	-0.003
Flat. Back_Plane	0.023	0.038	0.015	0.024	0.063	0.039
Perp. Vane_Bot_X-	0.047	0.061	0.014	0.039	0.045	0.006
Perp. Vane_Mid_X-	0.062	0.081	0.019	0.051	0.062	0.011
Perp. Vane_Tip_X-	0.059	0.086	0.027	0.045	0.060	0.015
Perp. Vane_Bot_X+	0.057	0.074	0.017	0.040	0.047	0.007
Perp. Vane_Mid_X+	0.070	0.090	0.020	0.045	0.057	0.012
Perp. Vane_Tip_X+	0.077	0.101	0.024	0.057	0.072	0.015
Perp. Brazing_X-	0.008	0.011	0.003	0.108	0.012	-0.096
Perp. Brazing_X+	0.040	0.042	0.002	0.157	0.102	-0.055

Table 5.1 Deviation [mm] on the shape of the electrodes after the annealing heat treatment for the T-shaped elements of the module 16

Module 16	E electrode 1			E electrode 2		
	Before H.T.	After H.T.	Delta	Before H.T.	After H.T.	Delta
Flat. Base_Plane	0.091	0.199	0.108	0.063	0.095	0.032
Flat. Brazing_X-	0.049	0.079	0.030	0.092	0.125	0.033
Flat. Vane_Bot_X-	0.034	0.049	0.015	0.039	0.053	0.014
Flat. Vane_Mid_X-	0.029	0.032	0.003	0.038	0.036	-0.002
Flat. Vane_Tip_X-	0.028	0.033	0.005	0.056	0.043	-0.013
Flat. Vane_Bot_X+	0.045	0.047	0.002	0.111	0.109	-0.002
Flat. Vane_Mid_X+	0.044	0.042	-0.002	0.117	0.110	-0.007
Flat. Vane_Tip_X+	0.056	0.059	0.003	0.121	0.112	-0.009
Flat. Brazing_X+	0.085	0.075	-0.010	0.102	0.084	-0.018
Flat. Back_Plane	0.067	0.213	0.146	0.034	0.097	0.063
Perp. Vane_Bot_X-	0.046	0.054	0.008	0.060	0.067	0.007
Perp. Vane_Mid_X-	0.064	0.076	0.012	0.068	0.072	0.004
Perp. Vane_Tip_X-	0.055	0.059	0.004	0.079	0.070	-0.009
Perp. Vane_Bot_X+	0.050	0.053	0.003	0.143	0.138	-0.005
Perp. Vane_Mid_X+	0.064	0.064	0.000	0.146	0.139	-0.007
Perp. Vane_Tip_X+	0.080	0.087	0.007	0.150	0.138	-0.012
Parall. Brazing_X-	0.181	0.406	0.225	0.210	0.349	0.139
Parall. Brazing_X+	0.103	0.239	0.136	0.349	0.449	0.100

Table 5.2 Deviation [mm] on the shape of the electrodes after the annealing heat treatment for the E-shaped elements of the module 16

Module 15	T electrode 1			T electrode 2		
	Before H.T.	After H.T.	Delta	Before H.T.	After H.T.	Delta
Flat. Base_Plane	0.063	0.063	0.000	0.066	0.122	0.056
Flat. Brazing_X-	0.004	0.007	0.003	0.005	0.018	0.013
Flat. Vane_Bot_X-	0.031	0.038	0.007	0.037	0.046	0.009
Flat. Vane_Mid_X-	0.030	0.043	0.013	0.047	0.065	0.018
Flat. Vane_Tip_X-	0.023	0.039	0.016	0.051	0.074	0.023
Flat. Vane_Bot_X+	0.026	0.034	0.008	0.059	0.071	0.012
Flat. Vane_Mid_X+	0.032	0.046	0.014	0.075	0.095	0.020
Flat. Vane_Tip_X+	0.037	0.055	0.018	0.078	0.102	0.024
Flat. Brazing_X+	0.025	0.024	-0.001	0.063	0.068	0.005
						0.000
Flat. Back_Plane	0.013	0.031	0.018	0.012	0.085	0.073
Perp. Vane_Bot_X-	0.037	0.046	0.009	0.042	0.053	0.011
Perp. Vane_Mid_X-	0.036	0.051	0.015	0.057	0.075	0.018
Perp. Vane_Tip_X-	0.037	0.055	0.018	0.059	0.085	0.026
Perp. Vane_Bot_X+	0.033	0.042	0.009	0.061	0.077	0.016
Perp. Vane_Mid_X+	0.036	0.051	0.015	0.078	0.099	0.021
Perp. Vane_Tip_X+	0.042	0.061	0.019	0.084	0.113	0.029
Perp. Brazing_X-	0.007	0.008	0.001	0.008	0.028	0.020
Perp. Brazing_X+	0.027	0.026	-0.001	0.008	0.074	0.066

Table 5.3 Deviation [mm] on the shape of the electrodes after the annealing heat treatment for the T-shaped elements of the module 15

Module 17	T electrode 1			T electrode 2		
	Before H.T.	After H.T.	Delta	Before H.T.	After H.T.	Delta
Flat. Base_Plane	0.068	0.072	0.004	0.095	0.121	0.026
Flat. Brazing_X-	0.005	0.006	0.001	0.004	0.008	0.004
Flat. Vane_Bot_X-	0.030	0.039	0.009	0.017	0.013	-0.004
Flat. Vane_Mid_X-	0.030	0.044	0.014	0.026	0.025	-0.001
Flat. Vane_Tip_X-	0.022	0.040	0.018	0.022	0.022	0.000
Flat. Vane_Bot_X+	0.036	0.048	0.012	0.039	0.037	-0.002
Flat. Vane_Mid_X+	0.045	0.062	0.017	0.034	0.034	0.000
Flat. Vane_Tip_X+	0.045	0.067	0.022	0.032	0.033	0.001
Flat. Brazing_X+	0.056	0.055	-0.001	0.124	0.117	-0.007
						0.000
Flat. Back_Plane	0.018	0.021	0.003	0.016	0.048	0.032
Perp. Vane_Bot_X-	0.032	0.041	0.009	0.019	0.018	-0.001
Perp. Vane_Mid_X-	0.038	0.052	0.014	0.029	0.029	0.000
Perp. Vane_Tip_X-	0.025	0.044	0.019	0.024	0.025	0.001
Perp. Vane_Bot_X+	0.041	0.054	0.013	0.042	0.040	-0.002
Perp. Vane_Mid_X+	0.047	0.065	0.018	0.037	0.035	-0.002
Perp. Vane_Tip_X+	0.053	0.073	0.020	0.036	0.036	0.000
Perp. Brazing_X-	0.007	0.006	-0.001	0.007	0.010	0.003
Perp. Brazing_X+	0.058	0.059	0.001	0.130	0.122	-0.008

Table 5.4 Deviation [mm] on the shape of the electrodes after the annealing heat treatment for the T-shaped elements of the module 17

The tables demonstrated small deviations in the order of some cents of mm induced from the annealing cycle. Displacements of the order of 0.1-0.15 mm were measured, but they were affected on the positioning of the electrodes, since they were placed horizontally supported on the back on the plane of the oven. The flatness of those supports was not good and the copper becomes soft at those temperatures.

The thermal stresses inside the electrodes after the EDM cut and the rough milling are very low, so the choice o perform a single annealing step is reasonable.

5.2 "Phase IV" of production: the finish milling of the electrodes

5.2.1 Introduction

In this phase the electrodes are milled to the final form. Since the very tight tolerances are requested for the machining of the single electrodes, lot of attention was paid on the design of the electrodes for the machining phases of each single electrode, involving a strict collaboration with the machining expert of the INFN workshop of Padova.

The design of the references for the alignment and the support for the milling operations is very important, in order to avoid deformations and alignments errors.

The choice of the same references for the alignment for the mill and the CMM was mandatory to validate the milling process, to discover and correct eventual problems linked to machining errors due to the types of tools, deformations induced by the milling operations, errors of alignment, etc.

For these reasons also the development of reliable CMM measuring strategies was very important to keep in control the process and eventually give feedbacks for the design and the machining operations.

Figure 5.11 shows a model of an E-shaped electrode as result of the finish milling operations.

In first phase the back the and the external surfaces of each electrode are machined: the slots for the coupling of the side steel flanges for the connections of the modules, the housing for the vacuum and the tuner flanges. The most

important is the machining of the reference surface for the alignment (figure 5.11).

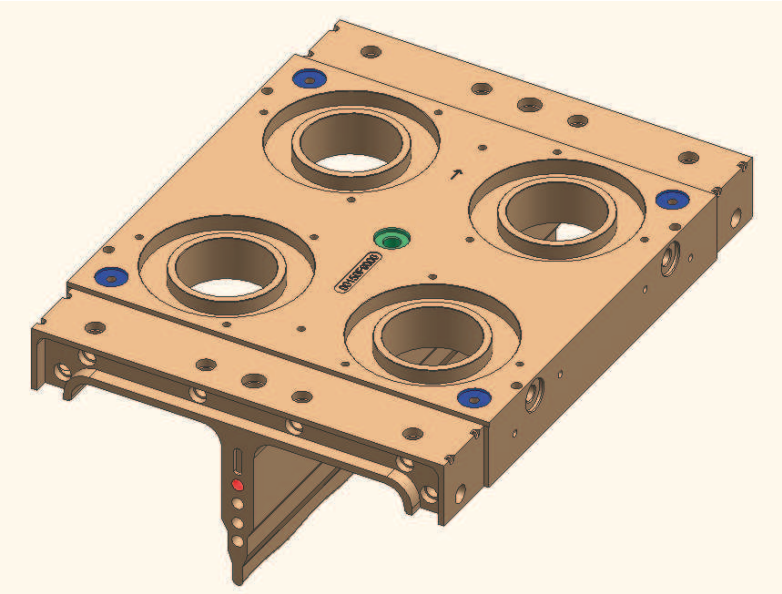

5.11 Finish milling of the copper electrodes

Considering that a body in space has six degrees of freedom and considering a cartesian coordinate systems:

- A common reference plane is machined by means of four calibrated seats, blue colored. The plane define a normal axis (for example Z) and can be used to lock the Z origin. The other two axis (X and Y) can rotate around Z and their origin can translate on the plane with Z normal.
- Two references holes were bored on the sides of the electrodes, red colored. Idealizing the holes as a circles, the line that connects the two define an axis (for example X). In this way the rotation of the X and Y axes around Z is fixed, while the origins of X and Y remain free to translate.
- A reference hole was bored (green colored) to fix the translation of the X and Y origin.

In the second phase the reference plane and the center hole are coupled to grinded AISI plate with a very precise pin in order to guarantee the maximum precision for the milling operations. In this step the final machining of all the internal surfaces is done.

Since the required tolerances imposed for the machining are tight, some tests followed by a dimensional quality control were performed in order to tune the machining parameters and the chose the right tool which guarantee the best performances.

The next paragraph will describe the importance of the feedback given by the dimensional quality control for the tuning of the machining step of the modulation.

5.2.1 Modulation test: validation of the machining phase of the pole tips of the electrodes

The most important part of the electrodes that form the RFQ cavity is the modulation, i. e. the sinusoidal shape on the pole tips of the electrodes. The tolerances on the position and form of the modulation are very tight, since they affect the beam dynamics and the frequency of the RFQ cavity. As mentioned on chapter 1, in order to reach the targets for the positioning of the pole tips of each electrode of maximum 0.05 mm from the beam axis and to reach the design specifications in term of beam dynamics, the tolerance for the pole tips was fixed on ± 10 μm in form and position from the external references.

In order to tune the correct parameters of the mill and to choice the right tool, some small scale 200 mm length (figure 5.12) and full scale 550 mm length modulation tests were performed on the mills of the mechanical workshop of the INFN of Padova and of the external company CINEL which have in charge the production of the last six modules of the RFQ.

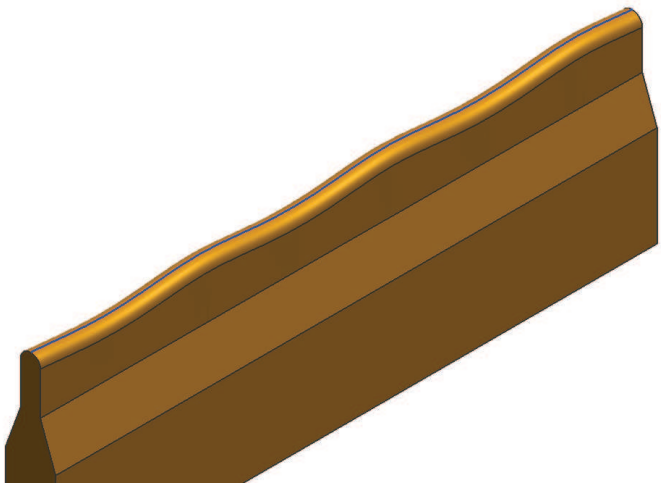

Figure 5.12 The small scale modulation test

The first tests were the milling of a small scale modulation test (figure 5.12). Three different components were machined with different tools, two at the mechanical workshop of CINEL who has in charge the production of the high energy last six modules, and one at the mechanical workshop of the INFN Padova.

Each test was then measured by means the Zeiss Accura CMM with the active scanning and the software Zeiss Calypso for the qualification of the modulation and the milling tools used as well as the accuracy of the milling centers. Many cross section of crest and valleys of the modulations and longitudinal scan on the crest of modulations were performed.

As follow, not all the results are reported, but only which were retained representative.

Since the main scope of these test was to found the right tools, the measurements regarded only the form of the modulation and not in position. Least squares best-fit algorithms are implemented onto the software in order to reduce the errors of form of the measured profile from the nominal translating or rotating the measured profile along the reference axes.

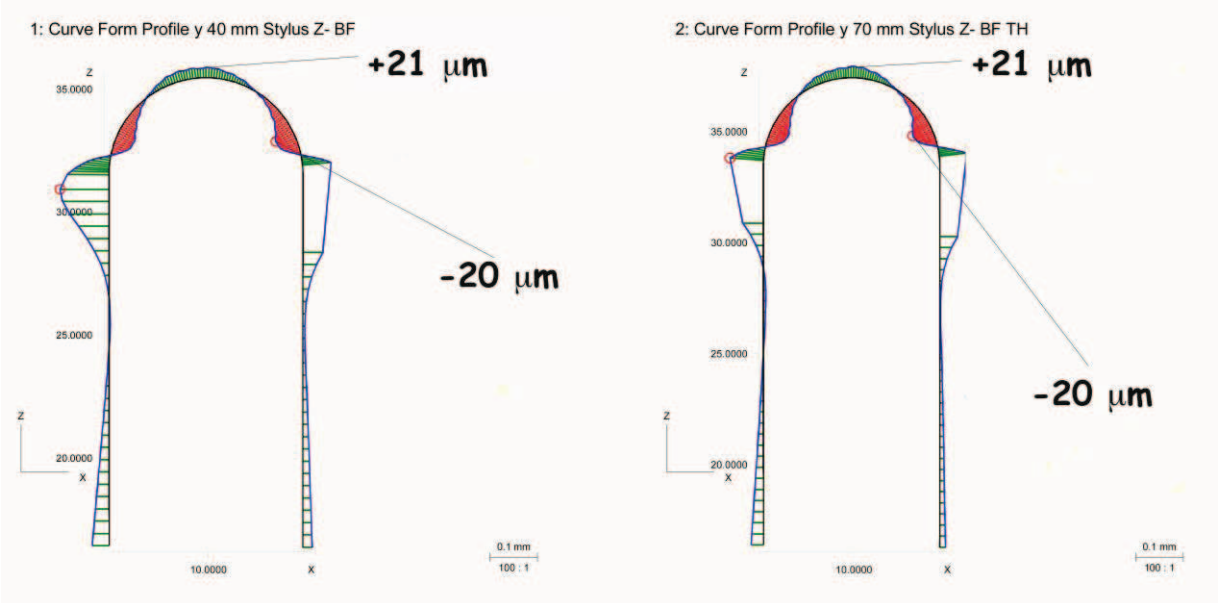

Figure 5.13 Results of the scans of a valley (left) and a crest (right) of the test milled by the external farm with a form tool.

In the first test CINEL considered to mill the modulation with a form tool. The choice seemed to be reasonable since the radius of the tip is constant along the longitudinal axis.

The report of the measurements of this test is visible on figure 5.13.

Some problems were encountered. The quality of the profile is not good and not acceptable for the beam dynamics point of view, with deviations from the nominal of -/+ 20 μm on the tip. The maximum deviation increase up to 40 μm (red circle on the left and right of figure 5.13) near the pole tip radius, and a strong gradient of the deviation from the vertical plane to the tip radius.

Figure 5.14 reports the results of the measurements on a valley and a crest of the second modulation test performed by CINEL using a ball end mill. This case shows better results than the previous one and the form is more regular. The deviations from the nominal profile are below the acceptance criteria, but not for the target criteria. The problem of such deviations was identified on the errors on the positioning of the mill, that was not working in stationary conditions. In fact the milling process started when all the parts of the machine was “cold”. The quality of the tip is not so good, since some crest and valleys can be seen on the two profiles of figure 5.14. The problem is linked to a not sufficient low pitch between the milling passes.

A correction of these problems was tried and solved, as it will reported on the results of a full scale modulation test milled at CINEL.

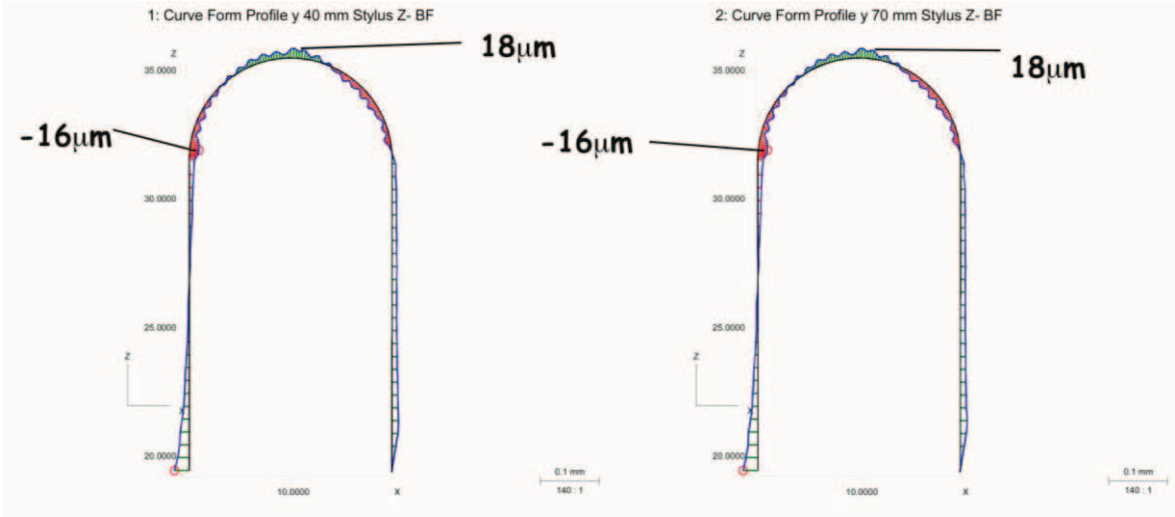

Figure 5.14 Results of the scans of a valley (left) and a crest (right) of the test milled by the external farm with ball end mill.

Another small scale modulation test was machined at the mechanical workshop of INFN Padova. A ball end mill was used for the milling of the tip radius, while another type of tool was used for the vertical planes of the mill.

The machining of the tip radius was of a very excellent quality, as on report of the measures on a valley and a crest cross sections (figure 5.15). The form of the real profile on the tip radius is all inside a band of -/+ 10 μm. The two red lines on each profile of figure 5.15 represent the deviation of -10 μm or +10 μm from the nominal profile.

Corrections can be made on the positioning of the mill to optimize the machining of the vertical planes.

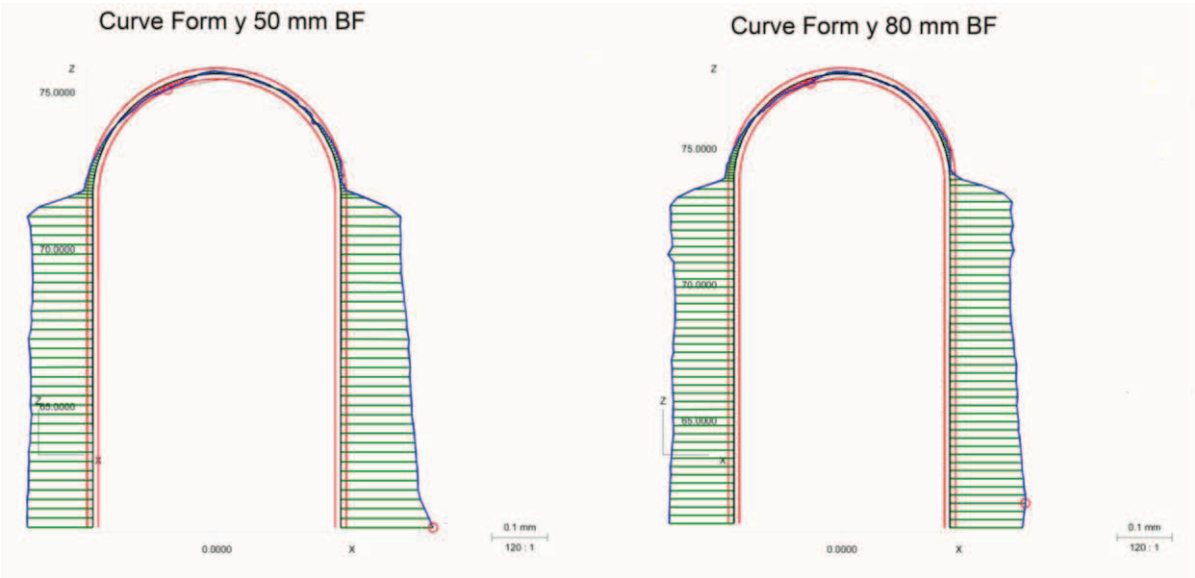

Figure 5.15 Results of the scans of a valley (left) and a crest (right) of the test milled by the INFN of Padova farm with a ball end mill.

After the two small scale tests, CINEL machined another workpiece reproducing the full scale modulation of the module 16 before starting the production of the final modules (figure 5.16). The scope of the test was to control the corrections made on the milling parameters after the machining of the small scale tests.

Figure 5.17 and 5.18 report the results of the form of the crest of the modulation along the longitudinal Z axis. The quality is excellent, since the real profile is contained on the two red band of ± 10 μm from the nominal.

Figure 5.19 reports the results of the form o the tip on three different Z position of the work piece. Also this measurements shows the excellent quality of the form of the tip. The real profiles are inside the band of ± 10 µm from the nominal.

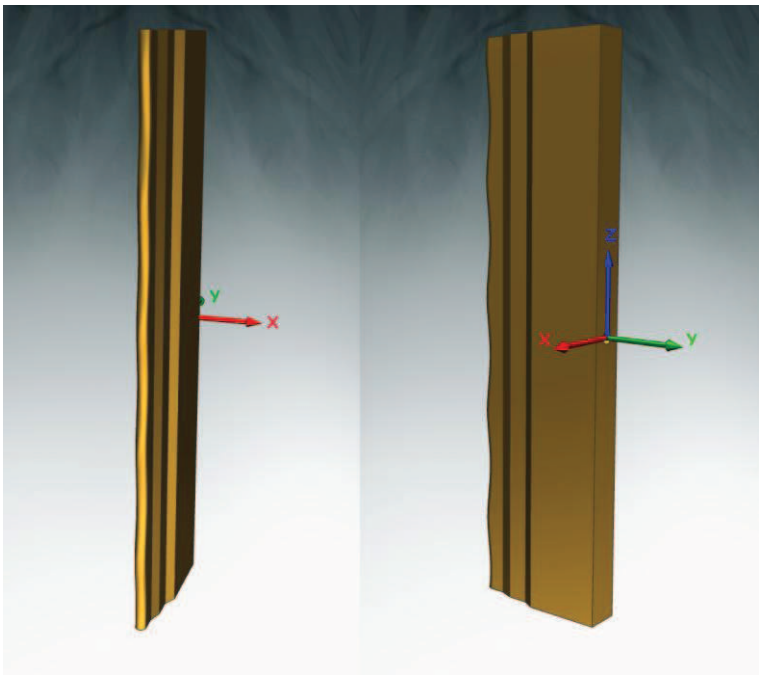

Figure 5.16 Full modulation test milled at CINEL

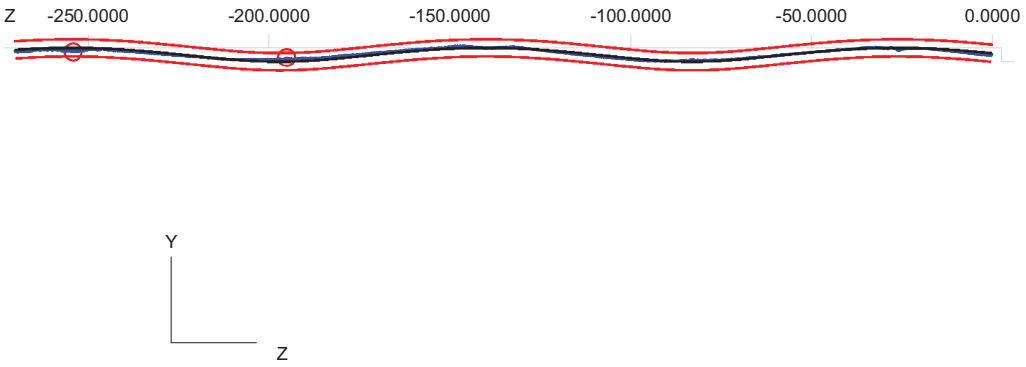

Figure 5.17 Report of the measurement of crest of the full scale modulation (Z- side) machined by CINEL

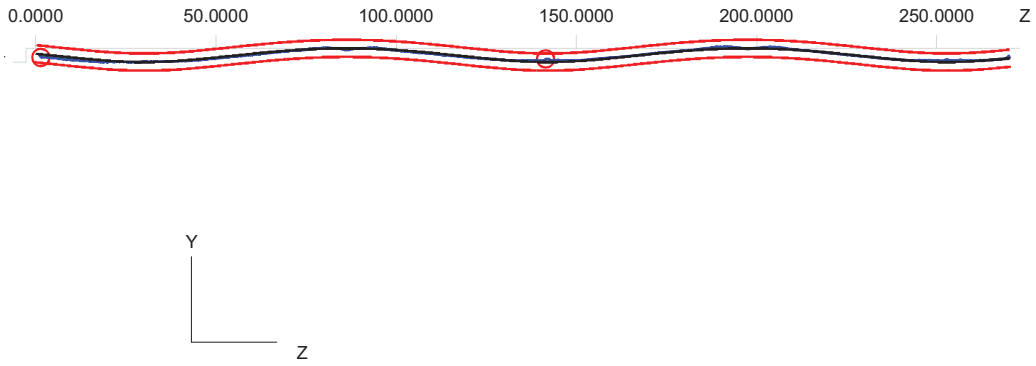

Figure 5.18 Report of the measurement of crest of the full scale modulation (Z+ side) machined by CINEL

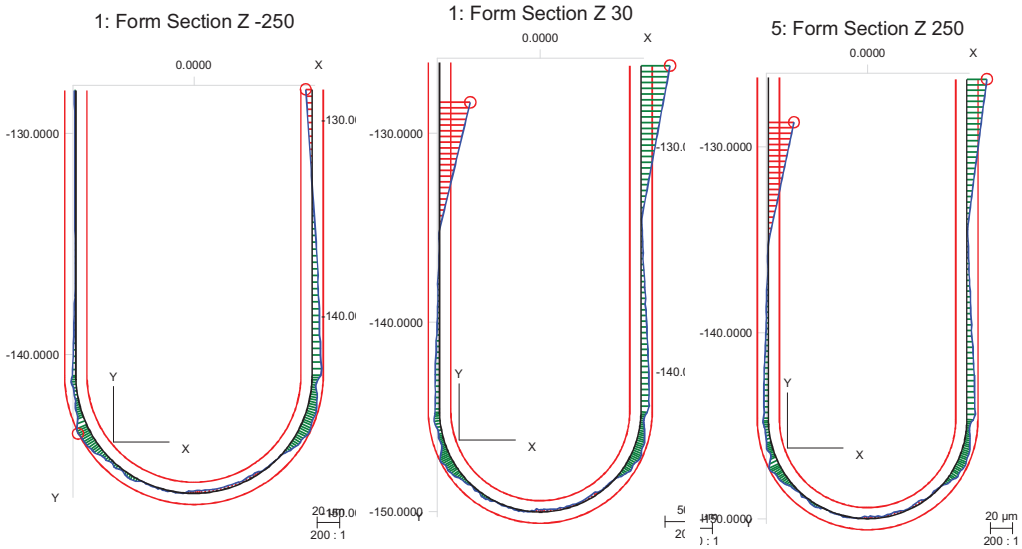

Figure 5.19 Report of the measurement scan of the modulation tip of the full scale modulation test machined by CINEL

5.2.2 Finish milling of the electrodes: dimensional quality control

Once the results obtained on the tests of the modulation were positive, the finish milling of the electrodes could start.

Since I was deeply involved on the dimensional quality control of the production of the modules, in this paragraph the development of the strategy for the dimensional quality for each single electrode will be described.

The dimensional quality control in this phase is very important, not only to control if the each component satisfy the acceptance criteria or for the aspects that were discussed above.

The dimensional qualification of each electrode is very important also to have indication and optimize the quality of the assembly. This aspect will be described on the following paragraph.

In this phase all the elements of each electrode are qualified. According to the drafting of each electrode on this phase of production, the qualification consists on the measurement and the verification of the specified tolerances. In addition several scans were performed on the modulation and on the tip, and full profiles including the internal shape of the electrode and the brazing planes.

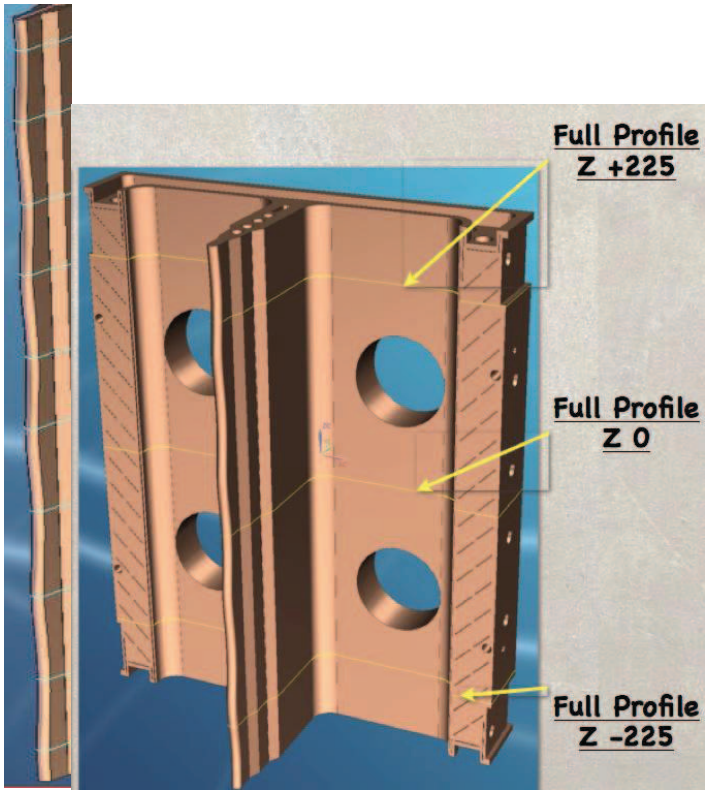

Figure 5.20 Profiles measured on the modulation of the electrodes and the "full profiles" for the E-shaped electrode

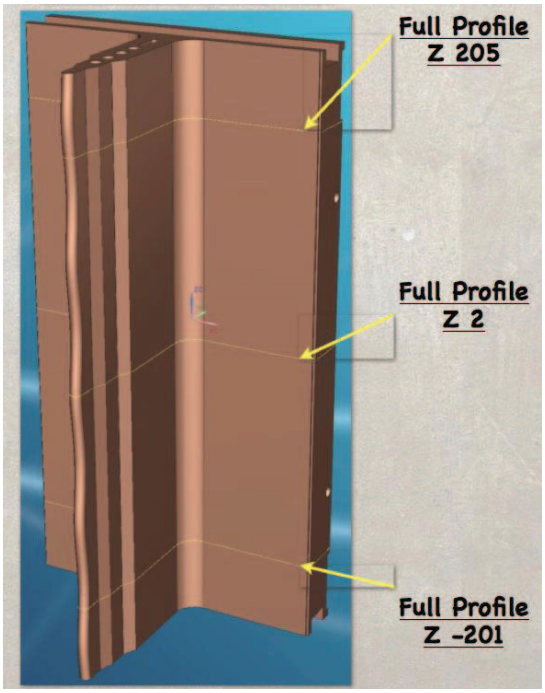

Figure 5.21 Example of "Full profiles" measured for a T-shaped electrode

However there are some aspects that are more important than others that determine the quality of the internal geometry (frequency) of the resonator:

- The position of the pole tip respect the alignment system, in particular the distance of the pole tip from the reference plane.
- The form (flatness and parallelism) and the position of the brazing planes from the reference plane.
- The distance of the reference holes on the side of each electrode from the reference plane

The first two aspects are very important for the quality of the resonator. They affect the position, or better the distance of the pole tips on the assembly, and thus the frequency. For example, errors on machining of the position of the brazing planes of the Es and Ts affects the distance between the E's pole tips.

This measurement could be performed by traditional single points. However, a continuous scanning is more efficient and easy to be understood. Figures 5.22 and 5.23 report as example the measurements of the deviation from the nominal profile by continuous scanning of the full profile of a T-shaped and an E-shaped electrodes.

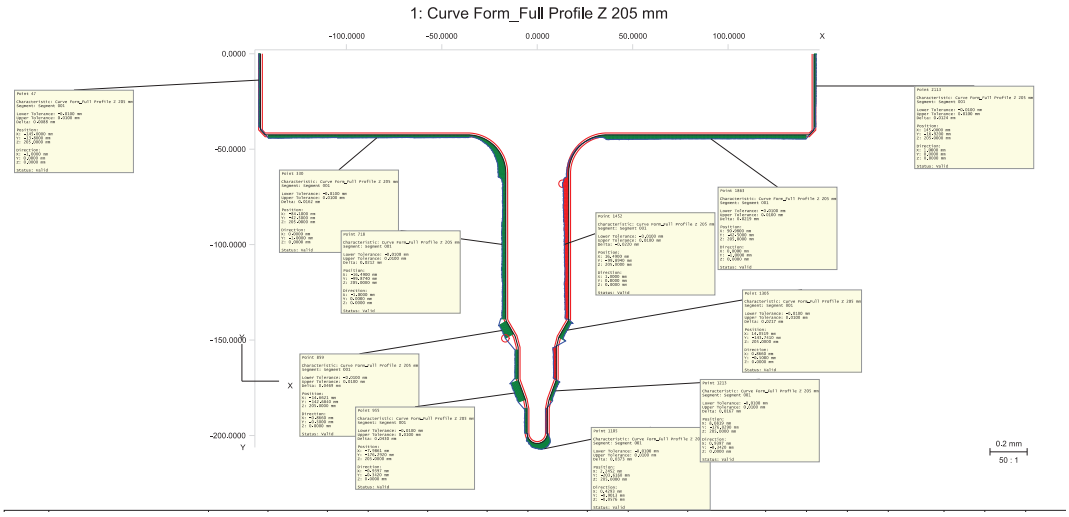

Figure 5.22 An example of the result of the scanning of a full profile for a T-shape electrode

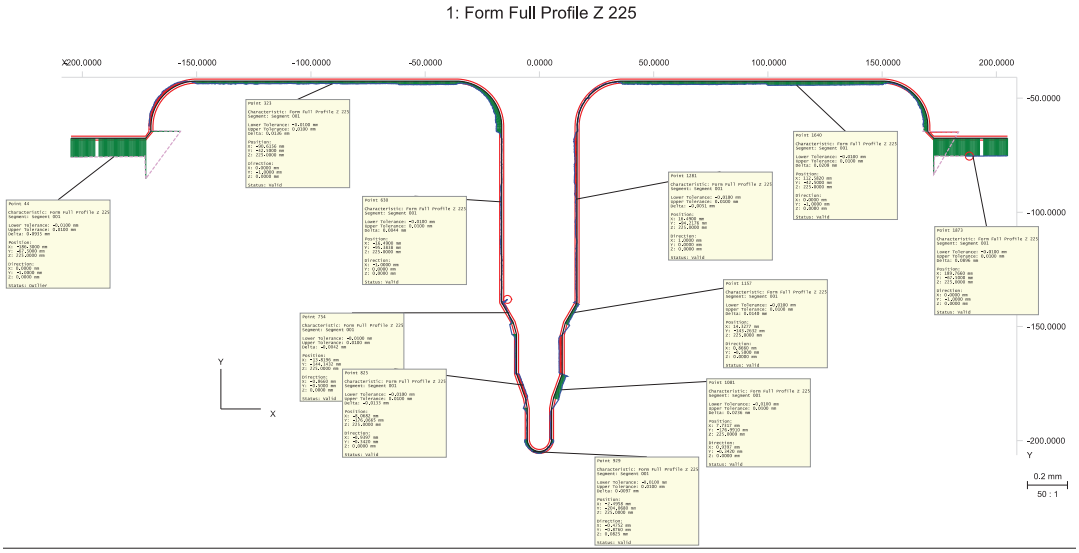

Figure 5.23 An example of the result of the scanning of a full profile for a T-shape electrode

With this type of measurement it is possible to define the position of the pole tip and the position of the brazing planes.

The third aspects is important on the optimization of the alignment of each electrode of the dry assembly of each module, as it will be described on the next paragraph.

From the experience made on the production of the first three modules, the machining of the modulation of the electrodes respect the tolerance of form of ± 10 μm. However, the distance from of the pole tip from the reference plane is not inside the target range of ± 10 μm, but in general machined in a ±20 μm.

Moreover, adding to this machining imprecision, errors can occur on the position of a maximum of on the machining of the brazing planes of the T's, while the shape tolerances are in general respected.

We decided to leave a stock material of 0.1 mm on the brazing planes of the Es. Analyzing the results of the measurements of the profile of the modulation and the full profile, the stock material to be removed from the brazing planes of the Es can be calculated in order to restore the position of the pole tips as close. Such operation was successful, since the amount of the stock material was always removed with errors below ±10 μm.

5.3 "Phase V" of production: the qualification of the dry assembly and the machining for the first brazing step

Once each electrode was qualified, the next step is the construction of the dry assembly. In this phase the 4 electrodes of each module are pre-assembled horizontally on the CMM (figure 5.24).

The optimal alignment of the element is performed by means the CMM, controlling the position of the reference side holes used for the alignment. The T-shaped and the E-shaped electrodes are kept together by means of grinded plates. Tapes of calibrated thickness were interposed between the grinded plates and the electrode in order to perform small adjustments on the relative displacements between the electrodes. In this phase also the errors on the machining of the pole tips of the Ts can be corrected, just sliding the Ts inside or outside the cavity. The system guarantee the positioning of the electrodes in a range of ±15 μm. RF measurements of the resonant frequency were performed by the RF experts of the LNL in order to assure the electromagnetic quality of the cavity and to control the correspondence with the geometrical measurements.

Once the optimal geometry of the cavity is defined, a tooling was mounted in order to lock the assembly to perform new machining operations for the vertical brazing steps (figure 5.24).

Figure 5.24 Dry assembly construction (left) and the cavity locked by the tool after the alignment of the electrodes (right).

In this phase some common zone between the Es and the Ts shaped electrode are machined:

- Some references plane between the back of the Ts and the side of the Es to reproduce the optimal geometry of the cavity and to mount the fixation tooling for the brazing, avoiding relative displacements between the Es and the Ts during the thermal brazing cycle, violet colored in figure 5.25.
- The slots for the two steel frames was also machined in this step in order to avoid misalignments between the Ts and Es, red colored in figure 5.25.
- The base of the cavity that have to be coupled to the support plate was also machined to avoid misalignments between the Ts and the Es, green colored in figure 5.25.

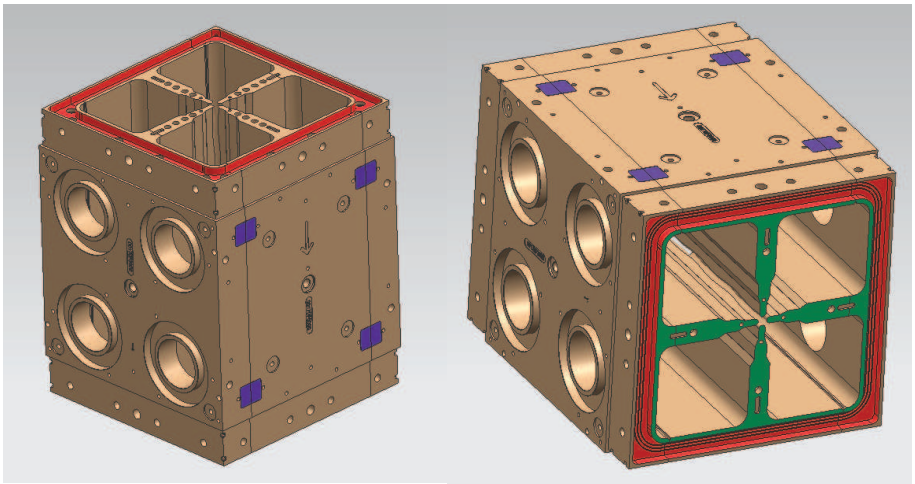

Figure 5.25 Machining of the reference common planes on Es and Ts before the first brazing step

Very precise holes are bored close to the pole tip on each side of the module, in order to quickly monitor the displacements at ends (figure 5.26).

After the machining the assembly undergoes to another CMM survey step to check if the electrodes don't move and to control the quality of the machining step, in particular if the housings for the steel frame respect the design tolerances.

In this phase also the steel frames for the vacuum sealing (figure 5.27) undergo to a dimensional CMM check, since these components will be mounted for the first brazing step.

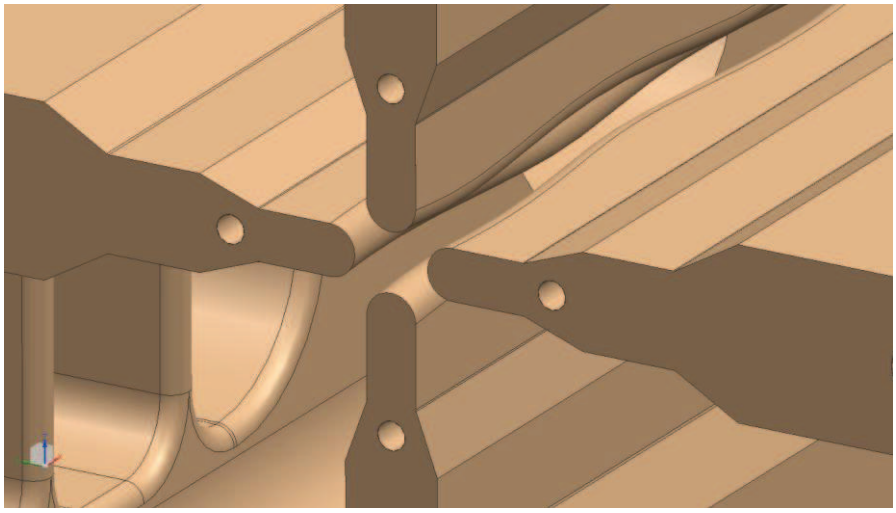

Figure 5.26 Four precise holes bored close the to the pole tips at each ends of the module

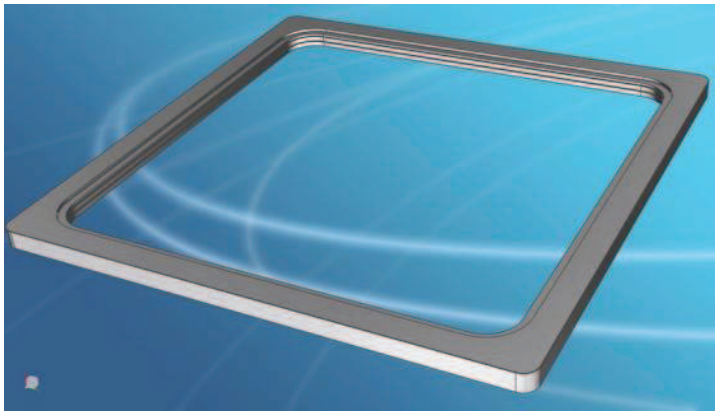

Figure 5.26 The steel frame for the vacuum sealing

5.4 "Phase VI" of production: the first brazing step and the dimensional quality control before the brazing and after the first brazing step

After the machining of the common plane the module is disassembled. Each component is chemically cleaned, the brazing alloy wires are put inside the grooves and then the module and the fixation tooling can be mounted for the first brazing step.

The this first brazing step the copper electrodes, the AISI frames and the copper caps of the cooling ducts are joined together (figure 5.27), using Palcusil 10. For the brazing at the LNL the thermal brazing cycle is performed in collaboration with the LNL expert of the brazing lab with the same methods described on chapter 3 and 4 (1D and 3D FE calculations). Differentiating from the 1st horizontal brazing of the module prototype 1 when only the copper elements were joined, we decided to introduce the steel frame in order to keep in contact together the components, since the integral thermal expansion of the copper and the AISI 316 LN at about 850 ˚C, as mentioned on chapter 3.

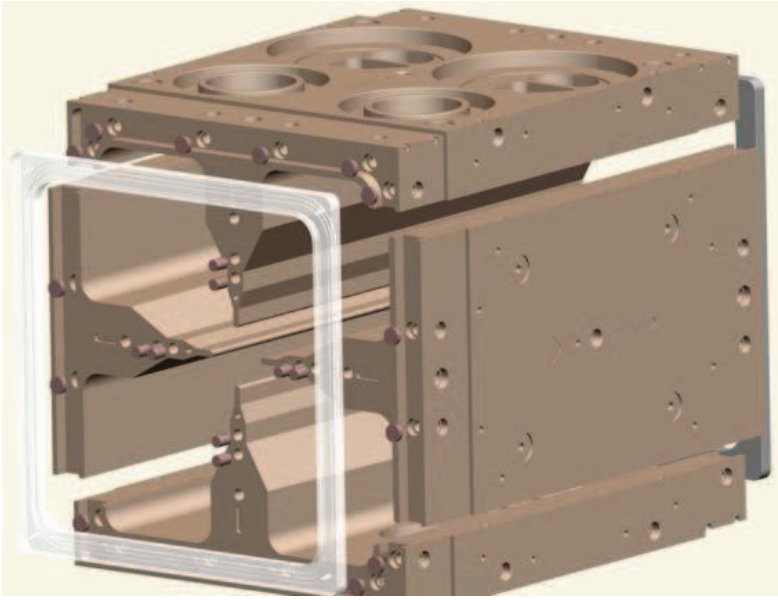

Figure 5.27 Exploded view of the component to be brazed on the first step

The control of the quality of the assembly is very important: the positioning of the brazing wires, the cleansing of the surfaces, the position of the electrodes and of the tooling.

Figure 5.28 shows the brazing tooling and the final brazing assembly. The module is supported on an AISI 316 LN grinded base by means of two layers of Alumina

(in red in figure 5.28, left side). Several AISI tools are coupled to the assembly by means of molybdenum TZM bars and pre-loaded with 150 N Nimonic 90 springs to keep in position the steel frames and to give a major constraint on the relative displacements between the electrodes. Alumina ceramics were interposed between the tools and the assembly to assure a certain thermal insulation.

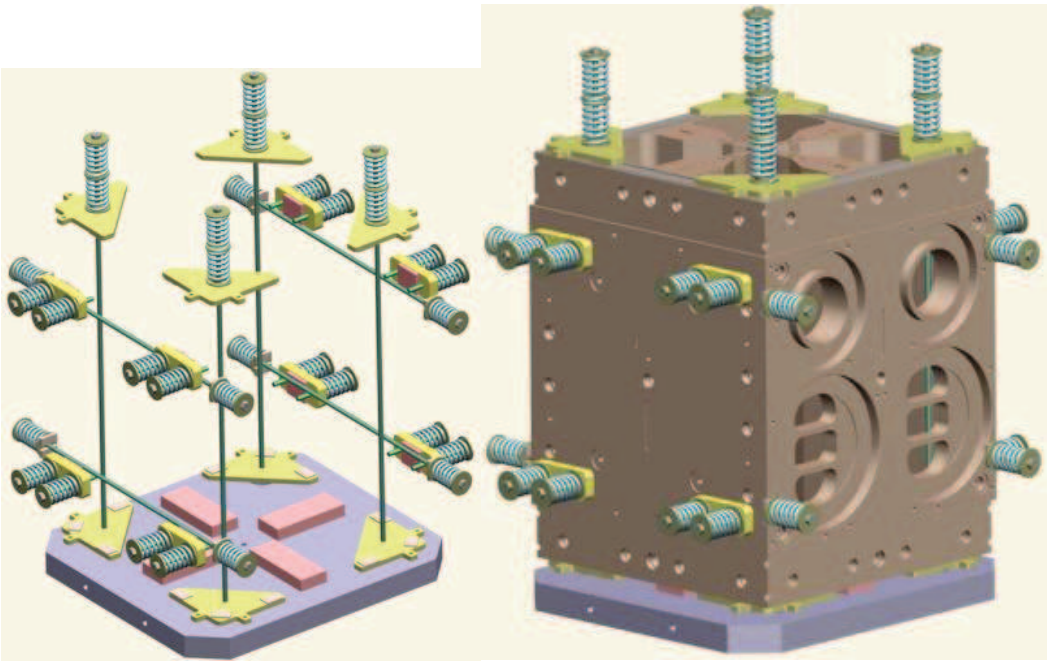

Figure 5.28 CAD models of the brazing tooling (left) and the brazing assembly (right)

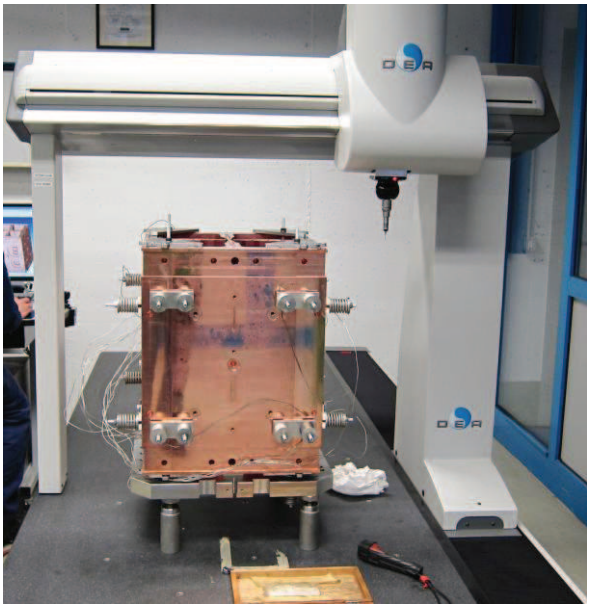

Figure 5.29 CMM survey before the brazing step

Once the brazing assembly is completed, dimensional checks are performed by means the CMM and the portable arm, since it undergoes to many handlings before it reaches the oven (figure 5.29).
The other dimensional check is performed after the brazing in order to control the displacements of the cavity induced by the process, in conjunction with the RF measures.
Optical inspection and vacuum tests are also performed to control the quality of the brazing joints.

5.5 "Phase VII" of production: the second brazing step and the dimensional quality control before the brazing and after the brazing step

In the second brazing steps all remaining AISI 316 LN parts are joined to the module (figure 5.31), such as the side flanges for the connection of the modules, the CF flanges for the connection of the vacuum lines/tuners/RF input, the cooling tubes, the pins for the inserts for the alignment by laser tracker and the pins to couple the module to the support.

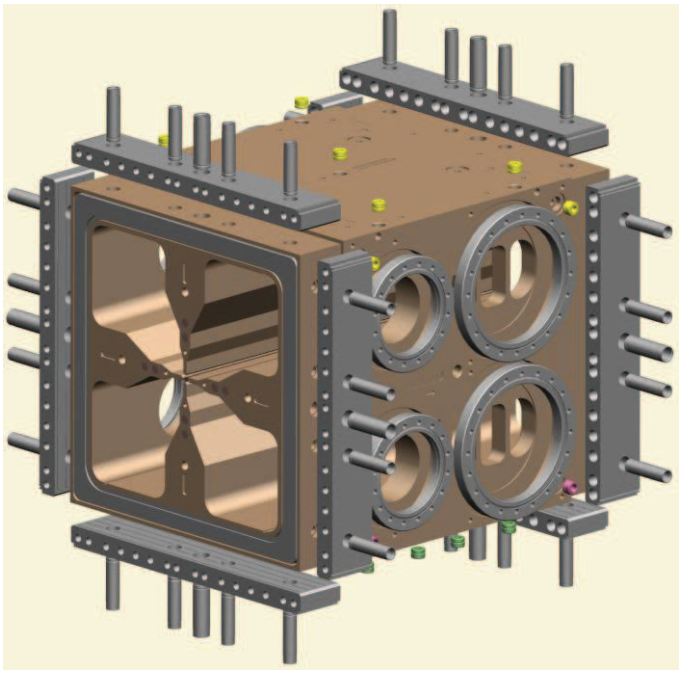

Figure 5.31 Exploded view of the components to be brazed on the second step

Cusil is the brazing alloy, and as for the first brazing steps and for the vertical brazing tests the design of the brazing cycle is performed in collaboration with the brazer of LNL by means of 1D simulations and 3D FE analyses.

Some milling operations precede the preparation of the assembly for the brazing, evidenced in blue in figure 5.32: the machining of the plane for the coupling of the side flanges, the machining of the housings for the CF flanges and the pins for the support and for the laser tracker alignment.

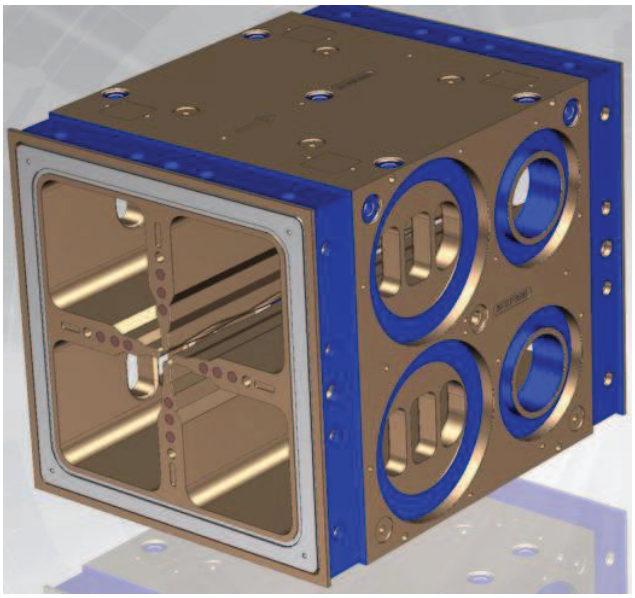

Figure 5.32 Machining operation for the second step brazing

Like the previous phase, accurate inspections on the position of the brazing wires, the cleansing of the surfaces, and the precision on the positioning of the various components.

Figure 5.33 shows the assembly of a module before the second brazing step with the fixation tooling. The design of the tooling came from the experience on the brazing tests of LNL described on chapter 2 and 3 for the fixation of the side bolted flanges. Special molybdenum flat springs were used for the fixation of the CF flanges and the pins for the laser tracker alignment and the coupling to the alignment base plate.

After this phase a CMM survey and RF measurements are performed to control the deformations of the cavity. As after the first step, the modules undergo to another vacuum leak test and to an accurate inspection of the brazing planes.

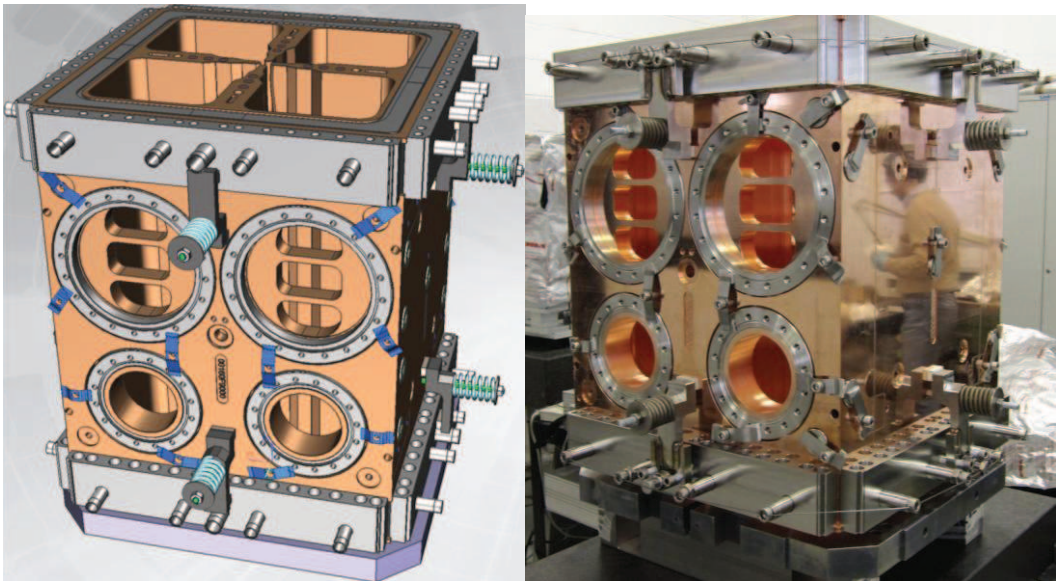

Figure 5.33 CAD view brazing assembly (left) and the module 16 before the second brazing (right)

5.7 "Phase VIII" of production: the machining after the second brazing and the qualification of the final module

In this phase, four AISI corners are TIG welded, providing a stiffer fixed end of the transversal joined section (figure 5.35). Then, according to the drafting attached to the appendix of this thesis, very precise milling operations are performed on this phase. The module is supported on the references of the E (the same used for the finish milling phase) without any element to be machined. Since the tolerances are so tight, we retained mandatory the acquisition of a five axis MMC (figure 5.34), in order to machine all the elements of the module with a single alignment and any reposition of the module.

Figure 5.34 The five axis MMC in the INFN of Padova mechanical workshop

The ends of the modules are machined on (figures 5.35 and 5.36):

- The AISI frames give the final length of the module. The contact occurs in this part when each module is connected to the other. Since it difficult to machine on tolerance all the frame surface, we decided to work only four precise zones (blue colored). The orange zones are machined 0.1 mm below the blue ones.
- The copper electrodes (green colored) are also machined 0.05 mm below the blue zones of the frames to free the thermal expansion of the modules. The total gap on the copper electrodes between two adjacent modules will be 0.1 mm and do not interfere for the beam dynamics. Since the electric field on the pole tips is considerable, radii will be machined on this zone (violet colored in figure 5.37)

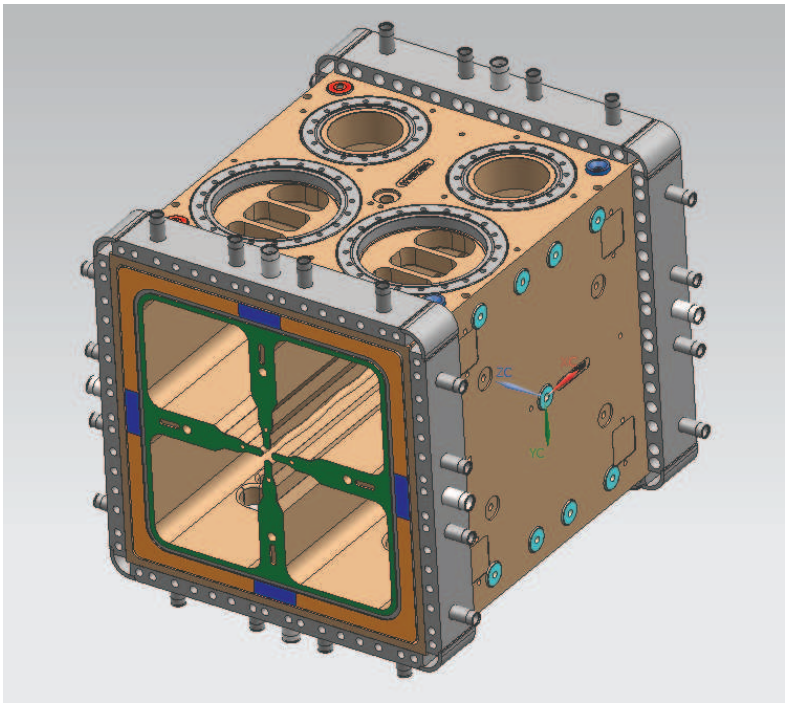

Figure 5.35 CAD model of the final machining of a module

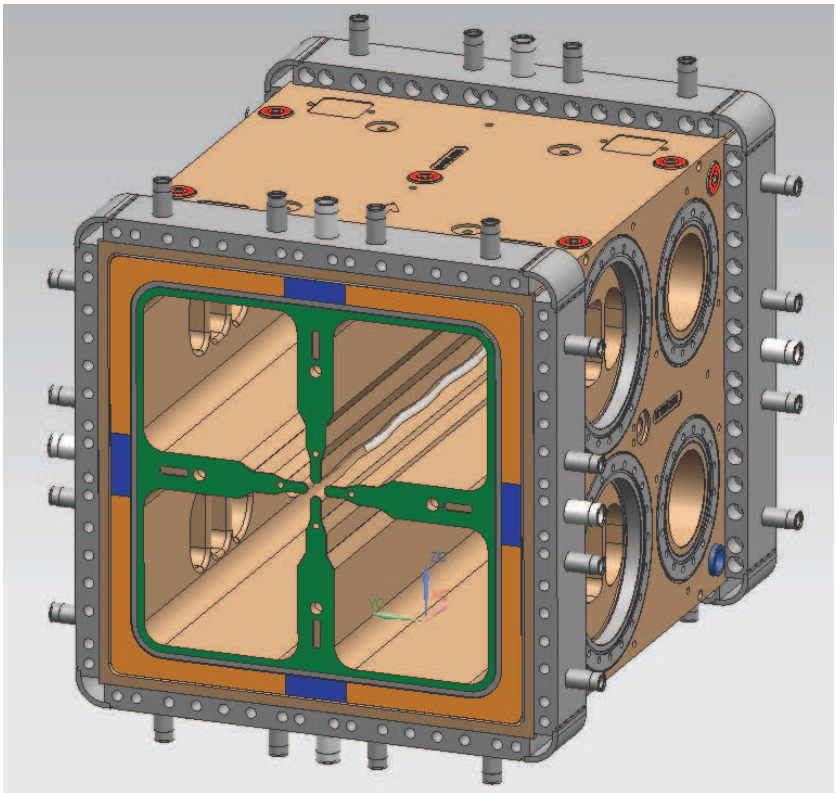

Figure 5.36 Alternative CAD view of the final machining of the module

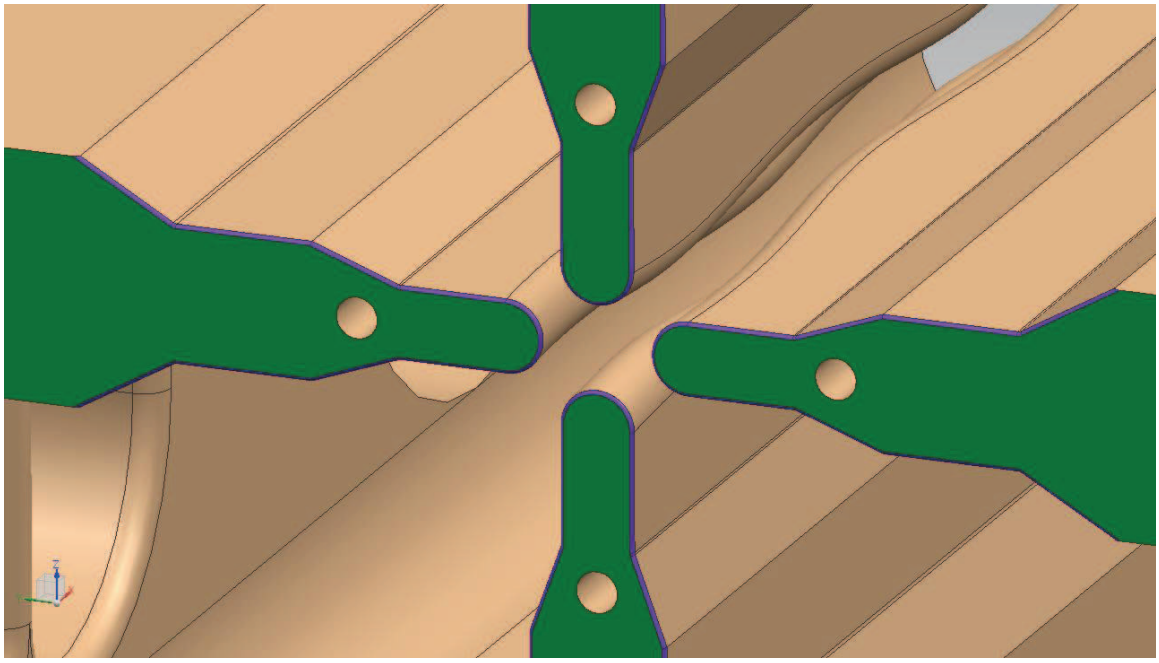

Figure 5.37 CAD view of the radii near the pole tips to machined for the smoothing of the electric field

The other machining operations regard the references for the inserts for the modules alignment systems (red colored on figure 5.35 and 5.36) and the references for the coupling to the support plate for the alignment (cyan colored on figure 5.36).

Once the machining phase is completed, the flanges for the cooling line connections are TIG welded (figure 5.38).

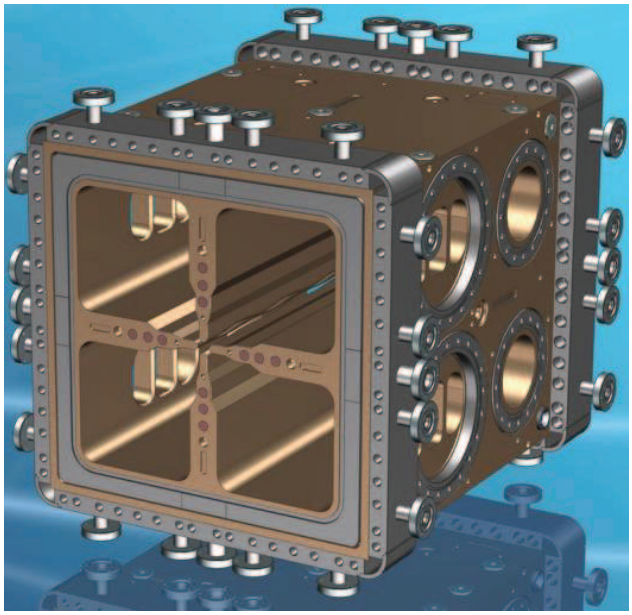

Figure 5.38 CAD model of the final configuration of a module

When all the production phases are completed, each module has to be qualified. Vacuum test is performed to all the parts, including the cooling ducts. The cooling ducts are also pressure-tested with water at 5 bar.

RF measures and CMM survey are performed to check the final frequency of the modules.

The dimensional CMM survey (figure 5.39) is a very important phase for the qualification of a module, not only for the control if the machining is on the design tolerances. The most important part of the dimensional control is the qualification of the position of the beam axis at the extremities of each module from the external references, i.e. the references used for the alignment of the modules by laser tracker.

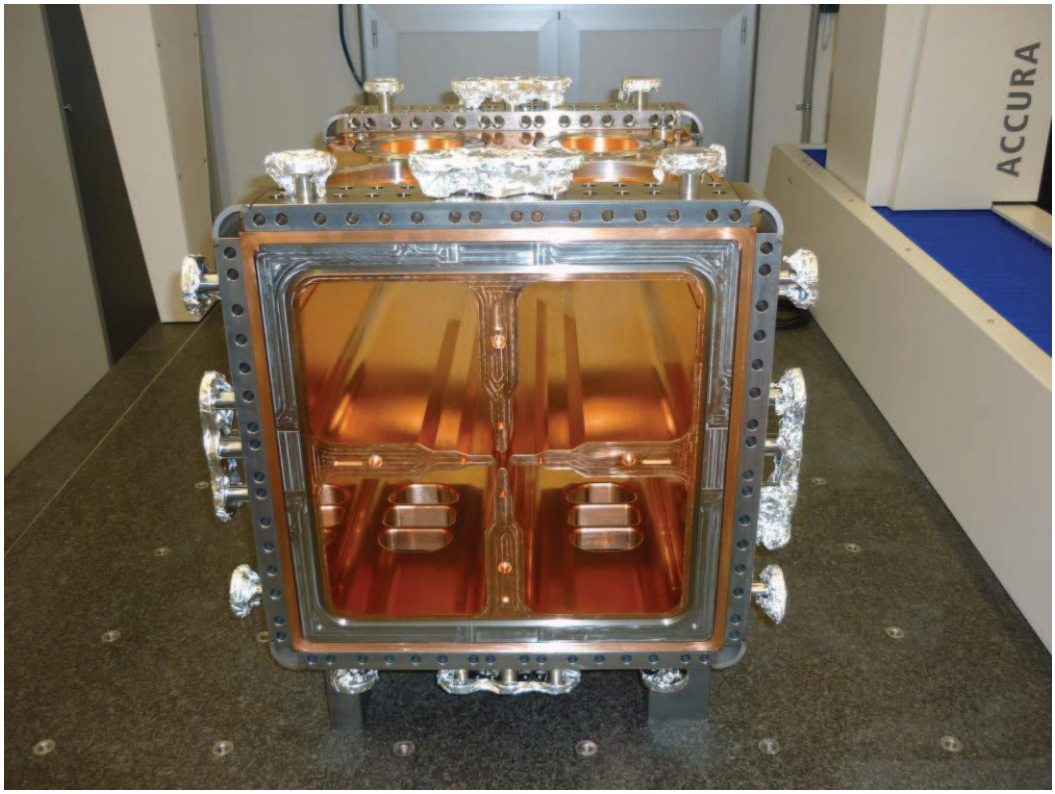

Figure 5.39 The module 16 on the CMM for the final dimensional qualification

5.8 Results of the first brazing of the module 16 and the module 2 of the prototype

In this paragraph the result of the first brazing step of the module 16 and the prototype 2 will be described, and particular care will be given to the measurement of the displacements from before to after the first brazing step will

be presented. The module 16 was brazed by the external farm CINEL who has in charge the production of the high energy super-module (last six module of the line). The prototype 2 was brazed at LNL. Due to some delay on the machining phase for the preparation for the first brazing (phase V) of the module prototype 2, we decided to braze firstly the module 16, i.e. the first final module on the production schedule.

Figure 5.40 shows a detail of the module 16 after the first brazing step with the brazing of the steel frame and of the cooling caps. The optical inspection confirmed an excellent quality of the brazing joint, since the meniscus of the filler was visible along all the brazing lines. The module passed successfully also the vacuum test.

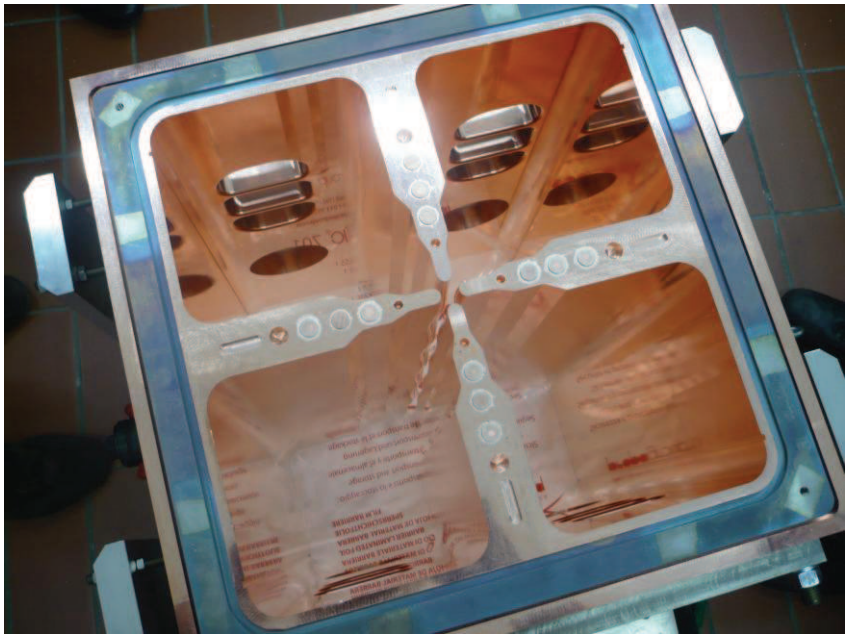

Figure 5.40 The module 16 after the first brazing step

Figure 5.41 reports the nomenclature of the electrodes and the system alignment used on the measurements. Lot of care was used for the definition of the alignment system. The following considerations are valid for the measurement procedures of the other modules of the line, including the prototype 2. We decided to use the same alignment system from the measurements before the first brazing step and for all the subsequent phases. In this way it is possible to monitor what happens to the cavity during the various phases of the production. Moreover, the same references are used for the CMM alignment system and the MMC, for the

same reasons described previously, i.e. the quality control of the machining operations and for the direct feedback on the milling parameters. The system alignment was constructed on the E 9000, by means the same references milled on the phase 4 of the production. Its back face is the only one that does not receive any machining operation on the next phases.

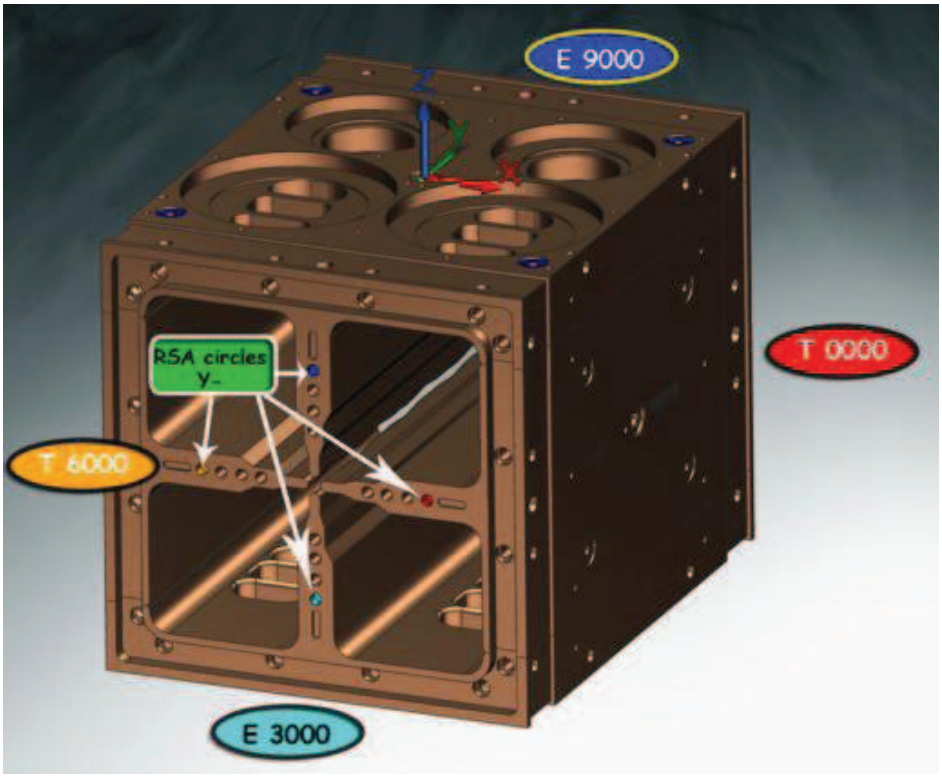

Figure 5.40 System alignment used for the CMM inspection since before the first brazing step until the fully complete module

The position of the reference hole of each electrode at both the extremities of the module were measured, in conjunction with the small holes close to pole tips, in order to have a simple measurement of the displacements of the pole tips.

Figure 5.41 and 5.42 reports a scheme of the displacements measured on the references holes on the Y- and Y+ sides of the module 16 induced by the first brazing step.

Similar values resulted from the holes machined close the pole tips on phase 5. However, these measurements were less accurate: an appropriate stylus small enough to enter on the holes was not available. Calibrated pins were mounted on such holes, but the errors of 0.01 mm on the repeatability of their positioning.

The Y+ side corresponds to the bottom face on the brazing assembly that was coupled to base AISI plate by means of ceramics.

The displacement of figures 5.41 and 5.42 are representative of the displacement of the pole tips, considering the vane is a rigid part that follows the vessel deformation.

A different behavior of the top and the bottom of the cavity (considering the brazing assembly) on the Ts was registered. The problem is quite absent on the Es, with maximum differences of 15 μm.

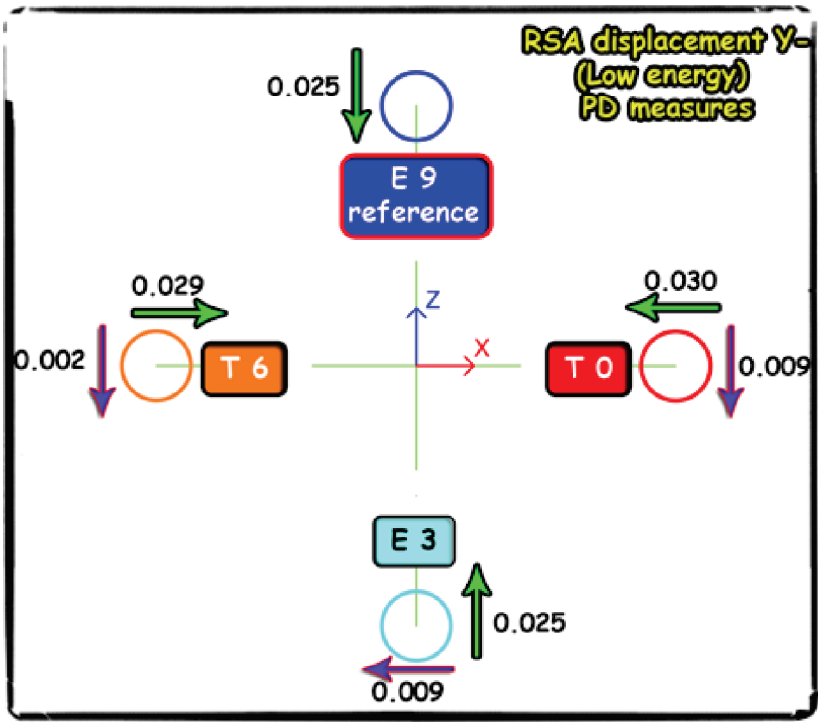

Figure 5.41 Displacements in [mm] of the reference holes of the electrodes on the Y- side

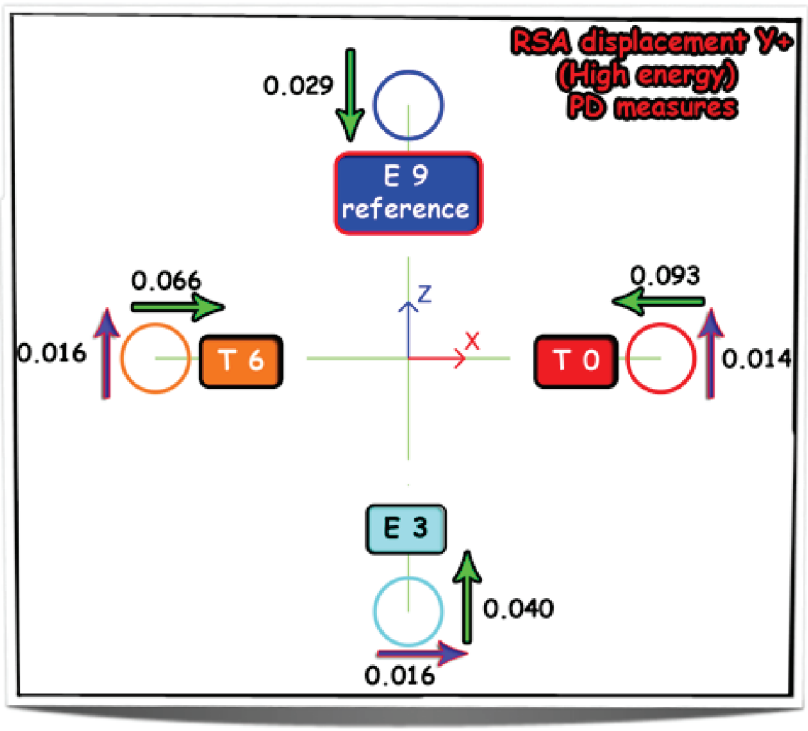

Figure 5.42 Displacements in [mm] of the reference holes of the electrodes on the Y+ side

In addition several longitudinal and transversal scans were performed (figures 5.43 and 5.44), in order to control the inside deformation of the cavity. The pole tips cannot be accessed for the CMM measurements, and the displacements can be related to those measured with the transversal profiles and the longitudinal profiles. Such assumption is true, excluding the zones near the steel frames at the extremities, and confirmed by the measurements of the deviations on inclined plane near the pole tip. The measures of the profiles confirmed a linear trend of the displacement of the profile between Y- and Y+ side.

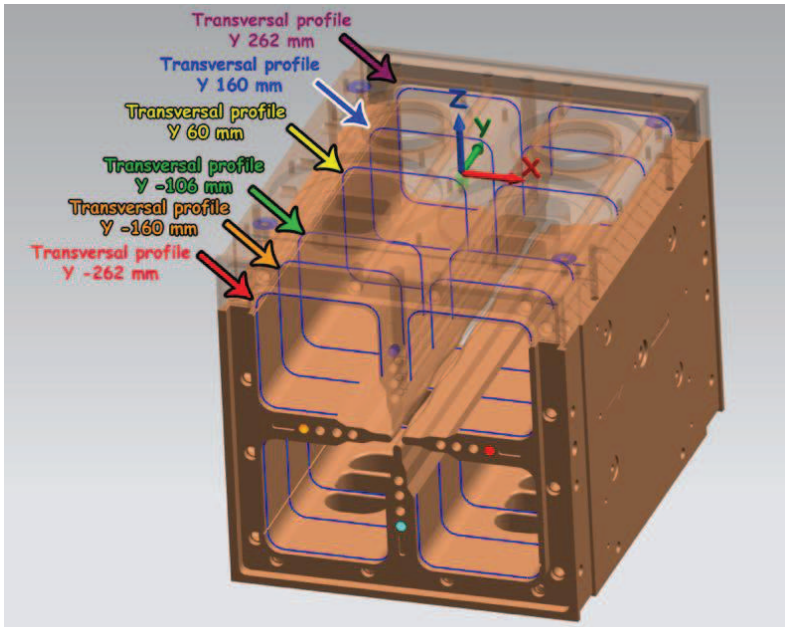

Figure 5.43 Transversal profile scanned by the CMM

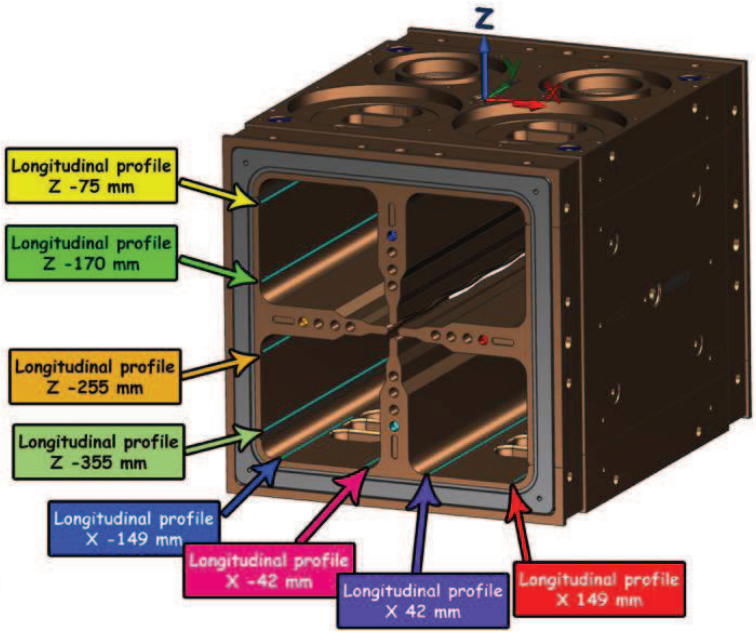

Figure 5.44 Example of longitudinal profile for the qualification of a module

The displacements measured on the module 16 after the first brazing were acceptable for the point of view of the resonant frequency, since it can be compensated by the tuners. We still tried to correct the problem of different deformations between the top and the bottom of the assembly. We thought that the friction with the alumina ceramics or an effect of constraint on the cavity by

the different thermal expansion by the steel frame during the brazing thermal cycle could be the possible causes.

An improvement was tried with the brazing of the module prototype 2, including a layer of 0.1 mm of graphite between the each couple of ceramics to reduce friction.

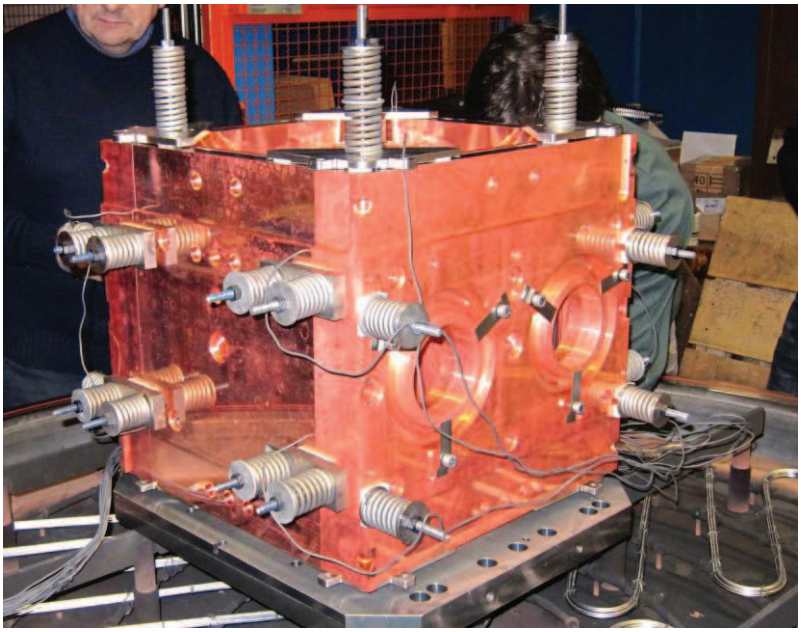

Figure 5.45 Module prototype 2 assembly on the LNL oven

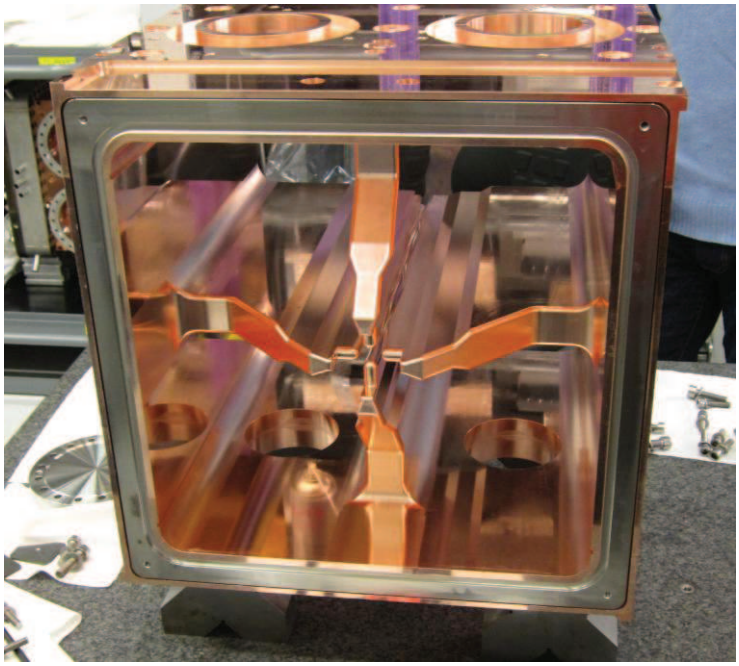

Figure 5.46 The module prototype 2 after the first brazing step

The first step of the brazing of the module 2 was performed at LNL (figures 5.45 and 5.46). As for the module 16, the prototype 2 was visually inspected. The joints, especially on the top side of the assembly, seemed perfectly brazed, and the meniscus of the metal filler was visible on all the brazing lines. An excessive accumulation of the brazing alloy was registered on the bottom of the assembly. Figure 5.47 and 5.48 evidence the aspect mentioned before: an unexpected flow occurred at the interface of the bottom steel frame, since large zones near the base of the electrodes accumulated large quantity of brazing material. Also the joints for the plugs of the cooling ducts showed an irregular wetting with large voids between the parts, and the brazing material was removed by capillarity by the alumina. Unlike the module 16, the caps for the cooling ducts were on the bottom side of the brazing assembly, since the module 2 of the prototype presents the termination cell for the closure of the electric field (figure 5.46).
In spite this defects, the module passed successfully the leak test.

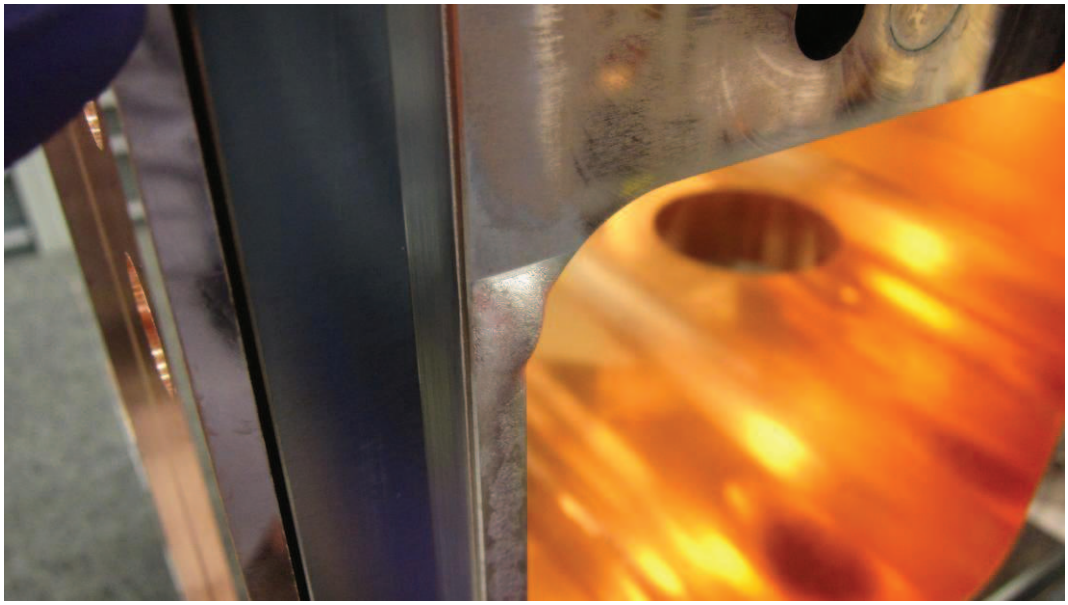

Figure 5.47 The accumulation of the brazing alloy near the steel frame at the bottom

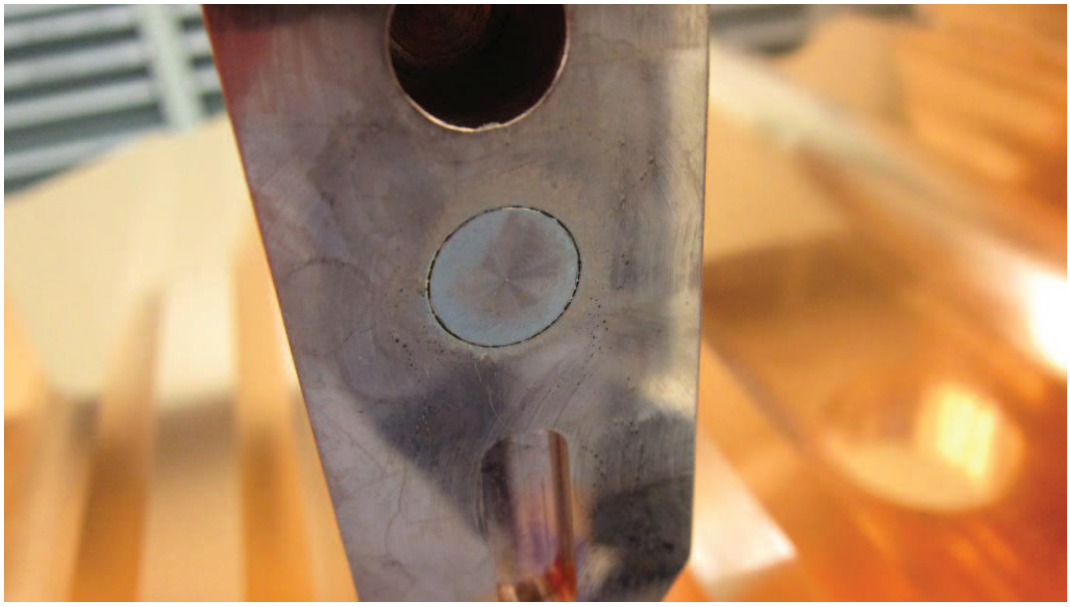

Figure 5.48 The poor brazing on the copper plug for the cooling ducts

Like the module 16, dimensional inspections were carried out to measure the displacements of the cavity induced by the brazing cycle. Since a CMM was not available at LNL, the PCMM was used and the displacements of the Ts relative to the Es were measured on the reference common planes, considering each E as reference. Figures 5.49 and 5.50 show the results.

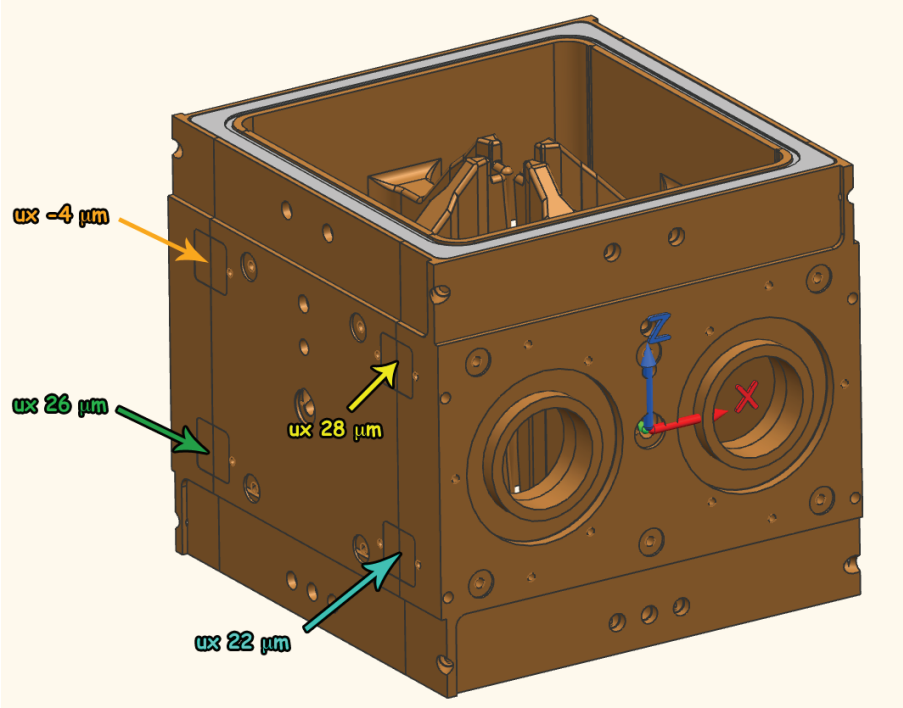

Figure 5.49 Displacement on X- side of the T-shaped electrode respect the two Es of the module 2 of the prototype after the 1st brazing step

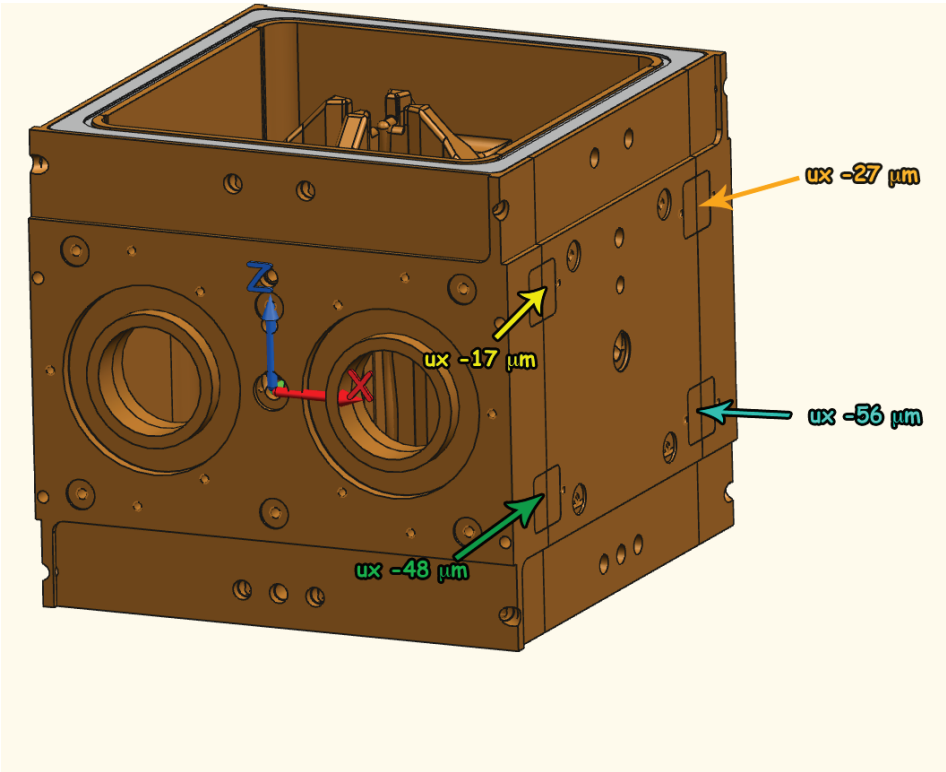

Figure 5.50 Displacement on X+ side of the T-shaped electrode respect the two Es of the module 2 of the prototype after the 1st brazing step

Also in this case, as for the module 16, a difference on the displacements of the Ts between the top and the bottom of the assembly was present mainly because of the different dilatation of the steel frame at the bottom of the assembly. However, as for the module 16, the frequency is not compromised since it can be compensated by the tuners.

5.9 The second brazing of the module 16: problems encountered and the third repair brazing

We decided to perform the second brazing of the module 16 before than module prototype 2, because of an accident on our MMC, so the machining operation for the second brazing could not be completed in time.

As reported on paragraph 5.8, in this phase the remaining AISI parts are joined to the cavity.

After the brazing, some defects were registered on the module:

1. A vacuum leak on one of the CF 150 flange (used for the connection of the vacuum lines)

2. A reduced brazed surface on the side flanges for the connection of the modules each other (an example is on the following figure 5.54).

The first defect could be easily repaired by brazing a small ring on a third thermal cycle at lower temperature (using InCuSil[2] 10 as metal filler).

Although we didn't have any explanation on the first defect, we thought that the causes of such defects could be related to:

- The stability of the AISI 316 LN plates, related to some problems on the stress release thermal cycle before the brazing.
- The different thermal expansion of the plates respect to the copper during the thermal cycle. Initially we thought to couple the steel plates into a copper groove (figure 5.49), in order to keep better the component in position. Unfortunately the respect of the coupling tolerance was not controlled, and since the steel parts heat and expand faster than copper inside during the brazing cycle, they could be forced to detach from copper.
- Problems on the fixation tooling to keep in position the steel plates.

For what concerning the second defect, since a repair could not be so easy, an accurate evaluation of the extension of the brazed surface was mandatory to calculate the mechanical resistance of the flanges. Visual inspection and ultrasonic tests were performed.

Figures 5.51 and 5.52 show the reference geometry used of the examined component, with the same orientation (top and bottom faces) it was inside the oven for the brazing cycle.

[2] Incusil 10, composition: 63% Ag, 27%Cu, liquidus: 730 °C, solidus: 685 °C

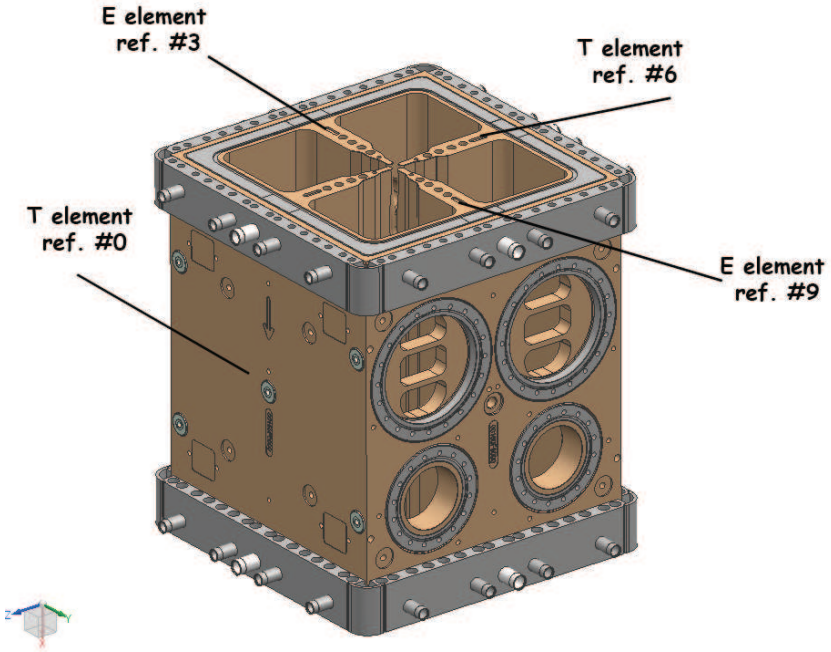

Figure 5.51 References used for the electrodes of the assembly

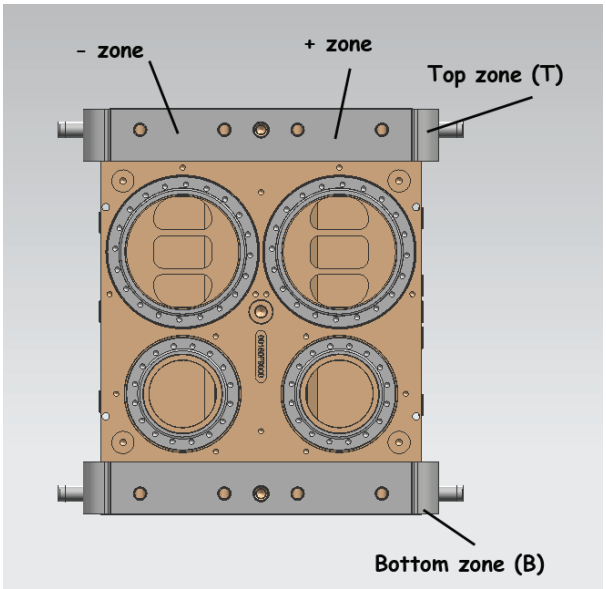

Figure 5.52 References for the different zones of the assembly

However, the UT tested zones were limited by the diameter of the transducer and the holes for the bolted connections (figure 5.53). In fact, since a small transducer with enough energy for the transmission of the signal was not available, a 2MHz with an external diameter of 40 mm was used. The analyses were performed through points on lines between the holes for the bolted connections.

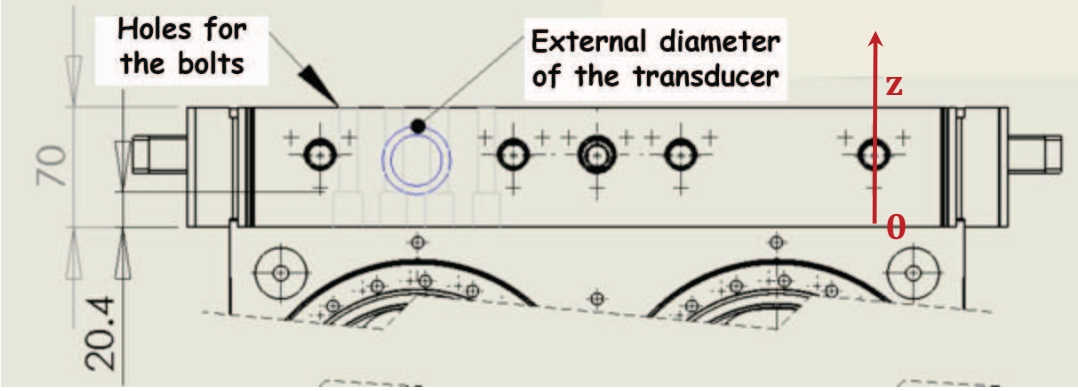

Figure 5.53 Detail of the measured zone with the position for the holes for the bolted connections (grey colored), the dimension of the transducer (blue colored) and the reference system for the measure (red colored)

As on figure 5.52, in this way the possibility of measure the steel flanges on two zones: one left (- symbol) and one right respect to the beam axis (+ symbol). Moreover each side of the RFQ presents two steel flanges: one on the top (T) and one on the bottom (B). Finally, the convention for the lateral faces of the RFQ (#0, #3, #6, #9).

Firstly, each flange was visually inspected by means a luminous torch to evaluate the brazed surface. The flange at the top of the E9 was judged as the worst one and the visual inspection showed that at least 30% was not brazed (figure 5.54).

Figure 5.54 Visual inspection of the top flange (T) on E9 side

Ultrasonic analyses were performed to investigate more precisely the extension and the quality of the brazed surfaces. On the following table (table 5.5) the type, setting of instrument and transducer (figure 5.55) are listed:

Instrument	Olympus Epoch 1000
Transducer	CN2R-24
Frequency	2 MHz
Diameter of the crystal	24 mm
Overall dimension of the transducer	40 mm
Energy	450 V
Damping	400 Ω
Mode	Puls/Echo
Wave type	square

Table 5.5 Instrumentation and measuring setting used

Figure 5.55 Instrumentation used

The transducer was calibrated by two AISI 316 LN blocks of well-known thickness to fix the zero and the velocity of the sound on the medium. Figure 5.56 shows an example of a measure on a flange on side E9B+ (bottom face E9 side, on the right respect to the beam axis).

TEST	

File:MOD16-CINEL

Description:

Inspector ID:000

Location Note:CINEL

24/02/2012 11:15

Id:000

1%	52.75	1TH	26.91	2TH	77.04	2%	96.00			Unit:mm - UT	

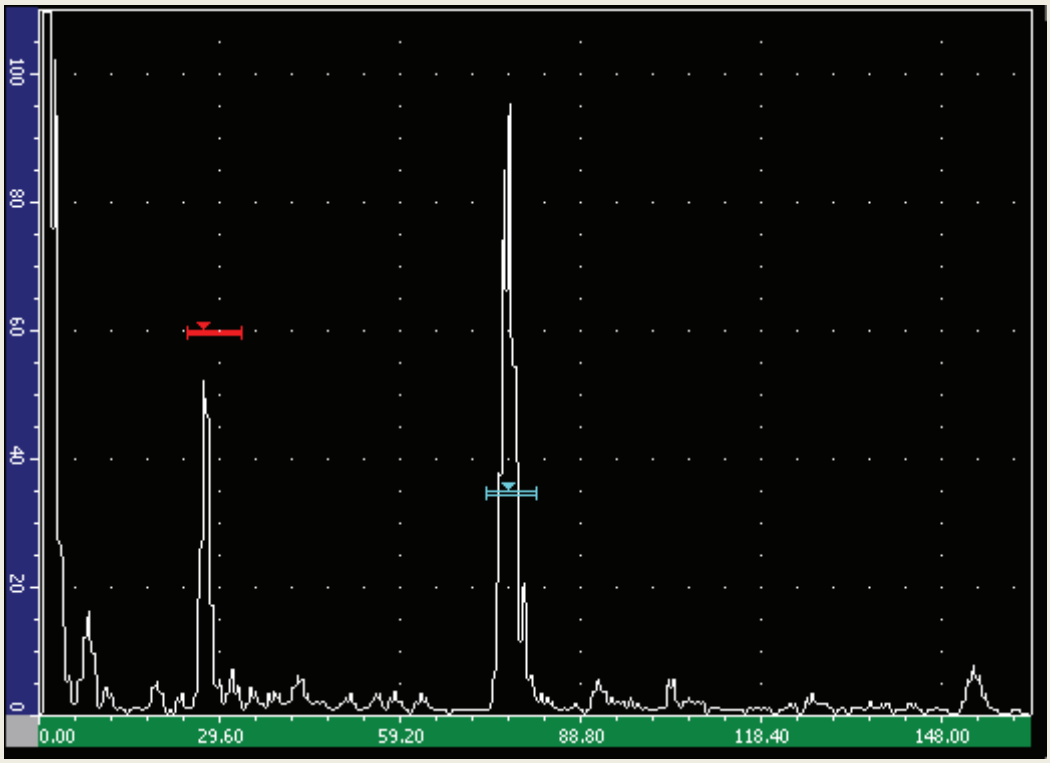

Delay:0.00		Range:148.00
Gain:30.6dB	PRF:480Hz	Mode:P/E
Velocity:5789m/s	Freq:2.00MHz	Filter:1.5-8.5
Zero:1.153µs	Energy:450V	Rect:Full
Angle:0.0°	Damp:400Ω	Thick:0.00
Reject:0	Pulser:Square	

Start:24.17	Width:9.20	Level:60%	Alarm:Off	1
Start:73.31	Width:8.64	Level:35%	Alarm:Off	2

Figure 5.56 Example of a UT measure on zone 9B+.

In this case two backwall at two different positions echoes are distinguishable: the first one at 27 mm and the second one at 77 mm. The first echo corresponds to the steel-copper brazing interface, while the second one to the reflection of the internal surface of the cavity. These lengths are similar to the geometrical ones shown on figure 5.57. The distance of the second backwall echo differs from the real geometrical measure because sound waves are slower on copper (v = about 4700 m/s).

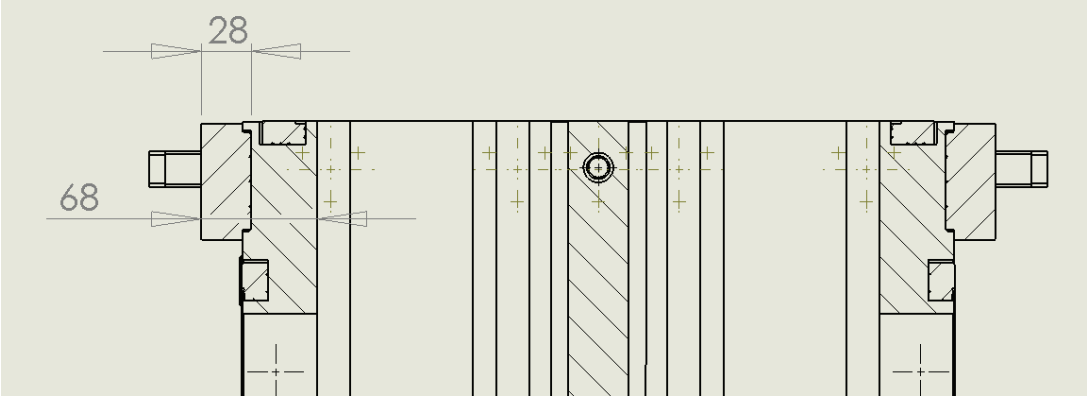

Figure 5.57 Geometrical distances of the measured echoes

We found that in general the joints of the flanges at the bottom side were better than the top. In particular the top flange on the E#9 was the most critical. According to figure 5.53 linear scans were performed to register the trend of the signal of the response echoes.

The following echoes were registered as function of z:

- The first backwall echo of the copper surface at 77 mm.
- The second backwall echo of the steel-copper interface at 54 mm.

The second backwall echo was chosen because less sensible to the coupling between the steel and the copper, since it is reflected two times.

The measures of the top flange of the E#9 were compared to those of the bottom flange on the same side. Since in this case the steel-copper coupling was good, the first backwall echo at the interface wall was used.

The position of the transducer was the same as in figure 5.48 and its position (z) was measured by a caliber (± 2 mm).

The measured values are expressed in arbitrary units of intensity to allow the comparison between different echoes measured with different amplifications. In

fact, considering that the output power by the transducer is constant, the power of the response to the power sent ratio is expressed by:

$$R\ [a.u.] = P[\%] \cdot 10^{-\frac{G[dB]}{10}} \qquad (5-1)$$

where P is expressed in percentage units of the full scale and G is the gain of the amplifier.

Following figures (5.58, 5.59 and 5.60) show the results of the analysis of the measures on the different zones.

The following consideration can be done:

- From the scan of the zone E9 T+ side the response echo of the copper disappears for z > 10 mm. The steel echo consequently increases and the steel-copper interface is not coupled.
- The scan on E9 T- side show an opposite trend of the two echoes and the end of the brazed zone can be estimated on a value of z between 30 mm and 40 mm.
- The scan on E9 B+ side shows a good coupling between copper and steel.

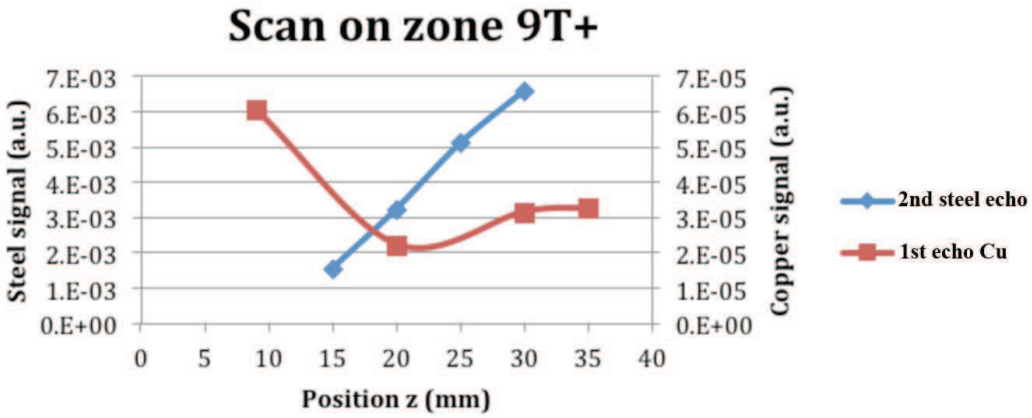

Figure 5.58 Graph of the trend of the two response echoes on the top (T) flange on E#9 + side.

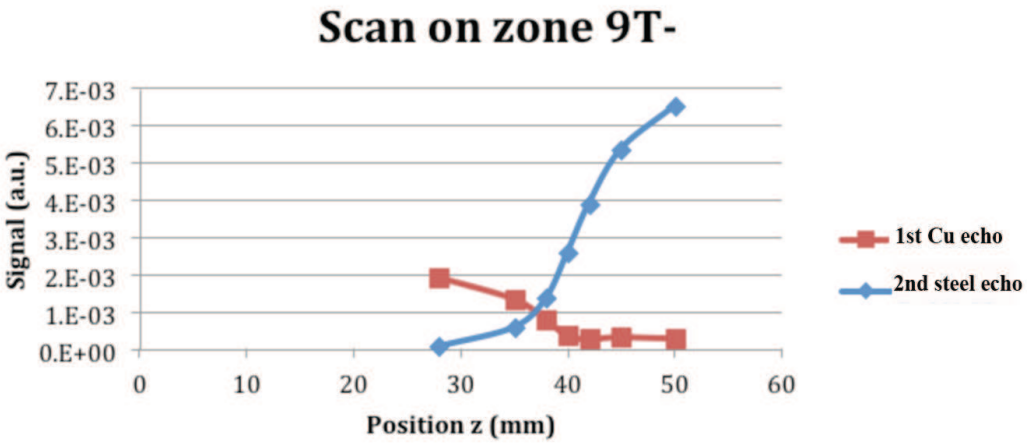

Figure 5.59 Graph of the trend of the two response echoes on the top (T) flange on E#9 - side.

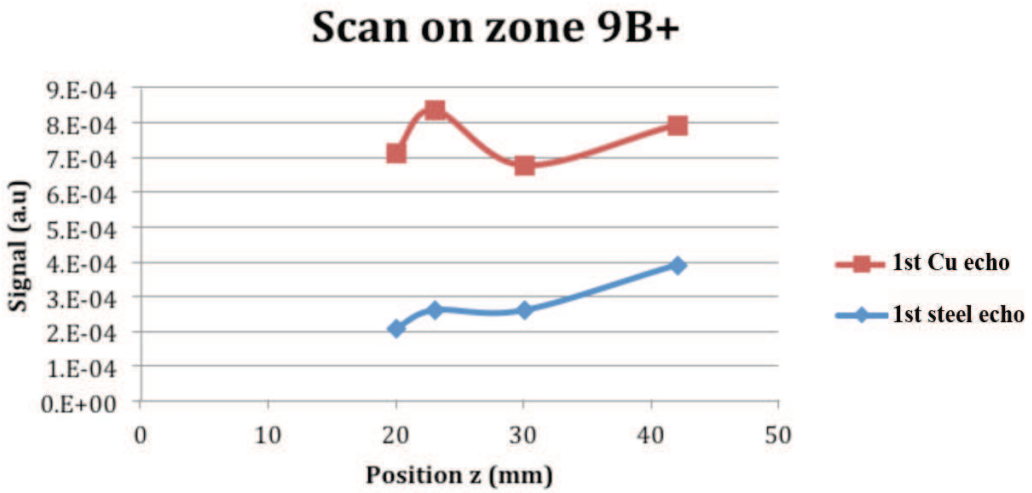

Figure 5.60 Graph of the trend of the two response echoes on the bottom (B) flange on E#9 - side.

In conclusion, the ultrasonic measures gave a better estimation than the visual inspection of the effective brazed surface between the steel and the copper. However a more accurate inspection was not possible, due to the complex geometry of the components and since a small transducer was not available.

The flange at the top of the E9 side presented the largest defects: at least 50 % of the left zone (-) was brazes, while the right one (+) for 10 mm to a total of 70 mm. With this indications we retained that the joint of the top flange at the E9 side could not support the load necessary to compress the Helicoflex vacuum seal.

We decided to restore the mechanical coupling of the flange by brazing (on the same thermal cycle for the repair of the vacuum leak on the CF flange) a series of steel pins (figures 5.61 and 5.62). Such operation was performed on each side flange, since another brazing cycle could lower the resistance of the existing connections.

The third repairing brazing cycle was successful:

- The module passed successfully the leak test
- The restoring of the mechanical connection on the side flange was successfully empirically tested: the vacuum test was performed using the Helicoflex seal, so the loads on the flanges was the same as on the operating conditions.

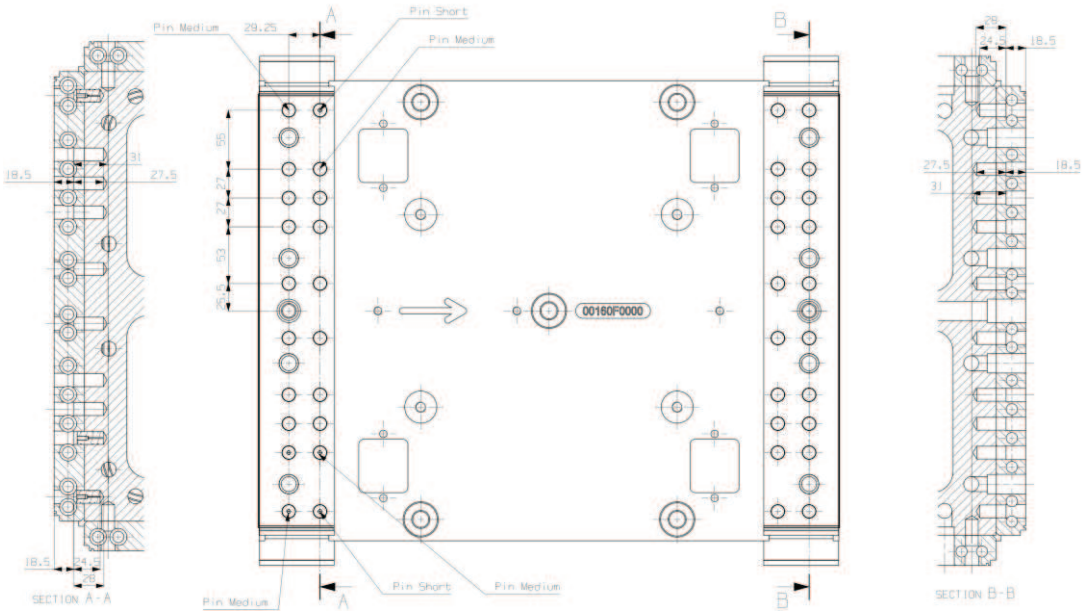

Figure 5.61 Overall drafting of the repair of the side flanges mechanical connections

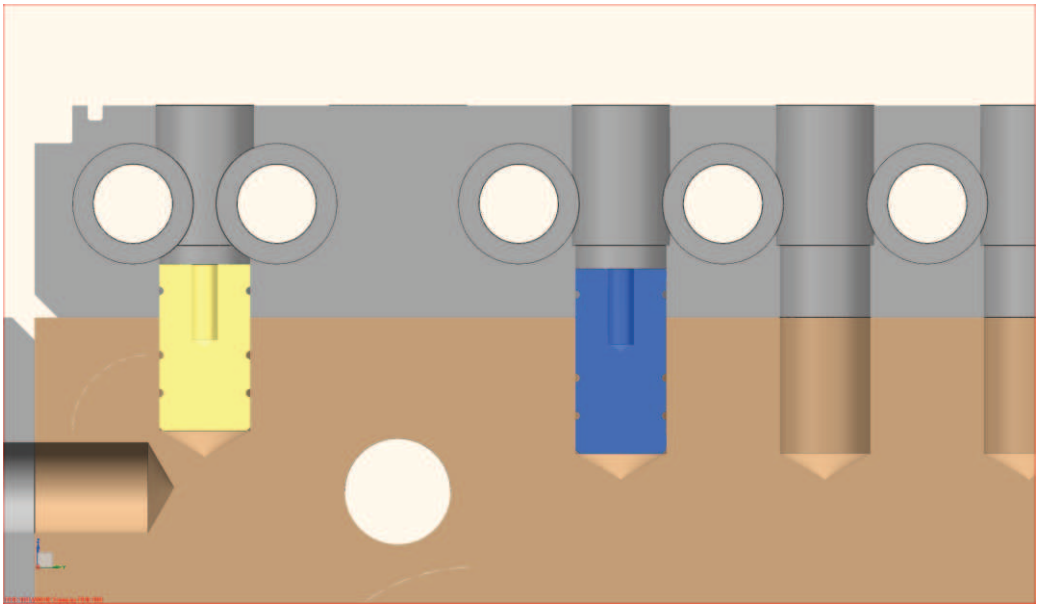

Figure 5.62 Detail of a section view of the repair of the AISI side plates mechanical connection

For what concerning the dimensional control, it was performed only after this third brazing step.

An enlargement of the cavity with displacement of the each electrode in the order of 0.1 mm was found.

However, besides this problems, the module fulfill the specifications in term of frequency and geometrical tolerances.

Figure 5.63 shows the trend of the deformation measured on module 16 after the third brazing phase. It was difficult to reconstruct what happened with this module, since any measure was performed after the second brazing and after the machining operation for the repair.

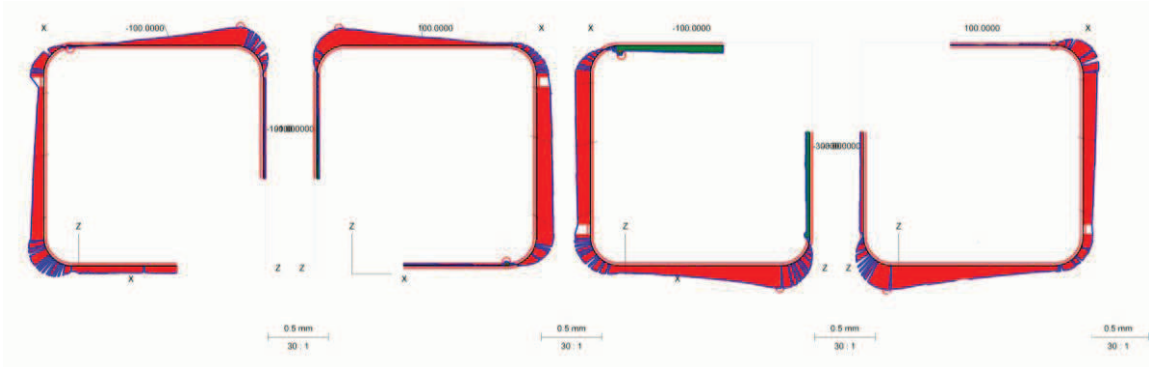

Figure 5.63 Form of the enlarged cavity after the third brazing cycle

We thought that the problem was related to the different thermal expansion between the copper and the AISI 316 LN. We thought that the real values that describe the different thermal expansion were not the same as described on chapter 3. A deep research was performed on the literature on the values of the thermal expansion between the copper and the stainless steel, and it seems that the different thermal expansion at high temperature was best represented by the following figure 5.64.

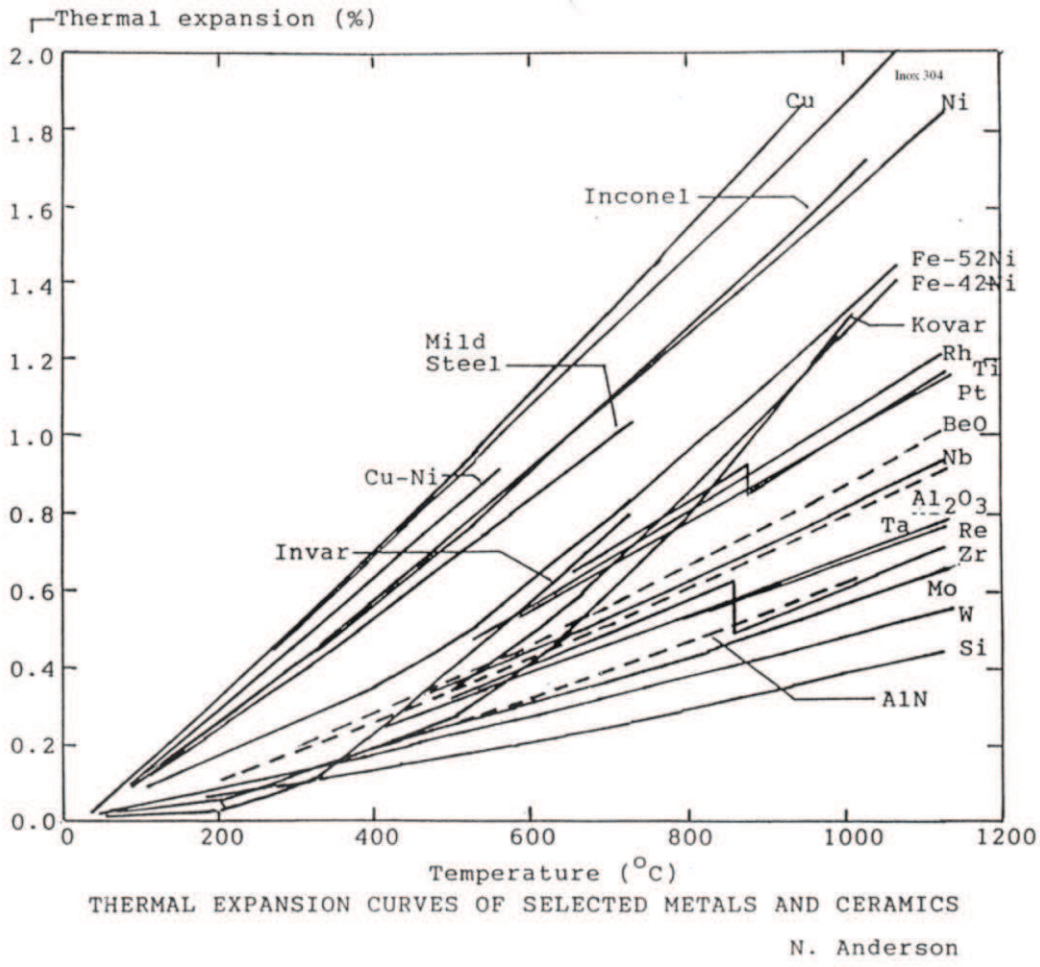

Figure 5.64 Thermal expansion of different materials[3].

[3] S. Sgobba, "Materials for high vacuum technology: An Overview", CAS-CERN Accelerator School and ALBA Synchrotron Light Facility: Course on Vacuum in Accelerator, Platja d'Oro, Spain, 16-24 May 2006, pp. 117-144

5.10 Improvements for the second brazing step: the second brazing of the prototype 2

After the problems of the second (partial brazing of the side flanges) and the third brazing steps (deformations of the cavity) of the module 16, we decided to introduce some improvements on the second brazing step: on the design of the steel flanges and the fixation tooling for the brazing assembly.

Due to the detachments of the steel side flanges on the second brazing of the module 16, we decided to change the design of such components, returning to the old solution of the module 1 of the prototype (figure 5.65). The coupling of the steel flanges into a groove on the copper was removed. With this solution the brazing area is increased, since only the part that coupled to the copper groove was considered to be brazed (figures 5.54 and 5.57).

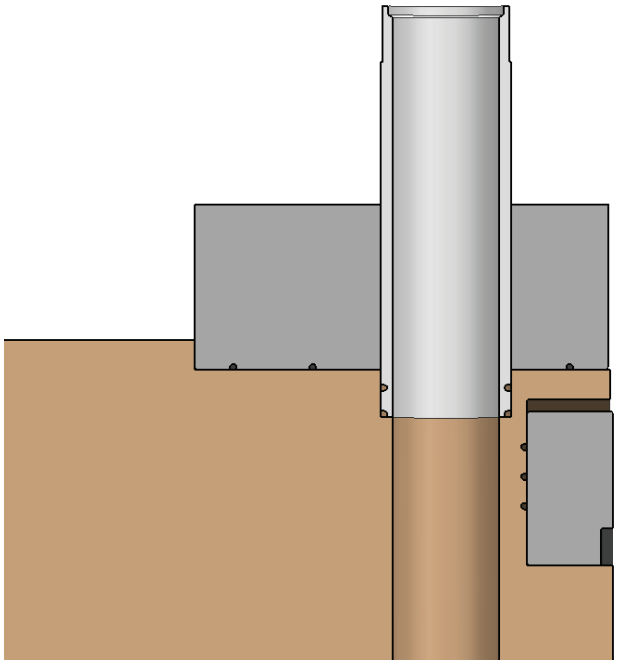

Figure 5.65 Section view of the module with the new design of the side flange

The other development on the design of side flanges regarded the reduction of the deformation of the cavity due to the different thermal expansion at the brazing temperatures between the copper and the steel.

We though to reduce the stiffness of the steel plates introducing some EDM cuts (figure 5.66).

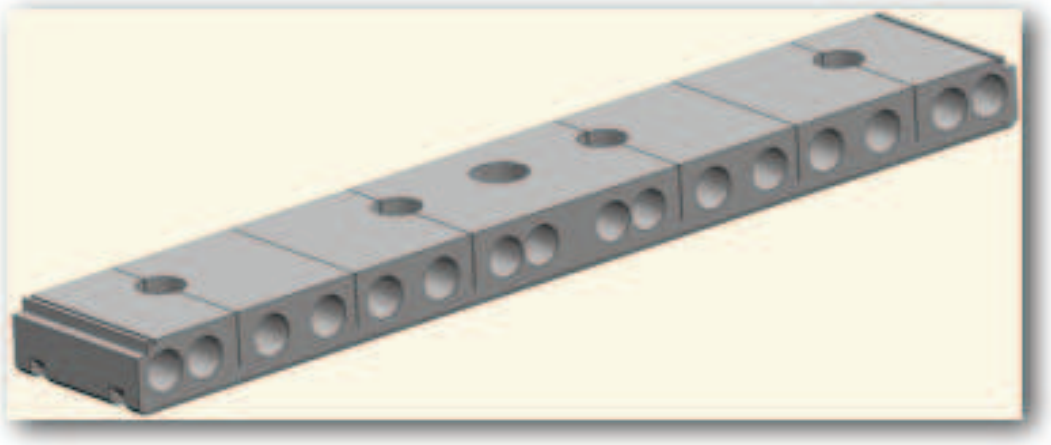

Figure 5.67 The new design of the side flanges with the EDM cuts to reduce the stiffness

This EDM cuts was performed only on the flanges of one only side of the prototype 2, in order to control the different effects on the deformation of the cavity. In particular the flanges without the cuts were mounted at the top of the assembly, on the zone of the termination cell: if larger deformations due to the differential thermal expansion occur, the frequency is less affected on this zone (figure 5.68).

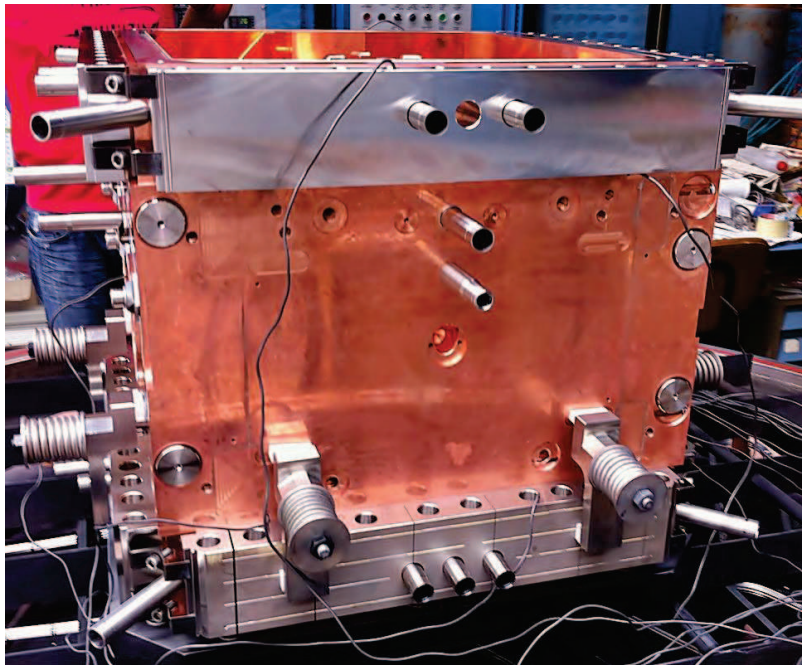

Figure 5.68 The brazing assembly of the prototype 2 on the LNL oven. The flanges with the EDM cuts are on the bottom side, while the flanges without cuts are at the top side.

Due to the problem of the detachment of the steel flanges on the second brazing of the module 16, we decided to develop a new fixation tooling for these flanges. Figure 5.69 shows the assembly that will be used for the second brazing of the module 17.

Special Molybdenum TZM springs were designed to keep the flanges together. The idea was to exploit the different thermal expansion (figures 5.70 and 5.71) between the AISI and the TZM. FE simulations were used for the optimization of the stiffness to estimate the load they give to the steel flange.

This kind of tooling presents lot of advantages than the previous one:

- It is easier and faster to mount.
- The TZM do not suffer creep even at 850 ˚C.
- The heat transfer by radiation to the components is much more uniform

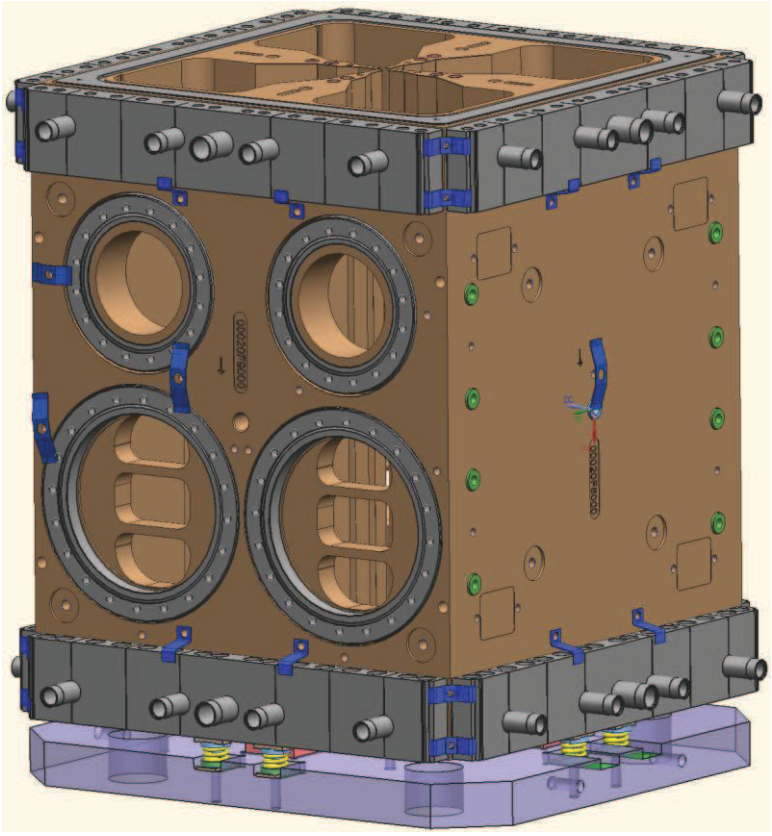

Figure 5.69 The brazing assembly for the second brazing of the module 17 with the new improvements

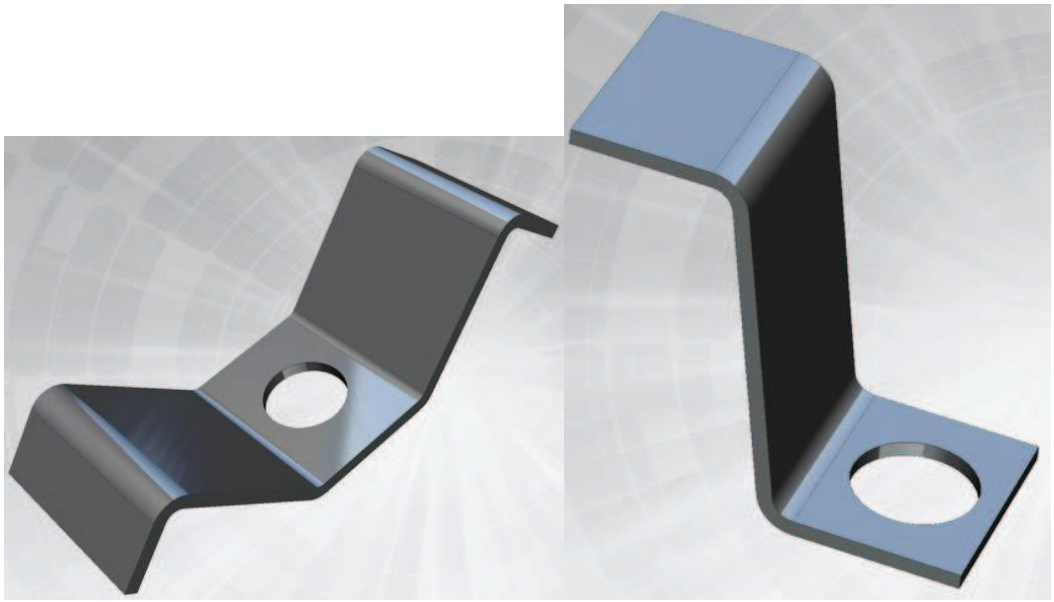

Figure 5.70 The TZM Molybdenum springs used to keep in contact the side flanges

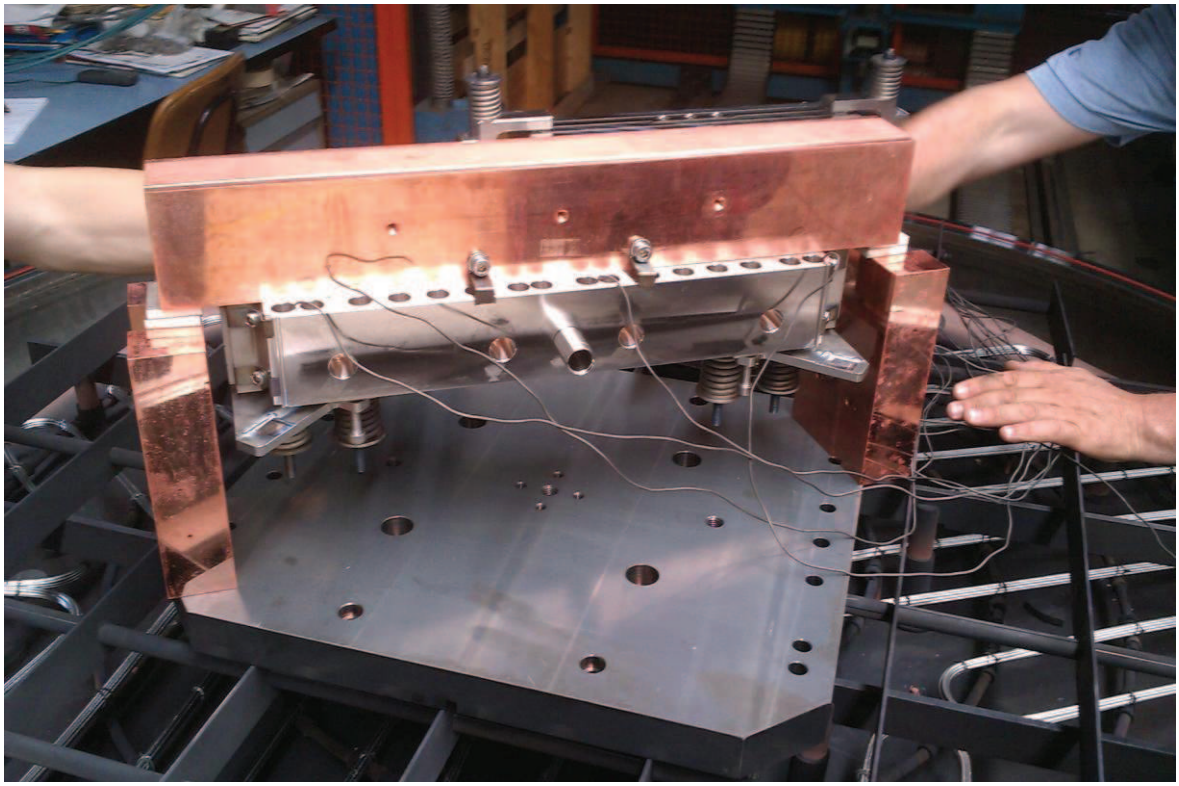

Figure 5.71 The brazing test for the new fixation tooling

A first brazing test (figure 5.71) was performed the new fixation tooling using Cusil as brazing alloy. Successful results were obtained from the functional point of view of the tooling. The tooling guaranteed a sufficient force to keep in contact the steel flanges. For the quality of the brazing point o view, discrete results were obtained. The adhesion of the steel parts was seemed to be quite discrete with some zones not joined, but an excessive accumulation of the brazing alloy was registered on the bottom of the assembly. Unfortunately no pictures were taken to document these problems. However, we thought that the problem could be related to an excessive time above the melting temperature of the brazing alloy.

The improvements on the fixation tool were tested also on the second brazing (with Cusil) of module of the prototype (figure 5.68), although partially: the new springs in the middle could no be mounted also on the second brazing step of the prototype 2 (figure 5.68).

The new fixation tooling worked well and any detachment of the side flanges was registered.

Due to the problems related to the test of 5.71, the expert of the brazing lab of LNL decided to reduce the permanence of the components above the melting temperature of the brazing alloy. Unfortunately, the problems in this case were even bigger. Poor brazing has been observed on the copper-side flanges joints and on the copper-steel tubes, since vacuum leaks were registered. A tape of 1.01 mm calibrated thickness could be inserted for about 15 mm on one of the flanges on the top side (figure 5.72) and the brazing alloy flew down from the same flange (figure 5.73).

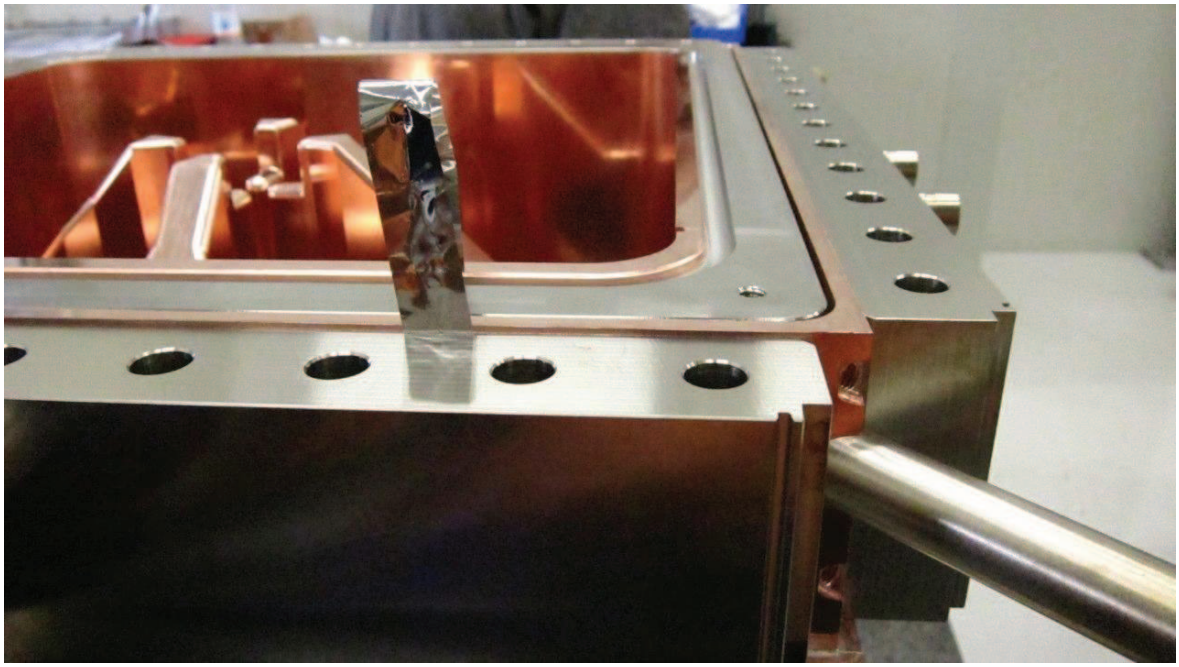

Figure 5.72 Poor brazing on one of the flanges at the top. The calibrated tape of 0.01 mm thickness could be inserted on the coupling surfaces for about 15 mm.

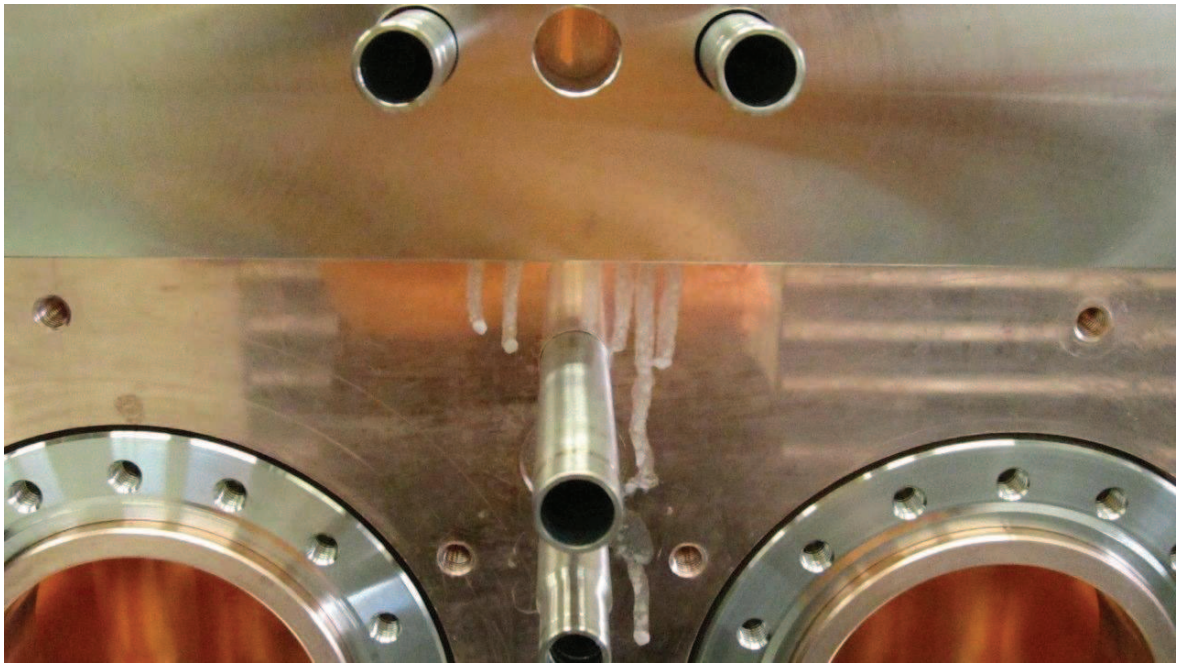

Figure 5.73 The flow of the brazing alloy from the same flange of figure 5.72

Ultrasonic inspection were also performed, to investigate with major accuracy the quality of the copper-steel side flanges joints. Respect to the analysis after the second brazing on module 16, a small transducer was available (a probe with an

external diameter of 6.25 mm and 5 MHz was used), while the remaining instrumentation was unchanged.

The calibration of the measure was made on the backwall echo at the interface of a not brazed joint. Then several points were measured on each flange (figure 5.74). The quality of the brazing joints was made considering the attenuation of the echo at the joint interface respect to the not brazed echo.

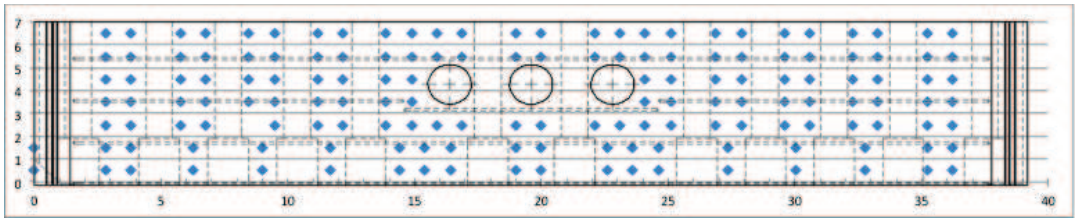

Figure 5.74 Example of measured points on one of the steel flanges. The positions on the horizontal and the vertical axis are expressed in [cm]

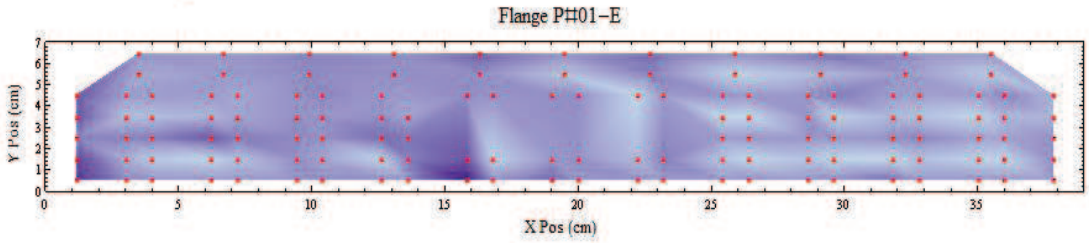

Figure 5.75 Result of the ultrasonic measure of a flange of the prototype 1

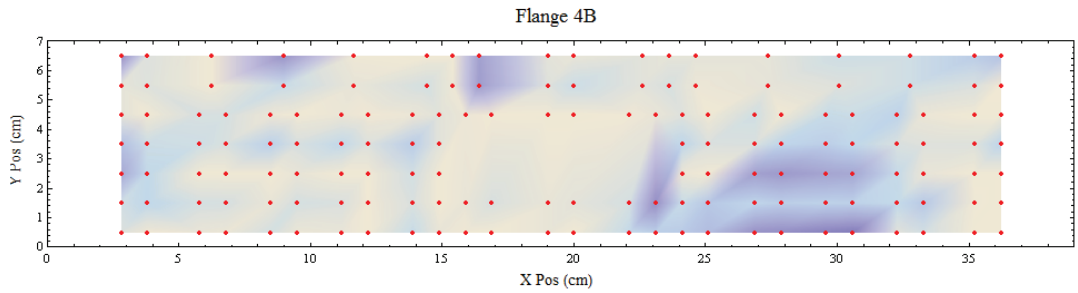

Figure 5.76 Result of the ultrasonic measure of the worst flange of the prototype 2

Figure 5.77 Strenght of the reflection of the peak at SS-Cu interface

The figures 5.75 and 5.76 show the result of the attenuation (according to the scale of figure 5.77) of the peak at the interface of the copper-steel side flange on one flange of the prototype 1 and the worst flange of the prototype 2. Other flanges of the prototype 1 were also UT inspected and the results were similar to that reported on figure 5.75. Comparing the results on the flanges of the prototype 1 and the prototype 2, the last one show large zones that are not brazed, since the very low attenuation of the signal. We attributed to this fact to a poor wetting of the steel by the brazing alloy. The prototype 1 UT measures demonstrate a good coupling between the steel and the copper, since the wetting and the adhesion of the steel by the brazing alloy is good.

The difference of the prototype 1 by the prototype 2 is that the surfaces to be brazed of the steels were nickel-plated in order to increase the wetting and the adhesion of the brazing filler. Some discussion are still opened on the necessity of the nickel-plating of the steel. Taking into account our experience, the CERN experience, nickel-plating is necessary if the brazing temperatures are below the 800 ˚C (as for Cusil).

We decided to restore the nickel-plating on the brazing surfaces of all the steel components of the next module 17.

CMM inspections were performed to control the differences on the deformation on the two different zones. Figures 5.78 and 5.79 show the result of an analysis performed by Mathcad software. The figures plot a magnification (using a factor of amplification of 100) of the deformation of the cavity after the second brazing respect to the nominal geometry (corresponding to real geometry after the first brazing) in correspondence of the middle of the flange with cut and without cut.

Analyzing the case of the side with flanges with cuts, the nominal curve and the blue curve are quite overlapped, and maximum displacements of 15 μm were measured.

Analyzing the profile in correspondence of the flange without cuts, a relevant enlargement of the cavity was measured.

Although the deformation was not symmetrical, the total enlargement (about 130 μm) for each side was conserved. The introduction of the cuts on the flange was a considerable benefit for the reduction of the deformation of the cavity.

Another time the use of the metrology with a continuous scanning probe CMM revealed to be very important for the design of the modules.

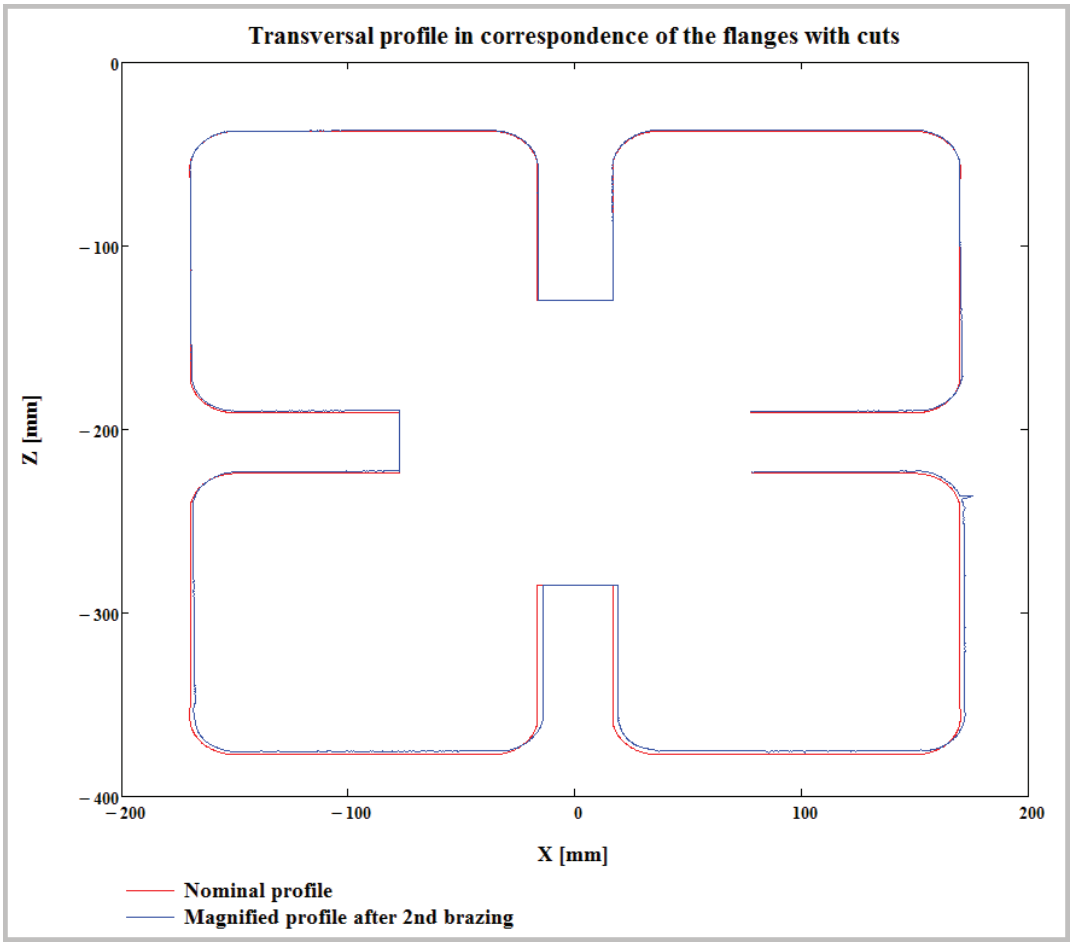

Figure 5.78 Magnified deformation of the cavity after the second brazing of the module 2 of the prototype respect to the first (nominal) on the bottom side (flanges with cuts).

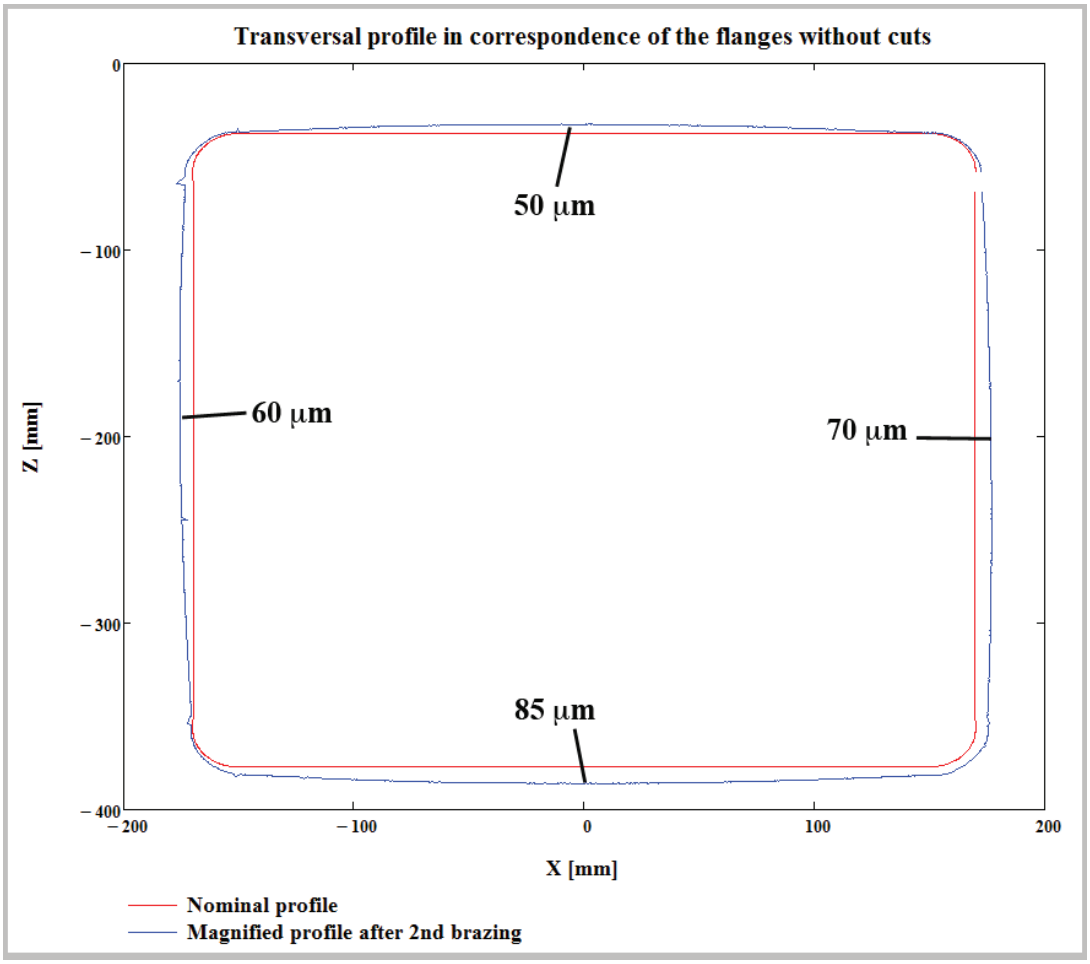

Figure 5.79 Magnified deformation of the cavity after the second brazing of the module 2 of the prototype respect to the first (nominal) on the top side (flanges without cuts).

5.12 Improvements on the design of the coupling between the AISI frame and the electrodes: the first and the second brazing steps of the module 17

In this paragraph will be described the new improvements and the results on the first and the second brazing step of the module 17, i. e. the second final module that was produced. As the module 16, the finish milling of the four electrodes, the machining operations for the preparation of the brazing steps, finish machining of the module and the two brazing steps were in charge to the external company CINEL.

All the quality assurance phases, such as the control of the brazing assembly and the dimensional control on the various step of the production were in charge to INFN.

The first improvement regards was for the first brazing step. Due to the different thermal expansion during the thermal cycle between the copper and the steel we decided to avoid the contact between the steel ring and the T element, leaving a gap of 0.3 mm. The coupling clearance between on the E side was maintained on 0.03 mm, in order to maintain a certain closure pressure on the brazing assembly (figure 5.80).

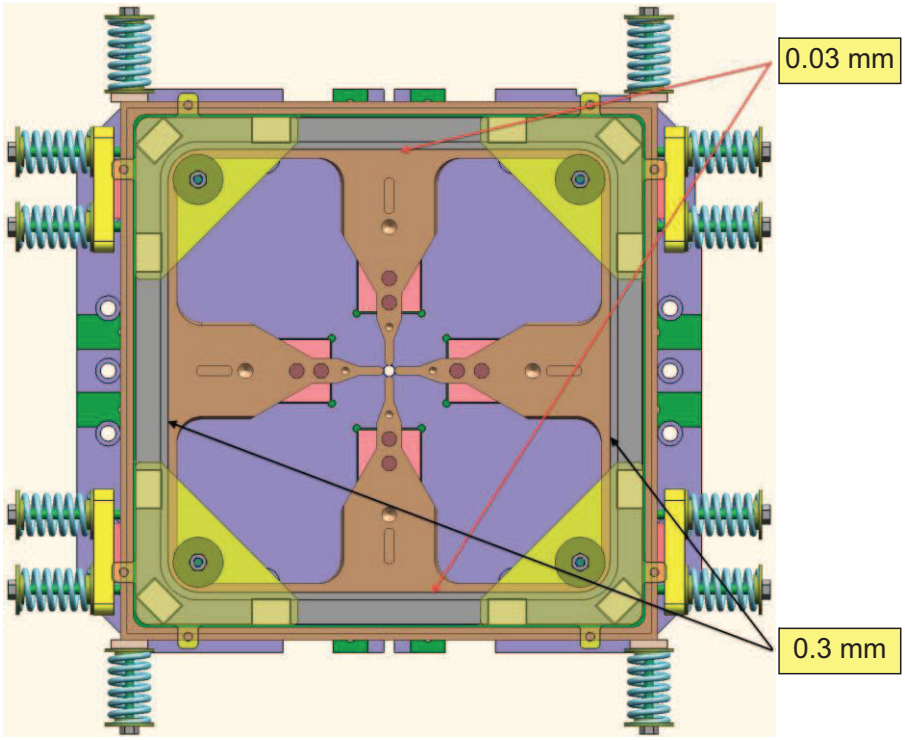

Figure 5.80 The new design of the coupling between the copper and the steel ring

According to figure 5.40, figures 5.81 and 5.82 report the displacement by means of CMM inspections of the reference holes of each electrode after the first brazing step on the Y- and Y+ side. Also for module 17 the Y- side corresponds to the top side of the brazing assembly and the Y+ to the bottom.

Relative displacement between the Ts and the Es was found, but this is not a problem for the frequency and the beam dynamics. What is important is that the different shrinkage between the Y- and Y+ sides observed on the Ts on module 16 and the module prototype 2 was not on module 17. The improvements on the

design of the coupling between the copper assembly and the steel frame were successful.

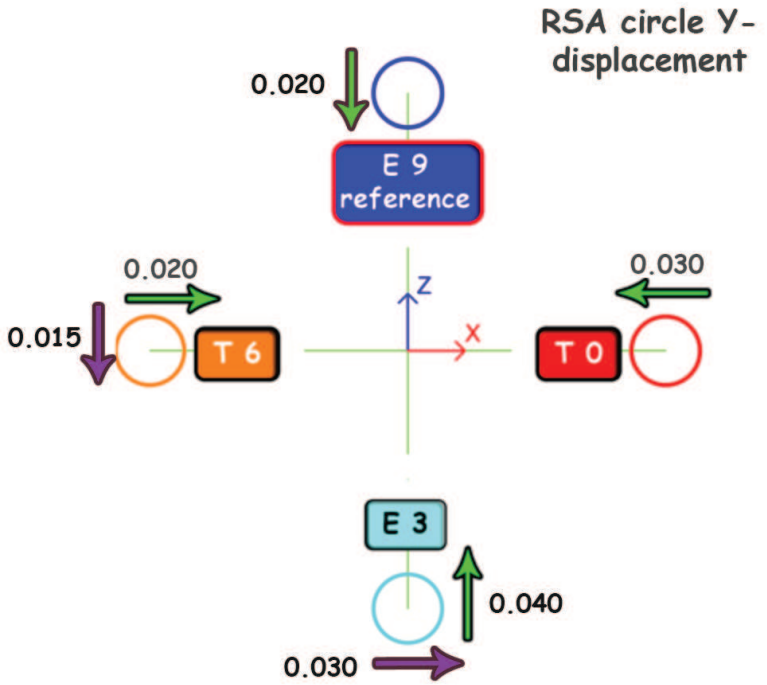

Figure 5.81 Displacements after the first brazing of the reference holes at the Y- side

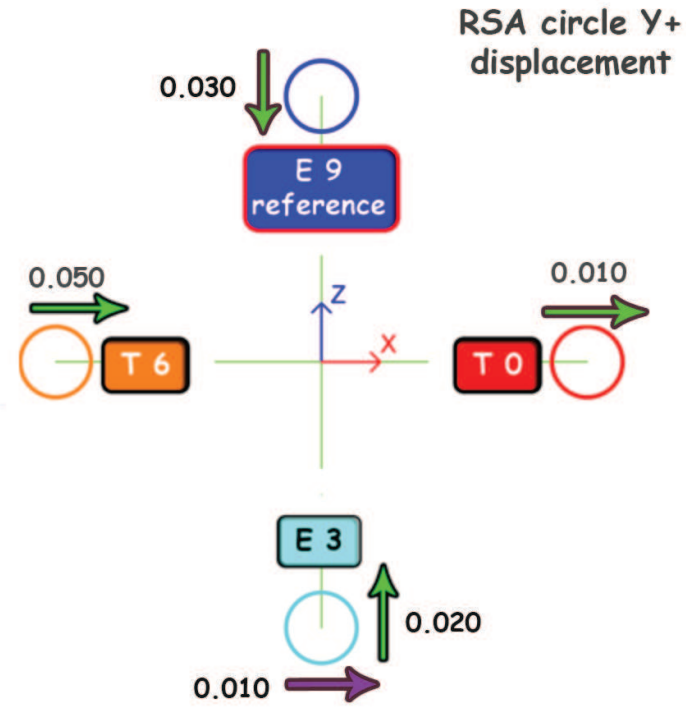

Figure 5.82 Displacements after the first brazing of the reference holes at the Y+ side

For what concerning the second brazing, taking into account the problems on the second brazing step of the module 2 of the prototype by the improvement of reducing the stiffness on the side flange by means EDM cuts, the solution was adopted on both sides (figures 5.69 and 5.83). The improvements on the fixation tooling used for the prototype 2 were used, since the successful results. The leak test was also passed successfully.

The choice of the nickel-plating of the brazing surfaces of the steel components was fundamental to achieve an excellent quality of the brazed joints (figure 5.84).

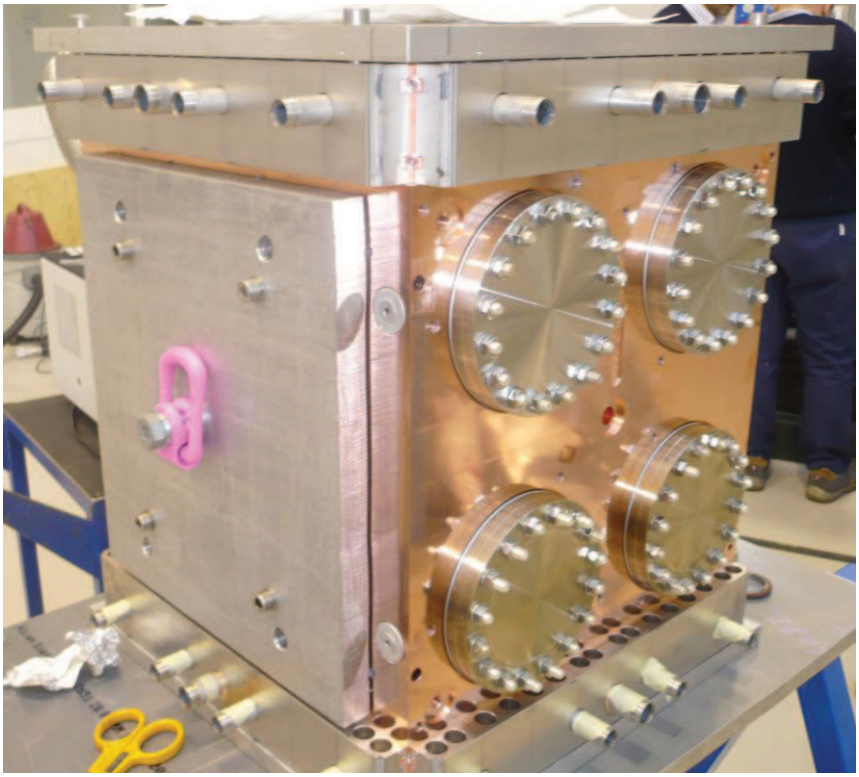

Figure 5.83 The module 17 after the second brazing

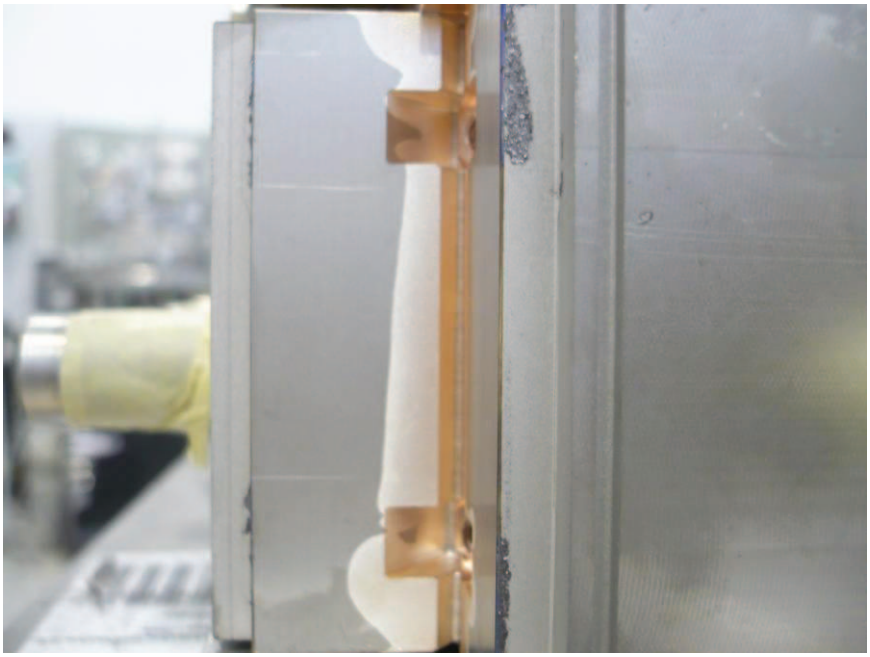

Figure 5.84 An example of the steel side flange to copper brazed joints: the excellent quality is underlined by the meniscus of the metal filler is visible along the brazing line

After the second brazing step CMM inspections were performed. Unfortunately, a complete measure of the cavity could not be reported on this thesis because some technical problems occurred on the CMM. The measurement was performed only on one side (Y-, according to figure 5.40).

Figure 5.85 reports the displacements calculated by CMM inspections of the reference holes after the second brazing step at the Y- side, respect to the geometry of the first step.

An enlargement of the cavity was found, and the displacements are quite similar but of opposite design respect to those measured after the first brazing step. Some transversal profile scans were performed also in the middle of the cavity and the results are similar than those presented on figure 5.85.

The RF measurements after the second brazing step performed by the LNL experts, confirmed such values for the displacements.

This is an excellent result for the design of the modules, since the resonant frequency is largely inside the design specifications.

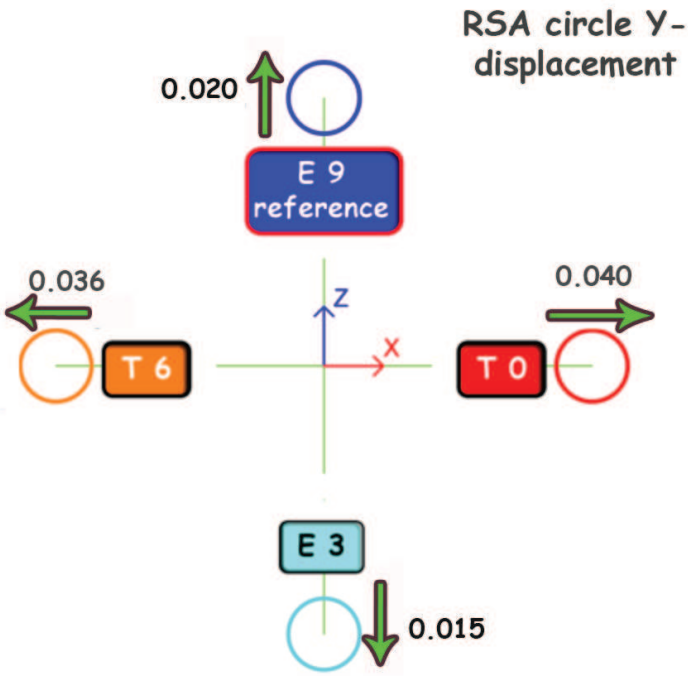

Figure 5.78 Displacements after the second brazing (calculate respect to the first brazing step) of the reference holes at the Y- side.

5.13 Conclusions

With the module 17, excellent results has been reached on the design of the modules and the on the brazing tooling.

However, the development of quality assurance strategies for the dimensional quality control and the quality of the brazed joints was mandatory, since various feedbacks were received for the improvements on the design.

For what concerning the dimensional quality control:

- The measures of the modulation of the pole tip could gave important information for the chose of the optimal milling parameters and for the construction of the optimal geometry of the cavity (from the re-machining correction on the brazing planes of the Es and the control of the optimal geometry on the dry assembly)
- The measures before and after each brazing steps gave very important information on the deformations of the cavity caused by the different thermal expansion between the AISI 316 LN and the CuC2.

Concerning the quality control of the brazing joints, the employment of the UT inspections was revealed as fundamental, in conjunction to the traditional visual and vacuum leak tests.

As an example the UT control after the second brazing step of the module 16 and on the prototype 2 for the estimation of the effective brazed surface and the quality of the couplings.

(This page is intentionalyy left blank)

CONCLUSIONS

At the end of this three years lot of work was performed with successful results, involving so many aspects, from the mechanical design of the resonator to the development of the quality control strategies of the process of production.
Considering how the thesis is organized, a series of conclusions is reported as follow.

On the first chapter, an overall description of the IFMIF project is given. Some aspects regarding the advantages of the nuclear fusion were illustrated. The fundamental importance of this project on the nuclear fusion research program was described. Since the RFQ design and production were in charge to the INFN, particular care was given to the description of the characteristics of this machine.

On the second chapter the design of the cooling system was presented. Lot of work was initially done on the choice of the type of the cooling ducts (threaded or smooth). Since on the surfaces of the cavity RF power dissipation occurs, an accurate design of the cooling system is mandatory to keep in control the deformations and the resonant frequency of the cavity. Thermal fluid-dynamics numerical analyses were initially performed to estimate the enhancement of the convective coefficient for the threaded ducts, involving different packages (Ansys CFX, STAR CD, Comsol) and operators (the CFD team of CERN). Due to the different results of the simulations and the behavior of the two types of cooling ducts, an experimental test was performed. The experimental setup was fundamental for the design of the cooling ducts: although the threaded ducts were more efficient, they do not guarantee the uniformity of temperature as for the smooth ones. The experimental setup was also fundamental for the tuning of thermal FE and CFD simulations. Finally, CFD and thermal-structural FE simulations were performed for the design of the cooling system of the modules. Successful results were obtained, since the operational specifications were satisfied.

On the third chapter the first tests for the development of a vertical brazing technology are described. We retained mandatory to develop in-house brazing technologies to perform R&D on the design of the brazing groove, the brazing fixation tooling. The INFN of Padova and the LNL brazing lab were deeply involved. Two C shaped components length 400 mm were vertically brazed, reproducing the same real conditions of the

definitive modules. Two different design of the brazing grooves design were tested. Investigations of the wettingcapability were also performed by joining some simple copper block in different positions (vertical and horizontal) and with different design of the brazing grooves. Another test was performed: the coupling of a AISI 316 LN flange of the miniprototype. 1D and 3D FE thermal numerical analyses were developed in collaboration with the expert of the LNL brazing lab for the prediction and a more precise design of the brazing thermal cycle with successful results.
The introduction of the ultrasonic control of the brazing joints, in addition to the traditional visual inspections and leak detections, was retained fundamental. The UT inspections under immersion condition gave useful information on the design of the brazing grooves.

On the fourth chapter new developments on the vertical brazing technology were described. In particular a single step brazing was tried on two small-scale prototypes. The results were successful, confirmed by the optical inspections and ultrasonic scans of the brazing scans (in collaboration of the external company BYTEST).
Moreover, low (max. 20 μm) relative displacements were registered by before the brazing step.
Improvements on the tuning of the 1D simulations by 3D FE simulations of the brazing thermal cycle were performed with successful results.

On the fifth chapter the production of the prototype 2, and the definitive modules 16 and 17 is presented. Particular care was taken on the importance of the quality assurance of the production process (dimensional and UT inspections). Up to now the cavities were qualified prevalently by RF measures. These measures give only global results on the quality of the cavity. The introduction and the development of the dimensional control by means a CMM with active continuous scanning technology was retained mandatory.
The continuous scanning revealed fundamental:

- To check the real geometry of the tip (modulation) with adequate accuracy
- To adjust and refine the CAM programs and the tuning of tooling
- To the optimize the dry assembly geometry of the cavity
- The displacement and the form of the cavity on each brazing step could be deeply investigated. Corrections on the design of the modules were made thanks to an

accurate inspection after each brazing steps. Not negligible deformations due to unexpected differences on the thermal expansion between the AISI 316 LN and the copper were measured by accurate scanning of the cavity. The problem was solved by introducing some cuts on the steel side flanges reducing their stiffness and modifying the coupling tolerance between the T element and the steel frame. With these improvements, very successful results were reached on the module 17.

APPENDIX 1

RFQ MODULE TECHNOLOGICAL PROTOTYPE

Abstract:

The IFMIF EVEDA RFQ consists of 18 modules with an approximate length of 550 mm. In order to test the production procedure a technological prototype, has been built. A complete prototype (full scale transversally, 30% shorter) has been machined in INFN and brazed at CERN, proving the production method. This prototype has been brazed following the same steps used for TRASCO RFQ, horizontal brazing for the four electrodes and the other copper details, vertical brazing for flanges and stainless steel details. Additional test on smaller scaled prototype were done to investigate the possibility of brazing in one step.

IFMIF/EVEDA Accelerator Prototype

RFQ MODULE TECHNOLOGICAL PROTOTYPE

RF-2 (AF03.1.2)

WBS : 4.05

A. Pisent, A. Pepato, P. Mereu, R. Dima, C. Roncolato, F. Scantamburlo

MODIFICATION TABLE			
Indication	Date	Modification type	Modified pages
A	13.02.2011	Draft creation	
B	19.04.2011	Preliminary Version	

Table of Contents

1. INTRODUCTION

The production of the IFMIF EVEDA RFQ accelerator is a quite challenging task due to the narrow tolerance of the pieces that should be guarantee also after some unavoidable thermal treatments. In facts, due to the complex and closed shape of the four vane RFQ, the polar expansions must be built separately and afterwards mechanically joined with the vacuum brazing technique.

In spite of brazing technique is a well proved for the construction of RFQ accelerators some risks are associated with the deformation of the machined parts at high temperature. The upper brazing temperature is around 800°C and at such temperature the copper suffers of thermal creep since the ratio T/T_f is around 0.7. Variations in the final geometry have a direct consequence on the beam dynamics, that was especially designed to minimize the beam losses.

In order to minimize the risks and to create and test all the production phases, a prototype module was built. The lateral dimensions are the same of the original modules, but the length is shorter: 400 mm instead of 550 mm.

Besides the copper parts that form the RFQ, the module was equipped with all the stainless steel parts such as the lateral ports for vacuum pumping, the hoses for the cooling channels, and the end flanges. The latter are made of 4 pieces for housing the screws and a frame for the gasket as shown in Fig. 1.

The RFQ cavity is realized by means of ultrapure copper CuC2, while all the coupling connections (vacuum ports, feeding cooling lines, tuners and couplers ports, tightness windows etc.) are made by stainless steel AISI 31LN.

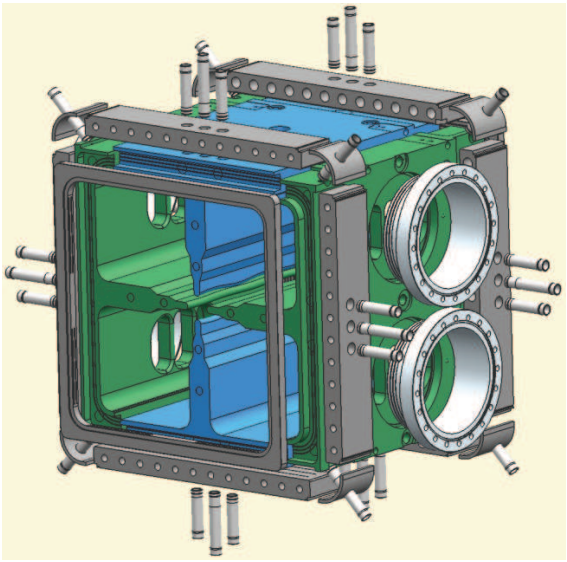

Fig. 1: Exploded view of the prototype module.

2. DESCRIPTION OF THE CONSTRUCTION PHASES

The construction phases for the copper parts of the prototype are summarized in the following block scheme. The red blocks represent the mechanical work, the green block the quality assurance tests, the orange blocks the thermal treatment (TT) or brazing (BZ), the blue block the chemical treatment. Chemical cleaning, thermal treatments and brazing of the parts have been done at CERN.

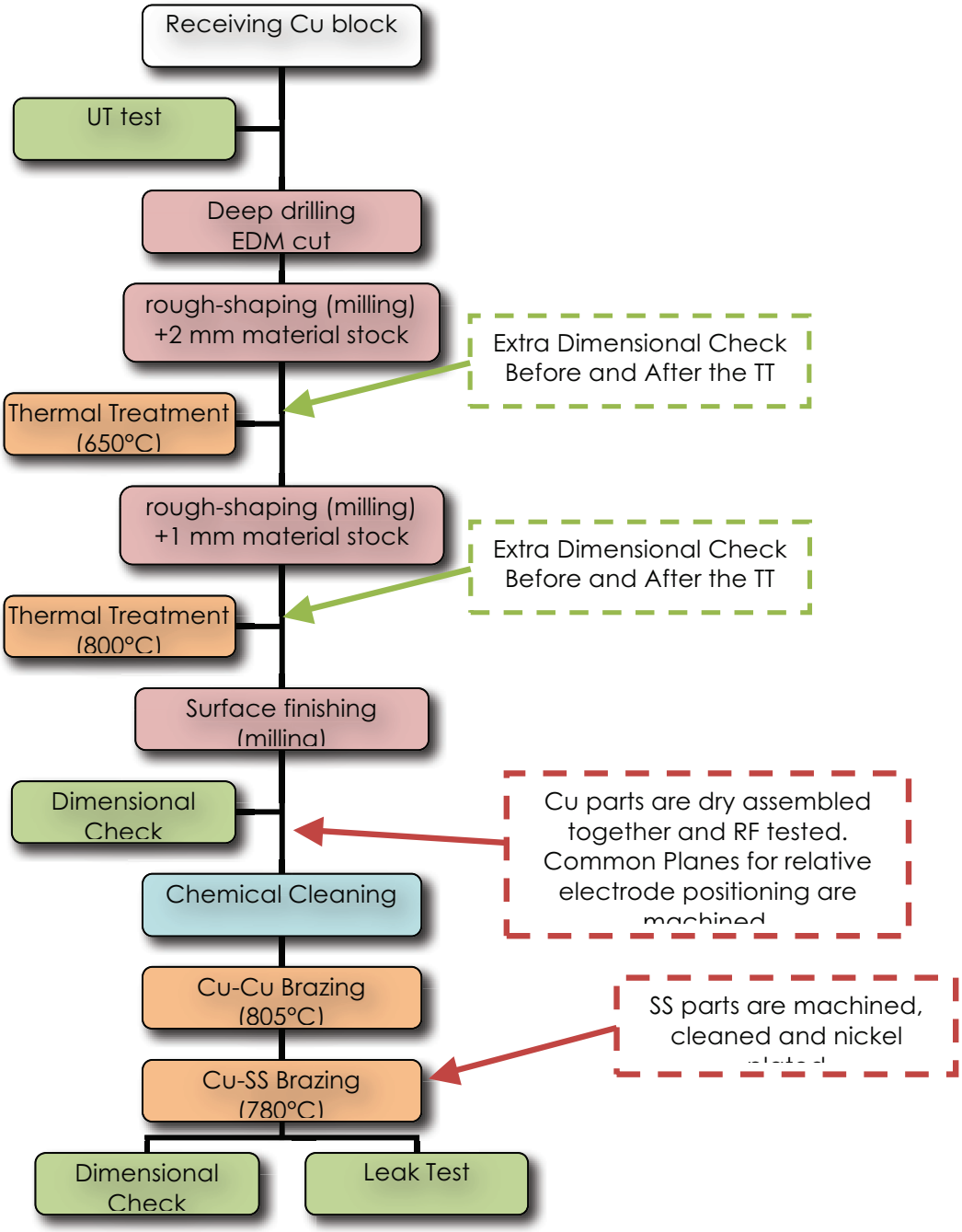

Fig. 2: Block scheme of the prototype construction

The copper parts are of two types: type E and type T as shown in the following pictures.

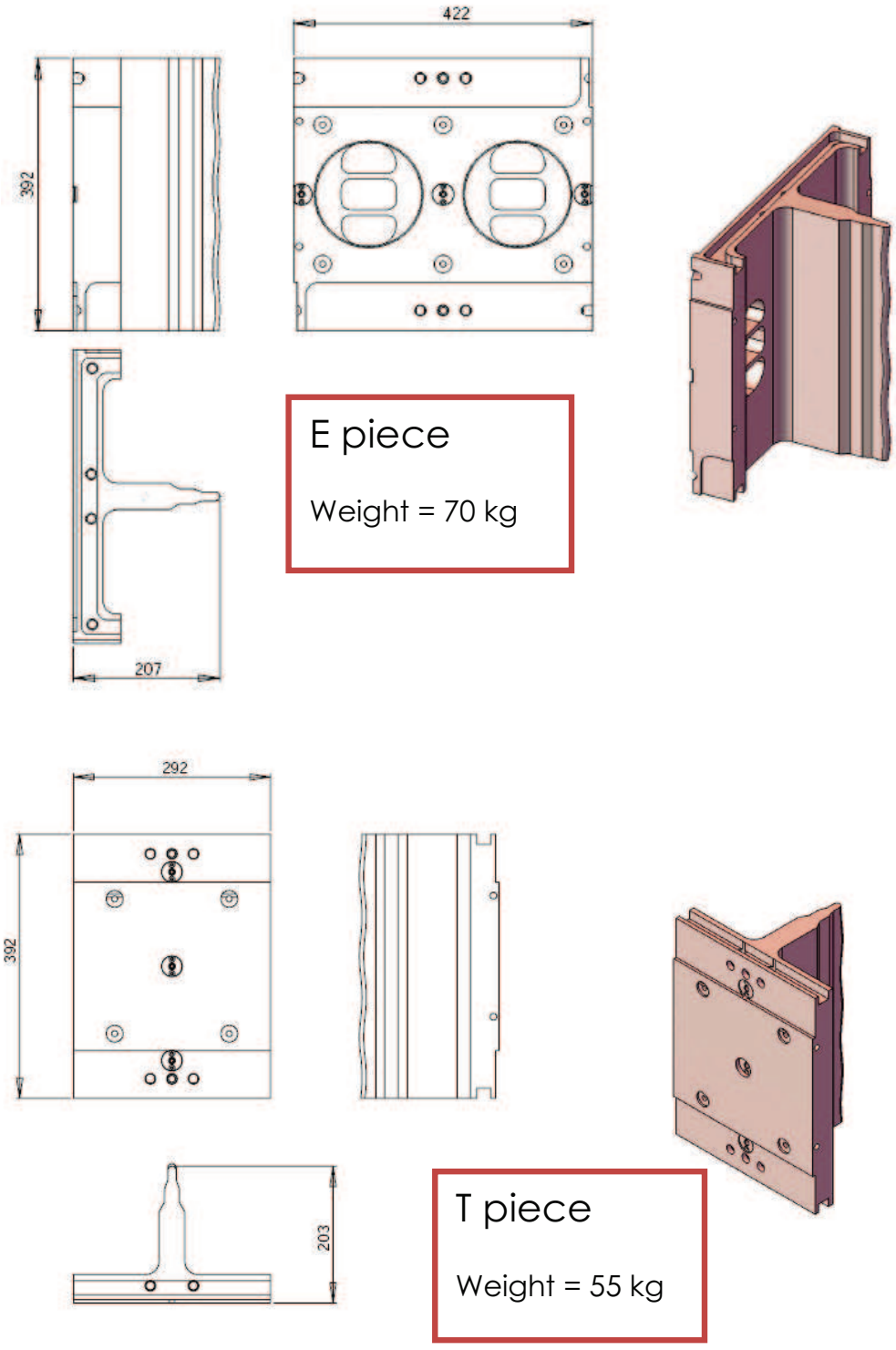

Fig. 3: Sketch of the two types of copper pieces that compose the RFQ module.

Both parts are deep drilled longitudinally and transversally to create the cooling channel. The entrance of the longitudinal holes are closed with brazed copper cylinders.

An Electrical Discharge Machine (EDM) cuts the pre-shaped parts from copper blocks with a material stock of 2 mm. Afterwards these are machined for shaping the modulation and the slots for end flanges and vacuum ports. An example for a type T piece is shown in Fig. 4.

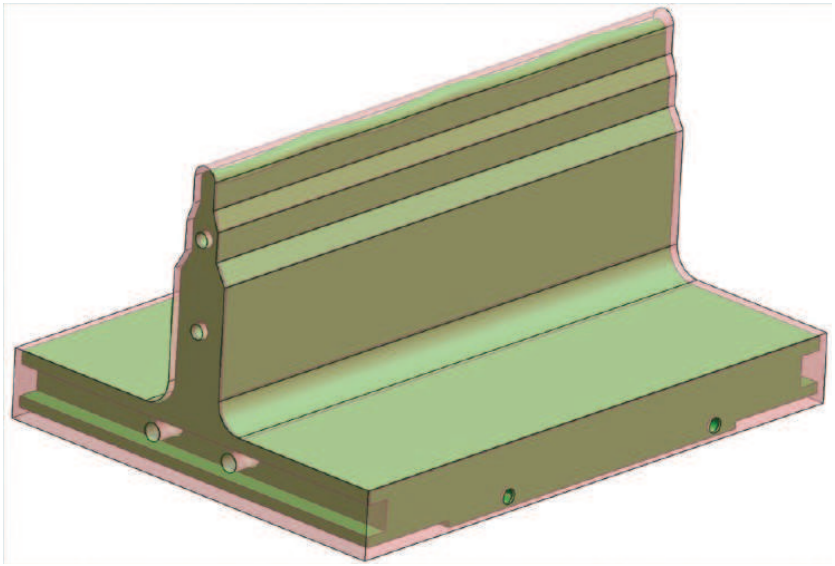

Fig. 4: Comparison between the EDM cut part (pink) and the final geometry after the milling (green)

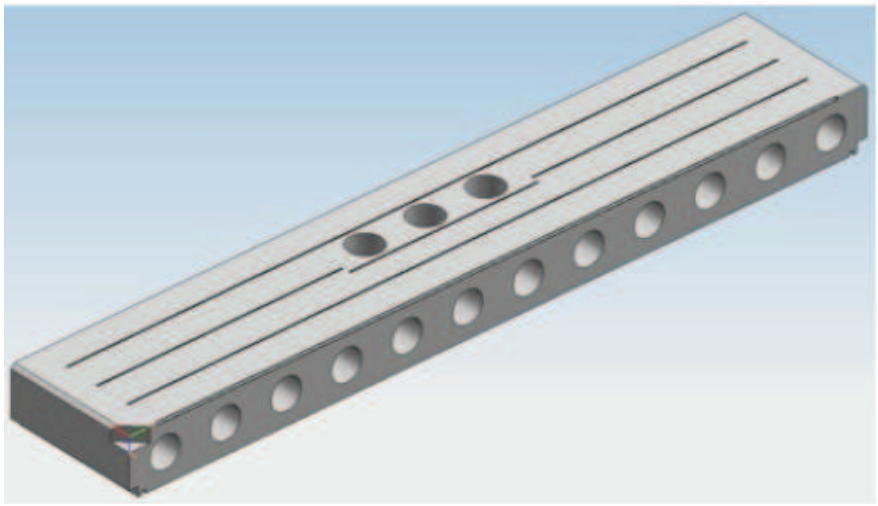

Fig. 5: View of a joining flange where the grooves for the brazing filler metal are shown.

All the surfaces to be joint are carefully remachined in order to create a smooth and flat area. For one junction only one surface is worked to house some brazing wires in several grooves, the other is just milled to be flat and smooth. Since the brazing was planned keeping the RFQ module horizontally all the bottom surfaces have the grooves.

All the copper and stainless steel parts are chemically cleaned before the thermal treatment to remove the residual lubricant that will carburize at high temperature polluting the material.

Before the thermal treatment, all the copper and stainless steel parts are chemically cleaned to remove the cutting oils, dust, fingerprints, etc. Since these parts will be in vacuum furnace at high temperature the chemical cleaning method will realize surfaces with as little desorbable gas as possible. Since this gas is in, or on, the surface oxide layer, the cleaning methods used for Cu and SS involve fluids which chemically remove this sometimes thick, dirty oxide and replace it with a thin, cleaner oxide.

The machined copper parts were cleaned at CERN (Fig. 6) following this recipe:

1. Vapour degreasing in perchloroethylene (C_2Cl_4) at 121°C.
2. Alkaline soak with ultrasonic agitation for 5 min. in an alkaline detergent above at 50°C.
3. Tap water rinse.
4. Pickling in HCl (33%) 50% by volume with H_2O 50% at room temperature for 1 to 5 min.
5. Tap water rinse.
6. Passivation in CrO_3 (Chromic acid) 80 g/l + H_2SO_4 (96%) 3 cm^3/l at room temperature for 30 s to 1 min.
7. Running tap water rinse.
8. Cold demineralized water rinse.
9. Dry with filtered air or dry N_2.
10. Wrap in Al foil

Afterwards the pieces were horizontally baked at 650/800°C for 6 hours. The heating ramp is 150°C/hr at maximum, whereas the cooling ramp is 50°C/hr at maximum until 300°C. The pressure is below 10^{-5} mbar through all the thermal cycle.

Two pieces were cleaned and heat treated at LNL following a different cleaning technique to avoid the utilization of the Chromic Acid. The cleaning is based on industrial detergents for removing the grease and oils followed by a room temperature bath of Ammonium Persulfate at 10% by volume. This chemical compound gently etches the copper surface and remove the former oxidation. The surface is then passivated in Citric Acid.

Besides the stainless steel pre-shaped parts were cut by hydro jet. These were sandblasted to remove the former dust and swarf and cleaned with industrial detergents. The heat treatment was at 950°C for 2 hours with a maximum heating ramp of 300°C/hr and a cooling ramp of 100°C/hr until 300°C.

Fig. 6: Chemical degreasing and annealing process performed at 800°C in vacuum condition.

Before and after the thermal treatment the dimension of the piece were checked by means of a portable 3D measuring arm (PMMT) and a continuous scanning measuring machine (CMM). The results are discussed in the following paragraph.

After, the surface finishing the four components are assembled vertically on the optical bench of the CMM. A common reference plane is realized by means of ultra-precise blocks that allow access also from the bottom. Once assembled the geometry is verified by the CMM and the PMMT, as shown in the scheme block sequence of Fig. 2.

The dry-assembled structure (see Fig. 7(left)) is then tested with the RF to control the frequency of the resonant modes (quadrupole and dipoles), the results are discussed below in this document.

Since there was no need of further machining for each elements, the structure is then tilted of 90° and a smooth milling machining of several common surfaces is performed for the re-alignment and positioning of the tooling foreseen for the first brazing (Fig. 7).

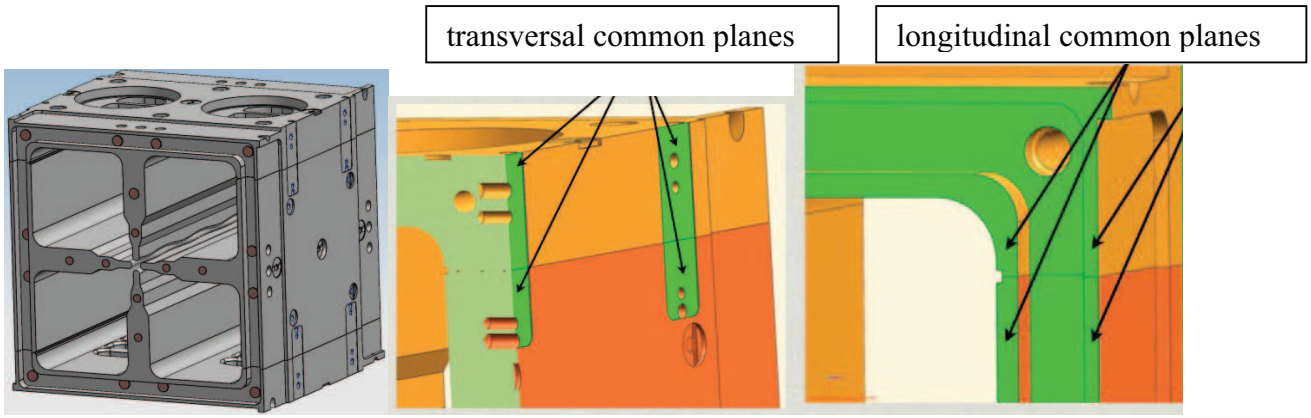

Fig. 7: Sketch of the position of the common planes for the positioning of the electrodes. (left) complete assembly; (centre) common planes in the X direction; (right) common planes in the Z direction

Using the common planes the copper parts were assembled at CERN for the first brazing phase at 815°C. The layout is shown in Fig. 8.

The contact support is made with small ceramic plates assuring a thermal insulation (to limit the conductive heat transfer between the stainless steel bar and the copper) and offering a very poor friction coefficient between elements. An inspection window is provided to follow the transition between solid to liquid of the brazing material to happen uniformly.

Two AISI 316LN grinded bars are foreseen to be used for the longitudinal alignment. Two molybdenum rods equipped with a couple of Nimonic-90 spring are placed symmetrically aside each coupling surface for the transversal alignment. They are effective on both directions, balancing the intrinsic unstable mass distribution of the single components. The crosscheck alignment of the components on several points guarantees a very precise position respect of the geometry defined with the machining of the common surfaces.

The springs will offer a residual force also at 815°C. In facts Molybdenum and Nickel based material are expected to be slightly affected by thermal creep. In the second brazing the springs are replaced with thick Molybdenum wires (Fig. 10).

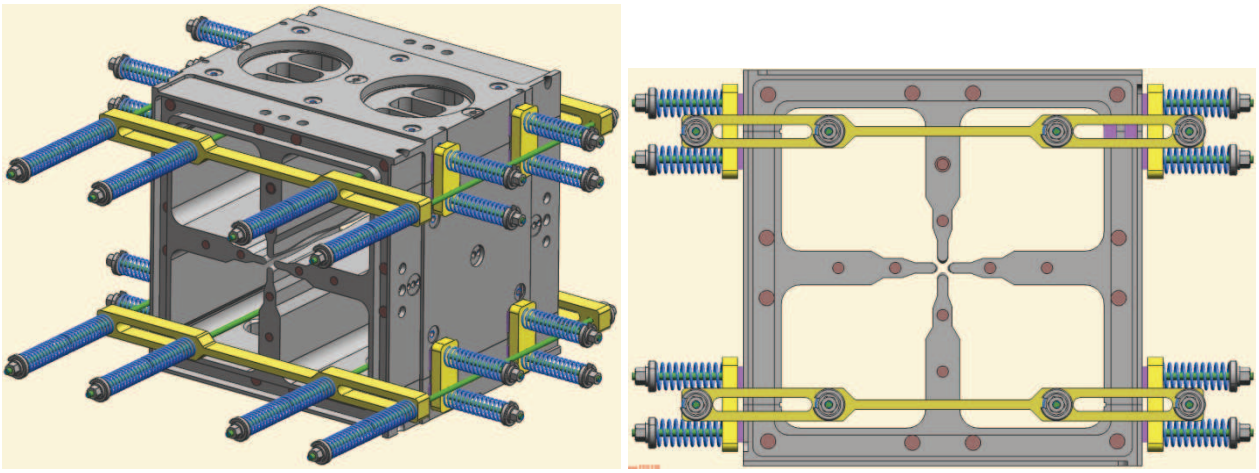

Fig. 8: The first brazing assembly tooling

The brazing filler metal for the first brazing consists of wires of 1 mm in diameter, which are carefully cut and placed into grooves of different length milled on the brazing surface. The material is Palcusil-5® based on the Ag-Cu-Pd alloy (Fig. 9). The design of the surface was to have a planarity below 0.03 mm with a number of groves for the filler metal calculated by assuming a constant spacing of 20 □m between each other and a clearance of 40 □m. The orientation is longitudinal respect to the beam axis.

The first brazing is performed at 815°C (horizontal) for the coupling of all the copper components, whereas the second brazing (vertical) is performed at 785°C for the coupling of all the stainless steel components. Stainless steel parts were beforehand nickel plated and the brazing filler metal is CuSil®.

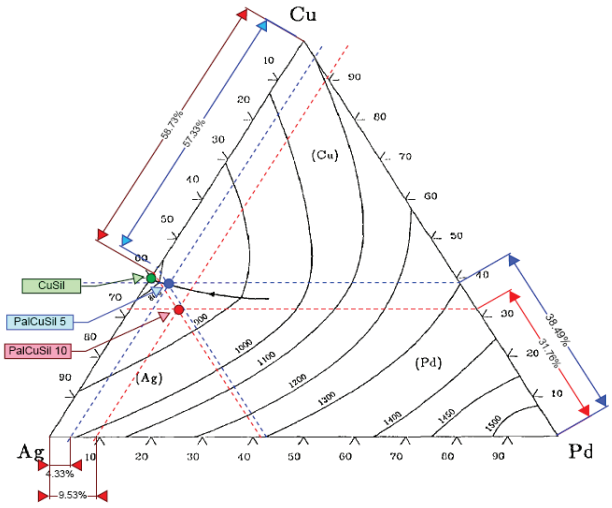

Fig. 9: Liquidus projection on a ternary diagram for the Ag-Cu-Pd system.
The commercial name of the typical brazing filler metals are reported in different colours.

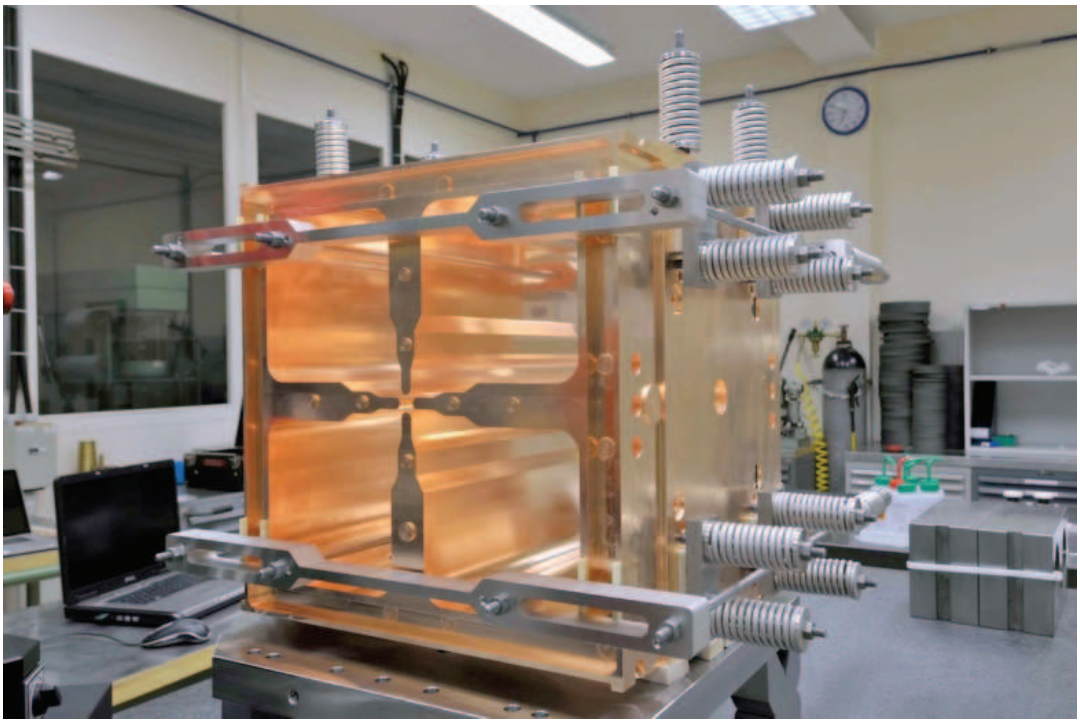

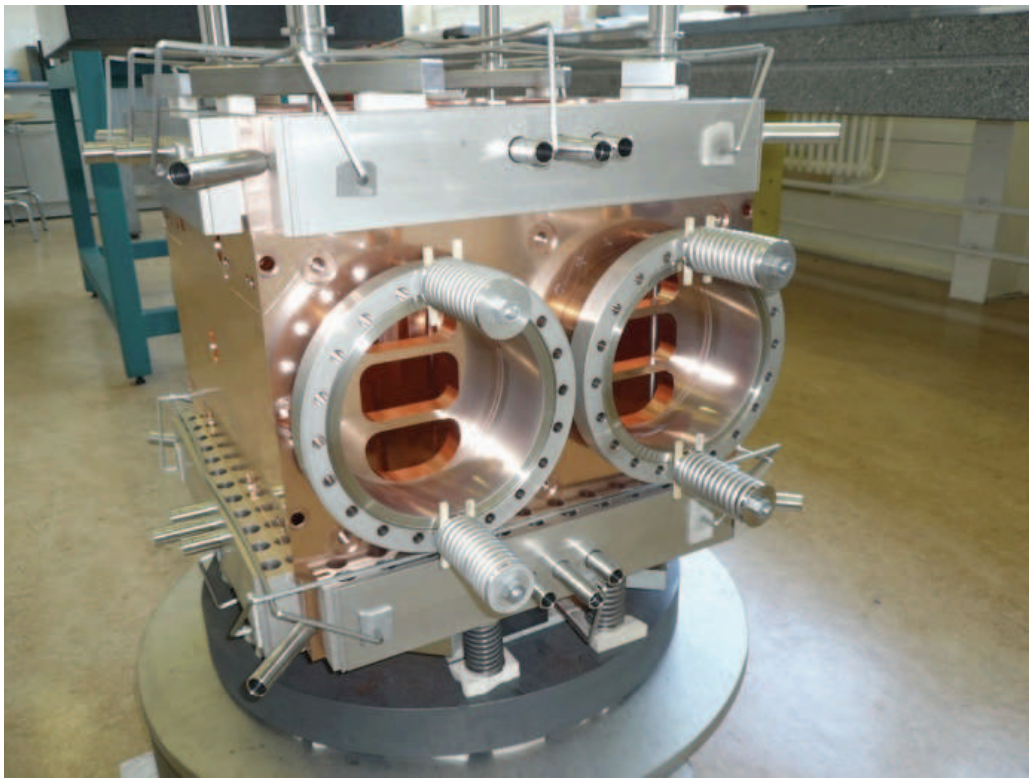

Fig. 10 –Pictures of the prototype assembled for the brazing.
(top) Cu-Cu horizontally brazing. (bottom) SS-Cu vertical brazing.

3. DIMENSIONAL QUALITY MEASUREMENTS

In the production phase of the copper parts, before and after the brazing, the four pieces were controlled dimensionally. The instrumentation used were a portable Cimcore Infinite 2.0 3D measuring arm (PMMT) and a Zeiss Accura continuous scanning measuring machine (CMM) with an accurancy respectively of 20 □m and 2-3 □m. While the portable arm measures with single points, the CMM allows to measure the features such as planes, circles, etc. with a very large number of points, in order to accurately investigate its real form. Moreover the measures profiles can be easily done, such as for the deformation of the internal cavity of the prototype.

The EDM cutting was validated by some measurements of flatness and perpendicularity of the four pieces respect to the Base Plane.

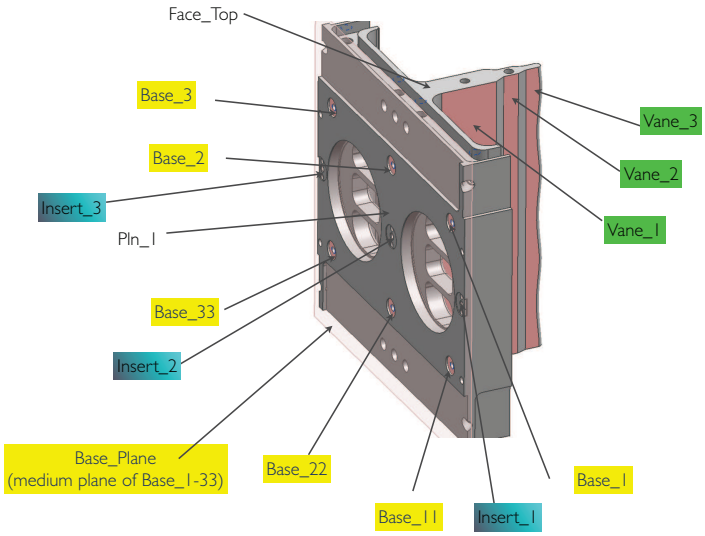

Fig. 11: Definition of the surface for the dimensional check in a E piece.

	Perpendicularity [mm]			
	T Top	E Right	T Bottom	E Left
Vane_1	0.092	0.075	0.164	0.086
Vane_11	0.071	0.105	0.208	0.122
Vane_1	0.081	0.072	**0.259**	0.134
Vane_2	0.035	0.086	0.114	0.062
Vane_22	0.056	0.056	0.21	0.057
Vane_2	0.07	0.058	0.153	0.117
Braze_1	-	-	-	-
Braze _2	-	-	-	-

	Flatness [mm]			
	T Top	E Right	T Bottom	E Left
Vane_1	0.074	0.05	0.118	0.085
Vane_11	0.043	0.061	0.144	0.083
Vane_1	0.039	0.054	0.165	0.089
Vane_2	0.031	0.049	0.04	0.028
Vane_22	0.038	0.027	0.168	0.033
Vane_2	0.036	0.015	0.122	0.06
Braze_1	0.058	0.047	0.062	0.052
Braze _2	0.056	0.041	0.064	0.056

Table 1: Perpendicularity and flatness for the four copper pieces after the EDM cutting.

Both perpendicularity and flatness measurement are expressed as rms deviation of the points of a surface respect to the interpolating plane. In the perpendicularity measurement the surface is a plane normal to the reference.

From these results the EDM cutting introduced a maximum deviation of 260 μm. This result is very important for the characterization of the precision of the process. The assumption of 2 mm of the material stock was sufficient. Moreover this can be reduced to 1 mm to reduce the stress during the future milling phase.

All the pieces were measured before and after the annealing phases to check their sensitivity to the thermal cycle (Table 2).

	0000119000						
	Start	After 650°C	Delta 0-650	After 800°C	Delta 0-800		
Perp. BasePlane	[mm]	[mm]	[μm]	[mm]	[μm]	Distance error	[mm]
Vane_1	0.022	0.019	-3	0.005	17	Braze_1 - Base_Pln	0.010
Vane_2	0.016	0.019	3	0.016	0	Braze_2 - Base_Pln	0.024
Vane_3	0.017	0.011	-6	0.007	10	Vane_3 - Vane_33	0.005
Vane_11	0.006	0.012	6	0.009	-3		
Vane_22	0.018	0.006	-12	0.012	6		
Vane_33	0.019	0.008	-11	0.020	-1		

	0000129003-final machining					
Perpendicularity		After 800 (LNL)	Flatness			
Base_Plane	[mm]	[mm]		[mm]	Brazing planes	
Vane_1	0.014	0.014	Vane_1	0.013		[mm]
Vane_2	0.013	0.015	Vane_2	0.013	Brazing_1	0.014
Vane_3	0.009	0.014	Vane_3	0.013	Brazing_11	0.018
Vane_11	0.029	0.015	Vane_11	0.014		
Vane_22	0.032	0.017	Vane_22	0.016		
Vane_33	0.027	0.022	Vane_33	0.019		

Table 2: Perpendicularity for a E piece after annealing phases.

It turned out that only small stress were introduced by the first two machining phases (light pink, yellow). In facts all the deviations are below 20 μm. An additional test of smooth milling shown similar deformations (green). In this way it is possible to produce the pieces with one annealing phase after the EDM cutting and the rough milling, whereas the smooth milling is carried out without any heat treatment.

The four pieces were assembled without brazing material (dry assembly) to check the geometry of the quadrupole. However, at the time of the tests it was only possible to describe the geometry in terms of planes – because the CMM machine were not yet delivered – and therefore the pole tips profiles could not be measured. The PMMT gave the relative shifts of two opposite pole tips (Fig. 12 and Fig. 13) from those a rectangular area can be defined. The barycentre of this rectangular was regarded as the beam axis of the resonator. This assumption is a good approximation provided the displacement are small compared to the mean aperture of the poles.

Additional information on the geometry of the dry assembly could be taken from the resonant spectrum of the cavity. This is characterized by three important modes: one frequency of quadrupole and two frequencies of dipole, as shown in Fig. 14. Measurements are done with open terminations, so that quadrupole and dipole frequencies are higher than for the operating

modes. In facts, the quadrupole frequency shift respect to the **initial frequency of 186 MHz** (measured with the first assembly and consistent with 3d simulations) gave an approximate estimation on the average pole tip displacement, since the parameter which affect most the frequency is the relative pole tip positions respect to the beam axis ($\partial f/\partial R_0$ = 7.6 kHz/□m), and the little frequency gap between the two dipole modes excluded significant asymmetric displacements.

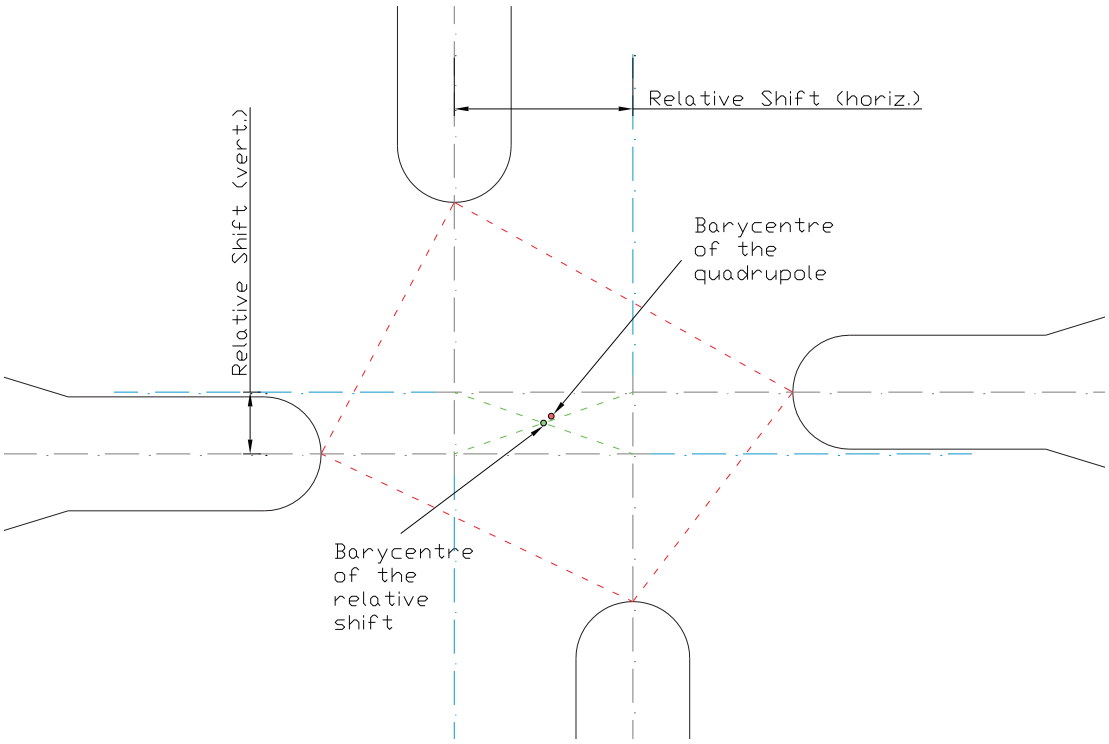

Fig. 12: Example of deviations from the nominal geometry

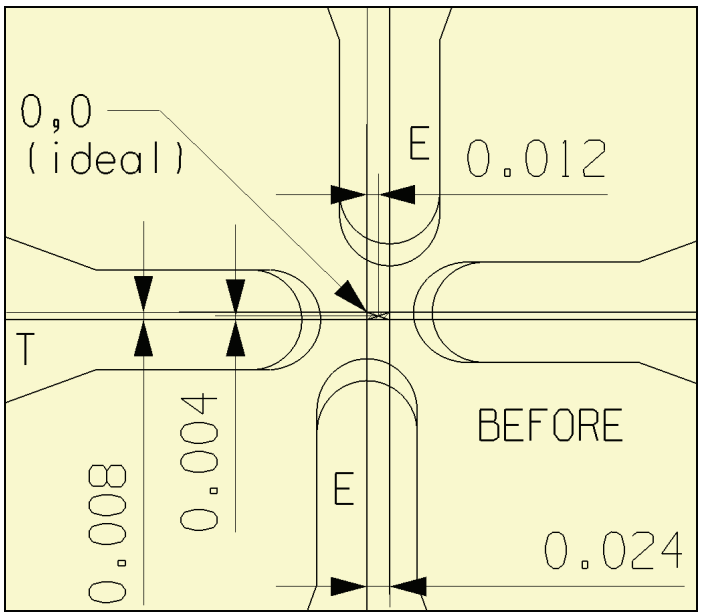

Fig. 13: Deviation of the relative pole tips before the brazing. (PMMT)

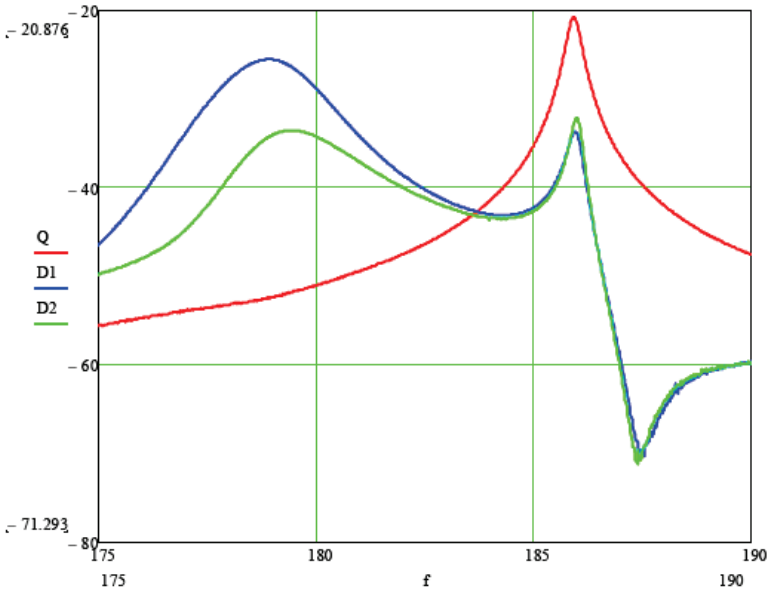

Fig. 14: Resonant spectrum for the cavity in the dry assembly

The actual shape of the resonator after the final brazing was deeply investigated geometrically by means of the CMM. Unfortunately the pole tips are not accessible with the stylus, and thus their displacements are given by the shifts of the side walls of the poles, and by the deformations of the base walls of the vanes (Fig. 15). This assumption considers the machining of the four pieces in tolerance.

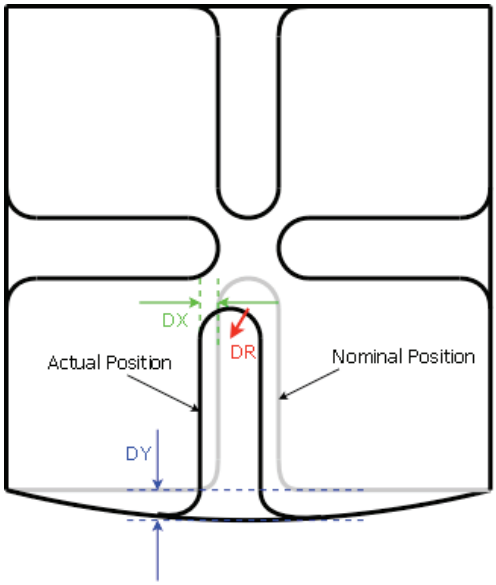

Fig. 15: Geometrical estimation of the pole tip displacement

The module was vertically aligned (Fig. 16) and some sections of the profiles at different values of Z (100 mm and 300 mm) where measured (Fig. 19). In addition, vertical lines on the base of each element were investigated (Fig. 18).

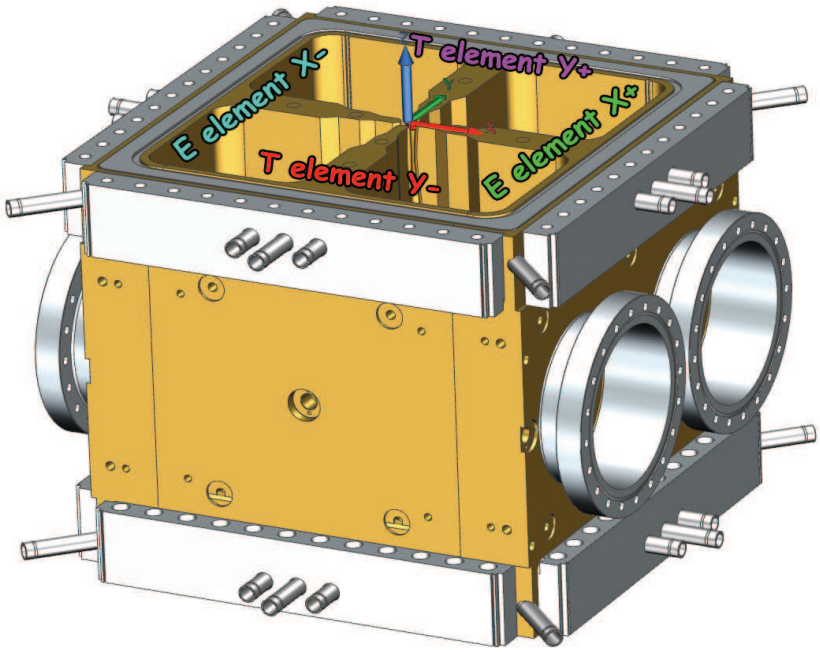

Fig. 16: Alignment and reference system for the geometry measurements.

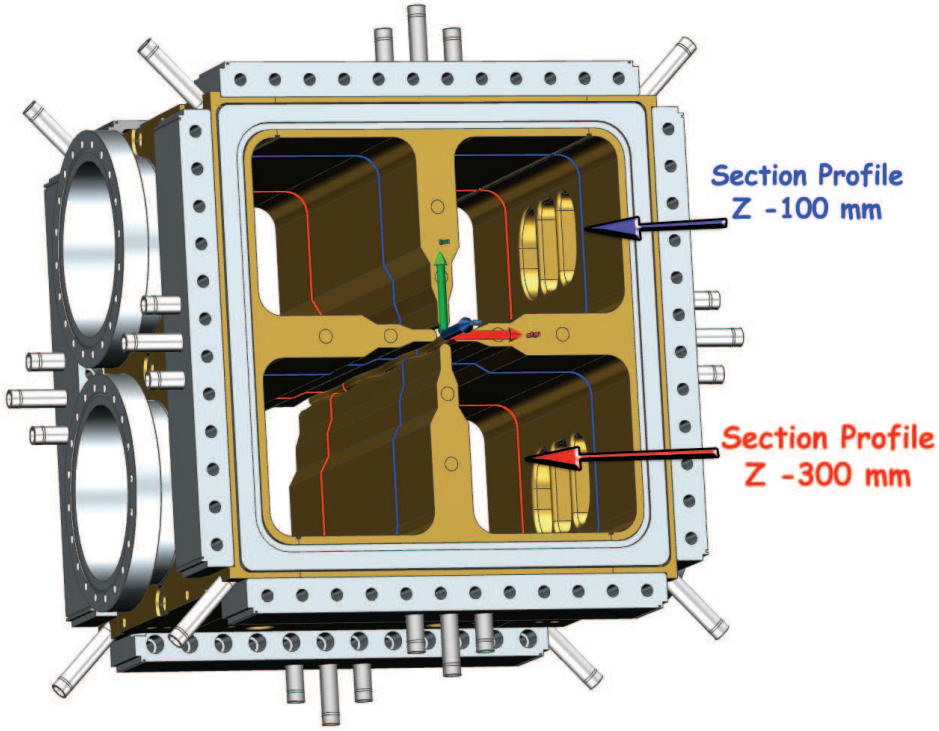

Fig. 17: Section profiles measured on the cavity.

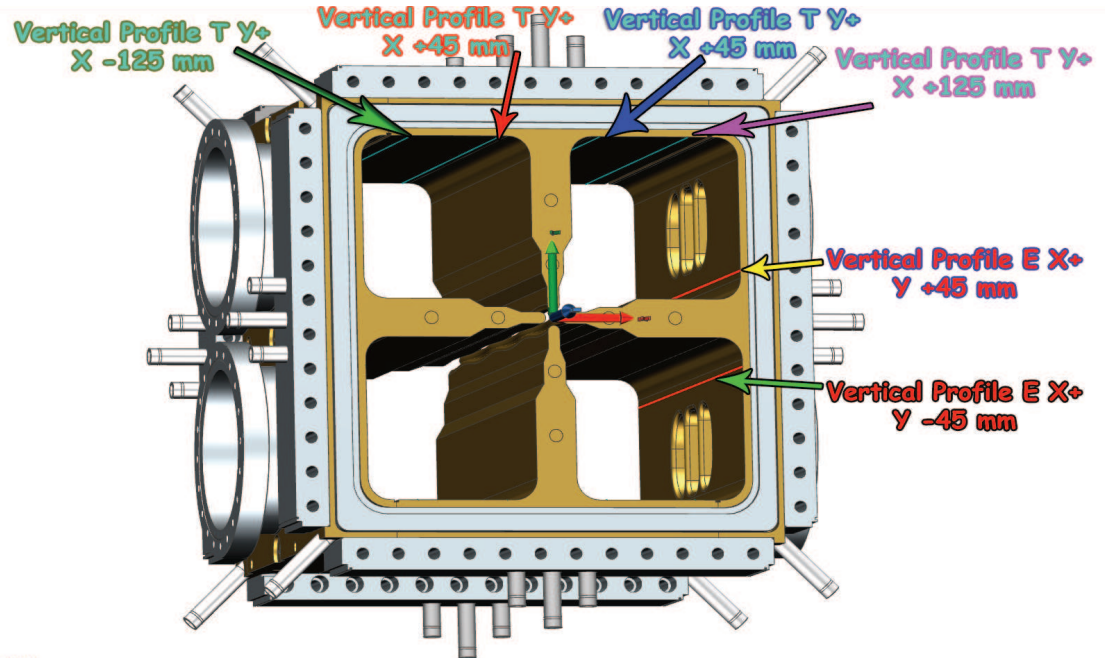

Fig. 18: Vertical profiles measured inside the cavity.

Some conclusions from the geometrical measurements are that the inner volume of the cavity was raised, and the side walls of the vanes were bowed like a barrel. Among the four side walls only the top one has not been either moved or deformed, as shown in Fig. 19. Moreover no significant rotation have been detected (below 0.5 mrad) in all the four pieces.

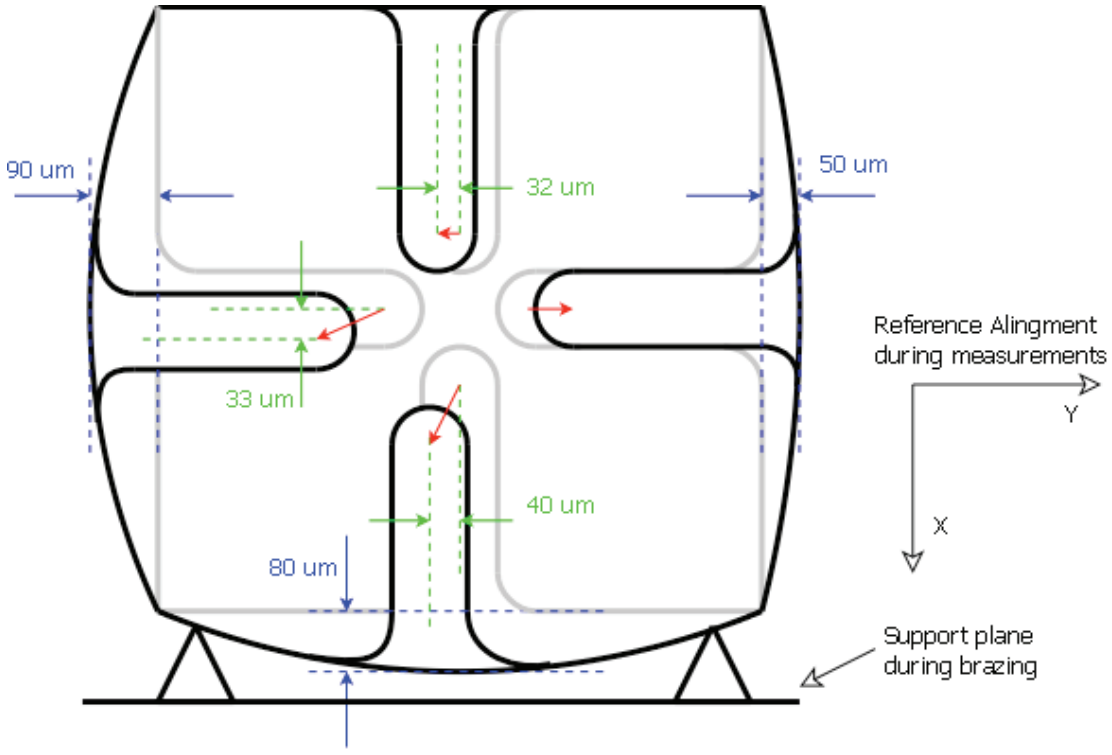

Fig. 19: Summary of the relative pole tips deformation after the brazing (CMM).

The deformations of the modules seem to be produced by the gravitational forces. The material is especially sensitive to these stresses when the thermal creep is active (0.7 of Temperature of melting)

The frequency change of the module after the brazing can be practically explained with these deformation as reported in Table 3.

Pole	ΔX	ΔY	ΔR_0
	[□m]	[□m]	[□m]
1	-40	-80	89.44
2	50	0	50.00
3	-32	0	32.00
4	-90	-33	95.86
	mean ΔR_0	**[□m]**	**66.83**
	$\partial f/\partial R_0$	[kHz/□m]	7.60
	Δf	**[kHz]**	**507.87**

Table 3*: Average pole tip displacement and related frequency shift.*

4. LEAK TEST RESULTS

The leak test for the RFQ prototype was carried out with a leak detector model 979 from VARIAN equipped with a TriScroll pump. According to the instrument's specification the minimum detectable leak rate is 5 x 10^{-10} mbar-lt/s with the standard sensitivity, and the calibration is made internally.

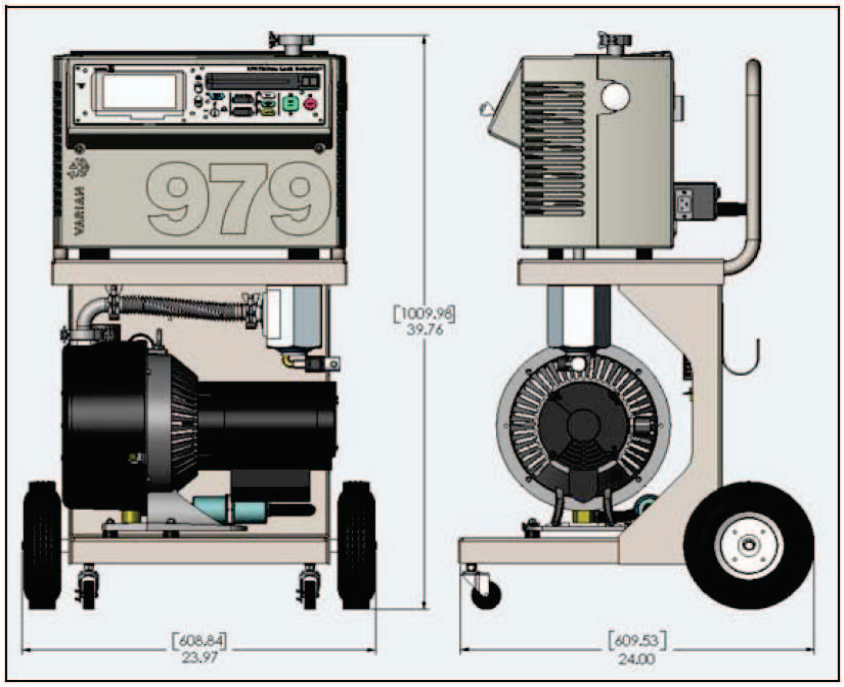

Fig. 20: Leak detector model 979 from VARIAN used for the leak test

The side ports of the RFQ prototype were closed with DN 150 CF flanges using OR NBR gaskets. The end flanges were instead closed with custom aluminium flanges equipped with a thin layer of vacuum plasticine. The orientation of the prototype was horizontal with the brazing joints on the vertical sides of the piece and the CF flanges on the top and the bottom.

The pumping of the system was done from one of the top flanges. The test did not show any variation of the helium sensor from the background level that was 5×10^{-10} mbar-lt/s.

5. SINGLE BRAZING PERSPECTIVE

From the point of view of the heat transfer by radiation, the vertical brazing seems reasonable because the radiation will not change much, since the height (550 mm) is not so different from the lateral dimension (450 mm). However, the filler metal braze is expected to flow in another way because the action of the gravitational force is opposite in some cases to the capillary force.

Some tests were done with copper to study the vertical brazing of some C like pieces long 400 mm (Fig. 21). These tests were at first done with the aim of studying the effect of the pieces and grooves orientations on the wetting of the brazing filler metal. They reveal a fine mechanical joint both in the middle of the assembly and at the ends, where the geometry is more complex due to the slot for the end flanges.

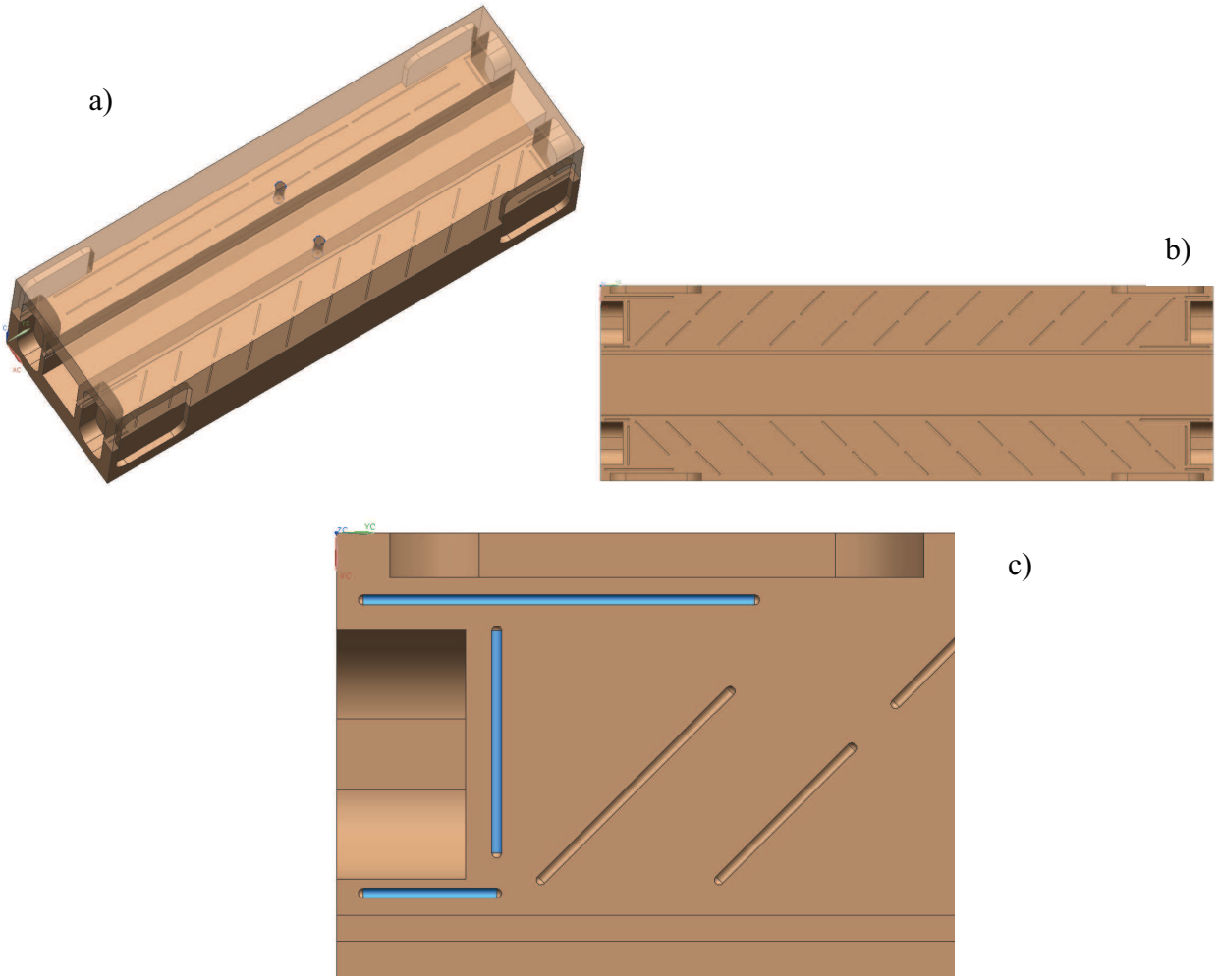

Fig. 21: View of the C pieces for the vertical brazing test. (a) 3D view of the assembly; (b) side view of one piece, showing the grooves orientation tilted 45°; (c) detailed view of the grooves at one end.

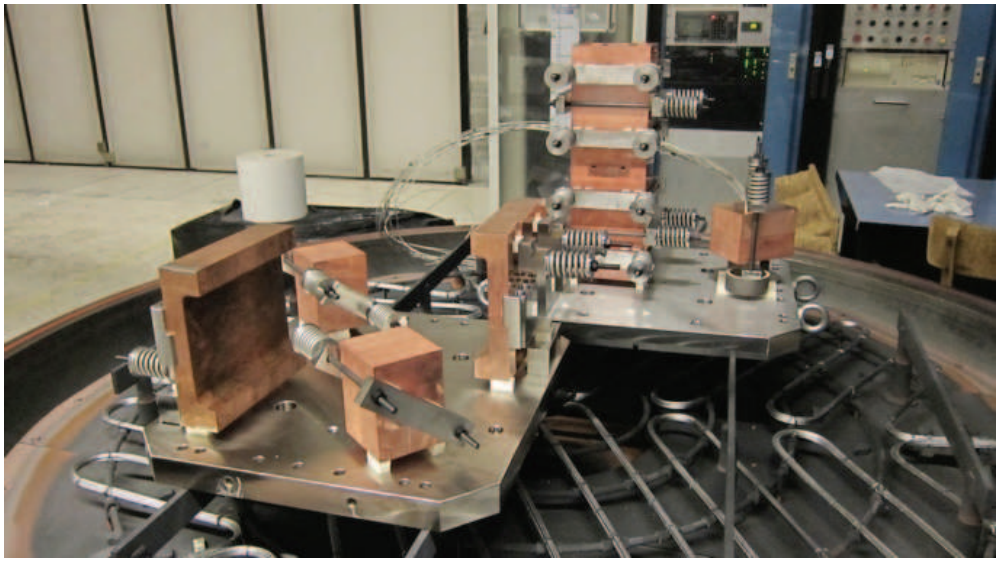

Fig. 22: Photo of the vertical brazing test for the type C pieces with springs along with some copper blocks. The copper and stainless steel joint was tested on two additional pieces.

Afterwards as final test, a small prototype of a RFQ module was assembled and brazed vertically (Fig. 23). The lateral dimension of the vanes are half of those of the final RFQ module, whereas the height is around 400 mm. This small RFQ was equipped with all the lateral flange and frames as the final one.

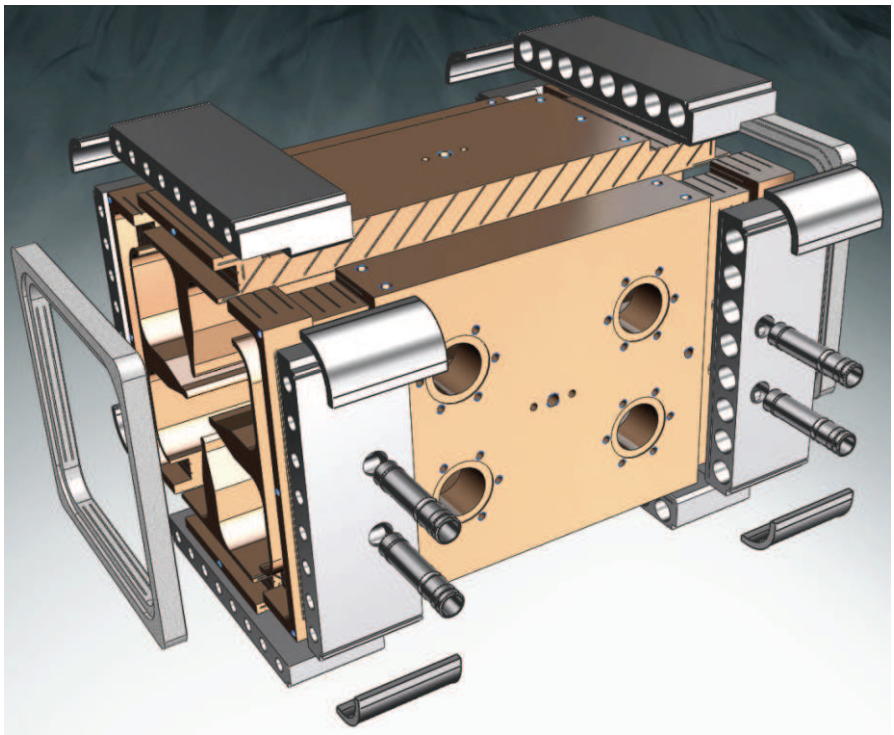

Fig. 23: Exploded view of the mini prototype RFQ for the vertical brazing test in one phase.

Several tools made of stainless steel 316LN for the final module was installed on the Molybdenum rods as in the former test (Fig. 24). The brazing filler metal was Palcusil-10.

From a visual inspection the joints were positive judged, but not completely molten. Moreover some cold spots on the side of the structure were found. Excessive flowing of the filler metal was seen on the base of the assembly due to a too large clearance between stainless steel and copper. However, the assembly passed the leak test successfully.

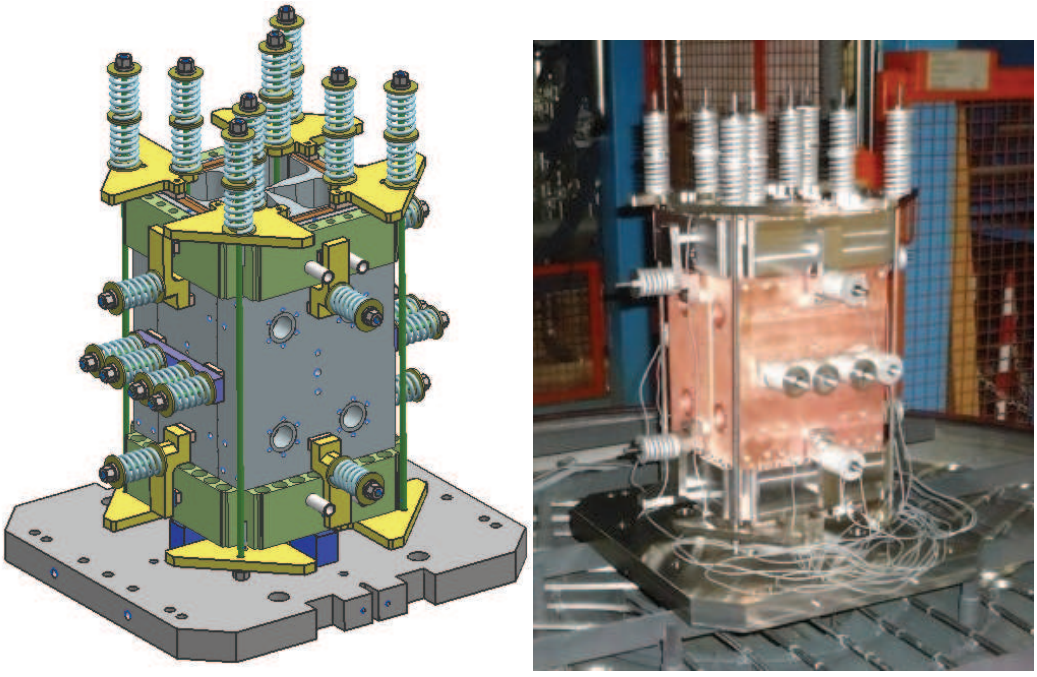

Fig. 24: Perspective view(left) and photo(right) of the brazing setup for a smaller scaled version of the RFQ The stainless steel and the copper parts are all brazed at once without nickel plating. The pieces were firmly held together by several springs made of Nimonic 90.

A second test with this similar assembly was done afterwards. A narrower clearance at the end flanges and a higher final brazing temperature turned out to be sufficient to eliminate the former problems.

Both RFQs were leak tested horizontally closing the end flanges and lateral ports with vacuum plasticine. The pumping of the system was done from one of the top flanges. The test did not show any variation of the helium sensor from the background level that was 5 x 10^{-10} mbar-lt/s.

A dimensional check was carried out with the CMM. Only the relative displacements between the pieces T and E were measured since some external reference planes were machined before the brazing (Fig. 25).

The piece was positioned vertically on the measurement plane. The results are summarized in Table 4. The deformations of the assembly seem to come from the planary of the brazing plane that can have some imperfections.

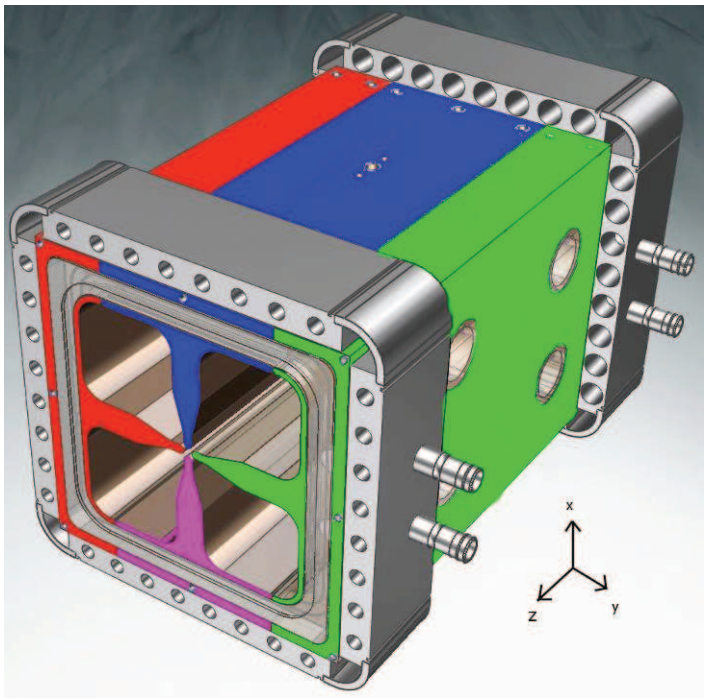

Fig. 25: Perspective view of the brazing setup for the definitions of the reference planes.

	Before	After	Delta
Shift (along X)	mm	mm	mm
Red with Blue	0.026	0.001	-0.025
Green with Blue	0.013	0.006	-0.007
Red with Pink	0.003	0.013	0.010
Green with Pink	0.020	0.013	-0.007
Shift (along Z)	mm	mm	mm
Blue with Green	0.015	0.001	-0.014
Blue with Red	0.004	0.027	0.023
Blue with Pink	0.006	0.031	0.025

Table 4: Shifts of the reference plane before and after the brazing.

6. CONCLUSIONS

The production of the first prototype is an important goal since all the production phases have been tested and many aspects could be better understood for the final production.

Concerning the machining the dimensional check of the pre-shaped parts, the EDM cutting guarantees a sufficient precision (260 □m). The metal stock will be reduced in the final production from 2 to 1 mm. The small deviations measured after the annealing phase suggested to join in one entire milling phase all the pre-shaping machining phase.

The chemical treatment and the brazing phases were successfully carried out and the reliability of further options have been proven.

The deformation of the module is not negligible, but is within the tolerance (vane tip relative position respect to beam axis with an error below 50 □m with 1 MHz of tuning range). The shape of the deformation suggested a role of the gravity forces; this is an additional indication for the vertical brazing alternative.

After this campaign of tests the vertical brazing seems feasible. Moreover, the design of the grooves turned out to be correct. The replication of the single step brazing is a confirmation of the reproducibility of the process.

The second prototype modules will be brazed vertically as final test before the production of the RFQ modules.

Mechanical tests should be done also on the copper stainless steel junctions to check if the interactions between the base metal and the filler metal have produced erosion or excessive diffusion. In fact copper between the austenite grains is supposed to strongly increase the rupture from fatigue.

APPENDIX 2
TECHNICAL DRAWINGS

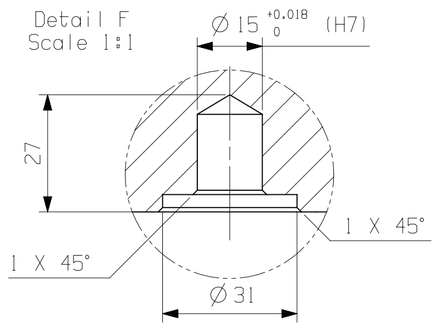

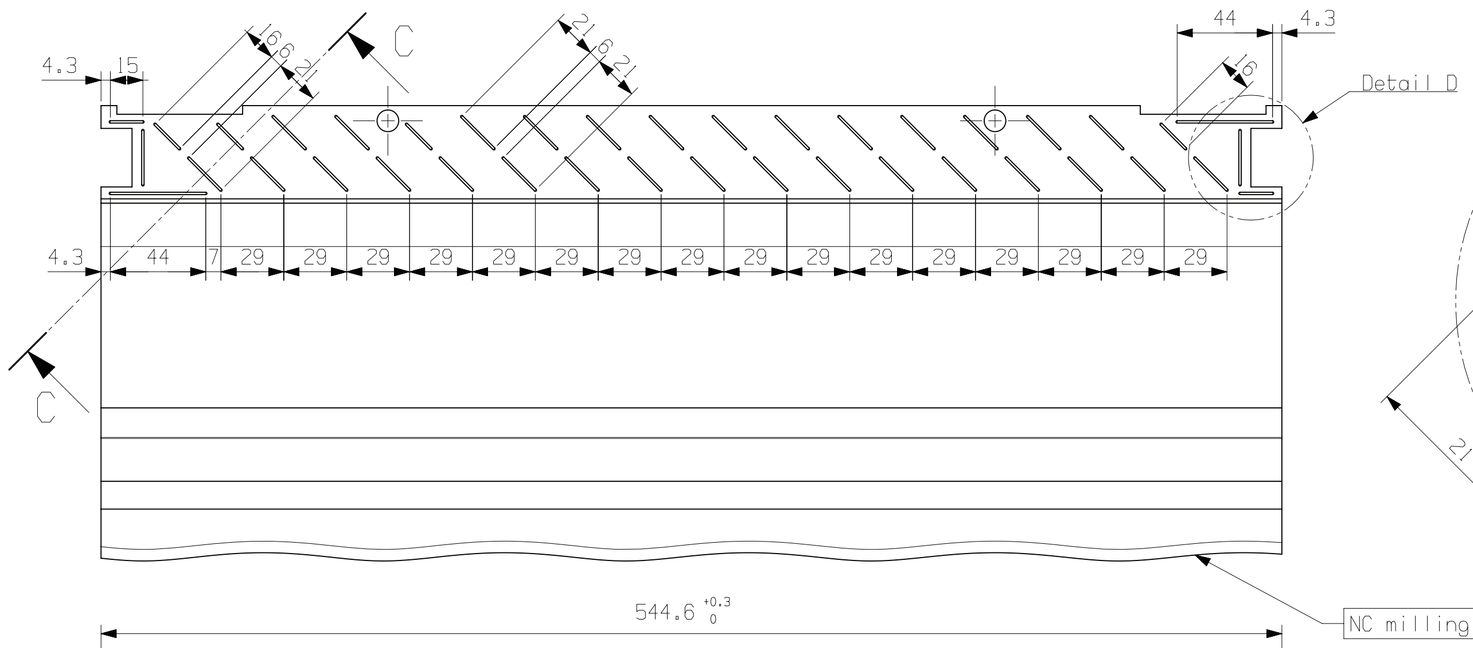

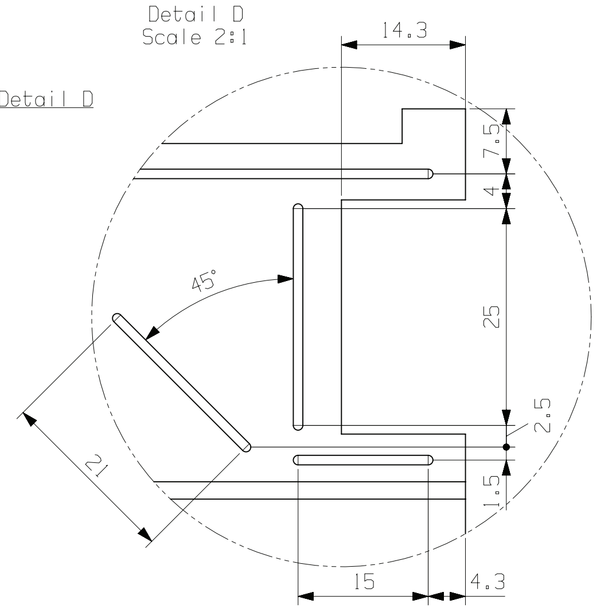

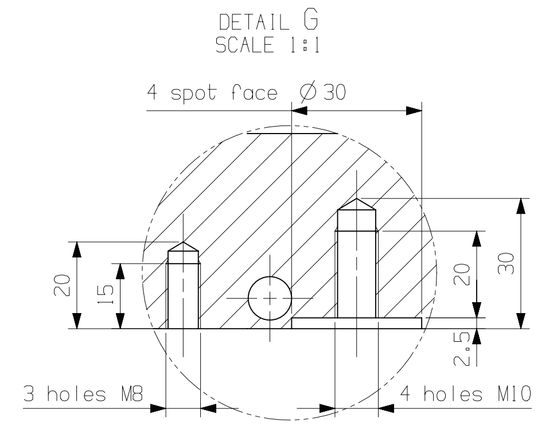

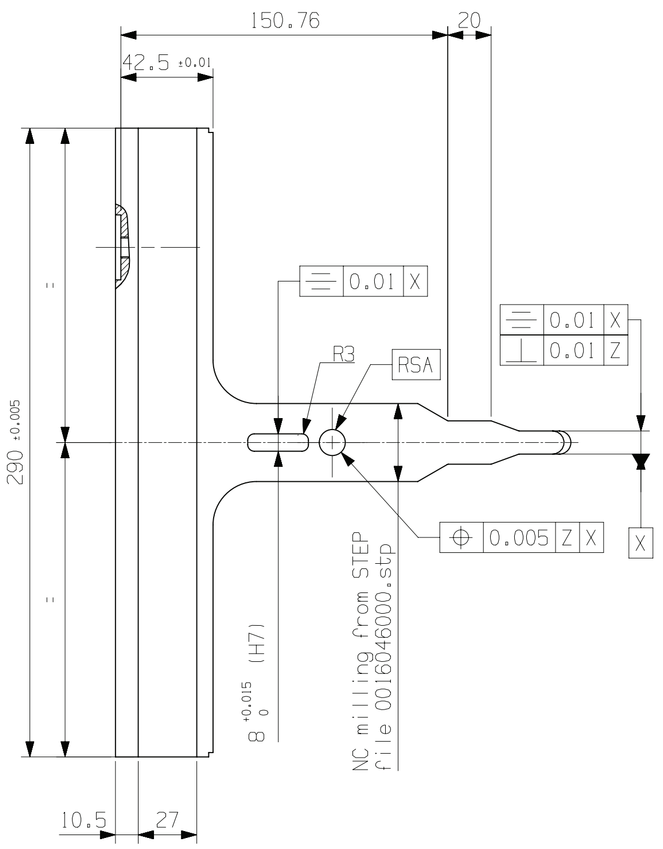

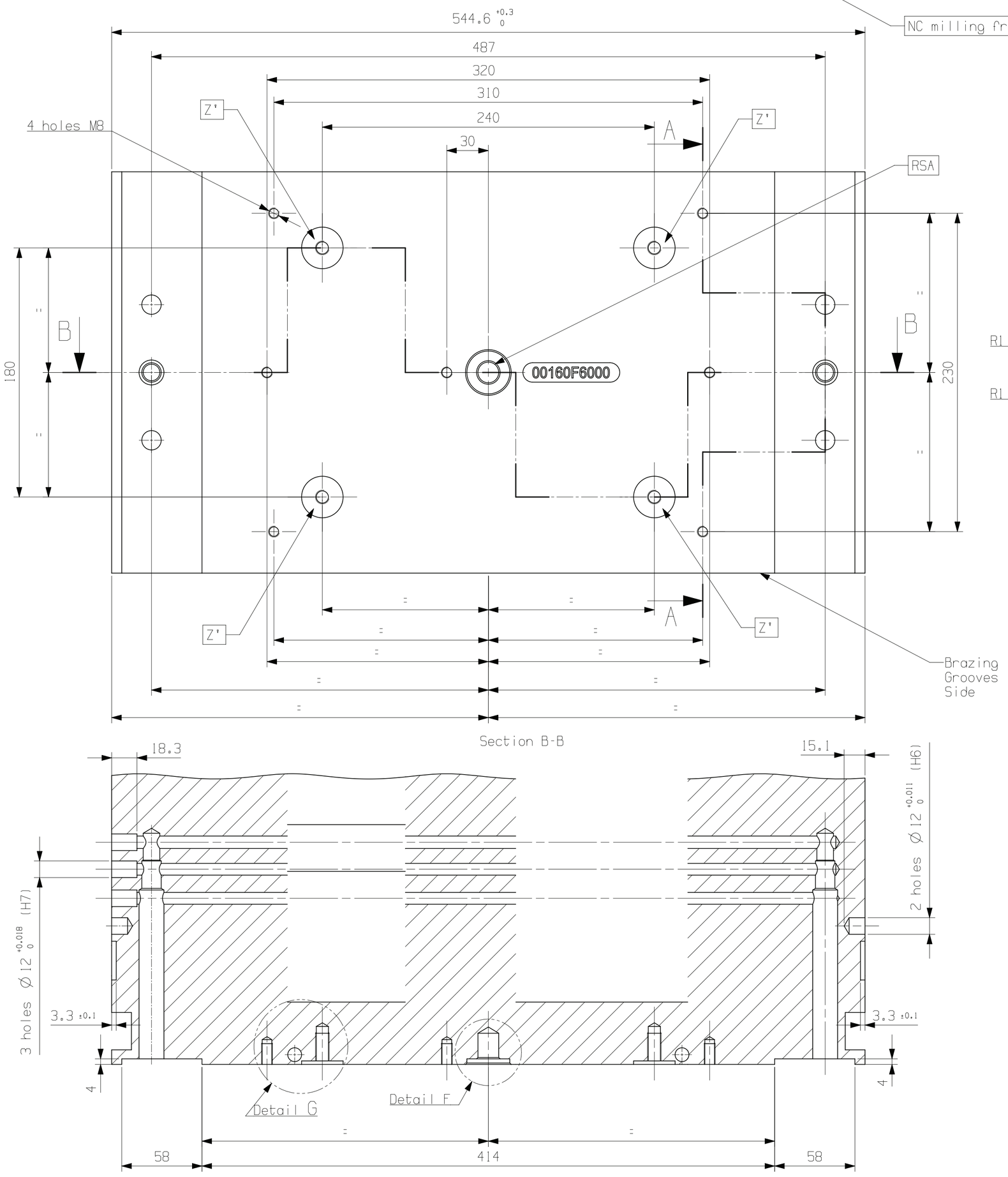

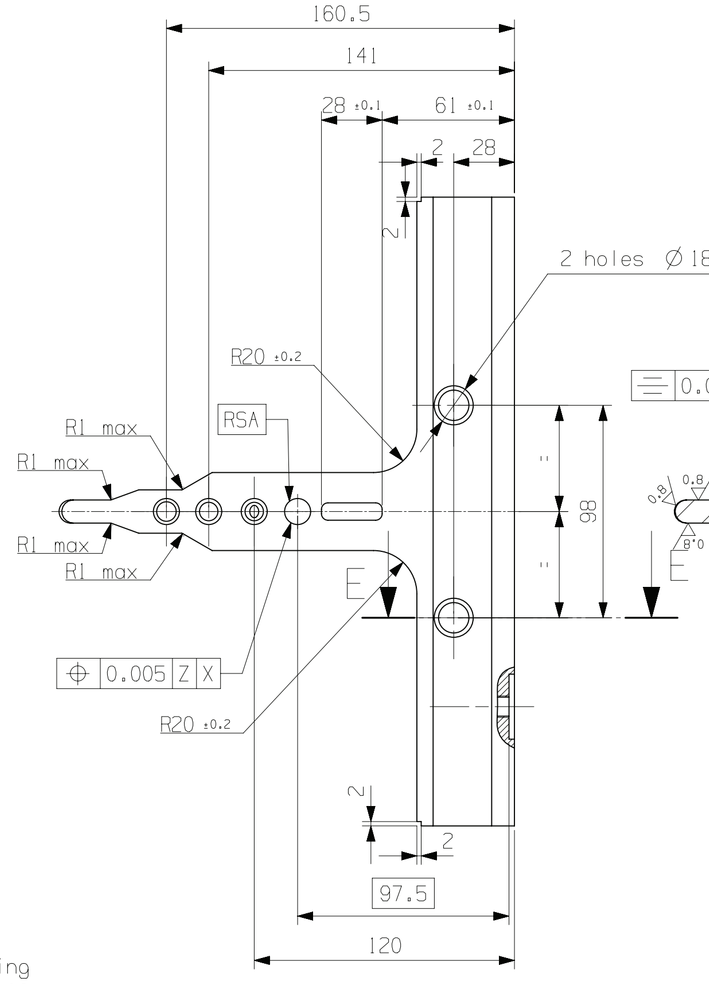

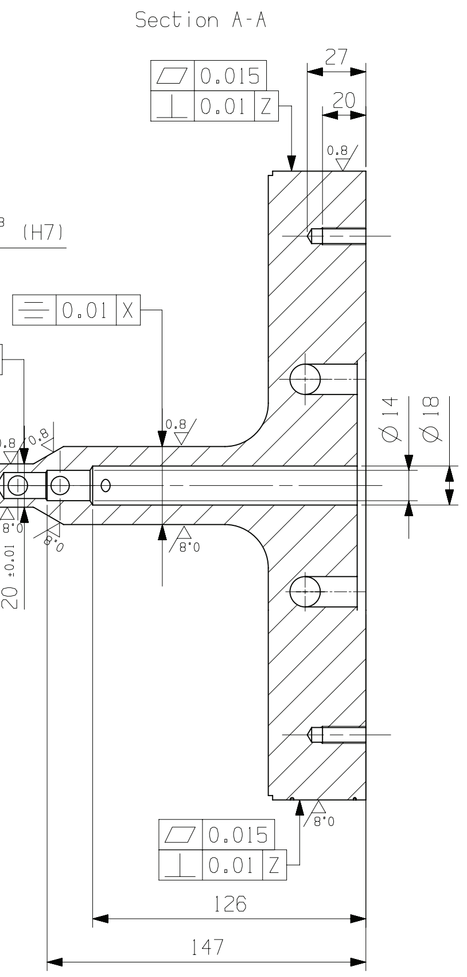

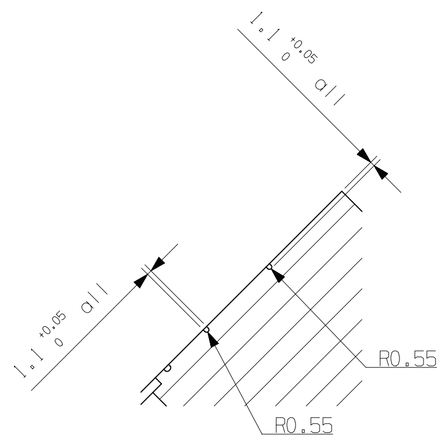

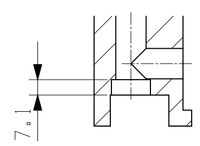

Treatment	MATERIAL		Chamfer	General surface finish	QUANTITY
	CuC2		□ x □□°	R_a (μm): 1.6	1

			GENERAL TOLERANCE									SCALE
Design	INFN	dd-mmm-yy	Dimensions mm	≤6	> 6	> 30	> 120	> 315	>1000	>2000	Shaft h12	1:2
Drawn	Romanato	26-Apr-11	Precision Class UNI 5303	± 0.05	± 0.1	± 0.15	± 0.2	± 0.3	± 0.5	± 0.8		
Check	R. Dima	27-Apr-11	Angular dimensions in mm	> 3 ≤ 6	> 6 ≤ 30	> 30 ≤ 120	> 120				Hole H12	
Appr.	name	dd-mmm-yy	Precision Class UNI 5307	±1°	±10'	±20'	±30'					

IFMIF EVEDA Accelerator System Group

INFN

Dipartimento di Fisica
Galileo Galilei
Via Marzolo n.8
35141 Padova
Tel.: +39 049 8277007
Fax: +39 049 8277031

Servizio Progettazione Meccanica
SEZIONE DI PADOVA

PROJECT RFQ IFMIF

TITLE: Quadrupole Bottom

DRAWING No.: 0016046000

SHEET 1

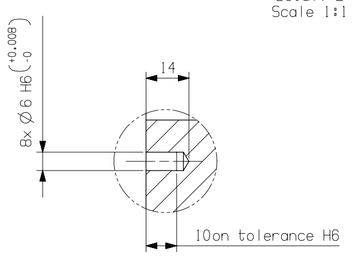

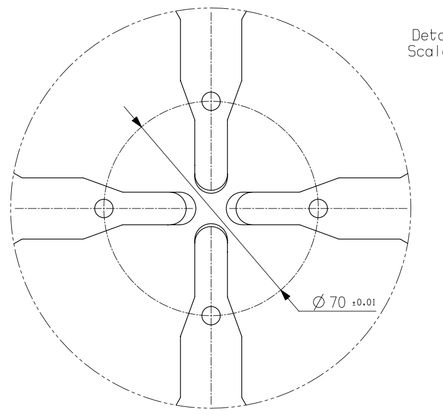

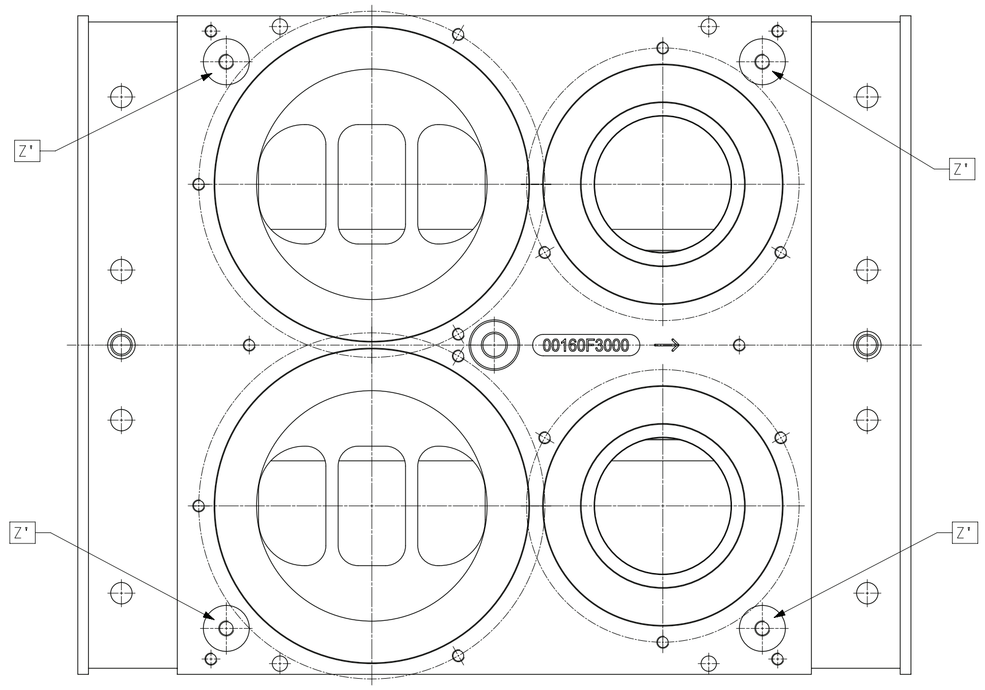

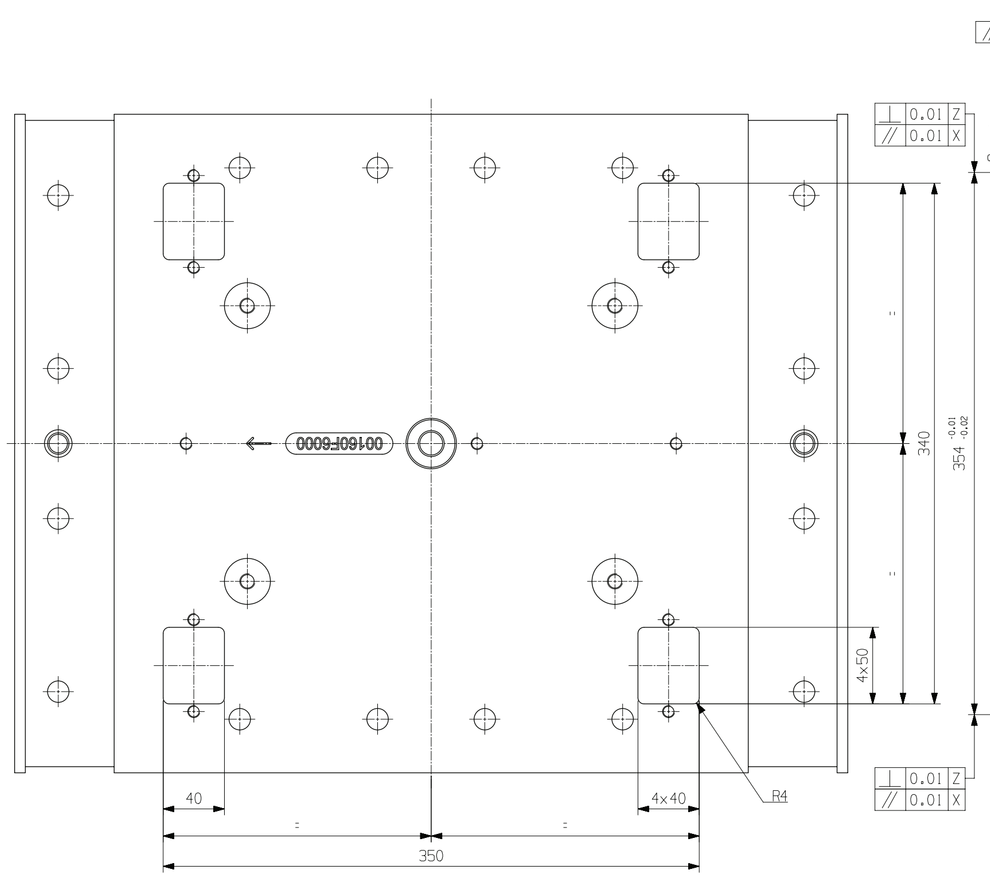

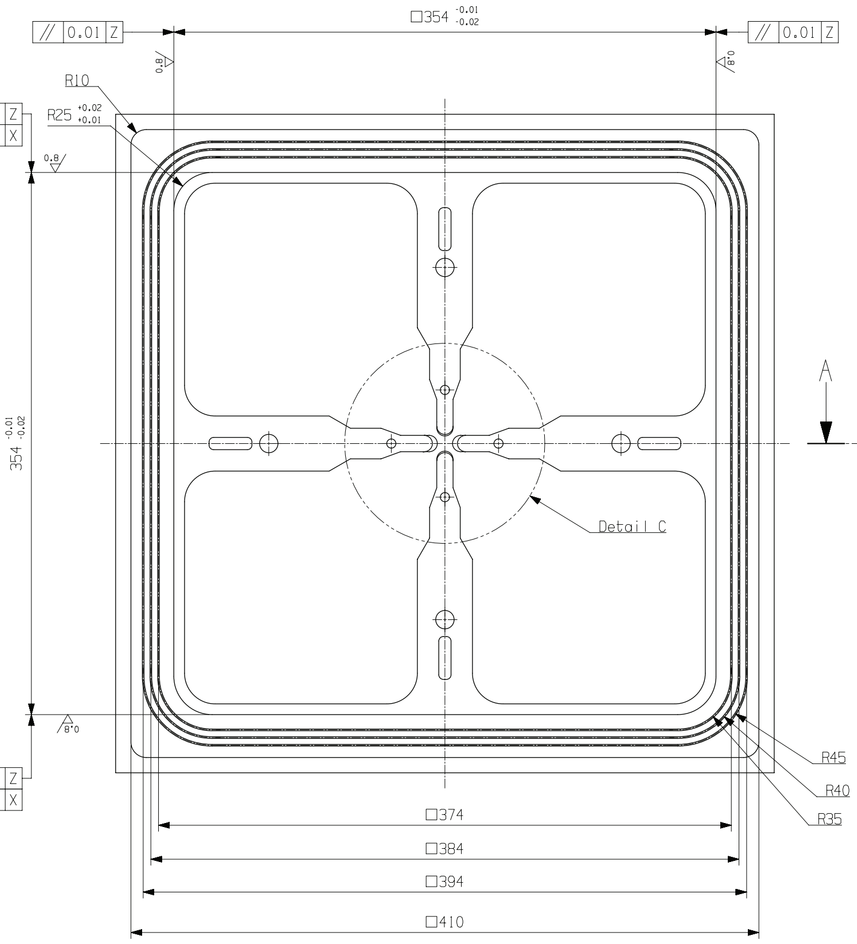

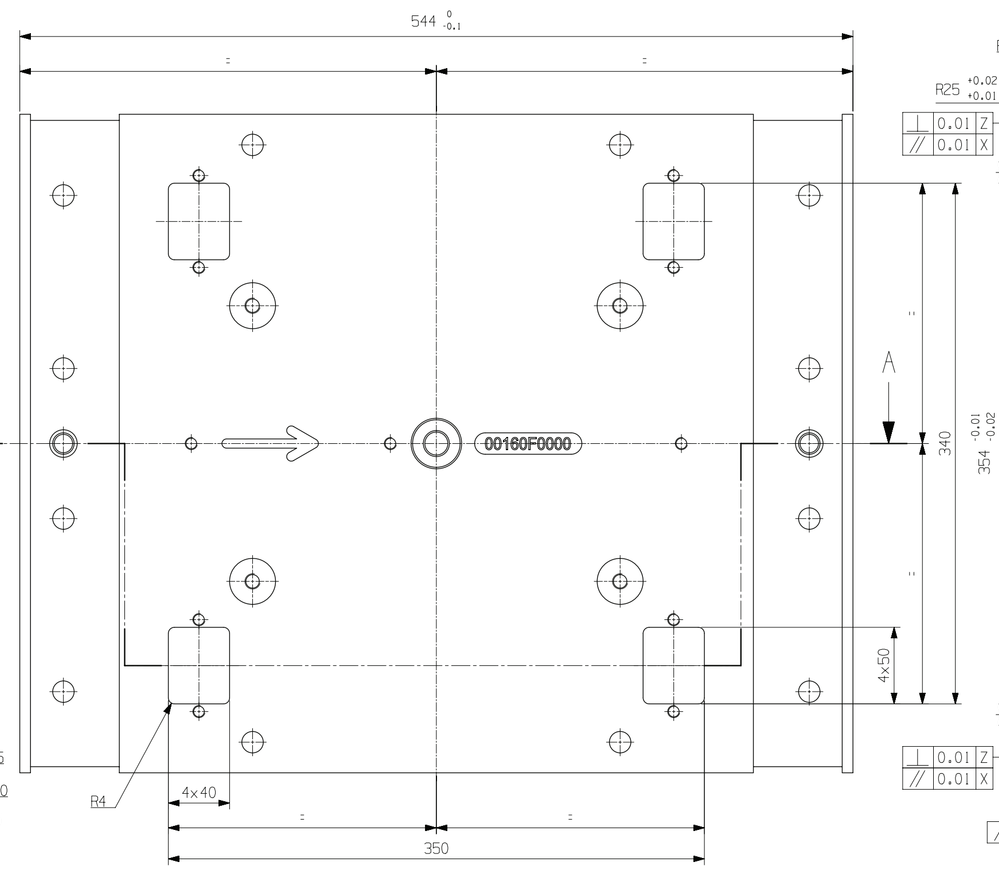

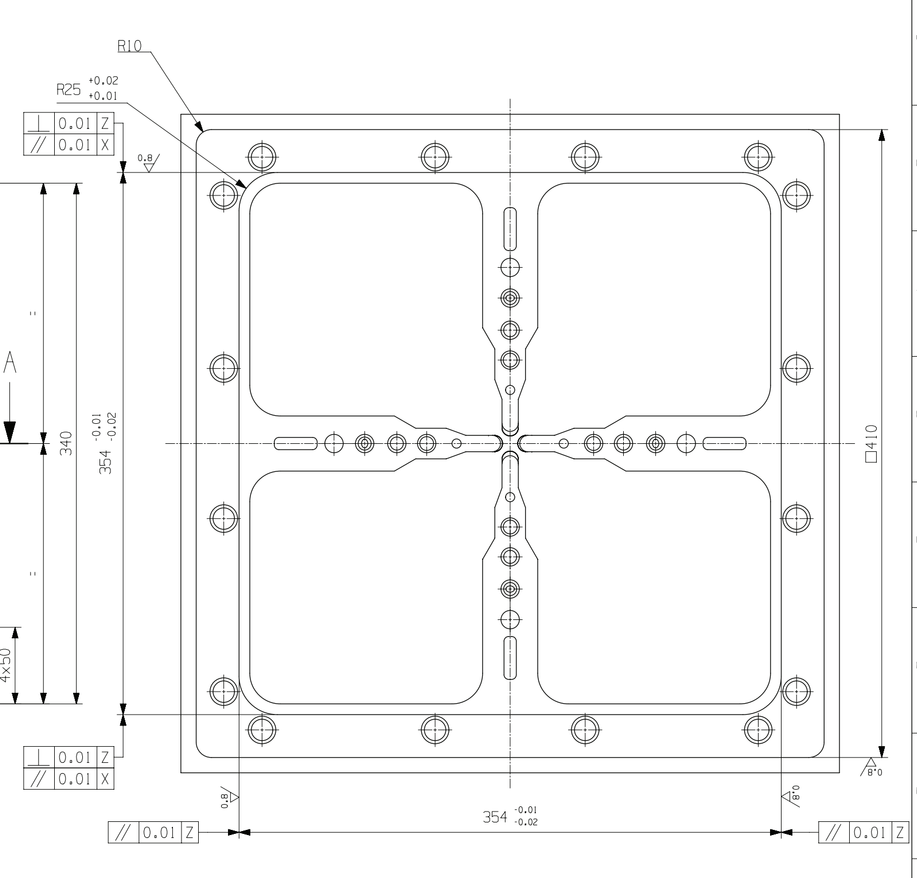

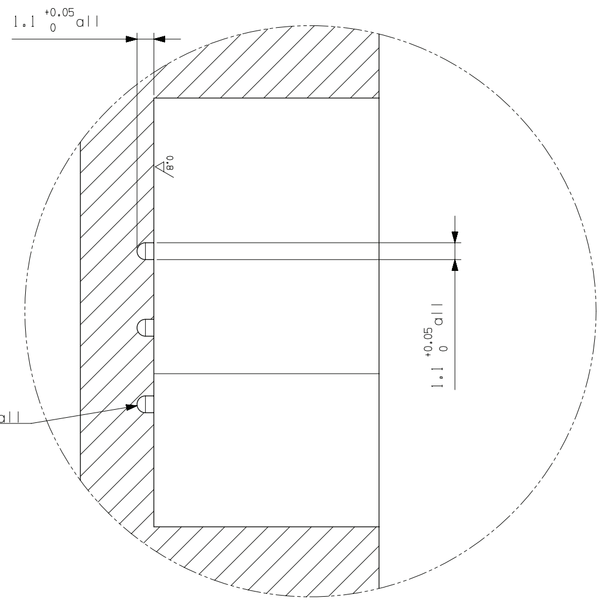

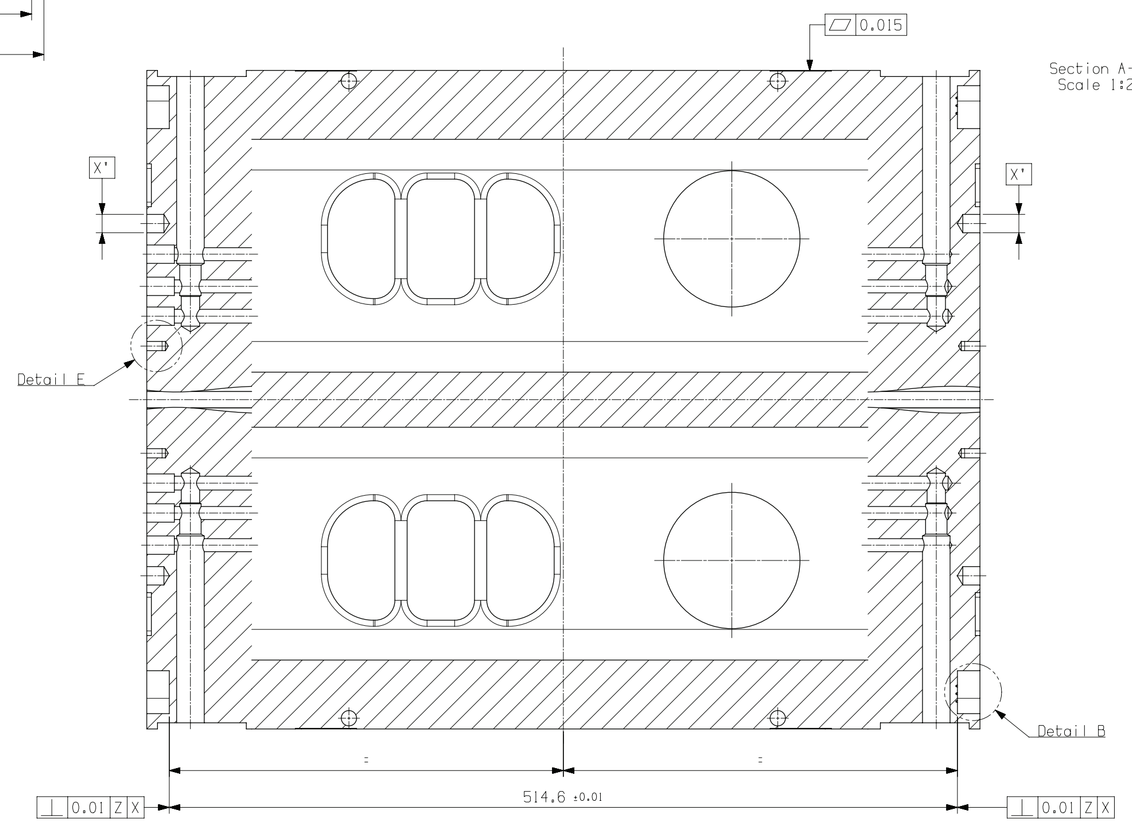

4xZ'=Z=RSA
Common Zone
▱ 0.01

2xX'=X=RSA

RSA= Reference Surface
for CMM Alignment

Treatment		MATERIAL	Chamfer	General surface finish	QUANTITY
		CuC2	□ x □°	R_a (μm): 1.6	1

													SCALE
Design	INFN	dd-mmm-yy	GENERAL TOLERANCE	Dimensions mm	=6	> 6	> 30	> 120	> 315	>1000	>2000	Shaft h12	1:2
Drawn	Romanato	14-Nov-11		Precision Class UNI 5303	± 0.05	± 0.1	± 0.15	± 0.2	± 0.3	± 0.5	± 0.8		
Check	R. Dima	28-Nov-11		Angular dimensions in mm	> 3 = 6	> 6 = 30	> 30 = 120	> 120				Hole H12	
Appr.	name	dd-mmm-yy		Precision Class UNI 5307	±1°	±10'	±20'	±30'					

IFMIF EVEDA Accelerator System Group
INFN
Dipartimento di Fisica
Galileo Galilei
Via Marzolo n.8
35141 Padova
Tel.: +39 049 8277007
Fax: +39 049 8277031
Servizio Progettazione Meccanica
SEZIONE DI PADOVA

PROJECT RFQ IFMIF

TITLE: Machining Before Brazing

DRAWING No.: 0416051000

SHEET 1

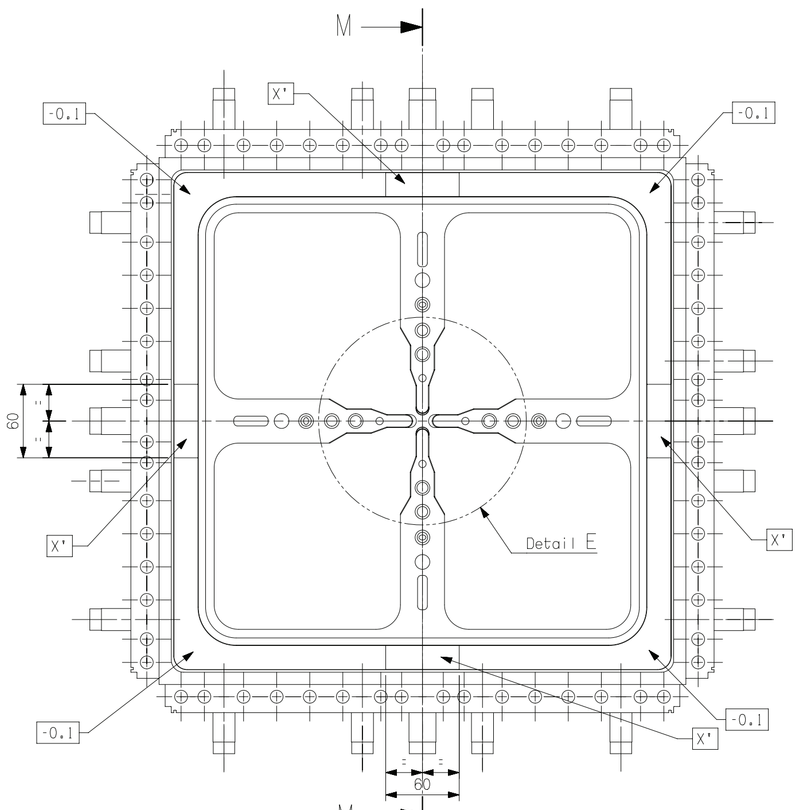

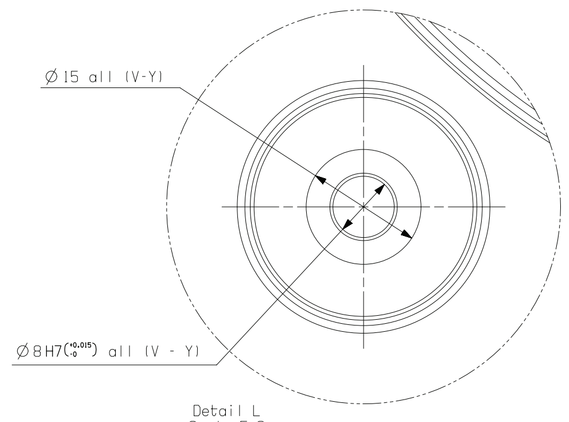

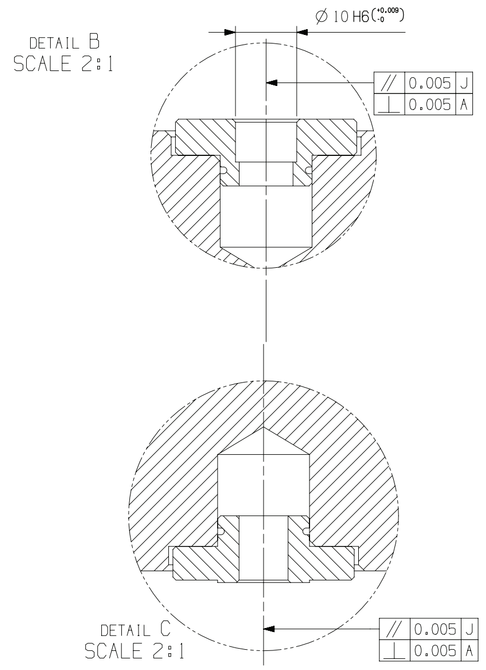

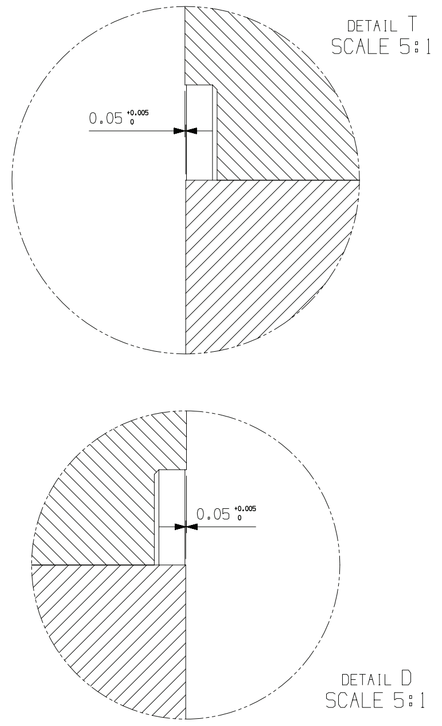

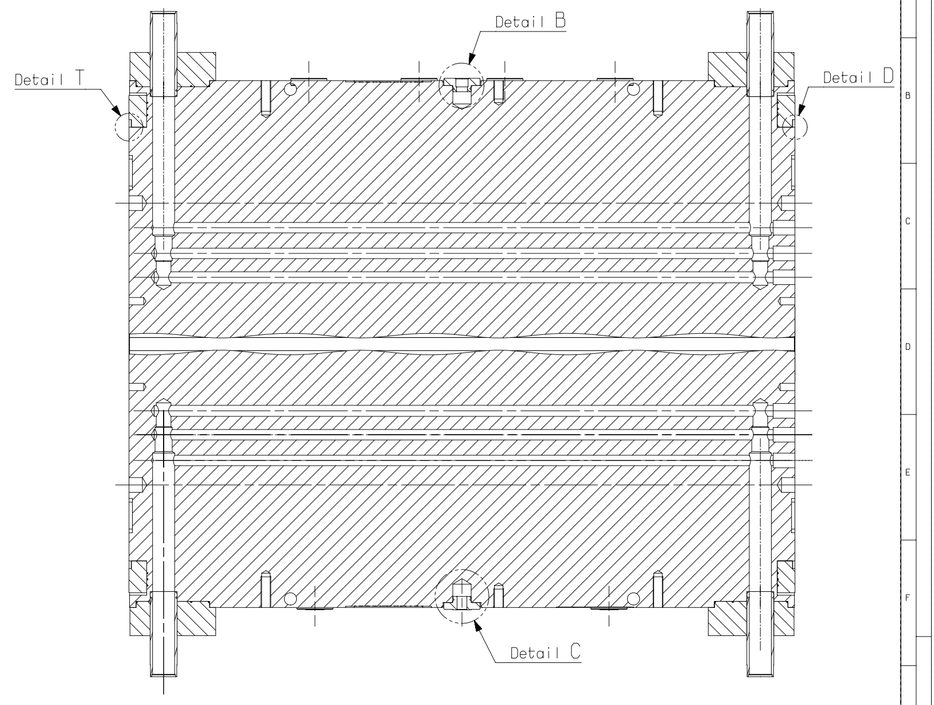

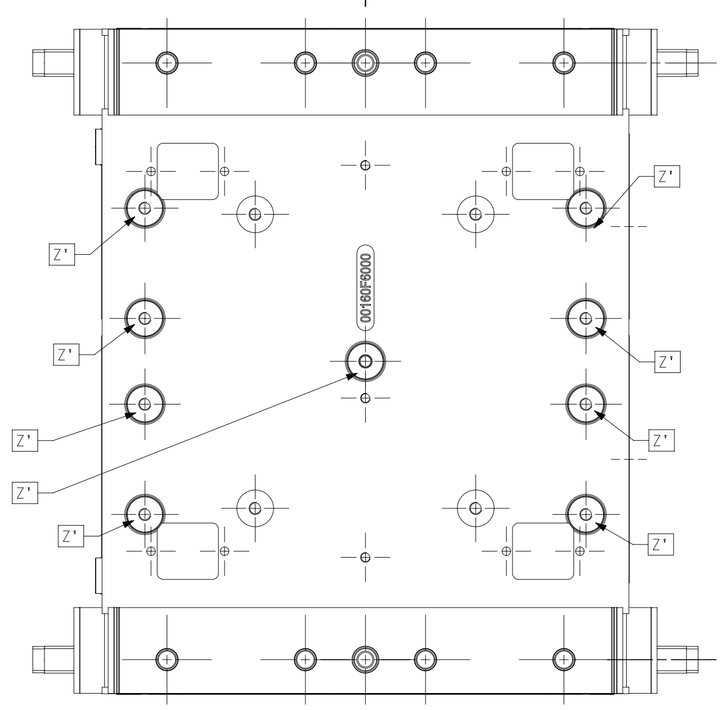

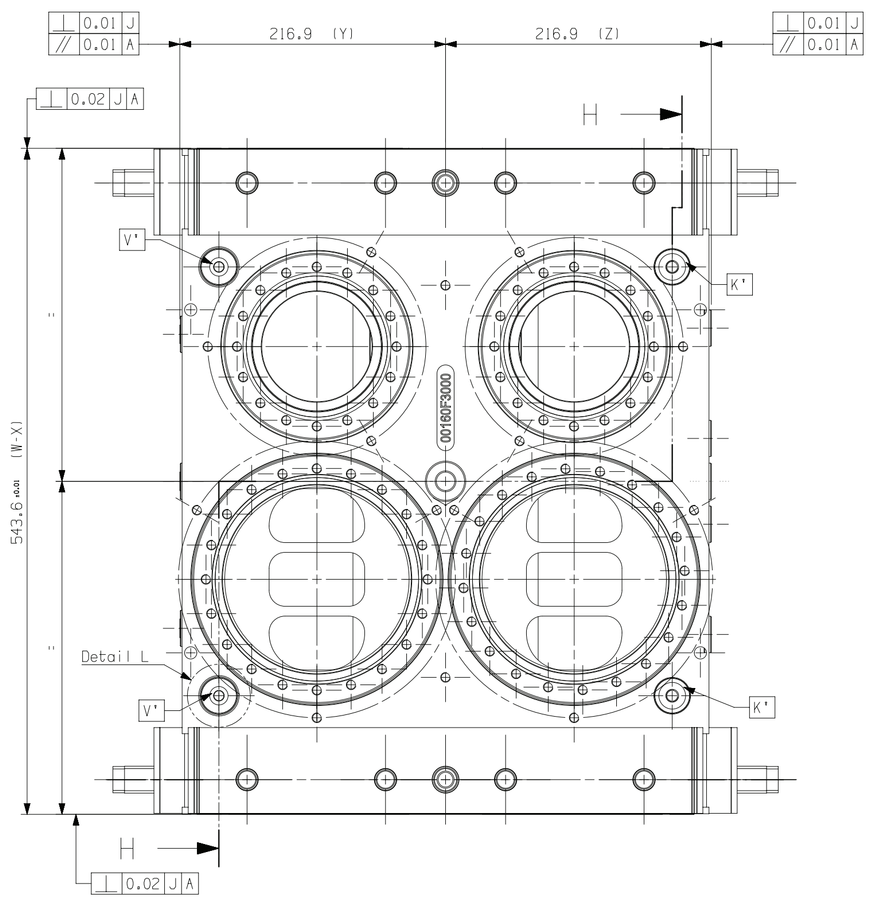

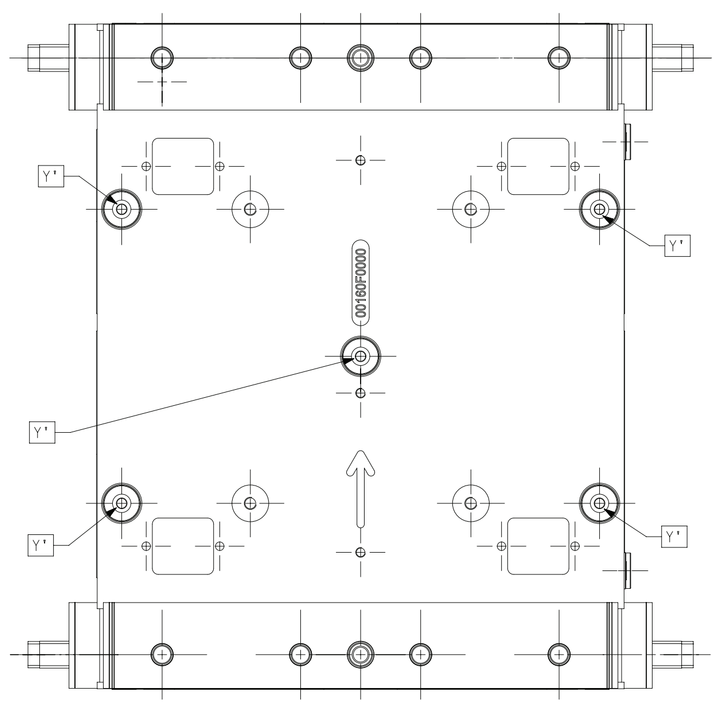

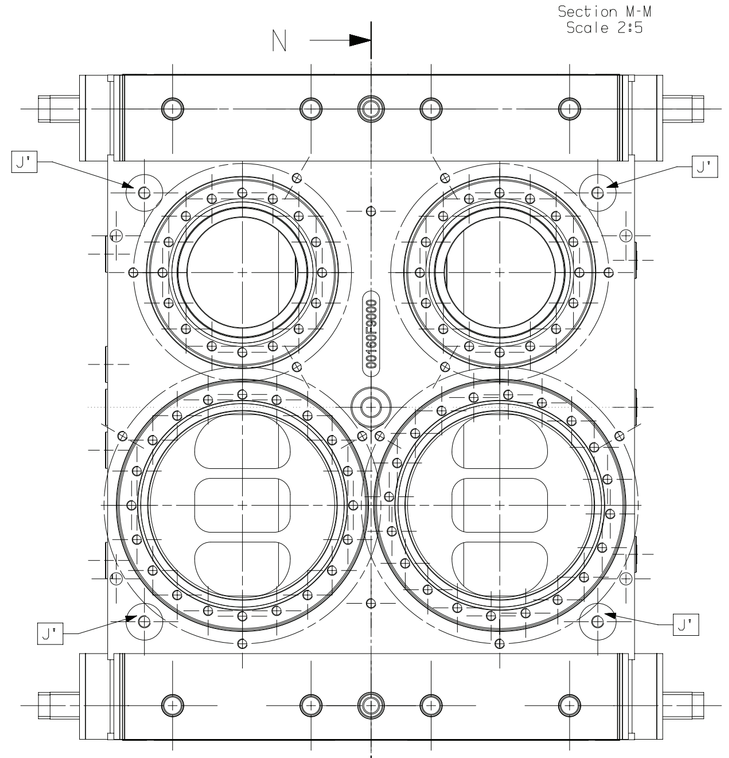

Section M-M
Scale 2:5

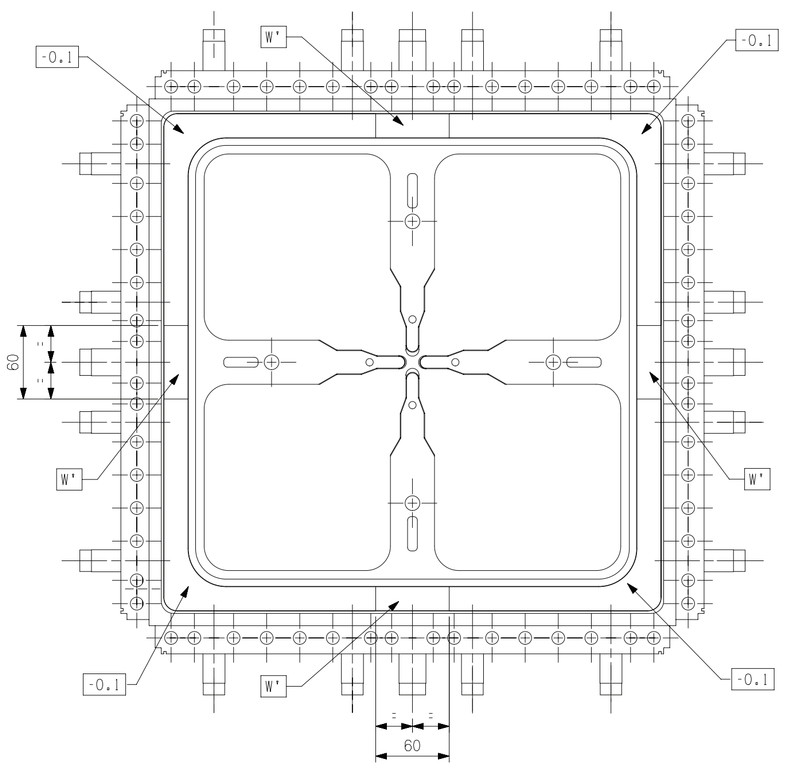

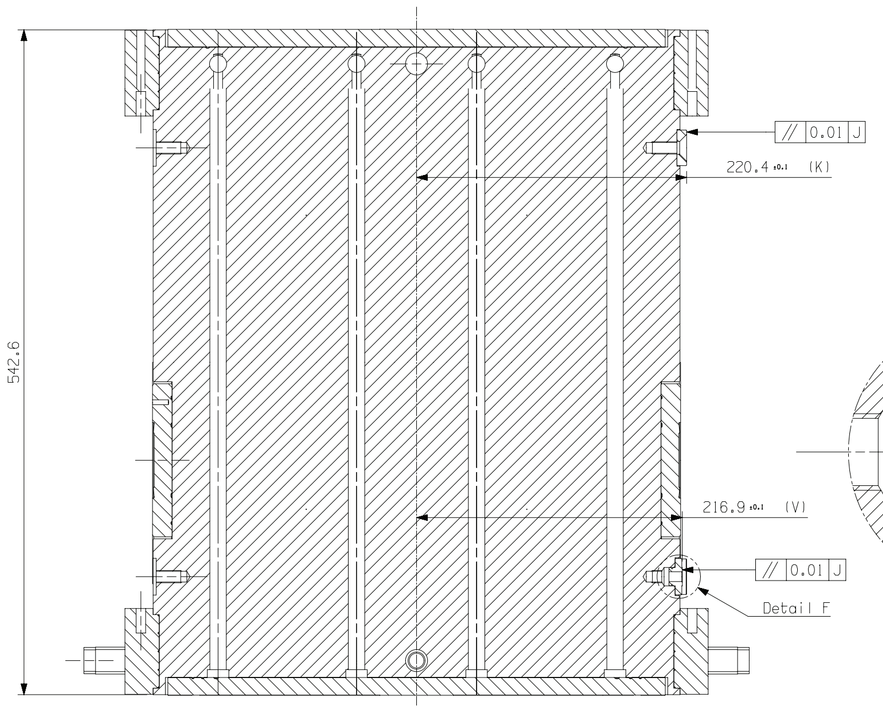

Section H-H
Scale 2:5

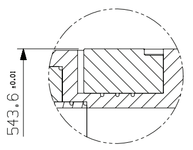

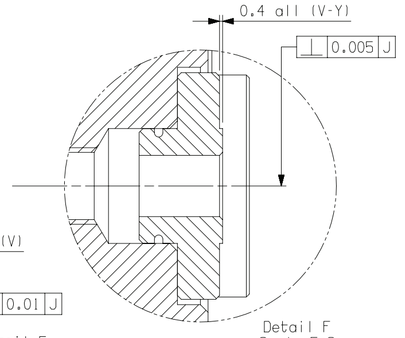

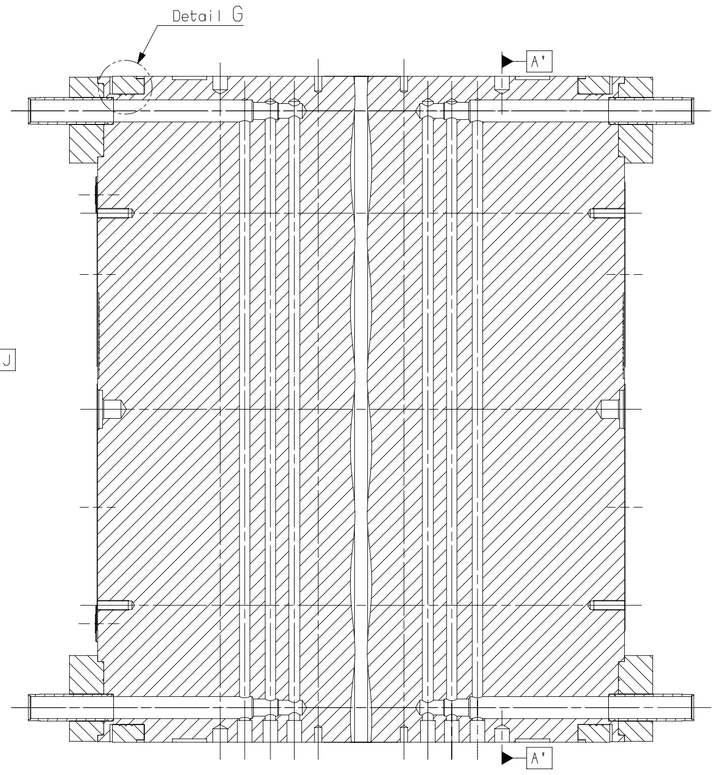

SECTION N-N
SCALE 2:5

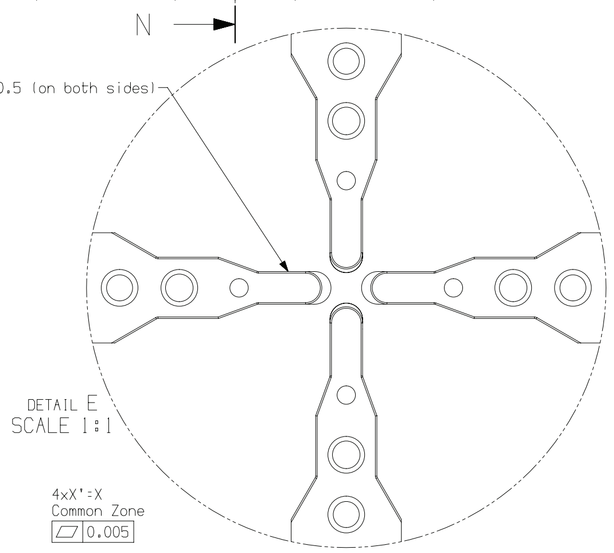

DETAIL E
SCALE 1:1

4xX':X
Common Zone
⏥ 0.005

4xW':W
Common Zone
⏥ 0.005

2xK':K
Common Zone
⏥ 0.01

2xV':V
Common Zone
⏥ 0.01

4xJ':J:RSA
Common Zone
⏥ 0.01

9xZ':Z
Common Zone
⏥ 0.01

4xY':Y
Common Zone
⏥ 0.01

4xZ':Z
Common Zone
⏥ 0.01

2xA':A:RSA

Treatment		MATERIAL				Chamfer		General surface finish		QUANTITY				
		CuC2				□ x □		Rz≤1.6		1				
Design	INFN	dd-mmm-yy		Dimensions in		≤ 6	> 6 ÷ 30	> 30 ÷ 120	> 315 ÷ 1000	> 1000	DIN 7168	h12	SCALE	1:2.5
Drawn	Romanato	05-Apr-12		Precision Class UNI 3383		± 0.05	± 0.1	± 0.15	± 0.3	± 0.5	± 0.8			
Check	R. Dima	29-May-12		Angular dimensions in		> 3 ÷ 6	> 6 ÷ 10	> 10 ÷ 120	> 120		Table	H12		
Appr.	name	dd-mmm-yy		Precision Class UNI 3397		±1°	±30'	±20'	±10'					

Istituto Nazionale di Fisica Nucleare
Sezione Padova
Via Marzolo, 8
I-35131 Padova
Tel.+39 049 8277000
Fax +39 049 8277102

Servizio Progettazione Meccanica
SEZIONE DI PADOVA

The current drawing, in accordance with the law, is INFN property. It cannot be copied, autho rized or used by thirds.

PROJECT RFQ IFMIF

TITLE: Machining after Brazing 2

DRAWING No.: 0405071000

SHEET 1/1